AD-A125 858 EXPERIMENTAL STUDIES OF LATERAL ELECTRON TRANSPORT IN 1/3
GALLIUM ARSENIDE-AL..(U) ILLINOIS UNIV AT URBANA
COORDINATED SCIENCE LAB M R KEEVER DEC 82 R-975
UNCLASSIFIED N00014-76-C-0806 F/G 20/12 NL

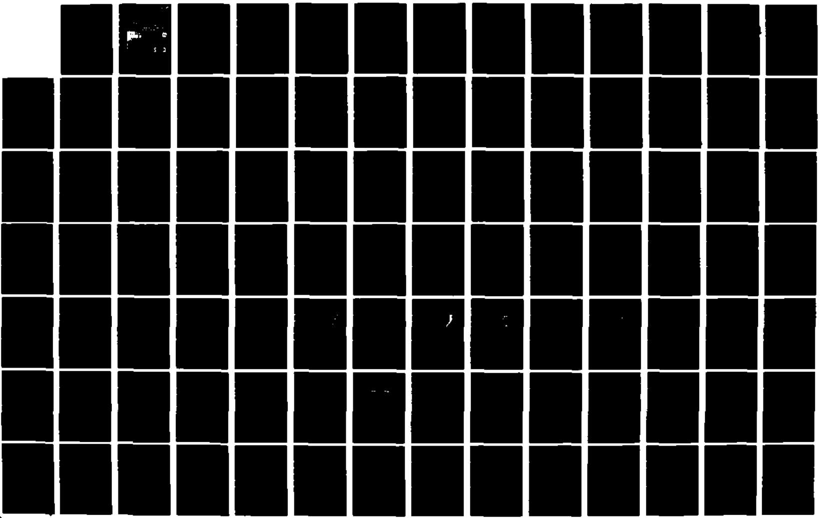

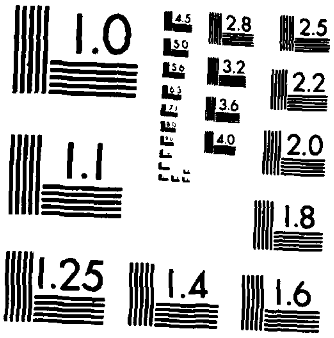

MICROCOPY RESOLUTION TEST CHART
NATIONAL BUREAU OF STANDARDS-1963-A

12

REPORT R-975 DECEMBER, 1982 UILU-ENG 82-2241

COORDINATED SCIENCE LABORATORY

AD A125858

EXPERIMENTAL STUDIES OF LATERAL ELECTRON TRANSPORT IN GALLIUM ARSENIDE-ALUMINUM GALLIUM ARSENIDE HETEROSTRUCTURES

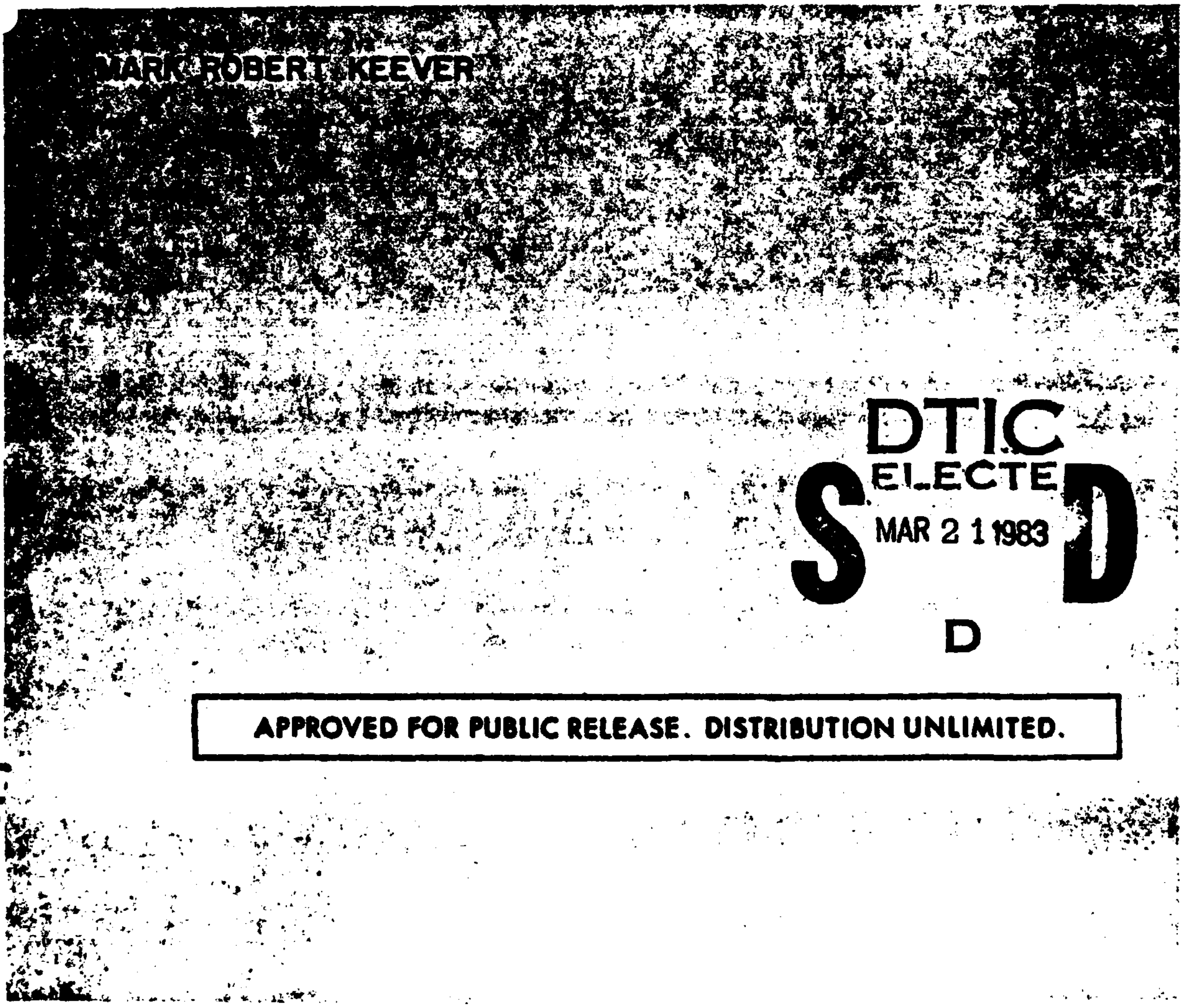

MARK ROBERT KEEVER

DTIC
ELECTE
MAR 21 1983
S D
D

APPROVED FOR PUBLIC RELEASE. DISTRIBUTION UNLIMITED.

DTIC FILE COPY

UNIVERSITY OF ILLINOIS – URBANA-CHAMPAIGN

REPORT DOCUMENTATION PAGE	READ INSTRUCTIONS BEFORE COMPLETING FORM
1. REPORT NUMBER	2. GOVT ACCESSION NO. AD-A125858
	3. RECIPIENT'S CATALOG NUMBER
4. TITLE (and Subtitle) EXPERIMENTAL STUDIES OF LATERAL ELECTRON TRANSPORT IN GALLIUM ARSENIDE-ALUMINUM GALLIUM ARSENIDE HETEROSTRUCTURES	5. TYPE OF REPORT & PERIOD COVERED Technical Report R-975
	6. PERFORMING ORG. REPORT NUMBER UILU-ENG 82-2241
7. AUTHOR(s) Mark Robert Keever	8. CONTRACT OR GRANT NUMBER(s) N00014-76-C-0806
9. PERFORMING ORGANIZATION NAME AND ADDRESS Coordinated Science Laboratory University of Illinois 1101 W. Springfield Ave. Urbana, IL 61801	10. PROGRAM ELEMENT, PROJECT, TASK AREA & WORK UNIT NUMBERS
11. CONTROLLING OFFICE NAME AND ADDRESS Office of Naval Research	12. REPORT DATE December, 1982
	13. NUMBER OF PAGES 216
14. MONITORING AGENCY NAME & ADDRESS (if different from Controlling Office)	15. SECURITY CLASS. (of this report) Unclassified
	15a. DECLASSIFICATION/DOWNGRADING SCHEDULE

16. DISTRIBUTION STATEMENT (of this Report)

Approved for public release; distribution unlimited.

17. DISTRIBUTION STATEMENT (of the abstract entered in Block 20, if different from Report)

18. SUPPLEMENTARY NOTES

19. KEY WORDS (Continue on reverse side if necessary and identify by block number)

Semiconductors
Heterostructures
Gallium Arsenide
Aluminum Gallium Arsenide
Hot Electrons
Real-Space Transfer

20. ABSTRACT (Continue on reverse side if necessary and identify by block number)

The electron-transport characteristics of modulation-doped GaAs-Al$_x$Ga$_{1-x}$As heterostructures have been measured over a wide range of temperatures using a diverse set of device structures. Short voltage pulses were used to apply a broad range of lateral (parallel to the interface) electric fields and the resulting current-field characteristics were determined using a sampling oscilloscope and x-y recorder.

It was observed that the high electron mobility in these structures initially increased as the electric field was increased from zero. The low-field mobility

20.

reached a maximum at fields below 500 V/cm and then dropped quickly at low temperatures for increasingly higher electric fields. At higher temperatures (200 K to 300 K) there was comparatively little change in the mobility for fields up to 2 kV/cm.

For higher fields (above 2 kV/cm) it was found that the electrons could gain enough energy to be thermionically emitted over the conduction-band discontinuity from the high-mobility GaAs to the low-mobility AlGaAs. This real-space transfer (RST) of electrons resulted in current saturation or various degrees of negative differential resistance (NDR) in the samples being studied. The characteristics of the NDR were found to be adjustable by changing the sample growth parameters such as the AlAs mole fraction, layer widths, and doping concentrations. It was also observed that the NDR could be significantly enhanced in many samples by illuminating the surface of the heterostructure. In a few structures, the increase in conductivity due to the photoconductive effect was found to persist at low temperatures long after the source of illumination was removed.

It was demonstrated that the new real-space transfer mechanism could be used in the creation of fast electron switching and storage devices and also high-frequency oscillators. The frequency of the oscillation was shown to be controlled by an external circuit and was not dependent on the sample length. The NDR occurring at high fields due to RST will also have an important influence on all heterostructure devices such as FETs which depend on high-speed electron transport parallel to the layers.

EXPERIMENTAL STUDIES OF LATERAL ELECTRON TRANSPORT IN GALLIUM ARSENIDE-ALUMINUM GALLIUM ARSENIDE HETEROSTRUCTURES

BY

MARK ROBERT KEEVER

B.S., Iowa State University of Science and Technology, 1977
M.S., University of Illinois, 1979

THESIS

Submitted in partial fulfillment of the requirements
for the degree of Doctor of Philosophy in Electrical Engineering
in the Graduate College of the
University of Illinois at Urbana-Champaign, 1983

Urbana, Illinois

EXPERIMENTAL STUDIES OF LATERAL ELECTRON TRANSPORT IN GALLIUM ARSENIDE-ALUMINUM GALLIUM ARSENIDE HETEROSTRUCTURES

Mark Robert Keever, Ph.D.
Department of Electrical Engineering
University of Illinois at Urbana-Champaign, 1983

The electron-transport characteristics of modulation-doped GaAs-$Al_xGa_{1-x}As$ heterostructures have been measured over a wide range of temperatures using a diverse set of device structures. Short voltage pulses were used to apply a broad range of lateral (parallel to the interface) electric fields and the resulting current-field characteristics were determined using a sampling oscilloscope and x-y recorder.

It was observed that the high electron mobility in these structures initially increased as the electric field was increased from zero. The low-field mobility reached a maximum at fields below 500 V/cm and then dropped quickly at low temperatures for increasingly higher electric fields. At higher temperatures (200 K to 300 K) there was comparatively little change in the mobility for fields up to 2 kV/cm.

For higher fields (above 2 kV/cm) it was found that the electrons could gain enough energy to be thermionically emitted over the conduction-band discontinuity from the high-mobility GaAs to the low-mobility AlGaAs. This real-space transfer (RST) of electrons resulted in current saturation or various degrees of negative differential resistance (NDR) in the samples being studied. The characteristics of the NDR were found to be adjustable by changing the sample growth parameters such as the AlAs mole fraction, layer widths, and doping concentrations. It was also observed that the NDR could be significantly enhanced in many samples by illuminating the surface of the heterostructure. In a few structures, the increase in conductivity due to the photoconductive effect was found to persist at low temperatures long after the source of illumination was removed.

It was demonstrated that the new real-space transfer mechanism could be used in the creation of fast electron switching and storage devices and also high-frequency oscillators. The frequency of the oscillation was shown to be controlled by an external circuit and was not dependent on the sample length. The NDR occurring at high fields due to RST will also have an important influence on all heterostructure devices such as FETs which depend on high-speed electron transport parallel to the layers.

ACKNOWLEDGEMENTS

The author is deeply indebted to his academic advisor Professor K. Hess for introducing him to the field of hot electron transport in heterostructures and the concept of real-space electron transfer. His continual insight, guidance, and good humor have been greatly appreciated.

A special debt of gratitude is also owed to Professor H. Morkoç for providing the MBE heterostructure wafers and to Dr. M. Ludowise for providing the MOCVD wafers. Without the heterostructure material supplied by these men this research project would not have been possible.

The author also wishes to acknowledge the guidance, assistance, and support of Professors B. G. Streetman, N. Holonyak, Jr., and G. E. Stillman.

The author is grateful to Professor P. D. Coleman for demonstrating the tunable oscillation capabilities of a real-space transfer device.

The assistance and cooperation of B. Bereznak in performing some of the measurements of persistent photoconductivity and Corbino magnetoresistance are gratefully acknowledged.

The author is especially grateful to his good friend and co-worker Dr. J. D. Oberstar for providing many helpful suggestions and sharing his considerable technical expertise. His good humor and stories were also a constant source of enjoyment.

Special thanks go to S. Banerjee, S. S. Chan, and T. J. Drummond for their friendship and helpful cooperation and assistance in the laboratory. The author is also very grateful for the friendship and cooperation of J. Y. Tang, K. Brennan, T. C. Hsieh, P. Martin, P. Gavrilovic, Dr. H. Shichijo, W. Kopp, Dr. T. Windhorn, K. Byerly, and Dr. A. Bhattacharyya.

For their outstanding technical support the author is indebted to the CSL staff members C. Lofton, R. MacFarlane, A. Kimball, R. Gladin, L. Bandy, G. Bouck, B. Bales, B. Beaulin, N. Vassos, R. Ebeling, B. Champagne, and E. Kesler. The expert assistance provided by S. Brennecke in typing this lengthy manuscript is sincerely appreciated.

Finally, the author wishes to thank his parents for their support and encouragement throughout his many years of education.

TABLE OF CONTENTS

CHAPTER PAGE

1. INTRODUCTION

The study of heterostructures made from joining two or more III-V compounds began less than 20 years ago, but today it occupies a prominent position in semiconductor research. The swift growth of heterostructure research on GaAs and $Al_xGa_{1-x}As$ compounds stems from their many interesting properties which include a band structure that allows the construction of transferred-electron devices, a direct (adjustable) band gap for optical applications, and the ability to be epitaxially grown lattice-matched to each other. Of the variety of heterostructures currently being studied, it is this combination of GaAs and $Al_xGa_{1-x}As$ that has attracted the most research attention.

The first growth of a GaAs-$Al_xGa_{1-x}As$ heterostructure in this country was reported in 1967 when Woodall, Rupprecht and co-workers [1] reported the growth of $Al_xGa_{1-x}As$ on GaAs using liquid phase epitaxy (LPE). During the next few years this heterostructure was investigated solely for light-emitting applications such as heterostructure lasers.

In the early 1970's, the new epitaxial growth methods of molecular beam epitaxy (MBE) and metalorganic chemical vapor deposition (MOCVD) began to become important for growing a variety of multilayered GaAs-AlGaAs heterostructures. After the experimental realization of the concept of modulation doping in 1978 [5], new attention began to focus on the lateral (parallel to the layers) electron-transport characteristics of GaAs-$Al_xGa_{1-x}As$ heterostructures for use in devices such as FETs. This new interest in electron-transport devices using heterostructures resulted from the verification that lateral electron mobilities (in directions parallel to the heterolayers) in modulation-doped (MD) GaAs-$Al_xGa_{1-x}As$ structures are much larger than those of equivalently-doped bulk GaAs, especially at low temperatures. This enhanced mobility is attributed to the spatial separation of electrons in the GaAs from their parent donors in the AlGaAs and the effective screening of background charges, which significantly reduces the ionized-impurity scattering rate at low temperatures [5-10]. Modulation doping will be discussed in further detail in Chapter 2.

It has been proposed that the lateral high-mobility characteristics of MD heterostructures can be used to great advantage in the construction of high-speed FETs and other devices that need high-speed electron transport. Several laboratories are presently engaged in active research in this area [11-25] and to date, they have reported success in the improvement of GaAs-$Al_xGa_{1-x}As$ heterojunction MESFET (and MISFET) properties at low temperatures over those of a GaAs MESFET.

Several new concepts and device ideas using MD heterostructures have been introduced in the past several years. One suggested set of novel devices would utilize the innovative concept of real-space electron transfer between heterolayers as proposed by Hess and co-workers [26,27]. The real-space transfer mechanism is based on the thermionic emission of hot electrons from the high-mobility GaAs layer to the low-mobility AlGaAs layer in the presence of a laterally-applied high electric field. The transfer of electrons from high-mobility to low-mobility layers can lead to a negative differential resistance (NDR) just as in the Gunn effect [28,29]. In fact, the real-space transfer mechanism is analogous to the Gunn effect caused by a momentum-space (k-space) transfer. The advantage of the real-space transfer mechanism over the Gunn effect, however, lies in its degree of control of device characteristics. As will be discussed in Chapter 5, device properties such as the electric field threshold for NDR, and the peak-to-valley ratio can be adjusted by changing one or more parameters of the heterostructure growth process. Some of the attractive applications of real-space transfer include high-frequency oscillators [30], fast switching and storage devices [26,27,31,32] and constant-current regulators [28].

In order to efficiently design these RST devices and heterostructure FETs it is necessary to have a thorough understanding of the electrical and optical properties of the GaAs-$Al_xGa_{1-x}As$ heterolayers. At the time the author began his research, sufficient knowledge and understanding of the MD GaAs-$Al_xGa_{1-x}As$ electrical properties were lacking due to the infancy of the research on modulation-doped structures. There were also uncertainties about trapping and various photoconductive effects connected with these materials.

It has been the intent of the author to experimentally examine the electron-transport characteristics of GaAs-$Al_xGa_{1-x}As$ heterostructures in order to improve the understanding of their properties under applied electric fields. Emphasis has been placed on measuring the electrical responses of the heterostructures over a broad temperature range under conditions where a relatively high electric field (2 - 5 kV/cm) was applied parallel to the junction interfaces. It was believed that these conditions would produce significant insight into the characteristics of real-space transfer and also yield important information about the general hot-electron properties that are crucial to the operation of devices such as heterojunction FETs. The results of these high-field electrical measurements and the consequences for proposed devices will be discussed in Chapter 5. This chapter will also include data showing the general photoconductive characteristics of the heterostructures along with results obtained in collaboration with B. Bereznak on unusual persistent-photoconductive effects.

During the course of this research the author also discovered that several unexpected but very important effects can occur at much lower electric fields (mostly below 1 kV/cm). These low-field effects, which include extreme mobility changes at low temperatures [33,34] and an acoustoelectric effect [28,35], will be presented in Chapter 4.

2. BACKGROUND

2.1 Overview

In order to appreciate the versatility of GaAs-$Al_xGa_{1-x}As$ heterojunction devices it is necessary to understand how the structure of the epitaxial layers determines the mobility enhancement of the material. The following sections will outline the common epitaxial growth processes used to create the heterostructures in addition to providing a detailed description of how the enhanced lateral mobility in the heterostructures comes about. The importance of various growth parameters such as the AlAs mole fraction, layer widths, and carrier concentration in modifying the heterostructure mobility will be carefully identified. The quality of the GaAs-$Al_xGa_{1-x}As$ heterojunction interface will also be discussed in light of recent experimental studies. All of these factors are of fundamental importance in interpreting the experimental data presented in this work and in evaluating the performance of the devices that were fabricated and tested.

2.2 Epitaxial Growth Methods

2.2.1 Molecular Beam Epitaxy (MBE)

Molecular beam epitaxy (MBE) is relatively new among the epitaxial growth techniques and it has become a popular method for growing modulation-doped GaAs-$Al_xGa_{1-x}As$ heterojunction structures. This popularity stems from the fine degree of control that can be obtained in the doping of the heterostructures [3,5,36-38]. The control over growth rate and composition is precise enough that structures can be grown consisting of alternating monolayers of GaAs and AlAs [39]. The apparatus features which make such structures possible are primarily the slow growth rate (~ 1 Å/sec) and the accompanying low-growth temperature.

The wafer growth takes place in an ultrahigh vacuum in which a series of atomic and/or molecular beams impinge from high-temperature effusion cells onto a suitable substrate maintained at an elevated temperature on a heated pedestal. The temperature of, and hence the flux from, each effusion cell is precisely controlled by an electrical-feedback temperature-control system so that the composition profile can be very uniform. Shutters on each cell allow a given beam flux to be initiated or terminated in a time that corresponds to less than 1 Å so the thickness of each layer can be precisely controlled and the interface between two heterostructure components can be sharp -- even on an atomic scale. In addition, the use of molecular beams to supply material to the growing film makes it possible to include analytical tools such as a mass spectrometer, Auger analyzer, and grazing incidence HEED in the vacuum chamber by limiting the region exposed to high vapor flux.

Modulation doping of the GaAs-$Al_xGa_{1-x}As$ materials studied for this work was achieved by synchronization of Si and Al source fluxes so that only the $Al_xGa_{1-x}As$ layers were deliberately doped with Si-donor impurities. A variation of this procedure was sometimes used where the Si beam was shuttered in such a way that 20 - 300 Å of each side of every $Al_xGa_{1-x}As$ layer was not intentionally doped, thus keeping the Si dopant away from the interface region. The growth rate for the GaAs was usually 0.65 - 0.70 μm/hr with the substrate temperature in the range of 580 - 700°C.

MBE-grown wafers were used for the majority of the measurements performed in this research on GaAs-$Al_xGa_{1-x}As$ heterostructures.

2.2.2 Metalorganic Chemical Vapor Deposition (MOCVD)

Although the epitaxial growth of GaAs and $Al_xGa_{1-x}As$ by metalorganic chemical vapor deposition (MOCVD) was first reported in 1971 [2] it is only recently that this technique has been applied to the growth of modulation-doped GaAs-AlGaAs heterostructures [40,41]. Enhanced-mobility multiple-layer structures with properties similar to those grown by MBE have been grown by MOCVD, with growth rates of approximately 2.0 μm/hr [42].

For the MOCVD growth process, the sources of the group III elements Al and Ga are the metalorganics trimethylaluminum (TMAl) and trimethylgallium (TMGa), respectively. The source of the As group V element is the hydride arsine (AsH_3). Physical vapor-phase mixtures of these compounds are pyrolysed in H_2 at substrate temperatures ~ 650 - 750°C to form $Al_xGa_{1-x}As$ alloy films [43,44]. The alloy composition of the film is determined by the relative partial pressures of TMGa and TMAl in the reactor. The $Al_xGa_{1-x}As$ layers can be doped n-type with Se from the hydride source H_2Se.

H_2 is used as the carrier gas for the three metalorganic sources (which are liquids near room temperature) so the source partial pressures are determined by the H_2 carrier gas flow rates that are mass-flow controlled. The epitaxial layer thicknesses are then controlled by the timed sequencing of the appropriate gas-flow path-control valves. The minimum layer thicknesses occurring in any of the MOCVD structures studied by the author were 200 Å although MOCVD-grown layer thicknesses of much less than 20 Å have been demonstrated.

2.2.3 Liquid Phase Epitaxy (LPE)

Liquid phase epitaxy (LPE) is the oldest technique used for growing GaAs-$Al_xGa_{1-x}As$ heterolayers. To date, its principal uses have been in the growth of materials for heterostructure lasers [45], GaAs-AlGaAs heterojunction bipolar transistors [46-48], GaAs-AlGaAs charge-coupled devices [49-51], and other optical devices. Recently, however, this growth technique has also been used to grow modulation-doped GaAs-$Al_xGa_{1-x}As$ heterolayers with successful mobility enhancement [52-54]. Layers less than 500 Å thick can be grown with this method by employing the standard LPE multiple-well graphite boat and slider procedures. Using thin melt techniques [54] the LPE growth rate can be as low as 500 Å/min (3 μm/hr). Modulation-doped GaAs-$Al_xGa_{1-x}As$ structures are not commonly grown by LPE at present and the author did not perform measurements on any LPE heterostructures during the course of his research.

2.3 Layer Structure of Samples

2.3.1 MBE Structures

All the MBE modulation-doped heterojunction structures used for this research were grown on (100) oriented, Cr-doped, semi-insulating GaAs substrates approximately 600 μm thick. After standard mechanical-chemical polishing and free etching, any native oxide on the GaAs substrate formed during loading was removed by thermally heating the substrate to a typical temperature of 630°C. The actual growth of the heterostructure was then usually carried out at 600°C (although higher growth temperatures up to 750°C have been tested). For all normal samples the first layer grown on the substrate was an unintentionally-doped GaAs buffer layer ~ 1 μm thick.

The growth rate of the GaAs was set to ~ 0.7 μm/hr by adjusting the Ga effusion cell temperature, while the As flux was adjusted to obtain an As-stabilized surface condition. Above the GaAs buffer layer were grown from one to nine alternating pairs of Si-doped $Al_xGa_{1-x}As$ and undoped GaAs layers.

In many cases the $Al_xGa_{1-x}As$ layer was grown so that a thin portion of each side near the interface was left undoped. These "intrinsic" $Al_xGa_{1-x}As$ layers were included to enhance the electron mobility as will be described in Section 2.4.2. In most cases a 200 Å cap layer of GaAs was grown last on the top surface of the sample to reduce oxidation of the surface and to facilitate ohmic-contact preparation.

A schematic representation of a multiperiod GaAs-$Al_xGa_{1-x}As$ heterostructure is shown in Fig. 2.1. Each period of the heterostructure consisted of an undoped (~ 10^{14} cm^{-3}) layer of GaAs (200 - 1000 Å thick) followed above by an undoped "intrinsic" layer of $Al_xGa_{1-x}As$ (50 - 300 Å thick), a Si-doped (~ 10^{17} cm^{-3}) layer of $Al_xGa_{1-x}As$ (250 - 1500 Å thick), and a second intrinsic layer of $Al_xGa_{1-x}As$ with the same thickness as the first intrinsic layer.

In instances where the sample contained only one period, the top-most intrinsic $Al_xGa_{1-x}As$ layer next to the 200 Å GaAs cap layer was usually deleted as shown in Fig. 2.2.

2.3.2 MOCVD Structures

All MOCVD samples used in this research were grown on Cr-doped, semi-insulating GaAs substrates oriented 2° towards (110) from (100). Growths were performed at 730°C with a controlled growth rate of 0.04 μm/min. An

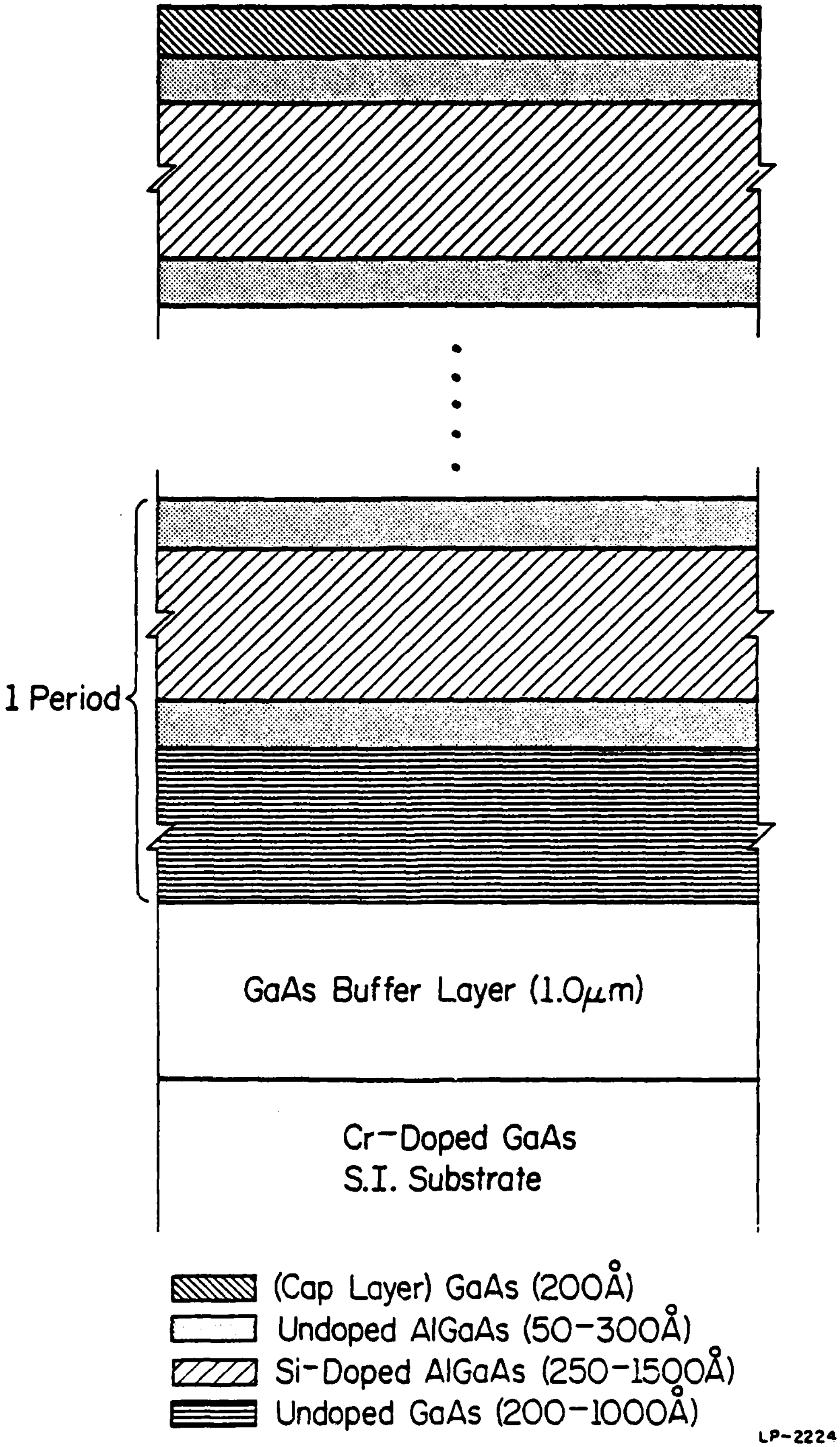

Fig. 2.1: Schematic representation of multiple-period modulation-doped GaAs-$Al_xGa_{1-x}As$ heterostructure grown by MBE.

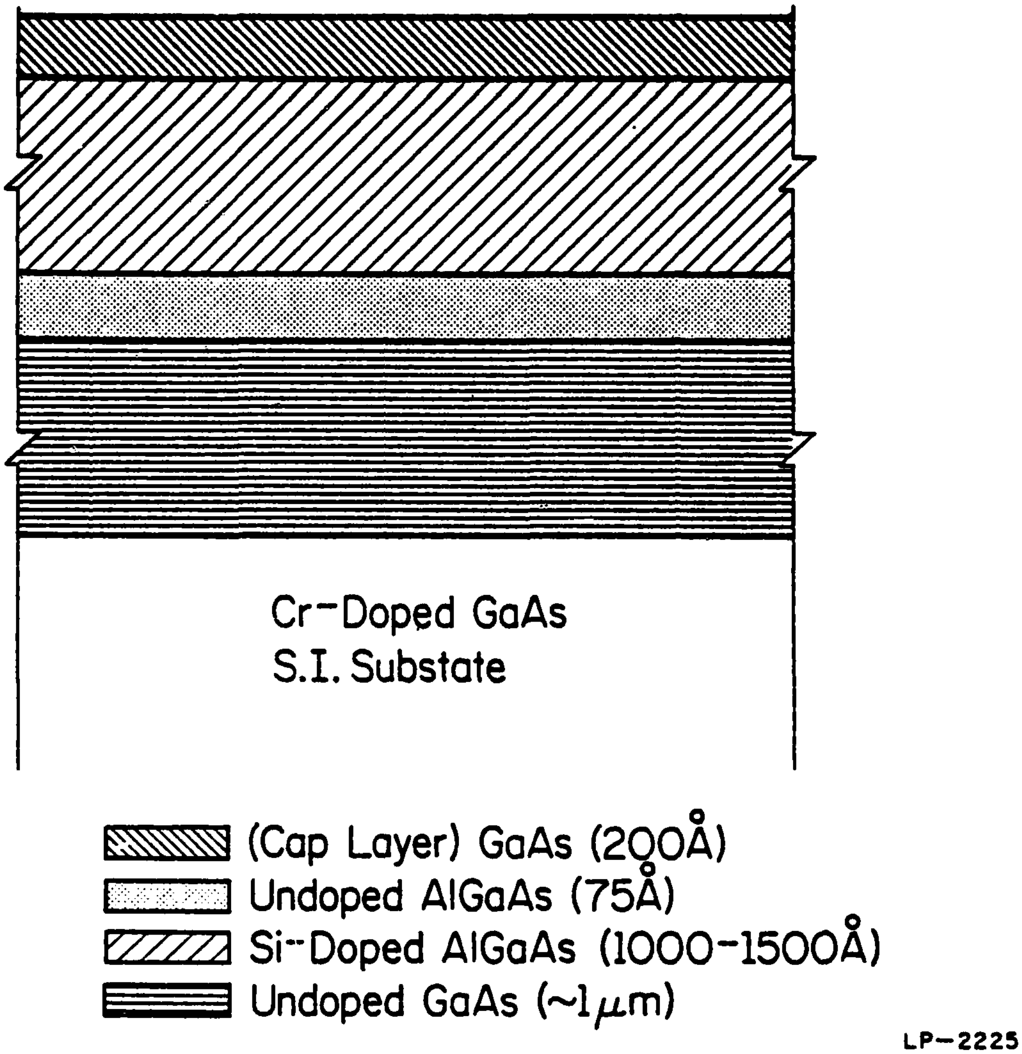

Fig. 2.2: Schematic representation of single-period modulation-doped GaAs-Al$_x$Ga$_{1-x}$As heterostructure grown by MBE. Note there is no intrinsic AlGaAs layer between the Si-doped AlGaAs layer and GaAs cap layer.

unintentionally-doped GaAs buffer layer (0.15 - 0.4 μm) was grown on top of the substrate before beginning growth of the following heterostructure periods. Each MOCVD period consisted only of one undoped (~ 4 x 10^{14} cm^{-3})GaAs layer and one Se-doped (~ 10^{17} cm^{-3}) $Al_xGa_{1-x}As$ layer, both of equal thickness. There were no "intrinsic" $Al_xGa_{1-x}As$ layers included in the MOCVD samples compared to the MBE ones. Structures contained from 3 to 20 periods of GaAs-AlGaAs layer pairs with the individual layer thicknesses ranging from 200 Å to 600 Å. All MOCVD wafers were capped with a thin layer of GaAs on the top surface.

2.4 Carrier Transport Characteristics

2.4.1 Conduction- and Valence-Band Discontinuities

For all the heterostructures studied by the author, the AlAs mole fraction x of the $Al_xGa_{1-x}As$ was in the range $0.15 < x < 0.40$ and the ternary Γ conduction band was direct. For $0 < x < 0.45$ the Γ direct energy gap E_G^{Γ} of $Al_xGa_{1-x}As$ is less than the gaps at the X and L indirect conduction bands and may be approximated as [45]

$$E_G^{\Gamma}\ (\text{eV}) = 1.424 + 1.247x. \qquad (2.1)$$

At the GaAs-$Al_xGa_{1-x}As$ heterojunction approximately 85% of the discontinuity in the band gaps between the GaAs and $Al_xGa_{1-x}As$ is located in the conduction band [58]. Thus the conduction-band discontinuity ΔE_c that forms a potential barrier at the interface for electrons in the GaAs may be expressed as

$$\Delta E_c = 1.060x\ (\text{eV}). \qquad (2.2)$$

Similarly the valence-band discontinuity ΔE_v which forms a potential barrier at the interface for the holes can be found using

$$\Delta E_v = 0.187x \text{ (eV)}. \qquad (2.3)$$

2.4.2 Mobility Enhancement

The lateral electron mobilities are enhanced in modulation-doped structures because only the larger band-gap material, here $Al_xGa_{1-x}As$, is intentionally doped with donors, leaving the nearby smaller band-gap GaAs layer essentially free of impurities. Due to the abrupt step in the band edges of the MBE-grown heterojunctions and the condition that a constant Fermi level be maintained throughout the heterostructure, the impurities in the $Al_xGa_{1-x}As$ ionize and electrons transfer across the heterojunction interface to the smaller band-gap GaAs layer. This charge transfer creates very strong internal electric fields (up to ~ 50 kV/cm) that cause substantial band bending in the vicinity of the heterojunction interface. The band bending strongly confines the carriers to a potential well next to the interface as shown in Fig. 2.3 and carrier motion in the direction perpendicular to the interface is quantized, forming a set of bound states. The subband structure of these bound states has been calculated by Mori and Ando [8,9] based on an effective mass approximation. Their calculated results for the Hall mobility will be discussed in further detail in this section.

Although the electrons are confined in the direction perpendicular to the interface, lateral motion (parallel to the interface) in the undoped GaAs remains unhindered and is essentially free from ionized-impurity scattering (the major factor limiting low-temperature mobility). This is

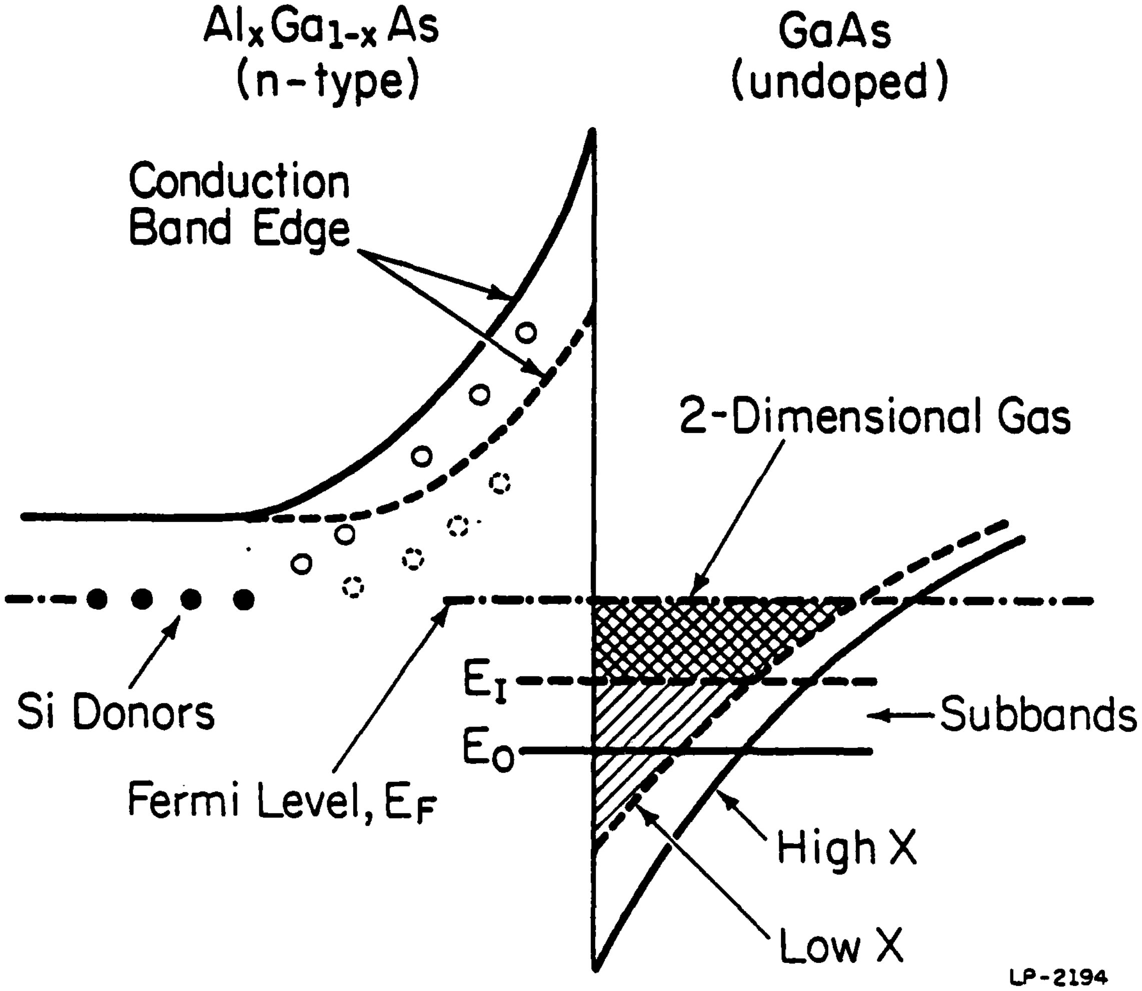

Fig. 2.3: Sketch of quasitriangular one-dimensional potential well formed by conduction-band edge at the interface. The two subbands are bound states of the two-dimensional electron gas confined in the narrow potential well.

due to the separation of parent donors in the AlGaAs from the electrons in the GaAs and screening of the backgrond impurities. As a result, the overall electron mobility of the heterostructure is significantly increased (particularly at low temperatures) over equivalently-doped bulk GaAs. This mobility increase has been experimentally verified overwhelmingly on many occasions by several laboratories using MBE [5,10,59-61], MOCVD [41], and LPE [53,54] growth techniques. It has also been demonstrated using Shubnikov-deHaas measurements [6,7,52,59,60,62,63], that the transferred electrons confined near the interface behave like a two-dimensional electron gas (2DEG). Incidentally, the analogous case of a two-dimensional hole gas (2DHG) at the interface of an undoped GaAs and p-type Be-doped $Al_xGa_{1-x}As$ layer has been similarly discovered [64].

Hess has shown that the differential scattering rate for the 2DEG due to ionized impurities decreases exponentially with the separation distance between them [65-67]. This fact indicates that the mobility of the electrons could be further improved by increasing the spatial distance between the ionized donors and the 2DEG by leaving a thin zone of the AlGaAs next to the interface undoped. Thus there would be a thin layer of undoped AlGaAs separating the electrons confined at the interface from the doped impurities inside the remaining AlGaAs layer. Fig. 2.4 depicts the conduction band-edge diagram of a MD GaAs-$Al_xGa_{1-x}As$ structure like that shown in Fig. 2.1 containing these thin undoped "intrinsic" $Al_xGa_{1-x}As$ layers. Putting this idea into experimental practice has led to still further improvement in the hererostructure mobility [68-76]. If the intrinsic AlGaAs layer is made too thick, however, the mobility of the structures is reduced. An explanation of this characteristic will be

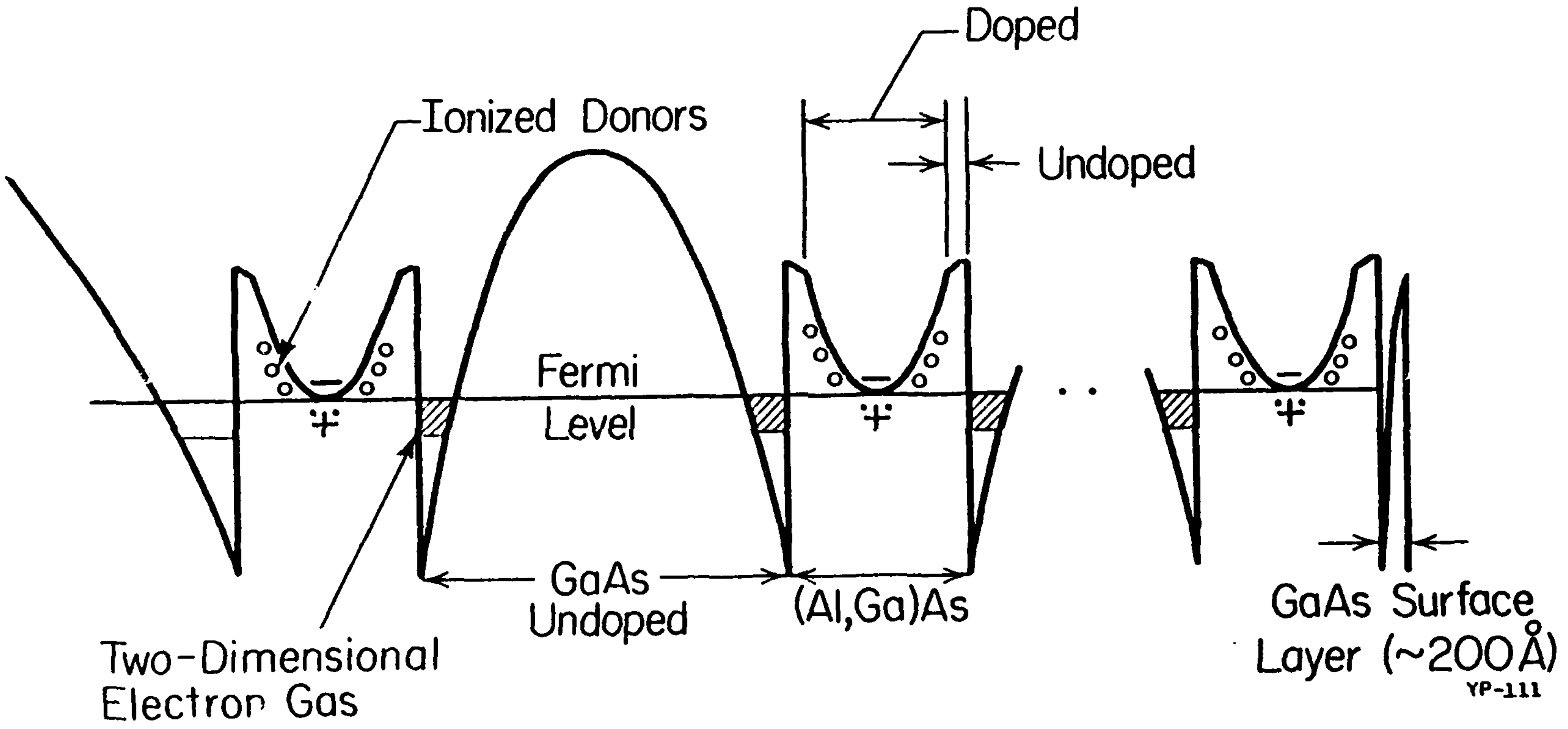

Fig. 2.4: Diagram of the conduction-band edge of a multiple-period modulation-doped GaAs-AlGaAs heterostructure with a thin, undoped AlGaAs layer between each doped AlGaAs and undoped GaAs layer [74].

presented in Section 2.4.2.1.

In all of the above-referenced experimental studies the mobility of the modulation-doped heterostructure was characterized by Hall-effect or van der Pauw measurements using relatively small electric and magnetic fields. Some of the reported measured Hall mobilities [75,76] have exceeded 300,000 cm^2/Vs at 10 K, 100,000 cm^2/Vs at 77 K, and have reached 9000 cm^2/Vs at 300 K. At this point it is important to recognize that the Hall measurements indicate the combined average mobility of the AlGaAs layer, the GaAs layer, and the two-dimensional electron gas at the interface.

It is the mobility, thickness, and carrier concentration of each layer which will determine the electrical properties of each structure that is studied through the application of an electric field. Since the remarkable characteristics of the devices fabricated and tested during this research depend so strongly on the important parameters that influence the mobility characteristics of the modulation-doped heterostructures, each of these parameters will be discussed in more detail in the subsequent sections. When possible, results will be included from recent experimental studies which have attempted to determine the optimum value of a particular parameter to achieve highest mobility in a certain structure.

2.4.2.1 Influence of Undoped AlGaAs Layer Width

It was reported above that the Hall mobility increases when an undoped AlGaAs layer is grown between the doped AlGaAs and the undoped GaAs, the reasoning being that it further separates the electrons in the GaAs from the ionized-impurity distribution in the doped AlGaAs and thus reduces the Coulomb interaction. However, it was found that if the intrinsic-layer width d_i was increased too much, the mobility would begin to decline. This indicates that there are other distance-dependent mechanisms such as electron screening effects which are important in determining the scattering rate. In order to better understand how the interaction of the various mechanisms that affect the scattering rate are dependent on the electron-donor separation, it is instructive to review the model presented by Hess [66,67].

Before proceeding with the details of the model, however, the reader is reminded that the effective distance from the donors to the maximum of the square of the electron-envelope wave function is dependent on the extent of band bending as well as the intrinsic-layer thickness d_i. This is illustrated in Fig. 2.5. Here z_o is the separation distance from the doped layer to the maximum of the square of the electron-envelope wave function for the lowest energy state E_o above the GaAs conduction-band edge E_c. Fig. 2.5(a) represents the conduction-band edge for negligible space-charge effects. The distance d_i is the spacing in the $Al_xGa_{1-x}As$ layer which is free of intentional doping. In Fig. 2.5(b) some band bending has become visible due to the effect of the space charge. Note that z_o is still nearly the same. Fig. 2.5(c) illustrates the case where the band bending is so strong that a quasi-two-dimensional layer has been formed at each interface. z_o is then much smaller for the same value of d_i. This causes a strong increase in the ionized-impurity scattering rate since it depends sensitively on the distance z_o as will be seen in Eq. (2.5) below. Optimizing this distance causes the major reduction of impurity scattering; all the other effects such as two-dimensionality have a smaller influence on the scattering rate and mobility.

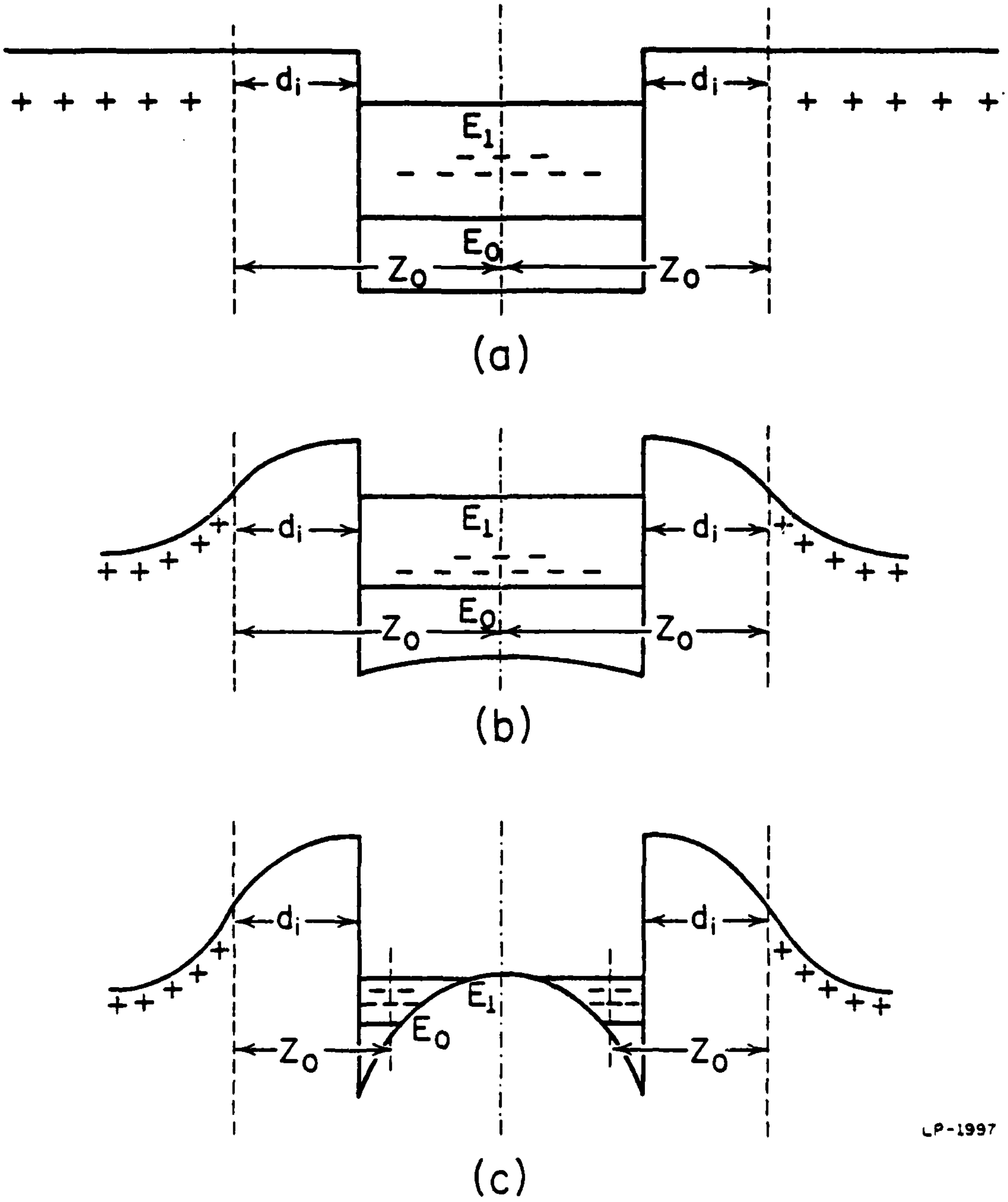

Fig. 2.5: Schematic diagram of conduction-band edge for (a) no band bending, (b) moderate band bending, and (c) strong band bending [67]. Note the change in Z_0, which is the distance of the donors from the maximum electron charge density.

The model presented by Hess [66,67] centers on simple screening effects and the scattering by a remote homogeneous distribution of impurities while ignoring multisubband conduction and multisubband screening of remote and background impurities. The electron distribution is approximated by a δ-like sheet of electron charge located at $z = 0$, where z is the direction perpendicular to the heterojunction interface. The donor impurities are homogeneously distributed at $z \geq z_o$. In the limit of a high electron density N_s at the heterojunction interface, the two-dimensional screening constant S is given by [77]

$$S = 2/a_B \tag{2.4}$$

where a_B is the effective Bohr radius in the GaAs. If the screening is strong, scattering occurs only for small angles ($kz_o > 1$) and then the scattering rate may be expressed by

$$\frac{1}{\tau} \simeq (2\beta/S^2)\ [16k^2 z_o{}^2 + 1]^{-1} \tag{2.5}$$

where

$$\beta = e^4\ m^*\ N_R\ (8\pi\hbar^3(\varepsilon\varepsilon_o)^2 k)^{-1}. \tag{2.6}$$

Here k is the absolute value of the electronic wavevector, m^* the effective mass, N_R the remote-impurity density, and ε the relative dielectric constant of the semiconductor. Eq. (2.5) also holds for background impurities (i.e., $z_o = 0$) and should allow an estimate of the influence of interface charges (kz_o small). If the true z dependence of the subband envelope functions is taken into account, the resulting formulae are much more involved. The essence of the theory, however, is reflected by Eq. (2.6), which was also derived by Price [78] if z_o is regarded as an adjustable parameter.

In order to understand the characteristics of the mobility dependence on z_o, one still needs to go into more detail. An estimate is easy only if one neglects both the background doping and the interface charges and employs the depletion approximation. Then the sheet density of electrons N_s at one interface becomes:

$$N_S = N_R W \tag{2.7}$$

where W is the depletion-layer width in the $Al_xGa_{1-x}As$. For $z_o = 0$ we have

$$W \equiv W_o = (2\varepsilon\varepsilon_o V_{bi}/e\ N_R)^{1/2} \tag{2.8}$$

where V_{bi} is the built-in voltage which is of the order of the conduction-band discontinuity. For $z_o \neq 0$, one can then write

$$N_S \approx (W_o - z_o)\ N_R. \tag{2.9}$$

Several factors which contribute to z_o include: the distance d_i in the AlGaAs, a contribution d' which arises from the statistical distribution of the donors (breakdown of the homogeneity approximation), and the average distance d" of the electrons from the interface.

When z_o increases, the electron transfer from the doped AlGaAs to the undoped GaAs becomes smaller and the electron density N_S at the interface decreases and as a result the screening also decreases (S becomes proportional to N_S for small N_S). This causes an increase in the scattering rates (Eq. (2.5)) which leads to the experimentally-measured decrease in mobility. Assuming the major effect is due to reduced screening alone, it is found (by differentiating over z_o) that the mobility has a maximum at

$$d_i \lesssim \frac{1}{2} W_o - d' - d'' \tag{2.10}$$

which gives $d_i \lesssim 150$ Å for $N_R \approx 10^{17}$ cm^{-3} and $d' + d'' = 100$ Å. In a real structure, the background impurities and interface charges (of extremely low density) will influence this value substantially; however, the symbol $<$ may still hold in Eq. (2.10).

In summary, the major features that influence the Coulomb scattering as a function of the intrinsic width d_i are:

(i): As long as N_S is constant, the scattering rate due to remote-impurity scattering decreases proportionally to ${z_o}^2$ for a homogeneous impurity distribution starting at a distance z_o from the electrons. However, this square law will be altered substantially by any deviation from constant N_R for $z > z_o$. For example, one obtains a ${z_o}^3$ law for the case of a δ spike of impurities.

(ii): When N_S begins to decrease with increasing z_o, this causes the screening constant S to be similarly decreased. The S^{-2} dependence of the scattering rate (Eq. (2.5)) then opposes the effects of (i) to decrease the mobility.

(iii): The dependence of z_o on d_i is affected by the Al mole fraction x and the impurity concentration which control the band-bending characteristics.

Several laboratories have reported the results of research performed to determine the optimum value of d_i to achieve the highest lateral mobility in various GaAs-$Al_xGa_{1-x}As$ heterostructures. The reported values of d_i have varied widely depending on the temperature at which the mobility was measured and the characteristics of the sample structure. A study of single-period GaAs-$Al_xGa_{1-x}As$ structures by Delescluse et al. [72] reported a peak mobility at 20 K for d_i = 90 Å, at 77 K and 100 K for d_i = 75 Å, and at 175 K and 300 K for d_i = 60 Å. The AlAs mole fraction was $x = 0.30$.

Morkoç and co-workers have reported results from several different studies [66,68,69,74] on single-period samples with $x = 0.25$ and 0.33, and three-period samples with $x = 0.20$. Although their findings varied somewhat, in general the single-period structures had peak 77 K mobilities for 50 Å $\leq d_i \leq$ 100 Å with a tendency for the peak mobilities of the $x = 0.33$ material to occur at smaller d_i values than for the $x = 0.25$ material. The 300 K mobilities tended to peak near d_i = 50 Å for both the one- and three-period structures and the peak 77 K mobility for the three-period structure occurred at d_i = 150 Å.

A study by Störmer et al. [70] on samples with 15 to 23 periods and $x = 0.12$, showed a steady increase of mobility with increasing undoped-layer thickness through d_i = 150 Å, which was the largest spacing investigated. On the basis of this data they were led to expect higher mobilities through further increase in the width of the undoped AlGaAs spacers.

The large variance in the characteristics of the samples studied by the different research laboratories makes it hard to efficiently compare the results, but some trends do seem to be visible. First of all, single-period structures usually have a peak in the low-temperature mobility near d_i = 75 Å with the 300 K mobility peak occurring at a slightly lower intrinsic-layer thickness. Typical results are pictured in Fig. 2.6 for $x = 0.25$ and Fig. 2.7 for $x = 0.33$ [66]. In both figures the electron mobility is seen to reach its maximum value at an intrinsic-layer thickness of ~ 75 Å for 77 K and ~ 50 Å for 300 K. In the case of multiple periods, the low-temperature peak mobility usually occurs at significantly larger

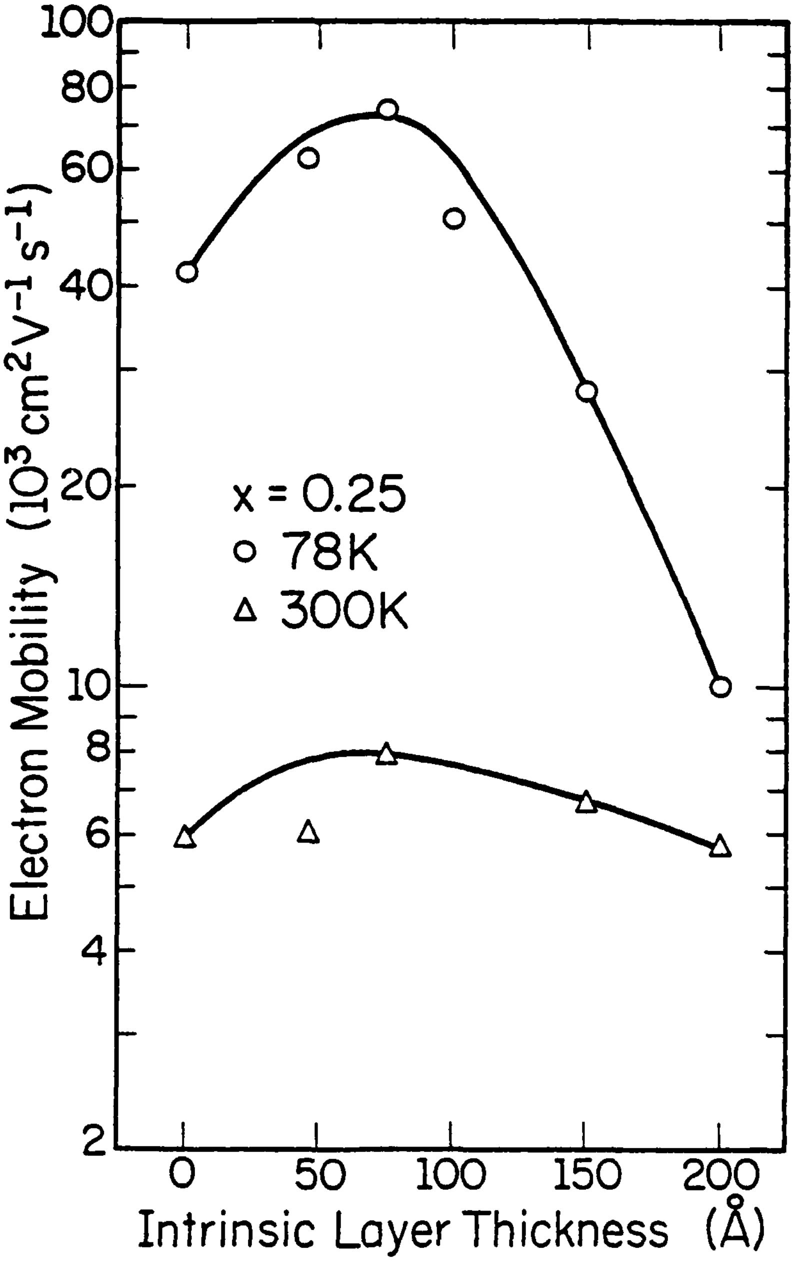

YS-81

Fig. 2.6: Electron mobility of $Al_{0.25}Ga_{0.75}As/GaAs$ modulation-doped heterostructures as a function of AlGaAs undoped layer thickness d_i at the interface at 78 K and 300 K [66].

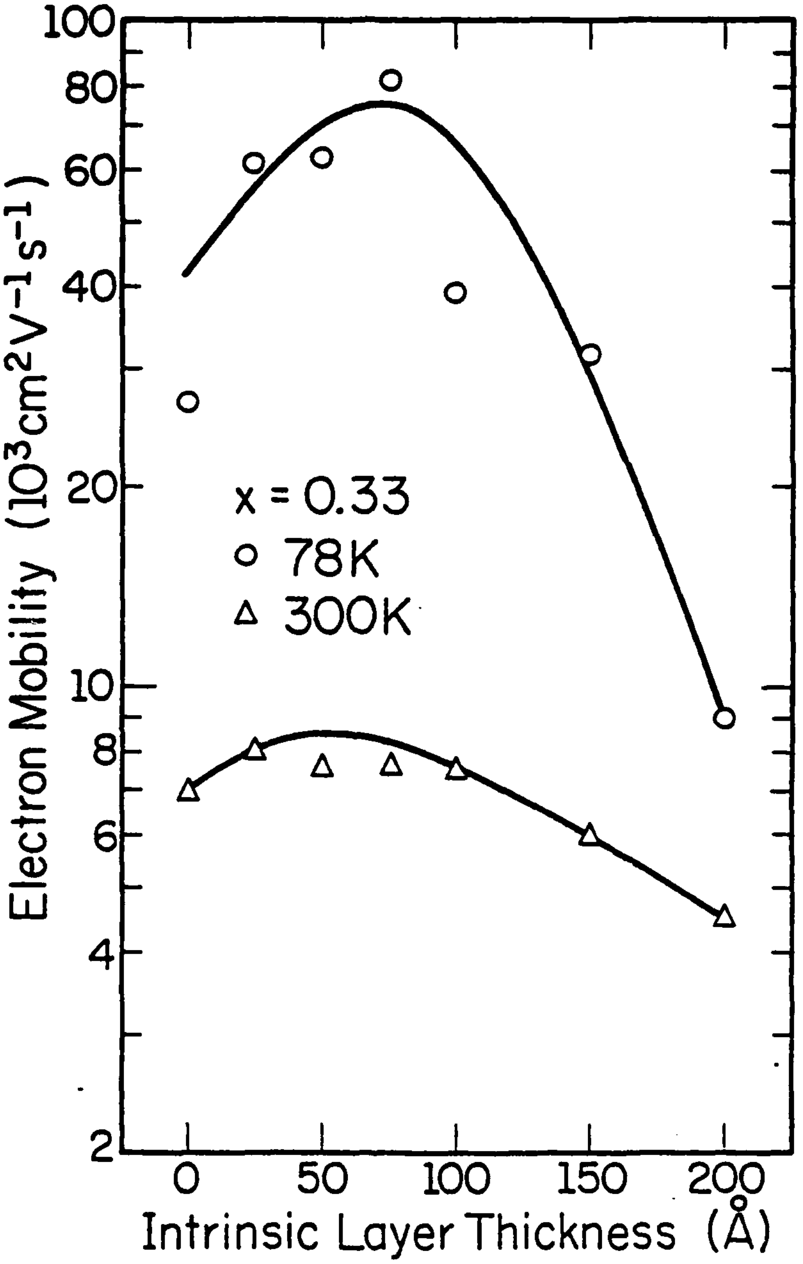

YS-82

Fig. 2.7: Electron mobility of $Al_{0.33}Ga_{0.67}As$/GaAs heterostructures as a function of d_i at 78 K and 300 K as in Fig. 2.6 [66].

intrinsic-layer widths than for single periods. An example is shown in Fig. 2.8 where the 77 K mobility peak ocurs at $d_i \sim 150$ Å for a three-period heterostructure with $x = 0.20$.

2.4.2.2 Influence of AlAs Mole Fraction

The AlAs mole fraction x in the $Al_xGa_{1-x}As$ material determines the conduction band-edge discontinuity (Eq. (2.2)) at the GaAs-$Al_xGa_{1-x}As$ heterojunction interface. The transfer of charge from the doped AlGaAs to the undoped GaAs is very senstive to the conduction-band discontinuity and is expected to increase rapidly with x up to the direct-indirect cross-over ($x \approx 0.45$) [54]. This is because an increase in the conduction-band discontinuity causes a thicker depletion layer in the AlGaAs as was seen in Fig. 2.3.

To separate the influence of the Al concentration on the mobility from that due to different electron densities, Störmer et al. [75] compared the mobility of a series of wafers with Al concentrations in the range $0.12 \leq x \leq 0.31$ all with the same electron densities in the GaAs. A low-temperature persistent-photoconductive (ppc) effect [6,75] (to be discussed in Chapter 5) was used to vary the electron concentration of each structure so that they would match. It was reported that the electron concentrations could be varied continuously over a large density range with this method. For a set of four samples with equivalent electron densities and Al concentrations of $x = 0.12$, 0.19, 0.29, and 0.31 it was found [75] that the mobility increased monotonically with decreasing Al concentration. This surprising dependence can be due to the interaction of several competing characteristics. In general, the crystal quality of AlGaAs is better for low Al concentrations, which leads to a better interface and improves the

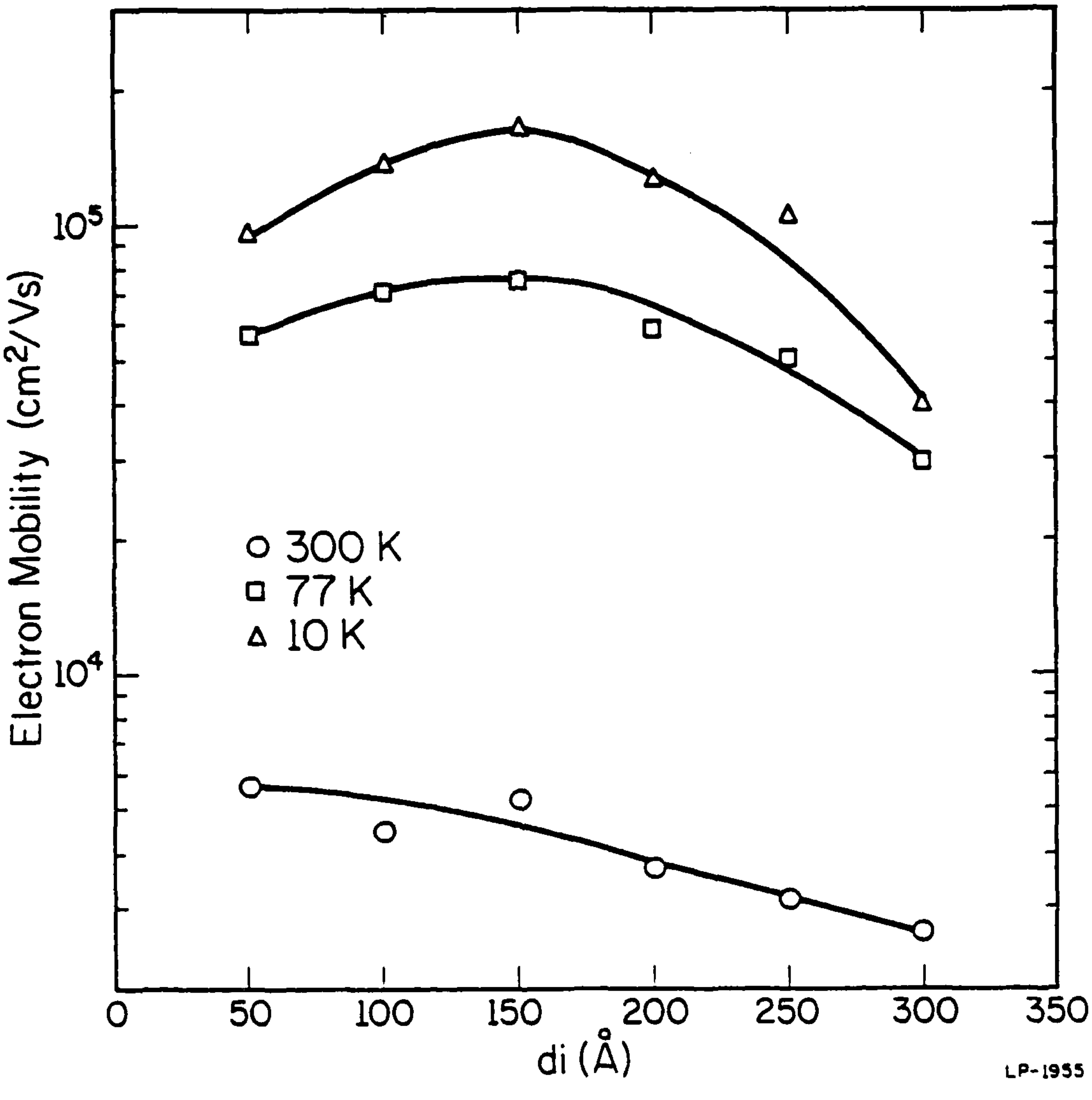

Fig. 2.8: Electron mobility of three-period $Al_{0.20}Ga_{0.80}As/GaAs$ modulation-doped heterostructures as a function of intrinsic AlGaAs layer thickness d_i at 10 K, 77 K, and 300 K [74].

mobility. However, lower Al concentration also reduces the energetic step in the conduction-band edge between the GaAs and AlGaAs, allowing the electron wavefunction to penetrate more deeply into the AlGaAs. This would cause increased scattering and reduced electron mobility. The results of Störmer and co-workers in this case indicate that the mobility alterations due to the first process exceeded those due to the second at least under the conditions of the study.

Another study reported by Drummond et al. [79] involved the study of the AlAs mole fraction in the range $0.18 \leq x \leq 1.00$. They found that the mobility at 10 K, 78 K, and 300 K increased with increasing AlAs mole fraction to reach a maximum near $x = 0.40$ and then decreased for higher values of x. Note that the peak mobility was achieved at an AlAs mole fraction ($x \approx 0.40$) near the direct-indirect band gap region. In this study, the electron concentration was not held constant and it was found that the sheet carrier concentration at 10 K, 78 K, and 300 K dropped as expected as x was increased for $0.18 \leq x \leq 0.38$. The decrease in concentration at 300 K was more pronounced than that at 78 K and 10 K. This was attributed to low-field parallel conduction [42] through the AlGaAs layer by electrons that did not transfer into the GaAs layer, particularly for small AlAs mole fractions. At 300 K more of the carriers remaining in the AlGaAs can contribute to parallel conduction, whereas at 10 K and 77 K those electrons remaining in the AlGaAs are frozen out. This results in an additional increase in the measured carrier concentration at 300 K as compared to low temperatures for small AlAs mole fractions.

It was reported by Drummond et al. that the energy of the Si donor level in AlGaAs measured from the conduction band increases substantially as x is increased [79]. A sharp increase in donor ionization energy above x = 0.30 has also been reported by Glew and Halberstadt [54].

2.4.2.3 Subband Structure Scattering Effects

The existence of a two-dimensional electron gas (2DEG) in the undoped GaAs layer near the interface has been experimentally demonstrated on many occasions by observing the orientational dependence of a magnetic field used to make Shubnikov-deHaas (SdH) measurements [6,7,52,59,60,80,81]. It has been calculated from experimental evidence that the width of the potential well at the interface is roughly 100 Å [6,52] and measurements indicate that one [52,80] or two [59,81] of the subbands formed in the well are occupied. Fig. 2.3 depicts the 2DEG formed at the interface with two subbands formed below the Fermi level.

Mori and Ando [8,9] have calculated mobilities for the electron motion parallel to the layers in modulation-doped GaAs-Al$_x$Ga$_{1-x}$As superlattices including band bending and the subband structure. The subband structures were calculated by a variational method and the charge-transfer effect was considered self-consistently in the Hartree approximation. The mobility was calculated by solving coupled Boltzmann equations and intersubband-scattering effects were included when the higher of the two subbands was occupied. It was found that when the excited (upper) subband was occupied by electrons, the mobility was reduced by the intersubband scattering.

Experimental evidence of mobility reduction due to intersubband scattering has been demonstrated recently [60,75,81]. The latest of these studies [81] made use of an electrode attached to the backside of the sample to conveniently vary the electron concentration in a modulation-doped heterostructure. This configuration allows one to sweep the carrier concentration and in turn the Fermi level continuously through the transition from one-subband population to two-subband population. In order to investigate electron scattering as a function of density and subband population, standard Hall and conductivity experiments were performed simultaneously with magnetoresistance measurements. A sharp drop in the Hall mobility μ_H was measured when a second subband began to be occupied as determined by magnetoresistance data. This abrupt drop in mobility was not observed in samples where a second subband could not be occupied. Consequently, the drop in mobility was interpreted as the onset of intersubband scattering which increases the scattering rate for the two-dimensional carriers. The experimental observations qualitatively reproduced all features of the density dependence of the mobility in the transistion regime where μ_H generally increases with increasing carrier concentration. This dependence is a result of improved screening of the ionized impurities which remain the major source of electron scattering. At the onset of two-subband conduction μ_1 of the ground subband drops considerably due to the onset of intersubband scattering. The theoretical mobility variation at the transition point is discontinuous, but experimentally it was found that although the transition occurred over a narrow density range, it was nevertheless smooth. It was suggested that a finite energetic width of the excited subband smears out the transition.

2.4.2.4 Influence of Doped AlGaAs Layer Parameters

It has been found that the width and doping level of the doped $Al_xGa_{1-x}As$ layers will significantly affect the electrical properties of the heterostructures.

For one study [73,74] a series of three-period structures were prepared and the thickness t of the doped AlGaAs was varied from 150 Å to 1000 Å in order to determine the effect of the layer thickness on the measured Hall mobility of the structures. Fig. 2.4 depicts the estimated conduction band diagram of the three-period GaAs-$Al_xGa_{1-x}As$ heterostructure with $x = 0.20$. The GaAs layer widths were each 1000 Å and the intrinsic AlGaAs widths were 150 Å. Since the thickness of the Si-doped (7×10^{17} cm^{-3}) AlGaAs was varied between 150 Å and 1000 Å, its band diagram will also change somewhat. For the thicker layers (t ~ 1000 Å) the center of the doped AlGaAs layers will be wider and more flat, and there will be more electrons left in the center that do not transfer. These electrons, associated with ionized donors in the center of the AlGaAs layers (particularly for thicker layers), are shown as dots in Fig. 2.4.

It was found that the mobility measured by van der Pauw-Hall techniques was relatively independent of the AlGaAs thickness t for values of $t \lesssim 500$ Å. For t = 1000 Å, particularly at 300 K, the electron mobility was seen to decrease as shown in Fig. 2.9. This decrease was attributed to the parallel conduction through the AlGaAs by electrons that do not transfer into the GaAs layers. The electron mobility of the 2DEG in the GaAs channel, however, should not be much affected by the remaining electrons in the AlGaAs. The overall mobility and electrical characteristics of the structure can nevertheless be altered significantly when the AlGaAs is not depleted of electrons and parallel conduction in the AlGaAs takes place.

For instance, if the AlGaAs is only partially depleted of electrons, the characteristics of the negative differential resistance (NDR) and related device phenomena due to the real-space transfer (RST) mechanism

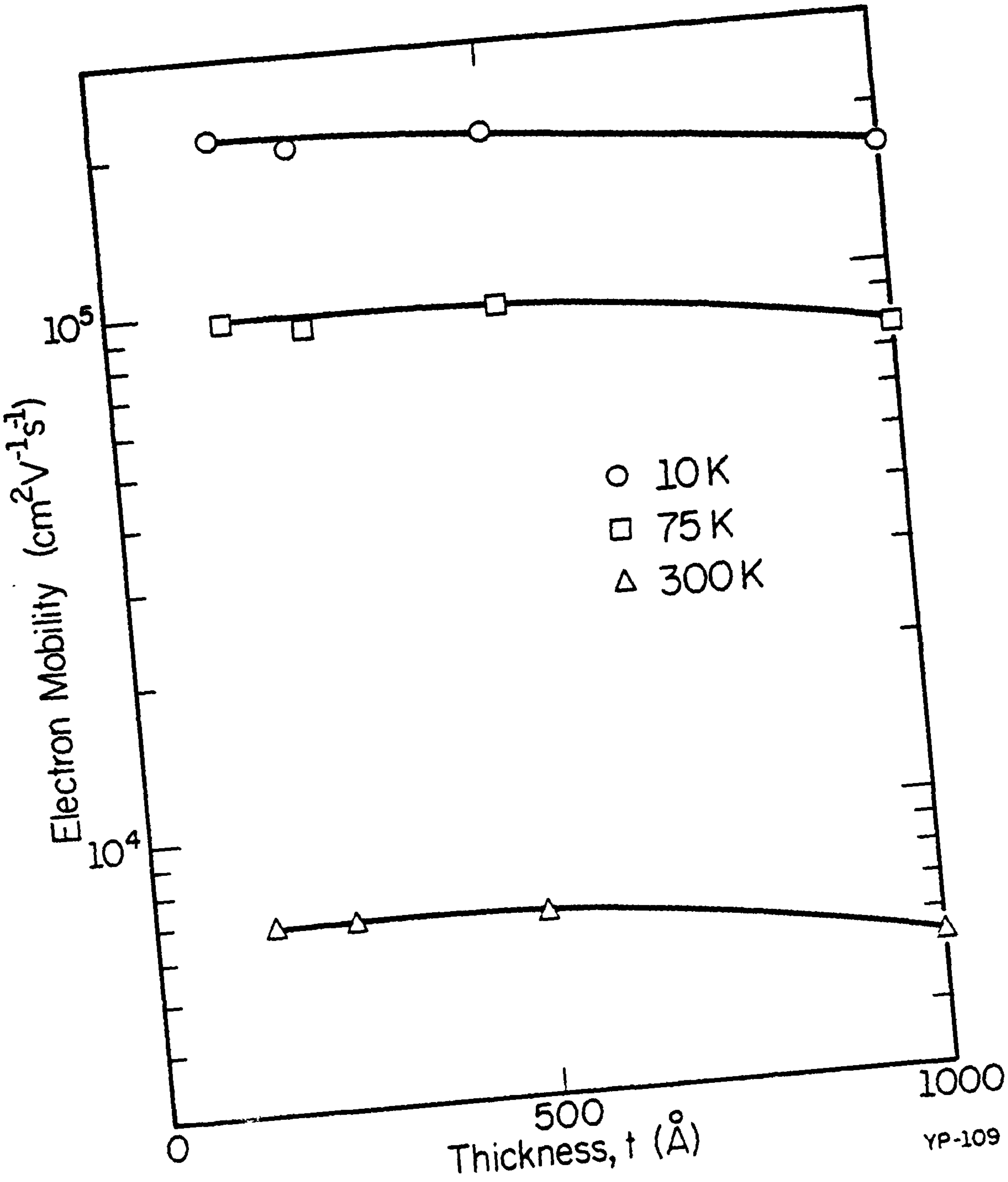

Fig. 2.9: Electron mobility vs doped AlGaAs layer thickness t for three-period modulation-doped $Al_{0.20}Ga_{0.80}As$/GaAs heterostructures at 10 K, 75 K, and 300 K [74].

(mentioned in Chapter 1) can be greatly affected. Since the magnitude of the NDR depends on the relative number of electrons that switch from the GaAs to the AlGaAs layers at high fields, it is necessary to deplete the AlGaAs initially to fully enhance the NDR.

In the structure described above the doping in the AlGaAs was high ($N_D \approx 7 \times 10^{17}$ cm^{-3}) and the AlAs mole fraction was only $x = 0.20$. Both of these factors contributed to the inability to deplete the AlGaAs layers that were 1000 Å thick. Decreasing the doping in the AlGaAs and/or increasing the AlAs mole fraction (to enhance electron transfer) should increase the depletion of electrons in the AlGaAs and reduce the parallel conduction. Device characteristics resulting from parallel conduction effects will be described further in Chapter 5.

A second study [69] was performed on single-period structures with $x = 0.25$ and $d_i = 100$ Å. The thickness of the doped AlGaAs was varied between 1000 - 2000 Å ($N_D \approx 10^{17}$ cm^{-3}). It was found that the mobility of the structure with $t = 1500$ Å was larger than that of the structures with $t = 1000$ Å or 2000 Å by a factor of 3. It was suggested that the mobility differences may be due to the amount of states occupied in the 2DEG subband structure.

Note that $x = 0.25$ was 25% higher and $N_D \approx 2 \times 10^{17}$ cm^{-3} was about 3 times lower in this second study than the corresponding parameters of the wafers in the first study. Then, for all other factors being about equal, it is possible that up to 2000 Å of the AlGaAs in the second study was depleted of electrons whereas 1000 Å of the AlGaAs in the first study was not depleted. This is a good example of the importance of the relationship among the doping level N_D, the AlAs mole fraction x, and the doped Al_xGa_{1-}

${}_{x}$As layer width t.

2.4.2.5 Influence of GaAs Layer Parameters

The width of the unintentionally-doped GaAs layers and the amount of their background doping can have an important effect on the mobility of a modulation-doped GaAs-Al$_x$Ga$_{1-x}$As heterostructure. The influence of the GaAs layer width on the mobility in nine-period structures has been recently reported [74]. In these structures the intrinsic AlGaAs thickness was d_i = 75 Å, the doped (7 x 10^{17} cm^{-3}) AlGaAs layer thickness was 1000 Å, and the AlAs mole fraction was x = 0.26. The electron mobilities at 10 K, 78 K, and 300 K were measured for five samples with the GaAs layer thickness ranging from 500 Å to 1500 Å. The results of these measurements are presented in Fig. 2.10. It is obvious that the mobility increased rapidly with increasng thickness up to 1100 Å after which it began to saturate. This may be an indication of the extent of the bending of the conduction-band edge in the GaAs. For GaAs layers much thinner than 1500 Å it was speculated that the band bending away from adjacent interfaces will overlap, affecting the shape of the potential well at the interface and consequently, the mobility. In any event, for small GaAs thicknesses, the influence of the ionized donors in the nearby AlGaAs on the electron mobility in the well (via a Coulomb interaction) will be more significant than in larger GaAs thicknesses. In addition, the amount of charge that can be transferred from the AlGaAs to the potential well in the GaAs (and hence the extent of the band bending) will be less in the thinner GaAs layers. Both of these factors reduce the mobility for smaller GaAs thicknesses.

The influence of the magnitude of the unintentional doping in the GaAs is fairly obvious. The whole principle of enhanced mobility from modulation

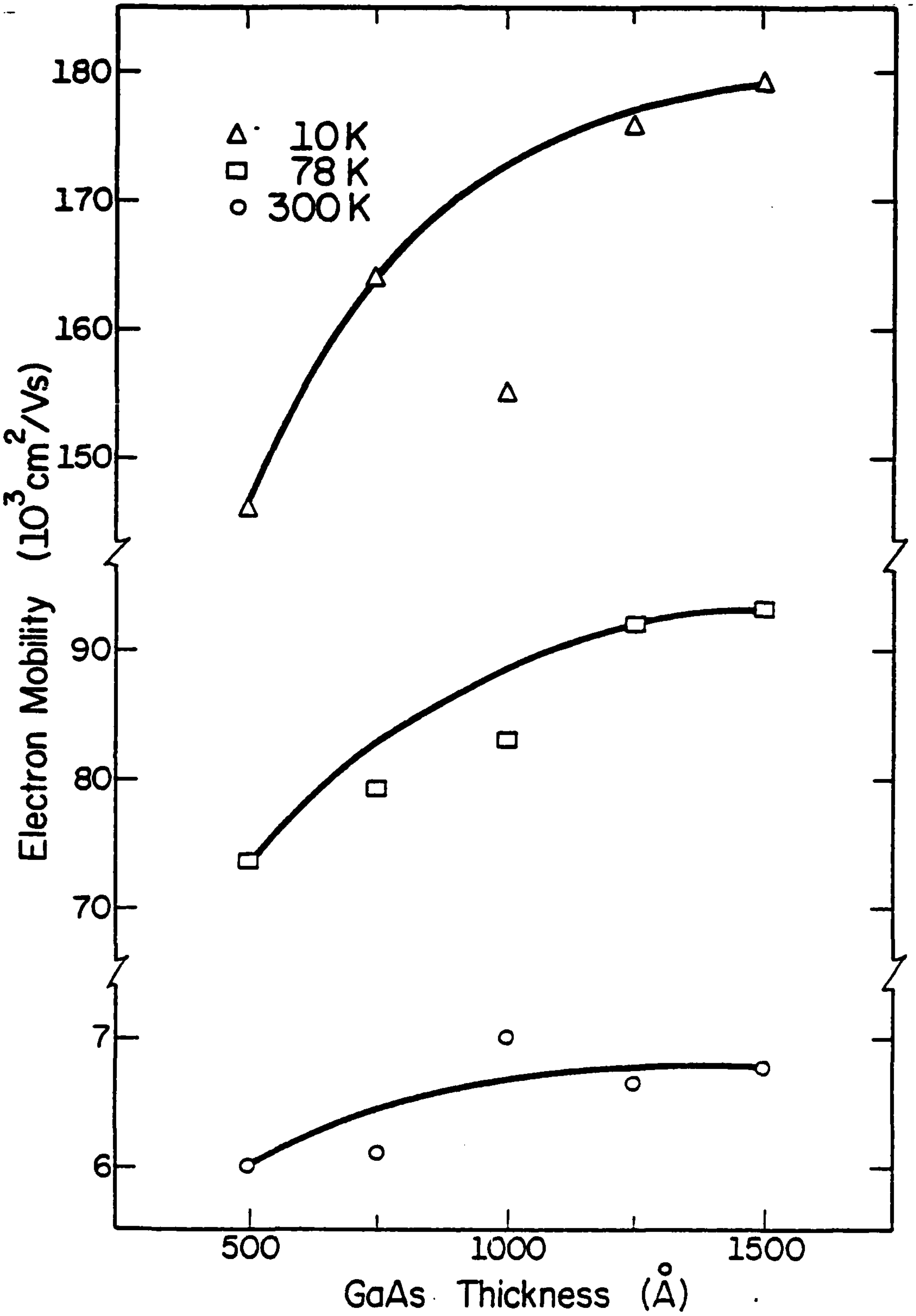

Fig. 2.10: Electron mobility vs GaAs layer thickness for nine-period modulation-doped $Al_{0.26}Ga_{0.74}As$/GaAs heterostructures at 10 K, 78 K, and 300 K [74].

doping, stems from the concept that the carriers transfer to a region (undoped GaAs) where there are fewer impurities to scatter the electrons at low temperatures. If the impurity concentration in the GaAs is inreased then ionized-impurity scattering will also increase and the mobility will decrease. Similarly, decreasing the background-impurity concentration in the GaAs will increase the mobility particularly at low temperatures.

A recent study was reported [82] in which the GaAs layers of several samples were intentionally doped with different concentrations of impurities. As expected, it was found that the mobility of structures decreased monotonically with an increasing concentration of background impurities in the GaAs.

2.4.2.6 Substrate Growth Temperature Effects

It has been reported that the quality of the GaAs-$Al_xGa_{1-x}As$ interface is strongly dependent on the substrate temperature during growth [83,84]. A recent study [76] has been made of the effect of the substrate growth temperatures on the mobility in modulation-doped GaAs-$Al_xGa_{1-x}As$ samples. The structure used to study the effect consisted of a 1 μm GaAs buffer layer separated from a 1500 Å doped $Al_{0.3}Ga_{0.7}As$ layer by a 75 Å undoped region of $Al_{0.3}Ga_{0.7}As$. The 75 Å thickness was chosen because it optimizes the mobility enhancement in single-period structures as discussed in Section 2.4.2.1. The AlGaAs was doped to a level of about 8 x 10^{17} cm^{-3} with Si.

While high quality GaAs can be grown at about 600°C, the quality of AlGaAs layers improves when the substrate temperature is increased above 600°C. Consequently, the substrate growth temperatures used for this study ranged from 580°C to 750°C. The mobility of the resulting layers was characterized by van der Pauw-Hall measurements between 10 K and 300 K. It was found that the mobilities remained high and stable throughout the substrate-temperature range 600 - 675°C. But below 600°C and above 675°C, the mobility decreased significantly. It was suggested that the observed reduction in mobility above 675°C was a result of microscopic degradation of structural properties of the heterointerface. Some of these factors are discussed in the following section.

2.4.3 Interface Quality

Throughout the previous sections on mobility enhancement it was assumed that the GaAs-AlGaAs interface was of sufficiently high quality for electrons to transfer freely across the interface to the high-mobility channel in the GaAs and form a two-dimensional electron gas (2DEG). In several cases, studies for interface states have reported that the GaAs-AlGaAs interface is indeed nearly ideal. One study [85] reported no evidence whatsoever for any traps or recombination centers associated with LPE-grown interfaces. Another study of MBE-grown structures examined optically, concluded that there was no evidence for alloy clustering in the material [86]. Evidence of alloy clustering, however, has been noted by other researchers in both MOCVD and MBE heterostructures.

It has been reported that at interfaces where the undoped GaAs layer has been grown by MBE on top of the doped AlGaAs layer, a 2DEG could not be obtained, or even if it did exist, showed very inferior transport properties [10,69,74,87-92]. Structures grown by LPE, on the other hand, did not seem to contain this problem [52]. This suggests that the poor-quality interface is due to some inherent difficulty in the directionality of the MBE growth procedure.

The inferior-quality interface has appeared in both single- (where the GaAs is grown on the AlGaAs) and multiple-period samples. In one study [74] on a variety of structures it was discovered that the interface carrier concentration at 10 K for three-period structures was about three times that of single-period structures (AlGaAs on GaAs) with the same parameters. For nine-period structures the sheet carrier concentrations were almost nine times those of similarly grown single-period structures. This indicates that there is a 2DEG at only one of the interfaces for each additional period. If the mobility enhancement were taking place on both sides of the doped AlGaAs layers, the sheet carrier concentrations would increase 5 and 17 times in the three- and nine-period structures, respectively.

As discussed in the previous section, the quality of the AlGaAs surface improves at higher temperatures. This has sparked several studies to investigate the influence of growth temperature on the mobility of "inverted" single-period structures where the undoped GaAs layer is on top of the doped AlGaAs. One study [88-90] compared the mobility characteristics of both "inverted" and "normal" single-period structures over a range of growth temperatures. The single-period modulation-doped GaAs-$Al_xGa_{1-x}As$ structures were grown by MBE in a substrate growth temperature range of 580 - 770°C for normal structures (having AlGaAs on top of GaAs) and in the range of 600 - 770°C for inverted structures (having GaAs on top of AlGaAs). The AlAs mole fraction was $x = 0.30$. The reader is referred to any one of the three referenced papers for full details of the growth procedures. Results showed that average 78 K mobilities of about 90,000 cm^2/Vs were obtained in the normal structures for the growth range 600 - 680°C. Above 680°C, some degradation in mobility was observed. The inverted structures, on the other hand, exhibited a very strong dependence on the substrate temperature. In the range 600 - 675°C there was no mobility enhancement and the 78 K mobility of the inverted structures did not exceed 2000 cm^2/Vs. The mobility increased dramatically at 700°C to a peak of about 8500 cm^2/Vs, which is about twice that of bulk GaAs with an equivalent carrier concentration. Above 700°C the 78 K mobility was found to degrade monotonically up to 770°C.

The sharp dependence of electron mobility in the inverted structures on growth temperature indicates that the interfacial properties vary quite substantially when GaAs is grown on AlGaAs. The best interface seemed to occur for a growth temperature of 700°C which agrees quite remarkably with the 690°C best value reported by Weisbuch et al. [84] using photoluminescence measurements. It was suggested that the low mobilities obtained in the inverted structures for substrate temperatures below 675°C were possibly due to metallurgical roughness at the interface and/or possible vacancies. The surface mobility of Al is greatly reduced below the congruent evaporation temperature of AlAs (700°C), which can result in an imperfect seeding mechanism during the AlGaAs growth. This imperfection can lead to a metallurgically-rough AlGaAs surface and thus, a rough interface when the GaAs is grown on top. Another mechanism that might have caused the low mobilities below 675°C was the possible formation of group III vacancies (most likely Al) and also probably arsenic interstitials. This is thought to be caused [91] by excess arsenic on the surface during growth, which decreases the surface-diffusion lengths of group-III atoms, thereby inhibiting their incorporation into the lattice. The Al-As bond is stronger than that of Ga-As; therefore excess arsenic is more likely to be held by Al while it becomes buried in the growing layer. These two problems are reduced by increasing the substrate temperature which causes arsenic to desorb from the surface at an increased rate.

The influence of substrate growth temperature for the GaAs on AlGaAs interface in three-period structures has also been investigated [92]. It was found that the current-voltage characteristics improved when the growth temperature was increased from 600°C to 680°C. Although the electrical properties of the GaAs on AlGaAs interface were improved, the mobility was still much lower than that of the AlGaAs on GaAs interface. The improvement in the low-field current characteristics of these three-period structures grown at 680°C will be discussed more thoroughly in Chapter 4.

2.5 Summary

In this chapter the author has attempted to draw attention to many of the important factors that determine the electrical characteristics of GaAs-$Al_xGa_{1-x}As$ heterolayers. The basic structure of a modulation-doped sample as well as the mechanism by which the electrons transfer layers to form a high-mobility region near the interface has been discussed at length. The development of a two-dimensional electron gas in the GaAs was seen to be highly dependent on the interface quality and other factors relating to growth. The importance of parameters such as the AlAs mole fraction, individual layer widths, and doping concentrations in determining the electron mobility in each layer, as well as the whole structure, has been emphasized. It is the relative sizes of these mobilities that will most strongly affect the electron-transport characteristics of devices made from these heterostructures when electric fields are applied parallel to the layers. The results of the field-induced transport characteristics nted in the following chapters will further illustrate the influence of growth parameters discussed so far and will also illustrate the ditional interesting electrical characteristics that can be created hrough various device-fabrication techniques.

3. EXPERIMENTAL PROCEDURES

3.1 Preparation of Test Samples

All modulation-doped GaAs-$Al_xGa_{1-x}As$ heterostructure samples measured in this research project were grown by MBE or MOCVD and had layer configurations of the type described in Sections 2.3.1 and 2.3.2. The test samples were cleaved from wafers and the surfaces prepared by standard methods of ultrasonic cleaning in solvents and deionized water. Sometimes the samples were also rinsed for a short while in buffered hydroflouric acid to remove any thin native oxide that had grown on the top surface. This oxide removal procedure was performed most frequently for heterostructure wafers where the top surface consisted of an AlGaAs layer rather than the usual GaAs cap layer.

3.1.1 Etching of Special Device Patterns

Some samples had conducting layers etched from the top surface in a specific pattern to obtain a special device structure. The regions to be left unetched were masked with black wax or AZ 1350 photoresist that was photolithographically defined using standard methods. The etching was done by immersing the sample in a solution of sulfuric acid (H_2SO_4), hydrogen peroxide (H_2O_2), and deionized water (H_2O) at a predetermined temperature. The temperature of the etching solution and the ratios of its three components was varied according to the etch rate and type of etched structure desired. One etching solution used frequently to etch mesa-shaped structures consisted of $H_2SO_4:H_2O_2:H_2O$ in the ratio 20:1:1. The etch rate of this mixture was approximately 1 μm/min at 18°C (etch rate varied somewhat from one structure to another depending on the growth parameters of the structures).

3.1.2 Metal Deposition for Ohmic Contacts

The metals used to form ohmic contacts on the samples were generally heated to evaporation temperature in a tungsten boat in a vacuum of 5×10^{-6} Torr or better. The evaporants were deposited on the top surface of the sample structure which was suspended upside down above the heated metal sources. The pattern of the contact metals deposited on the semiconductor surface was controlled by masking the sample surface with photolithographically patterned photoresist layers and using a metal-liftoff procedure, or by placing a metal shadow mask directly in front of the semiconductor surface.

The metal combination deposited most frequently to form the ohmic contacts consisted of an initial layer of AuGe (in its eutectic mixture of 88% and 12%, respectively) of approximately 1500 Å followed by a thin layer (~ 400 Å) of Ni. In later portions of the research the author also used vacuum deposited contacts of AuSn in their eutectic composition. For one portion of this work, low-field measurements were also performed on samples with ohmic contacts formed from Sn dots [34,74,92]. Of the metal combinations listed above, it is the AuGeNi system that has been the most widely used and studied in the literature [93-102]. Some of these reported findings will be presented in the next section.

3.1.3 Alloying or Sintering of Contacts

After the contact metals were deposited on the top surface of the samples (and metal liftoff performed if necessary), the device structures were placed on a graphite strip and heated in flowing H_2. Nearly all of the samples were alloyed at approximately 450°C for times ranging up to two minutes. The alloy times were kept to a minimum because it has been shown that increasing the high-temperature alloy time causes an increase in the contact resistance [96]. The heating rise time of the heater strip was about 1.5 min with a fall time of approximately 20 sec.

Several recent papers [93-97] have reported investigations of the metallurgical structure and electrical properties of these alloyed contacts on GaAs. Although the diffusion, redistribution and recrystallization of Au, Ge, Ni, Ga, and As after alloying is extremely complicated and not well understood, it is generally reported that a large amount of Ga outdiffuses to the surface during the alloying process [94,97]. Ge is an amphoteric dopant in GaAs but it has been shown that Ge acts as a donor in GaAs when excess As is present [103]. Thus, due to the outdiffusion of Ga to form AuGa regions at the surface, the Ge can indiffuse to occupy the vacated Ga sites and form an n^+ region under the contact.

The thin Ni layer prevents balling of the AuGe during alloying and helps to improve the surface morphology, although the resulting morphology after alloying is never very uniform. The surface of the alloyed contact typically contains dark clusters, a half micron to a few microns in size, surrounded by lighter regions of AuGa. The dark clusters have been identified as being rich in Ge and Ni [93,95]. The indiffusion of Ge is believed to be greatly enhanced by the presence of the Ni. By itself, Ge does not diffuse very deeply during the heating process, but Ge in the presence of Ni can diffuse (together with the Ni) to a few thousand angstroms into the GaAs during a long alloy period [95].

It has recently been reported [101-102] that an improvement in contact properties with good surface morphology can be obtained by sintering at low temperatures (275 - 330°C) below the eutectic temperature of the AuGe. When sintering at low temperatures it was reported that the use of a Ni overlay was unnecessary to prevent balling of the AuGe contact surface.

To investigate this idea, the author prepared several heterostructure test devices with only AuGe vacuum deposited as the contact material. These samples were sintered at 320°C in flowing H_2 until the contacts became ohmic (usually 15 min - 30 min). It was found, however, that the surface of the contacts became very rough due to balling of the contact materials. So from the standpoint of surface morphology improvement, there appeared to be no advantage in using the long-time sinter approach instead of the conventional alloy approach for the GaAs-AlGaAs heterostructures being studied. As will be shown in the following section, however, low-temperature sintering for long periods of time caused the contact constituents to diffuse to much greater depths in the heterolayers than short-time high-temperature alloying.

3.1.4 Contact Penetration Depth During Heating

During the alloy (or sinter) heating period the contact constituents such as Au, Ge, and Ni diffuse down from the top surface into the epitaxial layers below. The diffusion depth of the contact materials depends on the temperature and the length of time the heating process lasts. When a voltage is applied between two diffused contacts, a lateral electric field will exist between these contacts in the layers that have been penetrated by the contact materials. This electric field will be oriented mainly parallel to the layer interfaces.

Since some of the heterostructures studied have many periods of modulation-doped layers, it is important to know whether all of these layers are actually contacted when a particular alloying process has been performed. One would thus like to determine approximately how far the contacts diffuse for a given alloy temperature and time. Information of this sort has been published very little in the past since for a single-layer GaAs device the contact depth was not very important. It was therefore necessary to measure the contact penetration depths in several heterostructures ourselves for various alloy times. The depth profiles of the contact materials were measured using the technique of secondary ion mass spectrometry (SIMS).

3.1.4.1 Secondary Ion Mass Spectrometry (SIMS)

This technique makes use of ion beam sputtering to generate sputter-ejected material to be analyzed. The sample surface is sputtered with a primary beam of ions, such as Ar^+, O_2^+, or C_s^+. Scanning plates are used to raster the primary ion beam across the sample surface over an area larger than that used for analysis, with typical crater dimensions varying from 50 - 500 μm on a side. The sputtered atoms which become ionized (i.e., secondary ions) are extracted and transported by a special set of lenses to a double-focusing mass spectrometer. Through proper use of an aperture, only those ions originating from the flat-bottomed center of the sputtered crater give rise to the detected signal, thereby rejecting ions from the sloping crater walls which would adversely degrade depth resolution. Under well-controlled conditions, the current produced by the secondary ions at the output of the mass-analyzer detection system is proportional to the concentration of the investigated species in the sample. Plotting the secondary ion current versus time during sputtering produces a concentration profile of the atomic species being studied. A schematic diagram of the CAMECA IMS-3f system used during the SIMS studies is shown in Fig. 3.1. The direct imaging (ion microscope) mass analyzer consists principally of four main parts: an ion gun to produce the primary ion beam that sputters the sample, the collection optics for extraction and acceleration of the emitted secondary ions, a mass and energy filtering system for selecting the desired ion species, and a detection-display system for observing the chosen secondary ion signal. The entire apparatus is interfaced to a small desk-top computer (HP 9845B). A more detailed discussion of this system and its operation is available elsewhere [105].

3.1.4.2 Depth Profiles

For the profiles measured in this work, the O_2^+ primary beam was employed with currents ranging from 0.04 - 0.3 μA. The primary beam was rastered over an area of 250 x 250 microns. The collection optics were set to measure the ion signals for Ga, Al, Ni, Ge, Au and As. A Sloan Dektak mechanical stylus instrument was used to measure the resultant crater depths. These depth measurements together with the assumption of a constant sputtering rate were used to convert the sputtering time scale to a depth scale.

As discussed earlier, the surface morphology of the contacts was never particularly good. Dektak profiles across the contact surface indicated that the surface was fairly rough with the vertical uneveness sometimes

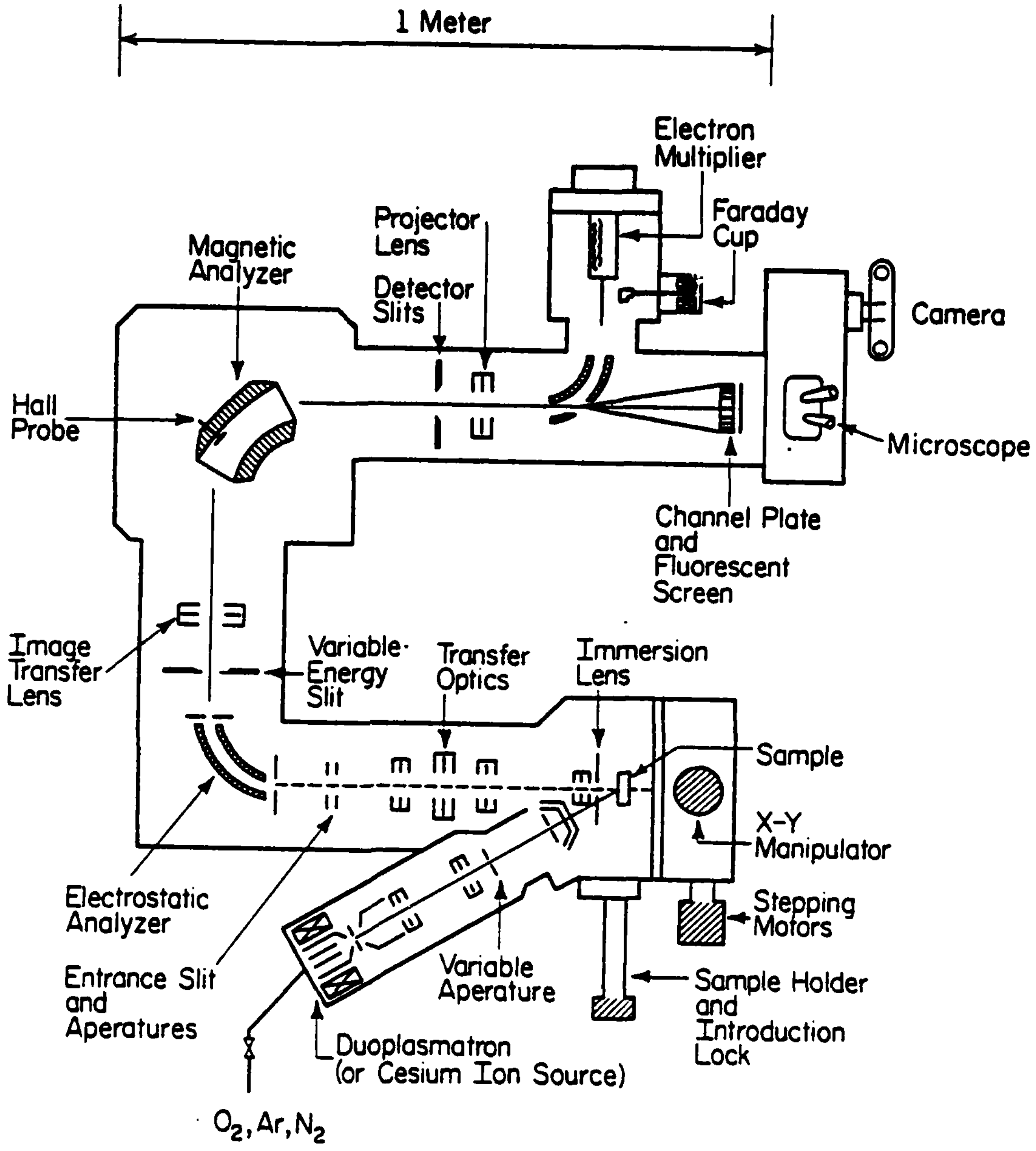

LP-1785

Fig. 3.1: Schematic representation of CAMECA IMS-3f direct imaging secondary ion mass spectrometer (after [104]).

exceeding 1000 Å. This means that when the material was being sputtered, the primary beam in one spot might have been sputtering ions from a different depth of the heterostructure than at another spot. This results in secondary ion information from different layers being detected together, and thus the information from adjacent layers was often averaged together. This can be seen in the following SIMS profiles where the distinct location of the Al in only the AlGaAs layers has been smeared out through much of the profile. In many cases, however, the location of the AlGaAs regions were still distinguishable. Although the precise location of all the contact constituents in the heterostructure will be somewhat smeared out due to the contact roughness, it is still possible to get a good estimate of how far the different materials diffuse into the semiconductor before they drop to their background concentrations as seen below.

The depth profile for a three-period MBE-grown sample, alloyed at 450°C for only several seconds, is shown in Fig. 3.2. Each period consisted of a 500 Å undoped layer of GaAs, followed above by a 50 Å undoped layer of AlGaAs, a doped 500 Å layer of AlGaAs and a second 50 Å undoped layer of AlGaAs. The AlAs mole fraction was $x = 0.17$. The first 2000 Å on the left side of the profile in Fig. 3.2 consisted of a metallic region extending above the top surface of the semiconductor. This material located on top of the heterostructure was labeled the "contact" region in the figure. The narrow peaks of Al and As on the top surface of the contact region may be due to the outdiffusion of these elements during alloying. It is also possible that these initial peaks were just an artifact from a previous sputtering run where the ion gun became coated by these materials. From Fig. 3.2 it is seen that the three metal contact constituents diffused

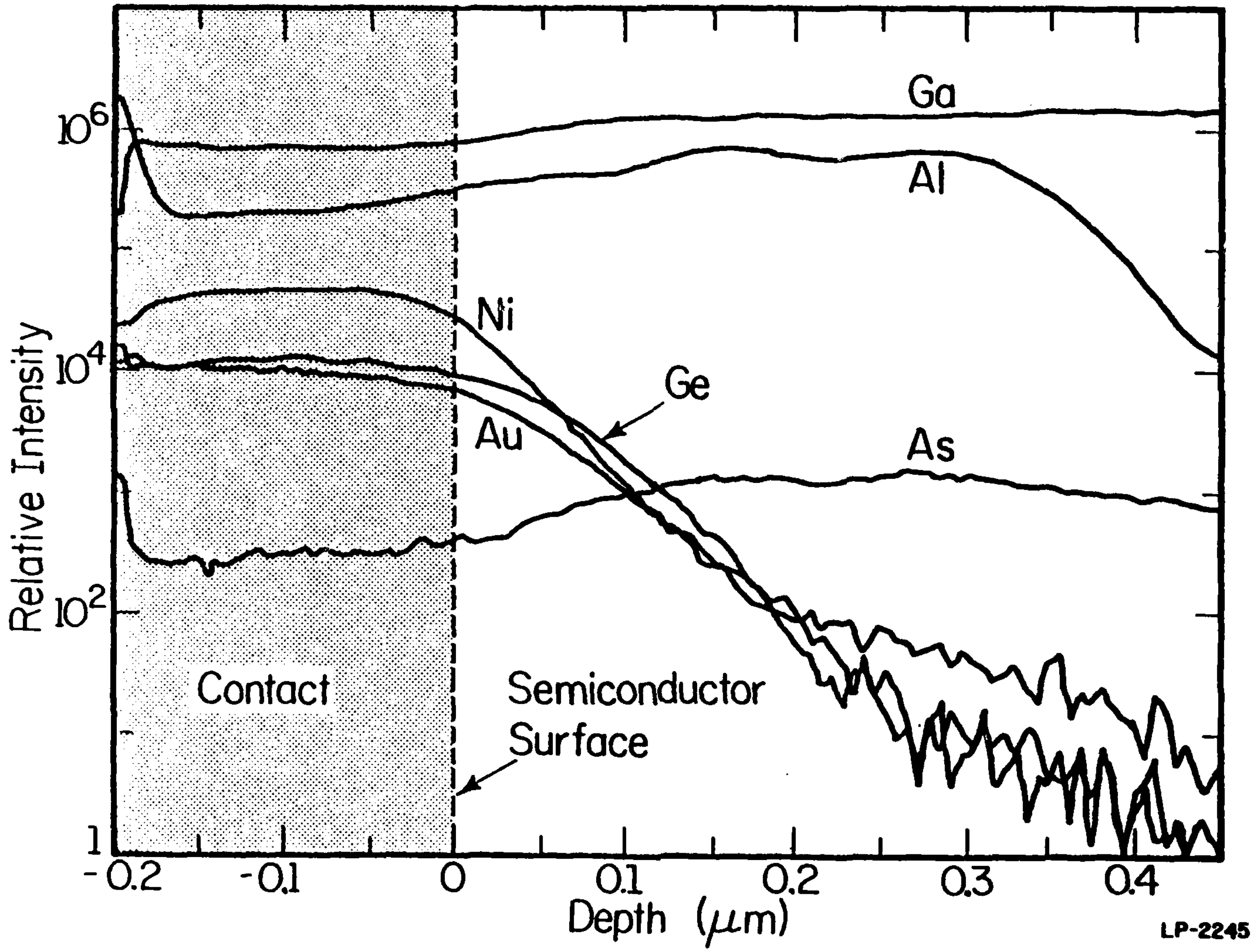

Fig. 3.2: SIMS profiles of contact material diffusion depths in a three-period MBE-grown sample that was alloyed at 450°C for several seconds.

3000 - 4000 Å into the semiconductor before their concentrations dropped to the background level. One would then expect that the ohmic contact region extends at least 2000 Å to 3000 Å into the heterostructure. Hence, just heating a sample up to the alloy temperature of 450°C and then cooling seems to allow sufficient penetration of the ohmic contact to properly contact a typical one- or two-period structure.

In order to contact more periods it is obviously necessary to alloy for longer times. Fig. 3.3 and Fig. 3.4 show the effects of alloying for 6 s and 16 s respectively at 450°C in a nine-period MOCVD-grown heterostructure. Each period consisted of one undoped GaAs layer 500 Å thick and one doped $Al_xGa_{1-x}As$ (x = 0.21) layer also 500 Å thick. It is seen in Fig. 3.3 that the 6 s alloy caused the Ni and Ge to diffuse in nearly 4000 Å. This closely resembles the distribution in the previously shown MBE structure (Fig. 3.2) with a similar alloy time.

The extended penetration of the Au in this profile is most likely due to the resputtering of Au that fell back into the sputtered crater, rather than an actual deeper diffusion of the Au during the alloy process. Since the atomic mass of Au is much greater than the other elements being measured, it is much more difficult to sputter the Au completely out of the crater. Thus, the measured concentration of Au is significantly less than that of Ni and Ge during the first portion of the SIMS profile and residual Au left in the crater continues to be resputtered well after the Ni and Ge have been depleted at greater depths.

Comparing Fig. 3.4 to Fig. 3.3 indicates that increasing the alloy time from 6 s to 16 s causes the contact penetration depth to increase by another 1000 - 2000 Å if all other factors were equal. This would probably be deep

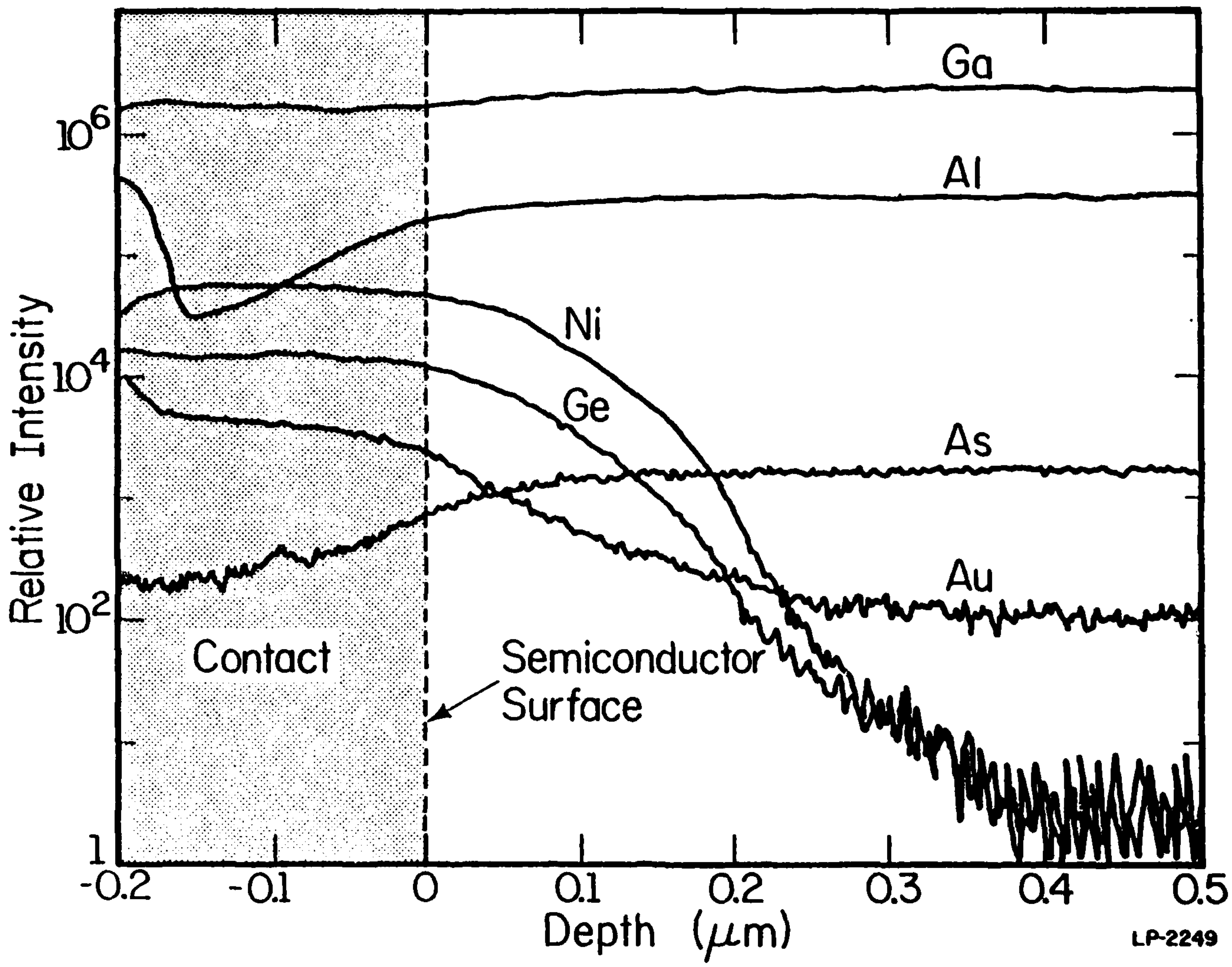

Fig. 3.3: SIMS profiles showing contact metal diffusion depths following a 6 s alloy at 450°C in a nine-period MOCVD-grown GaAs-AlGaAs heterostructure.

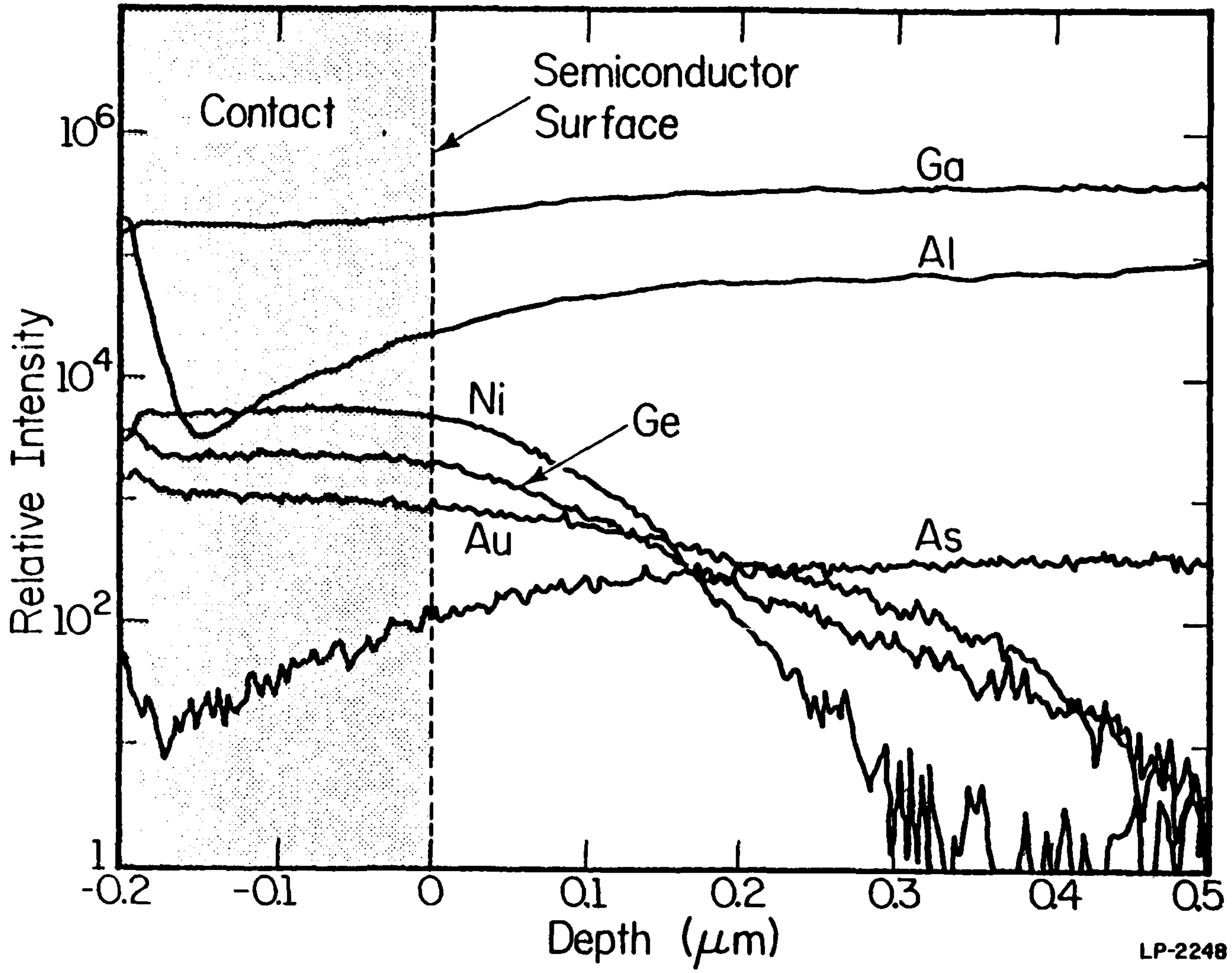

Fig. 3.4: SIMS profiles showing contact metal diffusion depths after a 16 s alloy under the same conditions as in Fig. 3.3.

enough to supply ohmic connections to the top four periods of the heterostructure. One must emphasize, however, that this is only an estimate and can only be used as such due to the approximate nature of the data obtained. In order to fully contact all nine periods of this heterostructure it would probably be necessary to alloy at 450°C for 1 minute or longer.

It was discovered that an alternate method of obtaining deeply-diffused ohmic contacts could be realized with low-temperature (275 - 330°C) sintering. AuGe contacts were sintered at 320°C in a three-period heterostructure grown by MBE. Each period contained an undoped layer 1000 Å thick of GaAs and a 250 Å doped layer of $Al_xGa_{1-x}As$ (x = 0.18). The profiles for a 15 min sinter and a 38 min sinter are presented in Figures 3.5 and 3.6, respectively. It is obvious from these profiles that the Au and Ge penetrate much more deeply in this case than in the previous alloyed profiles. Sintering until the contact became ohmic (15 min) caused an ohmic contact penetration depth of $\gtrsim$ 1.5 μm, whereas 38 min gave a penetration depth of $\gtrsim$ 2.0 μm. The location of the three AlGaAs layers in each figure is easily discernible, especially in Fig. 3.5, by the three bumps in the Al profile.

3.1.5 Sample Mounting for Measurements

Following contact evaporation and alloying, individual samples were securely mounted in nearly all cases to TO-18 (two pin) or TO-5 (ten pin) package headers. The semi-insulating substrate of each sample was bonded to the gold-plated header surface with a thin layer of conductive epoxy. One-mil gold wires were connected from each sample contact to one of the top header posts using a manual thermocompression wire bonder. The heat

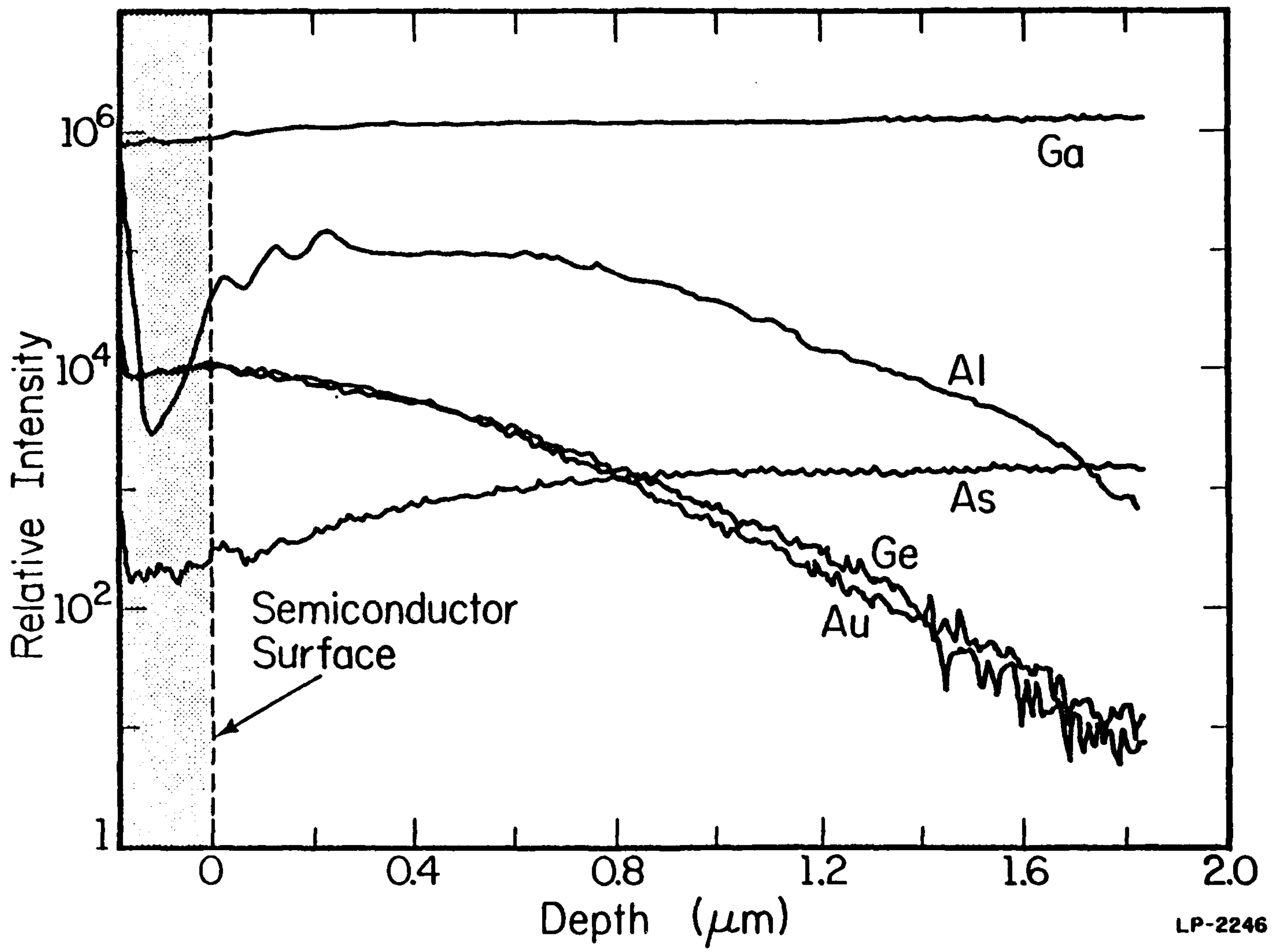

Fig. 3.5: SIMS profiles showing contact penetration depth following a 15 min sinter at 320°C in a three-period MBE sample.

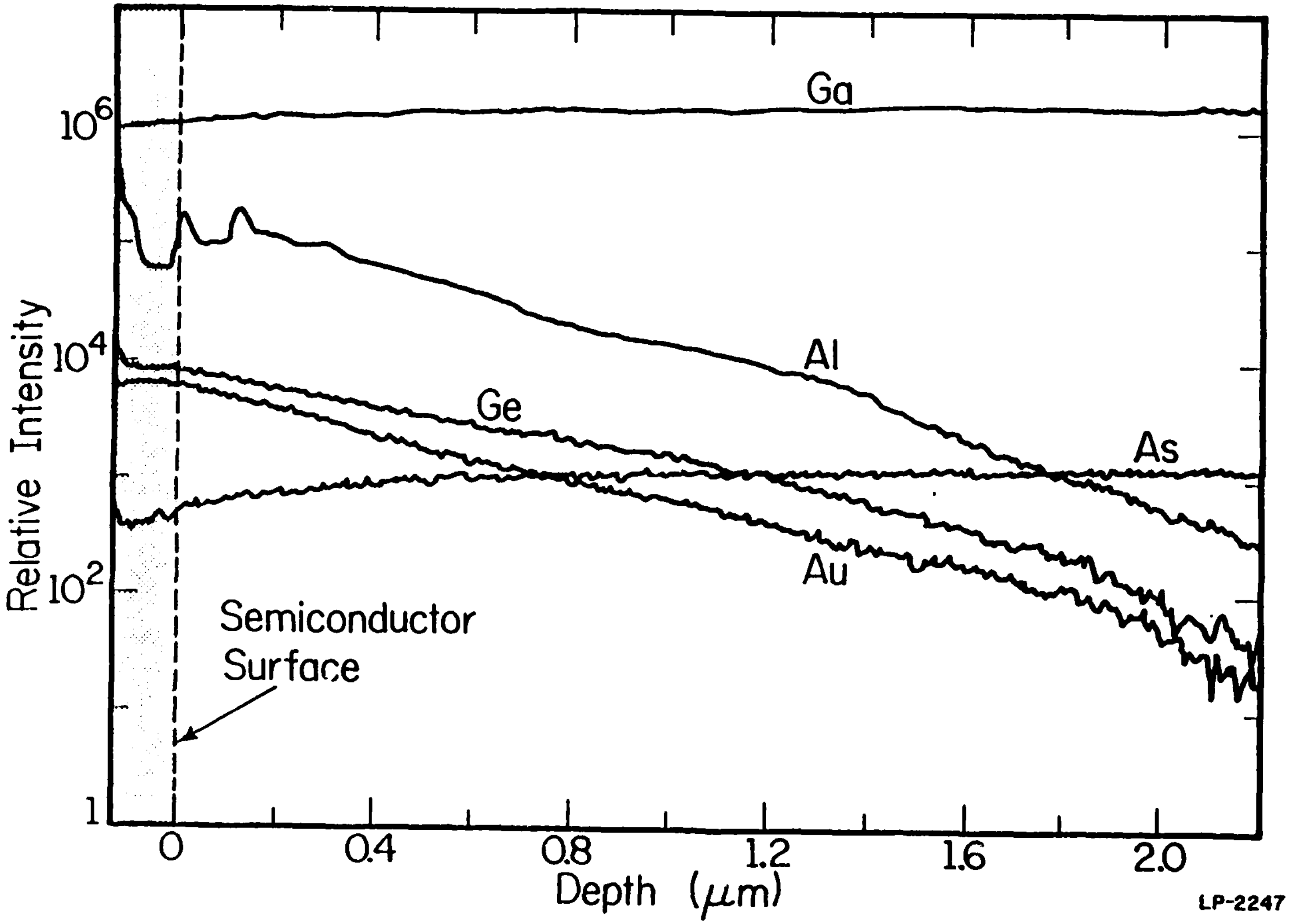

Fig. 3.6: SIMS profiles for a 38 min sinter at 320°C in the same GaAs-AlAs heterostructure as in Fig. 3.5.

supplied by the wire-bonder workstage was sufficient to cure the epoxy holding the sample to the header. The resulting sample package proved to be rugged, reliable, and versatile for a number of measurement techniques.

Samples mounted on TO-18 headers could be tested in GR insertion units at room temperature and at 77 K (by immersing in liquid nitrogen) under both light and dark conditions. Both the TO-18 and TO-5 header samples could also be easily mounted in the copper cold finger of closed-cycle helium cryogenics system allowing temperature-controlled electrical measurements in the temperature range of 7 K to over 300 K. A ten-wire electrical feedthrough into the evacuated sample chamber allowed access for all electrical measurements which could be made with the sample in the dark or illuminated with any external light source. The sample chamber of the cryostat could also be placed between the four-inch diameter pole faces of an electromagnet. Magnetic fields up to nearly 7 kG could be applied at any orientation to the sample while it was in the cryostat.

In some instances, samples were also tested under the higher magnetic-field conditions provided by a 120 kG superconducting magnet. Heterostructure samples tested in the superconducting magnet were mounted on small circular ceramic disks using indium solder. Two-mil wires were soldered from the sample contacts to gold pads on the disks and the disks were attached to a holder on a rod that could be inserted into the magnet. The orientation of the heterostructure surface was fixed perpendicular to the magnetic field in this case.

3.2 Current-Field Measurements

Nearly all of the measurements reported in this dissertation result from applying an increasing (or decreasing) voltage between two contacts in a sample and then measuring the resulting characteristics of the lateral current through the heterolayers between the contacts. The strength of the electric field, oriented parallel to the layers, is estimated by dividing the voltage applied across the contacts by the distance between the ohmic contacts.

In most cases, the voltage ranges used were sufficient to cause high electric fields in the heterolayers. Thus, short voltage pulses (300 - 1000 ns) were applied at low repetition rates to reduce heating of the heterostructure lattice. Fig. 3.7 depicts the standard test circuit used to measure the current-field characteristics of a sample. An inductive current probe and transformer (Tektronix CT-2/P6041) were used to measure the sample current without loading the circuit. The transformer supplied 1 mV/mA to a sampling oscilloscope. The pulse generator, current probe and transformer, and sampling oscilloscope all had 50 Ω input/output impedances. A measurement of the current versus voltage could be made at any time location on the pulses (from 1 ns to the end of the pulse) using the sampling oscilloscope. The current versus voltage measurements from the oscilloscope were recorded directly on an x-y recorder.

The structure of a typical test sample is shown in Fig. 3.8. The general layer structure shown on the left side of the figure was described in detail in Chapter 2. The device sketched on the right has the simplest contact configuration of any of the various device forms studied. This simple device consists of just two ohmic contacts, spaced a distance L

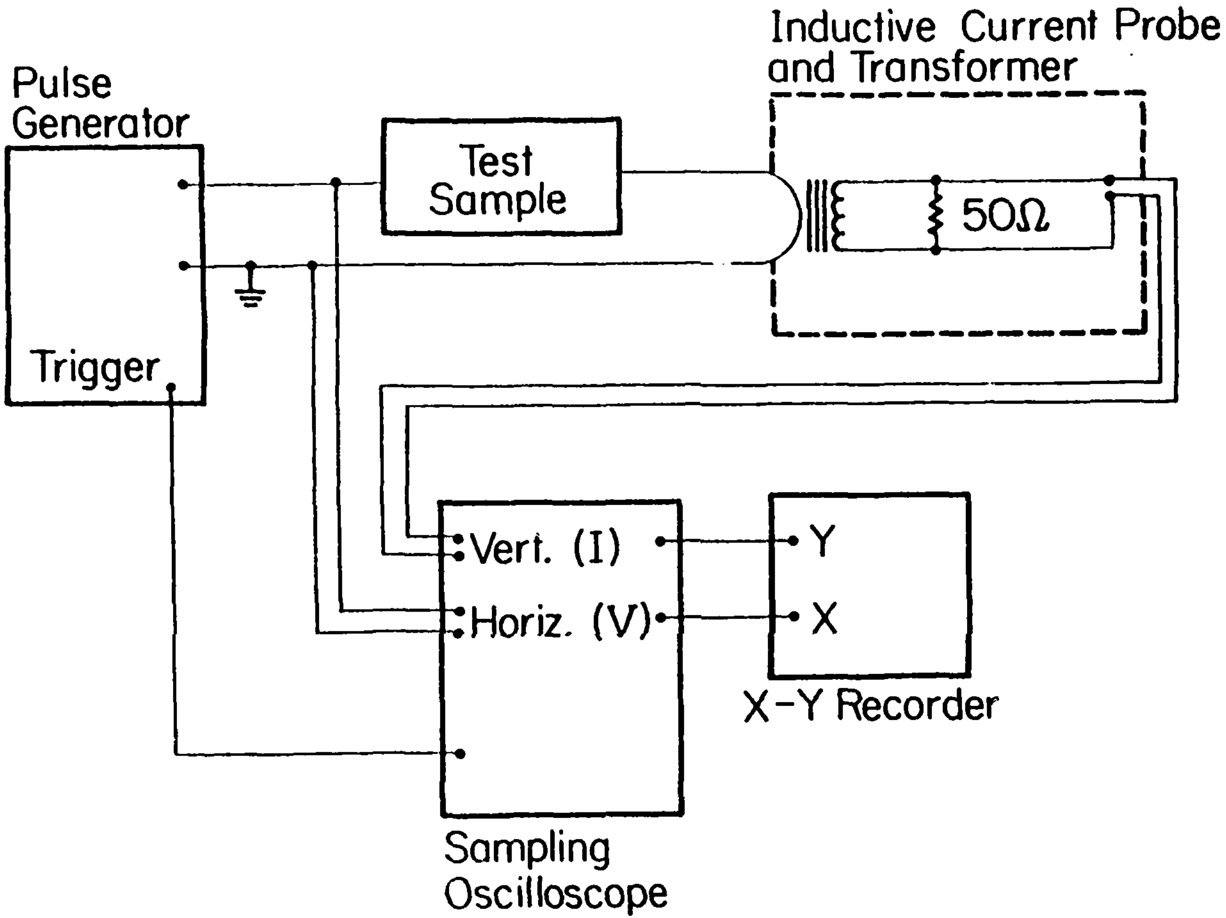

LP-2223

Fig. 3.7: Schematic of test equipment and circuit used to measure pulsed current-field characteristics in GaAs-AlGaAs heterostructure devices.

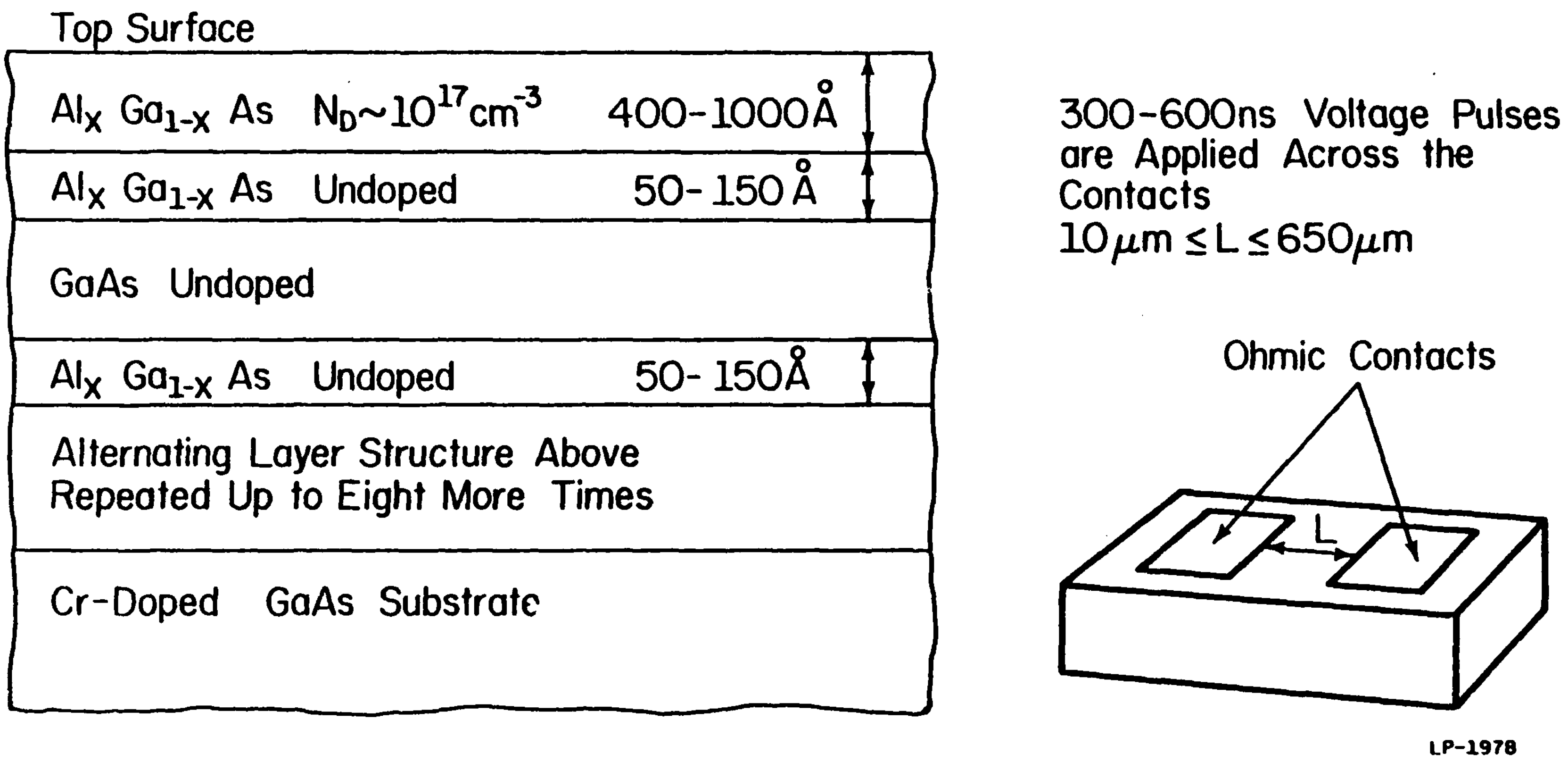

Fig. 3.8: Schematic diagram of general sample layer cross section and sketch of simplest two-contact sample configuration used to measure lateral current-field characteristics. The separation distance L of the two ohmic contacts was varied from 10 μm to 650 μm.

apart, which have been alloyed through all the conducting layers. The distance L could be varied from 10 μm to 650 μm. Voltage pulses were applied between the two ohmic contacts and the current-field characteristics of the heterostructure were then recorded, as just discussed, using the circuit of Fig. 3.7.

More sophisticated test structures involving etched-mesa patterns and four or six contact pads have also been fabricated and tested. Sketches of these structures will be shown later in the text when the corresponding measurement results are discussed.

A series of low-field measurements on a number of samples were also done employing a low-voltage voltage ramp as the voltage source. The voltage across the sample was measured directly by the x input of the x-y recorder. The current characteristics were recorded by using the y input of the recorder to measure the voltage across a small resistor placed in series with the test sample. These results are reported in Chapter 4.

4. LOW-FIELD MEASUREMENTS

4.1 Current-Field Characteristics

The influence of growth parameters such as the AlAs mole fraction x and intrinsic AlGaAs layer thickness d_i on the Hall mobility has been well documented, and was discussed in detail in Chapter 2. However, these mobility measurements were almost always made at very low electric fields and do not necessarily represent the electron mobility over a larger range of electric fields such as would be found in many devices.

In the following three subsections, measurements will be presented of the current-field characteristics of various sample structures for the electric field range 0 - 2 kV/cm. This is below the electric field values where the onset of real-space electron transfer or the Gunn effect is expected to occur. It has been reported that the electric field in the channel of a high-speed 1 μm gate normally-off FET [106] is about 2 kV/cm, so the results presented here may be helpful in predicting device performance.

The following three sets of measurements illustrate the effect of the AlAs mole fraction, the intrinsic AlGaAs layer thickness, and the number of modulation-doped periods on the low-field current-field characteristics. All of the measurements were performed on mesa-etched rectangular-bridge patterns of the type sketched in Fig. 4.1. The narrow bridge was 400 μm long by 40 μm wide. All conducting layers outside the pattern were removed using a chemical etch and each triangular pad contained an ohmic contact.

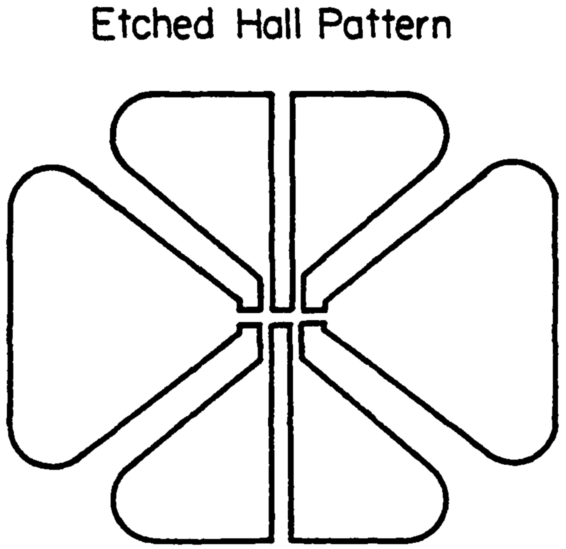

Fig. 4.1: Sketch of mesa-etched, rectangular-bridge Hall pattern used during current-field measurements. The narrow bridge was 400 μm long by 40 μm wide. Voltages were applied between the two larger end pads whereas the four side pads of known spacing could be utilized to check electric field uniformity along the bridge.

Voltages were applied between the two larger end pads while the four side pads of known spacing were used to verify the field uniformity along the narrow bridge.

For fields between 0 and 200 V/cm, a dc voltage ramp was used to measure the current-field characteristics since lattice heating effects were negligible. For fields between 200 V/cm and 2 kV/cm, 800 - 1000 ns voltage pulses were applied through the bridge. Details of these measurement techniques are given in Chapter 3. Measurements of the current and voltage were taken near the end of each pulse. Current-field (as well as van der Pauw-Hall) measurements were made in the temperature range of 10 K to 300 K.

4.1.1 Dependence on AlAs Mole Fraction

The set of structures measured for this investigation consisted of four single-period GaAs-$Al_xGa_{1-x}As$ samples with AlAs mole fractions of 0.16, 0.24, 0.32, and 0.36. The layer structure for each of the four samples was the same and is shown in Fig. 4.2. An undoped AlGaAs layer thickness of 75 Å was chosen because previous studies (discussed in Chapter 2) have shown that this thickness resulted in the highest mobilities in single-period structures. The top AlGaAs layer was 1500 Å thick and was doped to a concentration of $N_D \sim 10^{17}$ cm^{-3}.

The substrates were mounted on molybdenum blocks and introduced into an MBE system via a sample exchange chamber. The sample exchange chamber was then evacuated and the sample transferred to the growth chamber. The samples were initially outgassed at 630°C to desorb any oxides on the surface and then the temperature was reduced to 600°C before growth was initiated. The Ga flux was adjusted to obtain a 0.7 μm/hr growth rate and the Al flux was adjusted to obtain the desired AlAs mole fraction. The

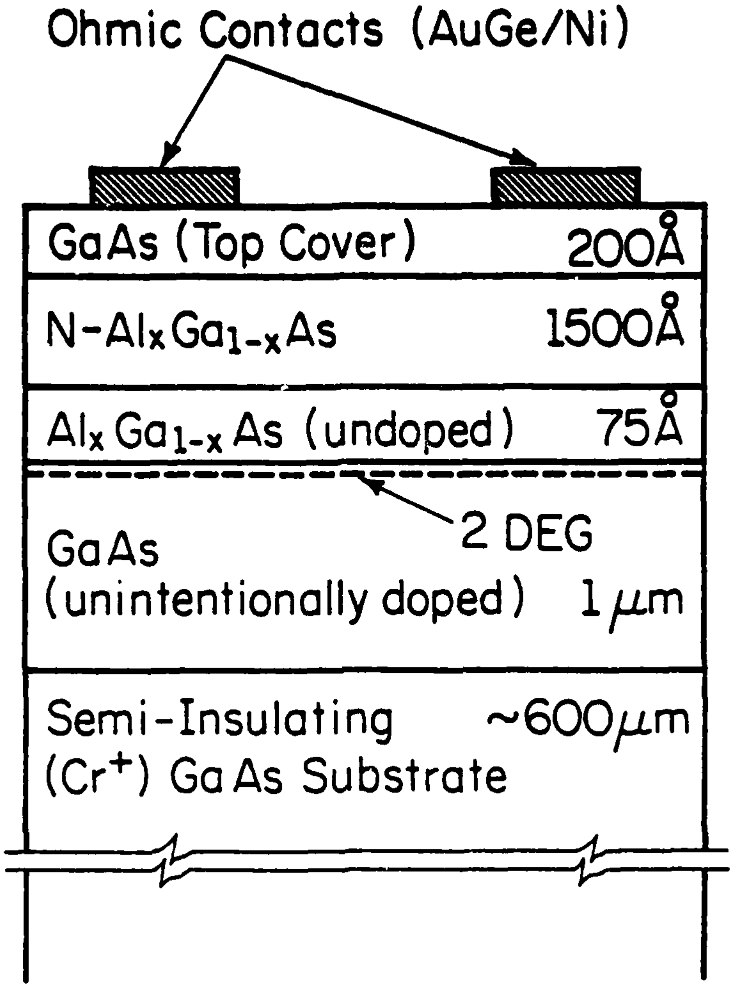

LP-2193

Fig. 4.2: Schematic illustration of single-period modulation-doped GaAs-AlGaAs structures used for AlAs mole fraction dependence measurements ($x = 0.16$, 0.24, 0.32, and 0.36).

growth was always performed under As stabilized surface conditions.

Van der Pauw-Hall measurements were made in the dark on samples which had been photolithographically defined and etched into cloverleaf patterns. Ohmic contacts were formed by alloying Sn dots at 400°C in a hydrogen atmosphere. The current vs. field measurement characteristics for these four structures at several temperatures between 10 K and 300 K are depicted in Fig. 4.3. The mesa-etched sample structure used to make these measurements is shown again in the inset of the top graph. The same scale of arbitrary units was used for each current axis to facilitate comparison (i.e., a current of magnitude 1.0 is the same for all four graphs).

It is seen from the graphs that the low-field conductivity of each structure increased as the temperature was decreased. This is especially obvious at electric fields below 300 V/cm where the initial slope of the curves increased with decreasing temperature. Since the electron concentration is not expected to change in this low field range, one can assume that the Hall mobility is proportional to the conductivity and so the mobility similarly increased with decreasing temperature. As explained in Chapter 2, this is expected since these modulation-doped structures should exhibit reduced ionized-impurity scattering at low temperatures.

The electron mobility at all temperatures also appeared to increase with an increase in the AlAs mole fraction. This can be seen in the current vs. electric field curves in Fig. 4.3 and also in the Hall mobility and sheet carrier concentration data at 10 K, 77 K, and 300 K obtained from Hall measurements and listed in Table 4.1. The largest measured value of mobility for these structures in the dark was nearly 200,000 cm^2/Vs at 10 K with an associated sheet carrier concentration of $N_s \sim 1 \times 10^{12}$ cm^{-2} for the

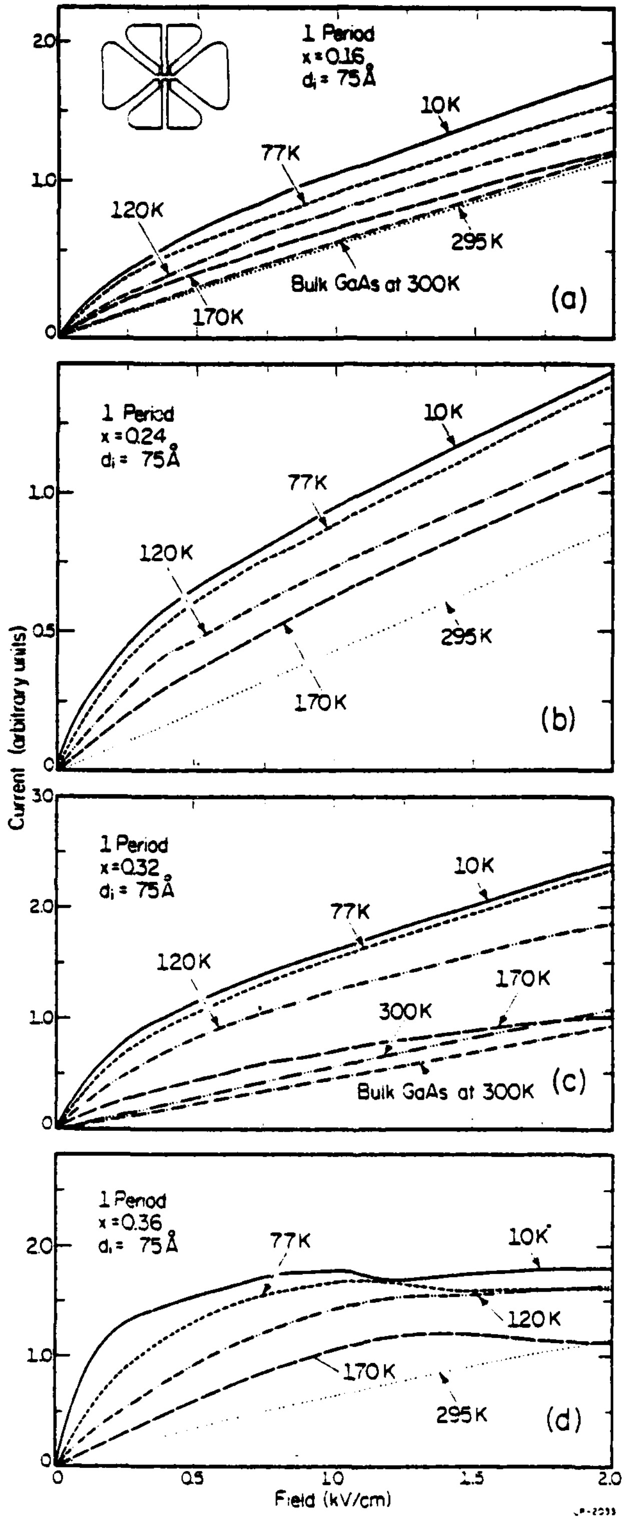

Fig. 4.3: Current-field characteristics measured up to 2 kV/cm for the sample structure depicted in Fig. 4.2 with AlAs mole fractions of x = 0.16, 0.24, 0.32, and 0.36. A magnitude of 1.0 on the vertical axis corresponds to the same value of measured current in all four samples.

TABLE 4.1:

Hall mobility in cm^2/Vs and sheet carrier concentration in cm^{-2} at 10 K, 77 K, and 300 K for the single-period samples of varying AlAs mole fraction.

Wafer	Mole Fraction	Hall Mobility ($cm^2V^{-1}s^{-1}$)			Sheet Carrier Concentration (cm^{-2})		
	X	10K	77K	300K	10K	77K	300K
a	0.16	112,000	60,100	4160	4.94×10^{11}	6.75×10^{11}	3.30×10^{12}
b	0.24	141,000	75,600	4450	3.90×10^{11}	4.80×10^{11}	1.65×10^{12}
c	0.32	160,000	87,000	5310	6.90×10^{11}	7.80×10^{11}	1.38×10^{12}
d	0.36	199,000	90,000	7300	1.02×10^{12}	1.02×10^{11}	7.80×10^{11}

LP-2031

sample with the largest AlAs mole fraction ($x = 0.36$). Correspondingly, the mobility of the smallest AlAs mole fraction ($x = 0.16$) sample at 10 K was only half as large, $\mu = 112{,}000$ cm^2/Vs with $N_s \approx 5 \times 10^{11}$ cm^{-2}. The increased mobility for higher AlAs mole fractions is most likely due to a decreased Coulomb interaction between the donors in the doped $Al_xGa_{1-x}As$ and electrons in the GaAs. As x increases, the conduction-band discontinuity between the $Al_xGa_{1-x}As$ and GaAs at the interface also increases. This causes the penetration of the electron wavefunction in the $Al_xGa_{1-x}As$ to decay more quickly, so there is less wavefunction overlap between the electrons in the GaAs and the donor ions in the $Al_xGa_{1-x}As$. It has been predicted [66,67,78] that the mobility of the electrons is roughly proportional to the square of the distance separating the electron distribution in the GaAs from the donors in the doped $Al_xGa_{1-x}As$. Using the well known formula for a one-dimensional potential well, a quick and approximate calculation can be made to check if the reduced penetration of the wavefunction can account for the observed factor of two increase in the mobility. The electron wavefunction decays exponentially in the region of the AlGaAs where the electron energy is less than the AlGaAs-GaAs conduction-band discontinuity so the electron wavefunction for $z \geq 0$ can be expressed as

$$\psi \propto e^{-kz} \tag{4.1}$$

with

$$k = \sqrt{\frac{2m^* \Delta E_c}{h}} \tag{4.2}$$

where m^* is the effective mass, z is the distance component, and ΔE_c is the conduction-band discontinuity. When x is changed from 0.16 to 0.36, m^*

increases only slightly and ΔE_c increases by a little more than a factor of two. Thus, k changes by slightly more than $\sqrt{2}$ which in turn means that the wavefunction decays to a certain value for $x = 0.36$ in less than $1/\sqrt{2}$ of the distance that it did for $x = 0.16$. The effective separation of the electrons and donors in terms of the wavefunction overlap is thus increased by nearly a factor of $\sqrt{2}$ and the mobility $\mu \propto z^2$ is increased by about a factor of two, just as is found experimentally. Therefore, the wavefunction interaction change seems to be of the right order to correspond to the mobility change.

The small negative differential resistance (NDR) effects seen in Fig. 4.3(d) for the sample with the highest AlAs mole fraction ($x = 0.36$) can be explained in several ways. It could be caused by the trapping of the electrons in resonance states at the interface. If the interface is sharp and the barrier height between the GaAs and $Al_xGa_{1-x}As$ conduction bands is sufficiently high, resonance states, which are an intrinsic property of the interface, can be formed. As electrons become trapped in these interface energy states above the GaAs conduction-band edge, the current will be reduced, leading to a negative differential resistance. Another explanation for the NDR is the sudden onset of optical-phonon scattering [107]. Ridley [108] has predicted that such effects can occur as a consequence of the abrupt threshold for optical-phonon emission and the properties that all scattering rates are energy independent and inversely proportional to L (the thickness of the potential well), whereas the momentum relaxation rate associated with the absorption of polar-optical phonons is proportional to L. These properties are thought to lead to a negative differential resistance for pure polar-mode scattering.

It is seen from the graphs in Fig. 4.3 that the slope (conductivity) of any of the low temperature curves decreases significantly as the applied electric field is increased. This is especially noticeable for the larger AlAs mole fraction samples. The conductivity decreases most dramatically when the field reaches values near 250 V/cm and varies little for fields above 500 V/cm for most of the samples. The high temperature curves, on the other hand, show comparatively little change in conductivity as a function of electric field. An extra 300 K current-field line is included in graphs (a) and (c) to show the characteristics of a bulk GaAs (0.1 μm thick) FET channel layer with the same pattern and donor concentration of 1 x 10^{17} cm^{-3}. Only the 300 K characteristic curve is plotted because there is negligible improvement at low temperatures for this bulk GaAs layer.

If one assumes as before that the carrier concentration does not change in this low-field range, then the change in mobility with increasing electric field may be roughly approximated by the change in the slope of the current-field curves in Fig. 4.3. The slopes of the curves at several temperatures were roughly measured and plotted versus electric field for the three structures with the lowest AlAs mole fractions. The structure with the x = 0.36 AlAs mole fraction was omitted due to the slight NDR effects described earlier. The slopes were then normalized with respect to the low-field values of mobility as determined from van der Pauw-Hall measurements at that particular temperature. The resulting normalized mobility versus electric field graphs for the three structures with x = 0.16, 0.24, and 0.32 are pictured in Figures 4.4 - 4.6, respectively.

It is seen in Fig. 4.4 that the 10 K mobility for the x = 0.16 sample drops to 40% of its low-field value of 112,000 cm^2/Vs at an electric field

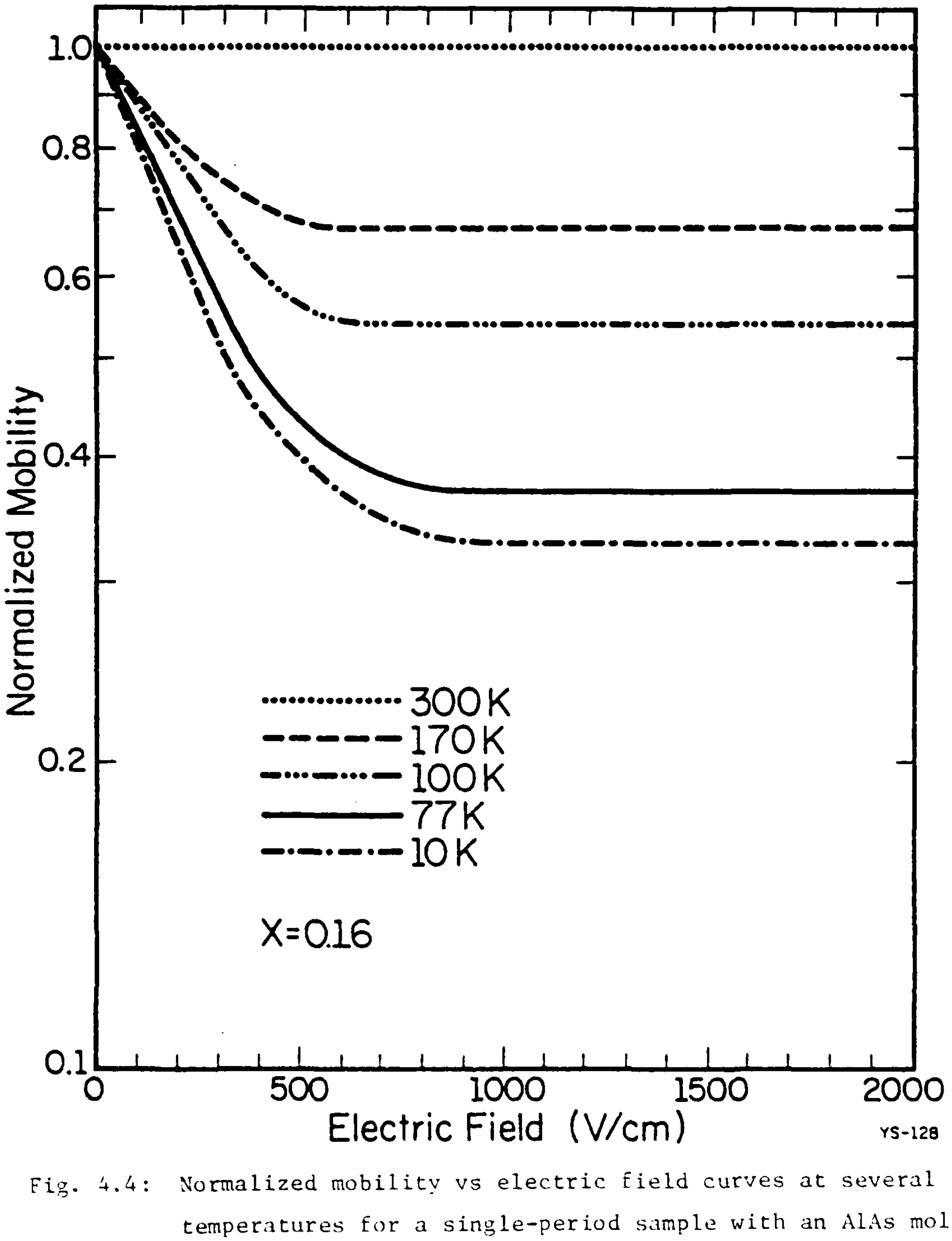

Fig. 4.4: Normalized mobility vs electric field curves at several temperatures for a single-period sample with an AlAs mole fraction of x = 0.16. The sample structure was the same as in Fig. 4.2. The mobility was normalized with respect to the Hall mobility measured with van der Pauw-Hall techniques at each temperature.

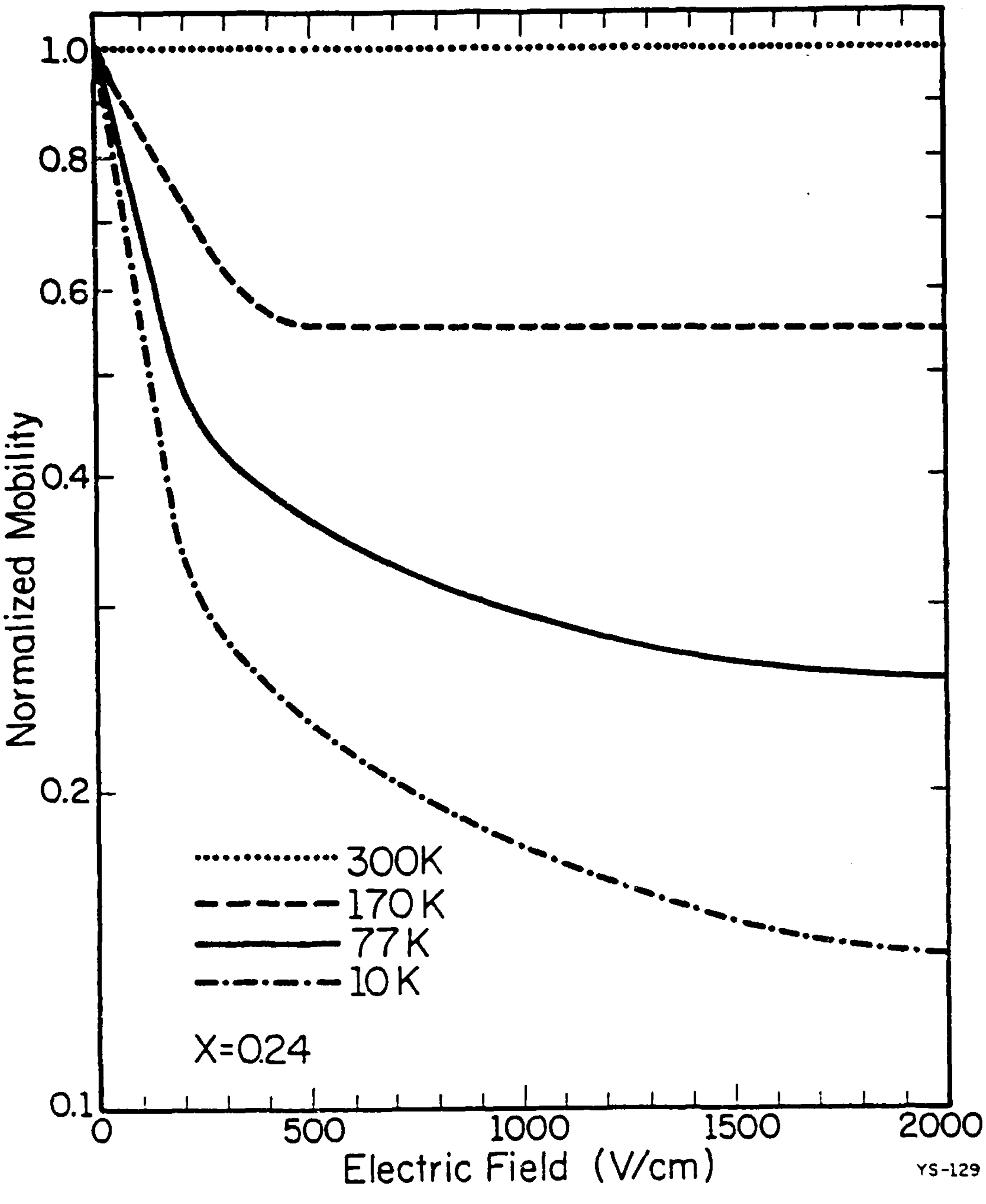

Fig. 4.5: Normalized mobility vs electric field curves measured using the same procedure as in Fig. 4.4 for a single-period sample with an AlAs mole fraction of x = 0.24.

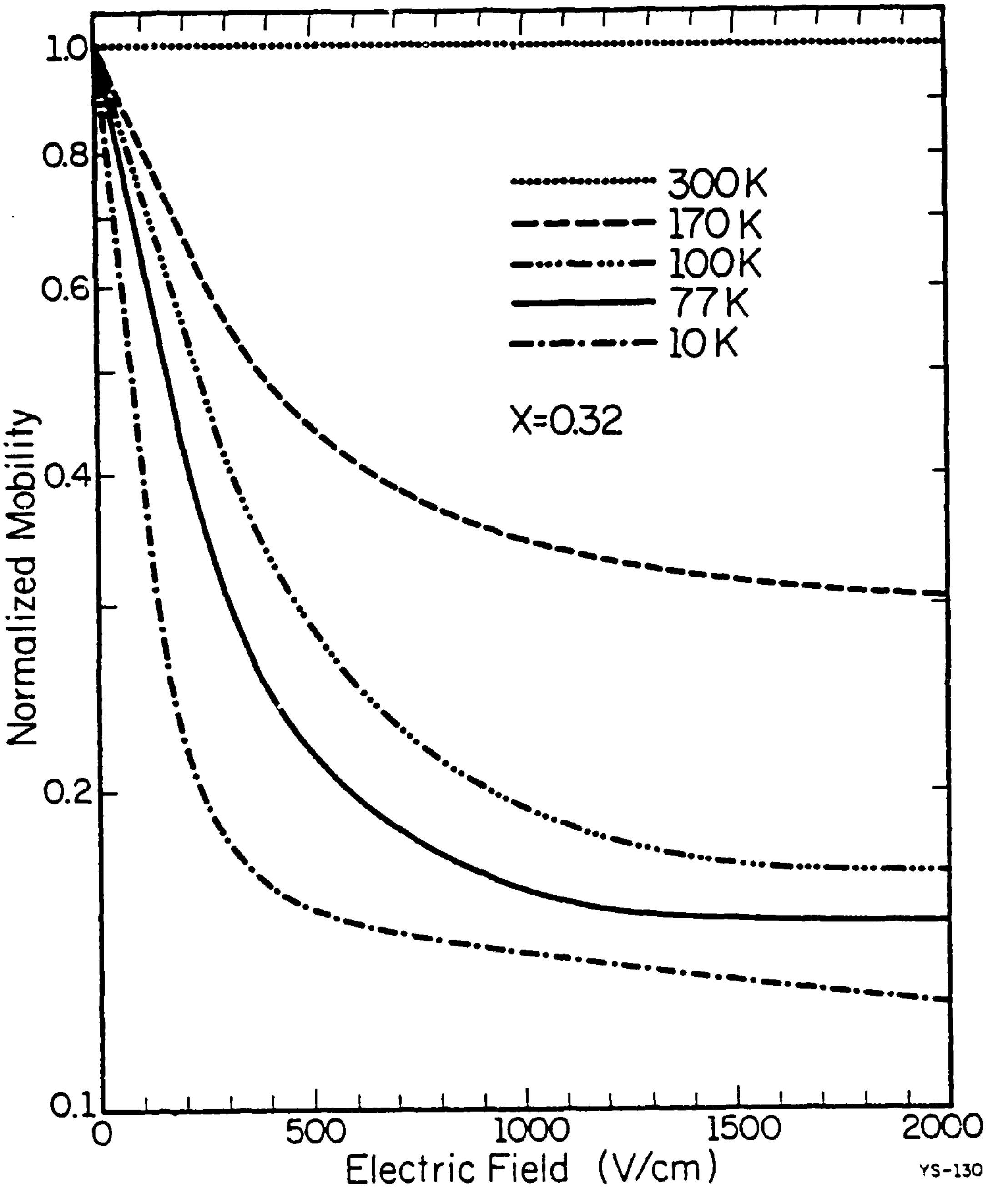

Fig. 4.6: Normalized mobility vs electric field curves measured using the same procedure as in Fig. 4.4 for a single-period sample with an AlAs mole fraction of x = 0.32.

of only 500 V/cm. The samples with higher low-field mobility show an even larger decrease in mobility with field. For instance, the 32% AlAs mole-fraction sample shows a mobility drop at 200 V/cm to about 20% of its zero-field value. It must be emphasized, however, that these values are only approximate and do not necessarily represent the actual value of the mobility reductions as a function of the electric field. The crudely measured curves in Figs. 4.4 - 4.6 do, nevertheless, illustrate the characteristics of the mobility decrease at very low electric fields and can be useful in identifying the important features. For instance, it is seen from Figs. 4.4 - 4.6 that for a higher initial mobility (higher x) the abrupt low-temperature mobility decrease is much larger and occurs at a smaller value of the electric field. Also, all three structures show a negligible change in room-temperature mobility as a function of the electric field strength up to 2 kV/cm. This field range is below the expected threshold field necessary for real-space electron transfer effects or the Gunn effect.

As will be discussed in Section 4.2, the drop in electron mobility at small electric fields may be due to the spontaneous emission of polar optical phonons and/or intersubband scattering effects. A more precise method for measuring the mobility versus electric field characteristics at low temperatures will also be discussed in the same section.

4.1.2 Dependent on Undoped AlGaAs Layer Thickness

To study the effect of the undoped (intrinsic) AlGaAs layer thickness on the current vs. electric field characteristics and mobility of these structures, six three-period structures were prepared with intrinsic-layer thicknesses of d_i = 50 Å, 100 Å, 150 Å, 200 Å, 250 Å, and 300 Å. The growth procedures were identical to those used for the single period structures in the previous section and a schematic of the three-period structures is drawn in Fig. 4.7. The Si-doped $Al_xGa_{1-x}As$ and undoped GaAs layers were both 1000 Å thick and the AlAs mole fraction was $x = 0.20$. As before, a 200 Å undoped GaAs layer was grown on the top surface to facilitate ohmic contact preparation.

The current vs. electric field characteristics for the 100 Å, 150 Å, 200 Å, and 300 Å intrinsic-layer thickness structures are shown in Figs. 4.8 - 4.11. These curves show the same general conductivity (slope) dependence on electric field as the four graphs in Fig. 4.3. The high temperature curves usually vary little in slope with increasng electric field, whereas the conductivity changes drastically at low fields for cryogenic lattice temperatures. The greatest conductivity changes occur below 500 V/cm where the electron sheet carrier concentration is relatively constant. Thus, the conductivity decreases are directly proportional to the decreases in mobility at these low fields. The higher the zero-field mobility, the larger the mobility decrease at low fields as in the case of the single-period structures described earlier. Significant changes in the electron mobility at fields up to 500 V/cm may be due to spontaneous phonon emission.

In the three-period structures the mobility increased with undoped layer thickness up to $d_i = 150$ Å and then decreased for wider layers. Mobility and sheet carrier concentration data for 10 K, 77 K, and 300 K are presented in Table 4.2. The peak mobility in the 150 Å intrinsic layer at 10 K is 164,000 cm^2/Vs in the dark with $N_s = 2.26 \times 10^{12}$ cm^{-2}. The 77 K and 300 K mobilities of the $d_i = 150$ Å structure are also higher than any of the other three-period structures.

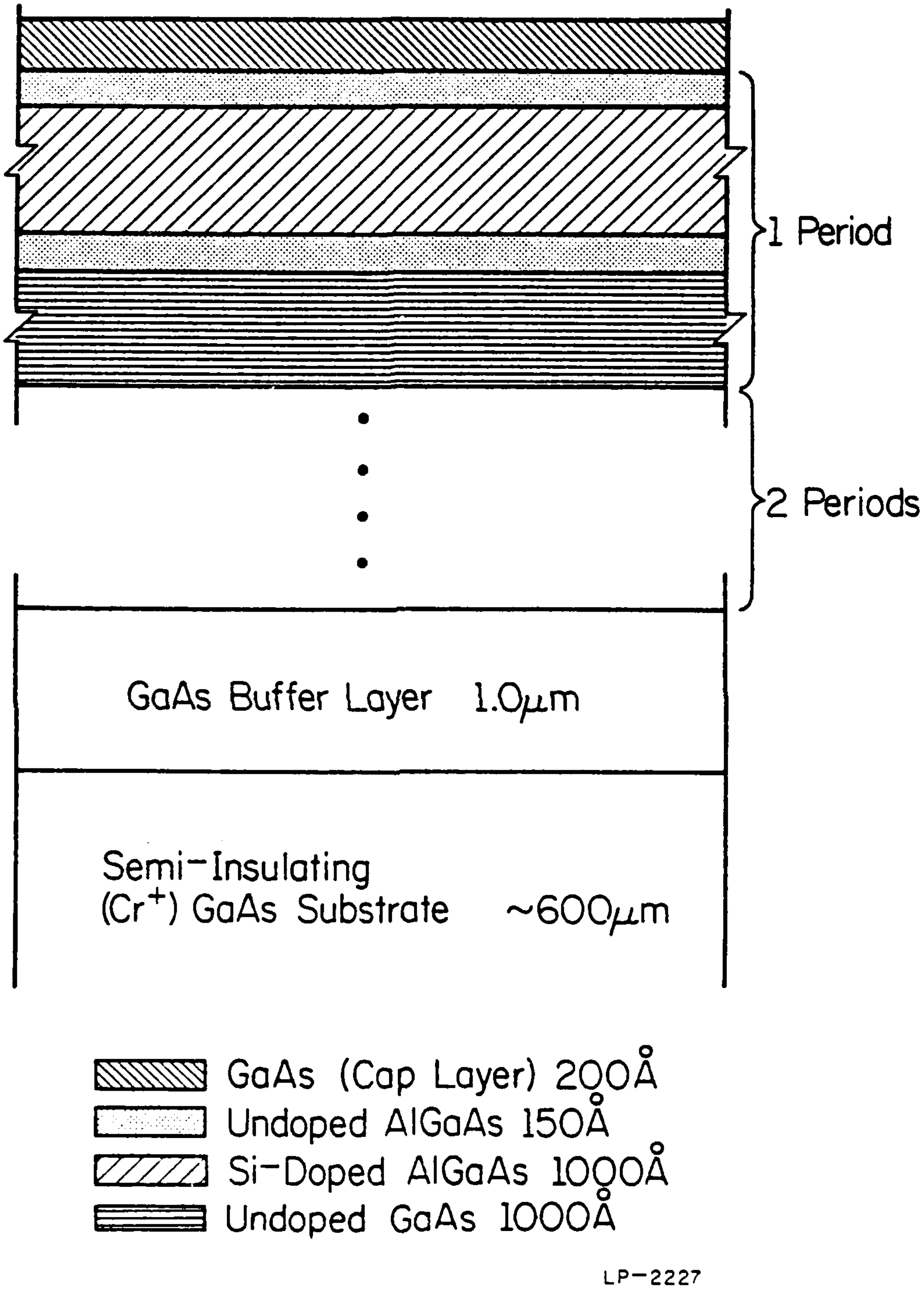

Fig. 4.7: Schematic diagram of the three-period modulation-doped heterostructure used to measure the influence of the intrinsic AlGaAs layer thickness. Measurements were made for intrinsic layer thicknesses of d_i = 50 Å, 100 Å, 150 Å, 200 Å, 250 Å, and 300 Å.

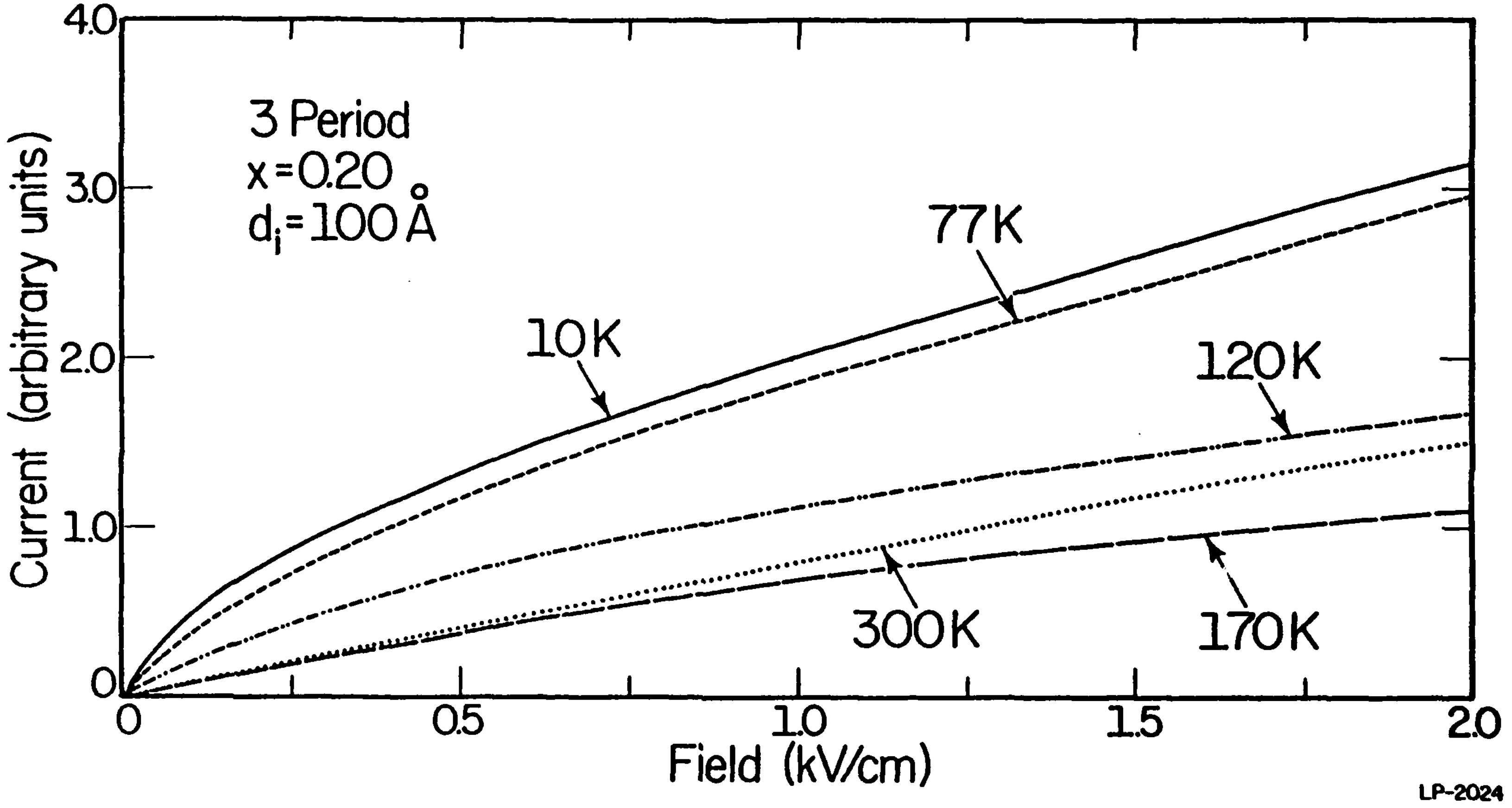

Fig. 4.8: Current-field characteristics at various temperatures for the three-period structure shown in Fig. 4.7 with d_i = 100 Å and x = 0.20.

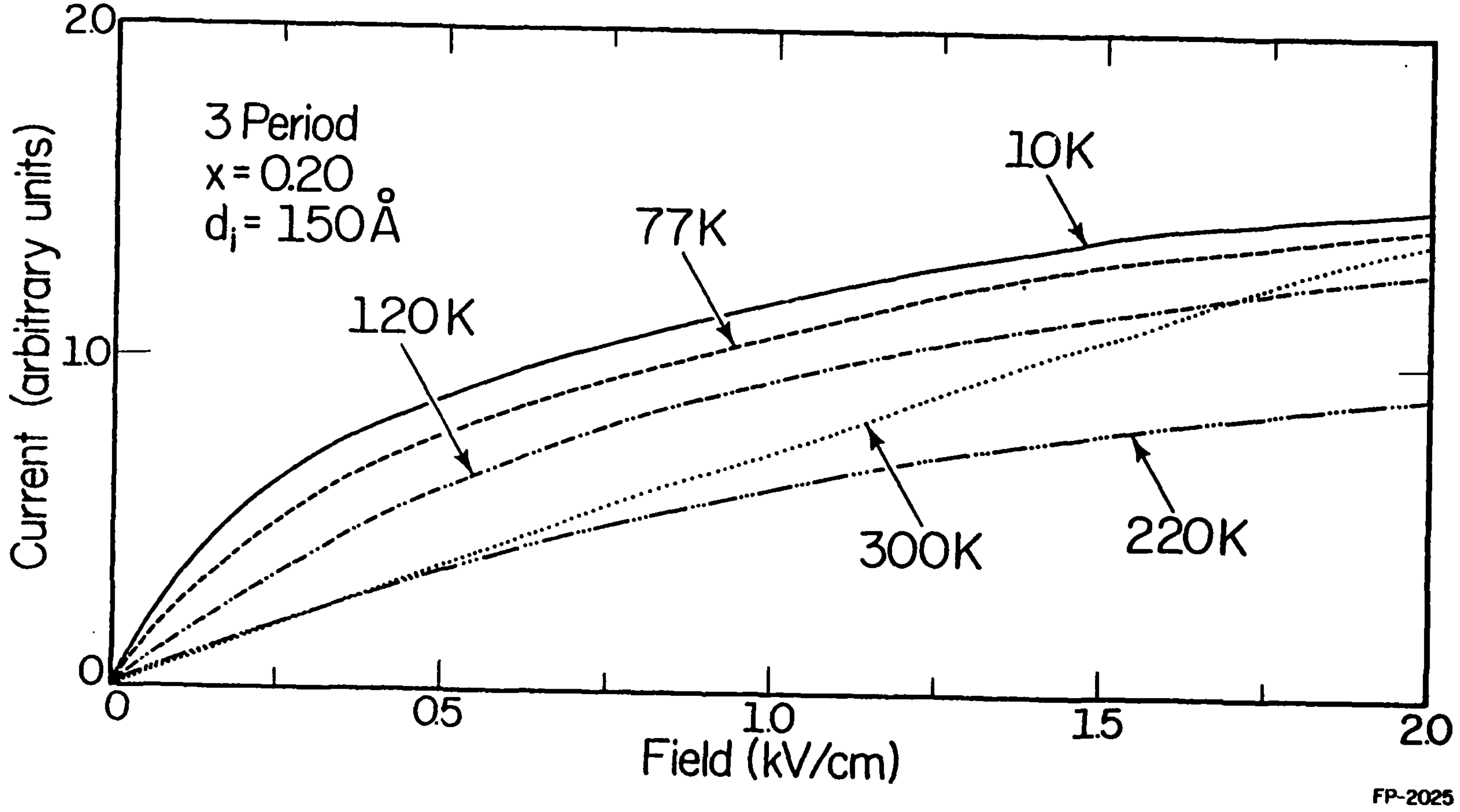

Fig. 4.9: Current-field characteristics at various temperatures for the structure shown in Fig. 4.7 with an intrinsic layer thickness of d_i = 150 Å.

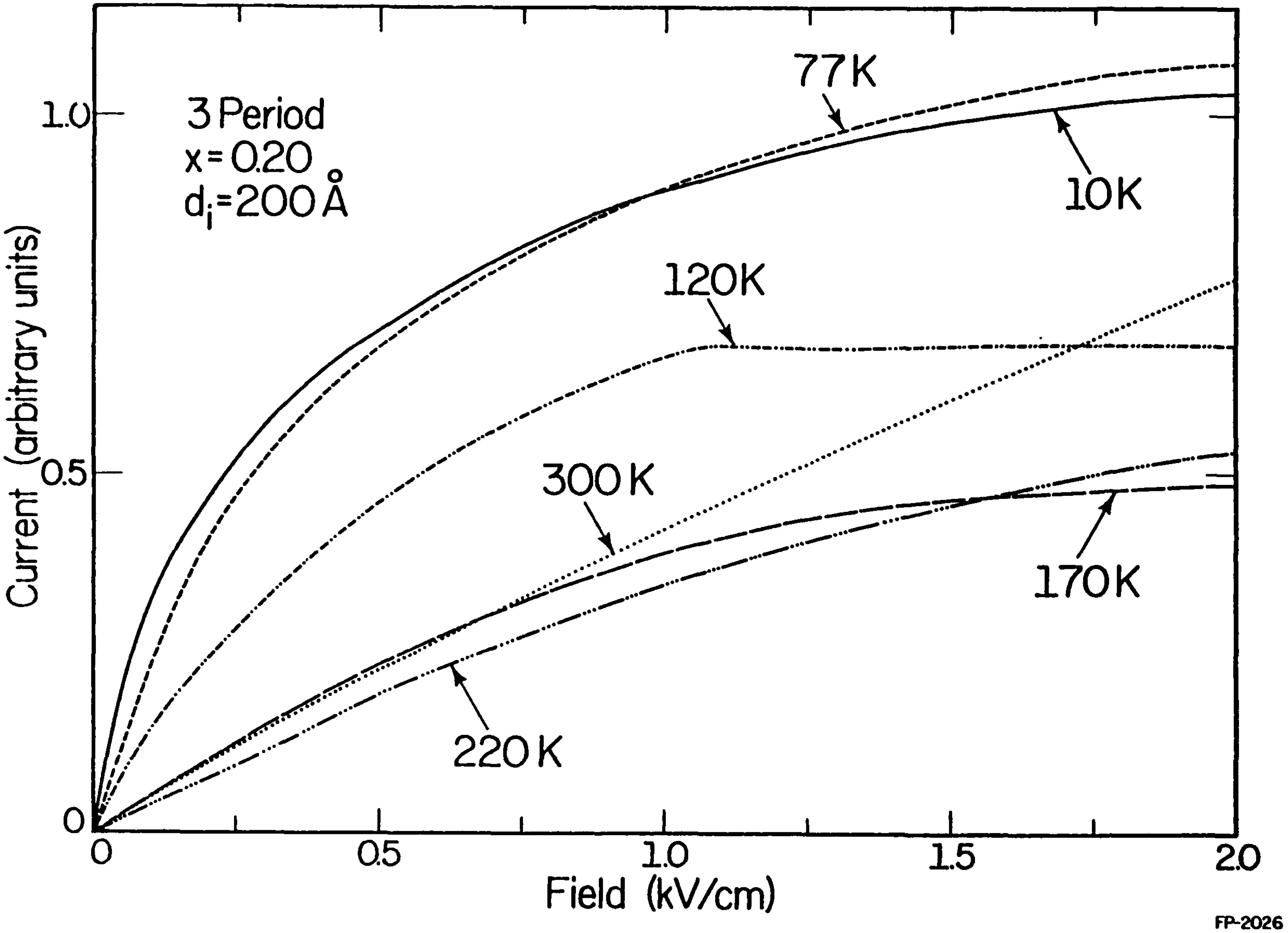

Fig. 4.10: Current-field characteristics at several temperatures for the sample structure shown in Fig. 4.7 with d_i = 200 Å.

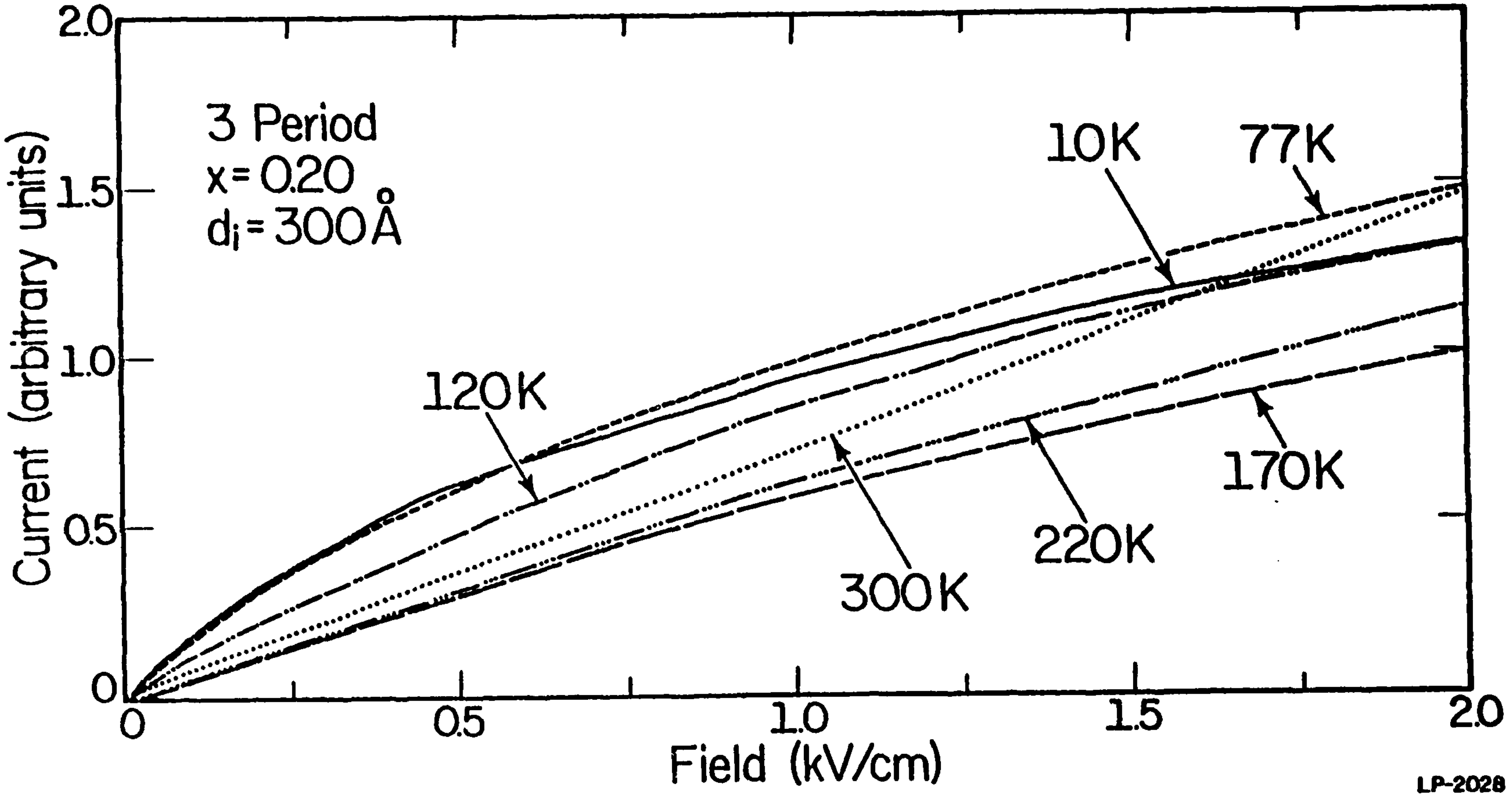

Fig. 4.11: Results of current-field measurements at various temperatures on the heterostructure depicted in Fig. 4.7 with an intrinsic layer thickness of d_i = 300 Å.

The theoretical proposal that the electron mobility increases approximately as the square of the separation distance between carriers and donors [66,67,78] can help account for the initial zero-field mobility increase with increasing intrinsic-layer thickness. However, the sheet carrier concentration, N_s, decreases (Table 4.2) with increasing layer thickness. This decrease in N_s results in reduced screening of the carriers in the GaAs which is responsible for the mobility decrease after a critical undoped-layer thickness is reached.

The three-period structures depicted in Figs. 4.8 - 4.11 exhibit an unusual property in that the conductivity decreases at first when the lattice temperature of the samples is cooled from 300 K. In Fig. 4.8, for instance, the conductivity at very low fields is nearly the same at 170 K and 300 K, but at higher electric fields the 170 K conductivity drops significantly below the corresponding conductivity at 300 K. This trend becomes even more prominent for larger intrinsic-layer thicknesses. In Fig. 4.11, the undoped layer thickness is 300 Å and the 170 K and 220 K lines are substantially lower in conductivity than the 300 K line even at very low fields. The conductivity reaches its lowest value at temperatures near 170 K before it begins to increase for lower temperatures.

It is believed that the initial decrease in conductivity is due to the freeze-out of carriers remaining in the doped AlGaAs which causes the conductivity in the AlGaAs to drop as the temperature is lowered. However, the conductivity of the electrons in the GaAs will be increasing with decreasing temperature due to the absence of significant ionized-impurity scattering. So it appears as though the conductivity drop in the doped AlGaAs dominates the current initially, but as the temperature is steadily

TABLE 4.2:

Hall mobility in cm^2/Vs and total sheet carrier concentration in cm^{-2} at 10 K, 77 K, and 300 K for three-period samples with varying undoped $Al_xGa_{1-x}As$ layer thicknesses.

Undoped Layer Thickness (Å)	Hall Mobility ($cm^2V^{-1}s^{-1}$)			Total Sheet Carrier Concentration (cm^{-2})		
	10K	77K	300K	10K	77K	300K
50 Å	95,700	60,700	5630	3.70×10^{12}	2.37×10^{12}	5.10×10^{12}
100 Å	139,000	73,700	4740	2.40×10^{12}	1.68×10^{12}	5.70×10^{12}
150 Å	164,000	76,300	6090	2.26×10^{12}	2.60×10^{12}	2.67×10^{12}
200 Å	127,000	71,320	5312	1.88×10^{12}	1.02×10^{12}	2.94×10^{12}
250 Å	106,000	59,600	3640	1.44×10^{12}	7.80×10^{11}	5.01×10^{12}

LP-2032

decreased, the conductivity increase in the GaAs becomes stronger and dominates for low temperatures. The transfer in dominance between the two mechanisms appears to occur near 170 K.

If the doped AlGaAs layer thickness is decreased, its influence on the overall conductivity of the sample should be reduced. This was verified for the case of the three-period sample shown in Fig. 4.12 which had a doped AlGaAs layer 250 Å thick, instead of 1,000 Å thick as for the previous samples shown in Figs. 4.8 - 4.11. The thickness of the undoped AlGaAs and GaAs layers were 150 Å and 1,000 Å, respectively (like the sample in Fig. 4.9). The 170 K curve in Fig. 4.12 is well above the 300 K curve throughout the field range up to 2.0 kV/cm. This sample displayed no noticeable decrease in conductivity as the temperature was lowered from 300 K.

4.1.3 Comparison of Single and Multiple Periods

In this section, the current-field characteristics of single-period, three-period, and nine-perio modulation-doped heterostructures are compared. These structures were grown by molecular beam epitaxy with substrate temperatures of 600°C and an AlAs mole fraction of $x \approx 0.30$. The structure of the single-period sample was the same as in the previous section (Fig. 4.2). The structure of the three-period was also the same as the last section (Fig. 4.7) except that the doped AlGaAs layers were 250 Å thick instead of 1000 Å thick. The undoped AlGaAs thicknesses of the three-period structure were 150 Å since these intrinsic layer widths produced the highest mobility three-period structures in the previous section. The nine-period structure, on the other hand, had intrinsic layer widths of d_i = 75 Å and undoped GaAs and doped AlGaAs layer widths of 500 Å

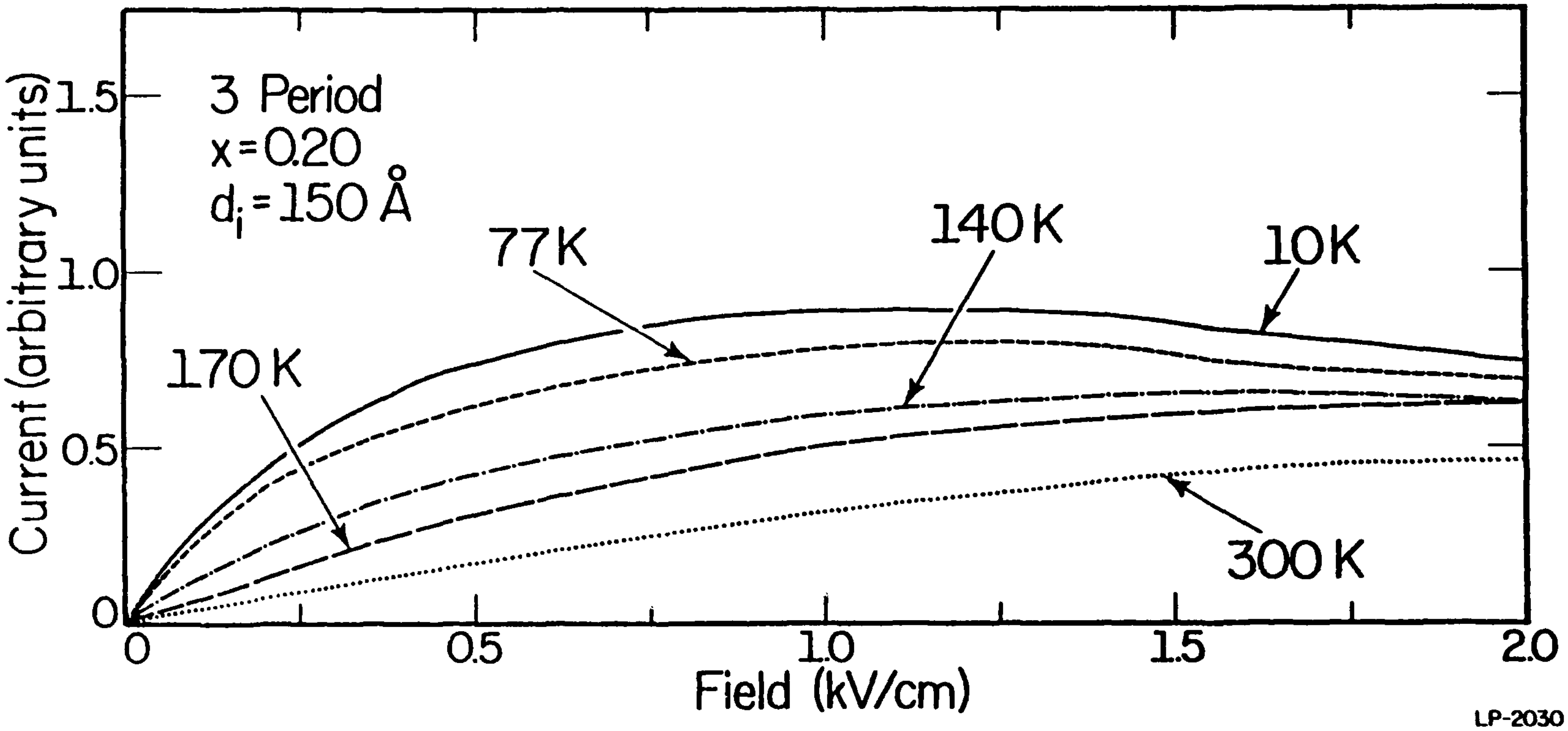

Fig. 4.12: Current-field characteristics at various temperatures for a sample structure like that measured in Fig. 4.9 but with a doped AlGaAs layer 250 Å thick, instead of 1000 Å thick.

and 1250 Å, respectively.

The current-field characteristics of the single-period sample are shown in Fig. 4.13 for temperatures from 10 K to 300 K. A large drop in conductivity (and hence mobility) is observed between zero and 500 V/cm as in the graphs shown before. At 300 K, however, the low-field mobility (μ = 7500 cm^2/Vs, for this sample) remains unchanged up to 2kV/cm. Similar low-field effects are observed for the three- and nine-period structures shown in Figs. 4.14 and 4.15, respectively. The current-field characteristics of the three-period sample, however, exhibit small negative differential resistances at 10 K and 77 K for electric fields near 1.5 kV/cm. The nine-period structure shows even more pronounced current fluctuations in a wider temperature range. There are several cases where the currents saturate and where different temperature curves intersect one another.

The occurrence of the negative differential resistances and current saturations in the multiple-period samples may be related to the poor quality of those interfaces where the GaAs is grown on top of the AlGaAs. The inferior properties of this type of interface were discussed in Section 2.4.3. Above a critical electric field strength, electrons may be transferring across the GaAs well from the high-mobility AlGaAs/GaAs interfaces to the low-mobility GaAs/AlGaAs interfaces. A significant number of electrons may then become captured in traps at the poor-quality interface, thereby reducing the effective number of high-mobility electrons participating in current conduction.

Since the quality of the GaAs on AlGaAs interface improves at higher growth temperatures (see Section 2.4.3), several three-period samples [illegible]

AD-A125 858 EXPERIMENTAL STUDIES OF LATERAL ELECTRON TRANSPORT IN 2/3
GALLIUM ARSENIDE-AL..(U) ILLINOIS UNIV AT URBANA
COORDINATED SCIENCE LAB M R KEEVER DEC 82 R-975
UNCLASSIFIED N00014-76-C-0806 F/G 20/12 NL

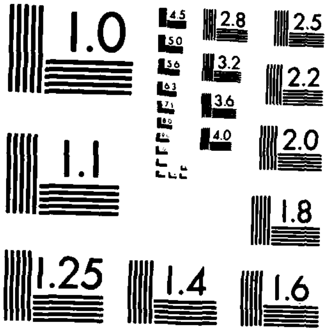

MICROCOPY RESOLUTION TEST CHART
NATIONAL BUREAU OF STANDARDS-1963-A

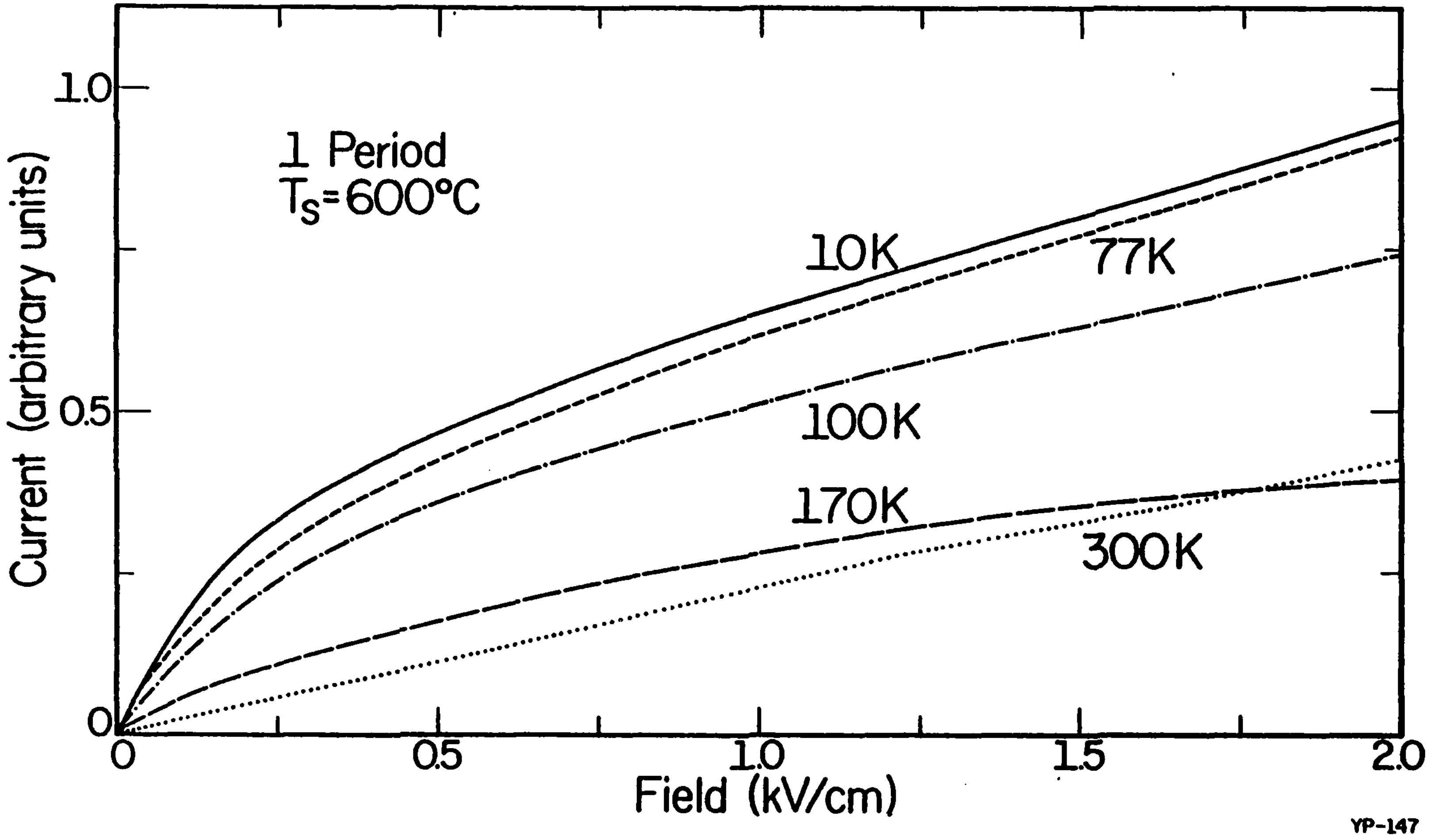

Fig. 4.13: Current-field characteristics at several temperatures for the sample structure shown in Fig. 4.2 with an AlAs mole fraction of x = 0.30.

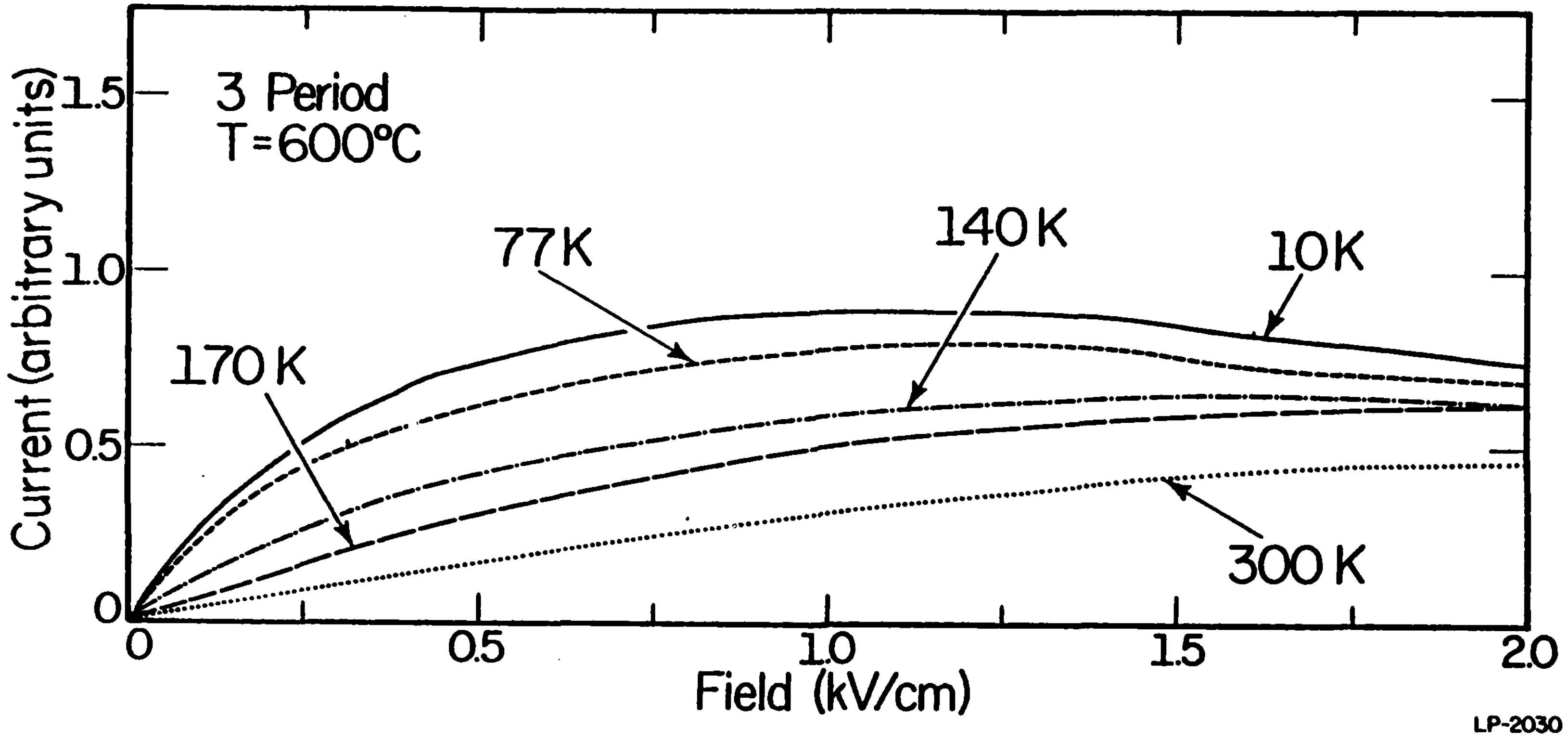

Fig. 4.14: Results of current-field measurements at several temperatures for a three-period heterostructure matching that shown in Fig. 4.7 except that the doped AlGaAs layers were 250 Å thick instead of 1000 Å thick. The AlAs mole fraction was $x \approx 0.30$ and $d_i = 150$ Å.

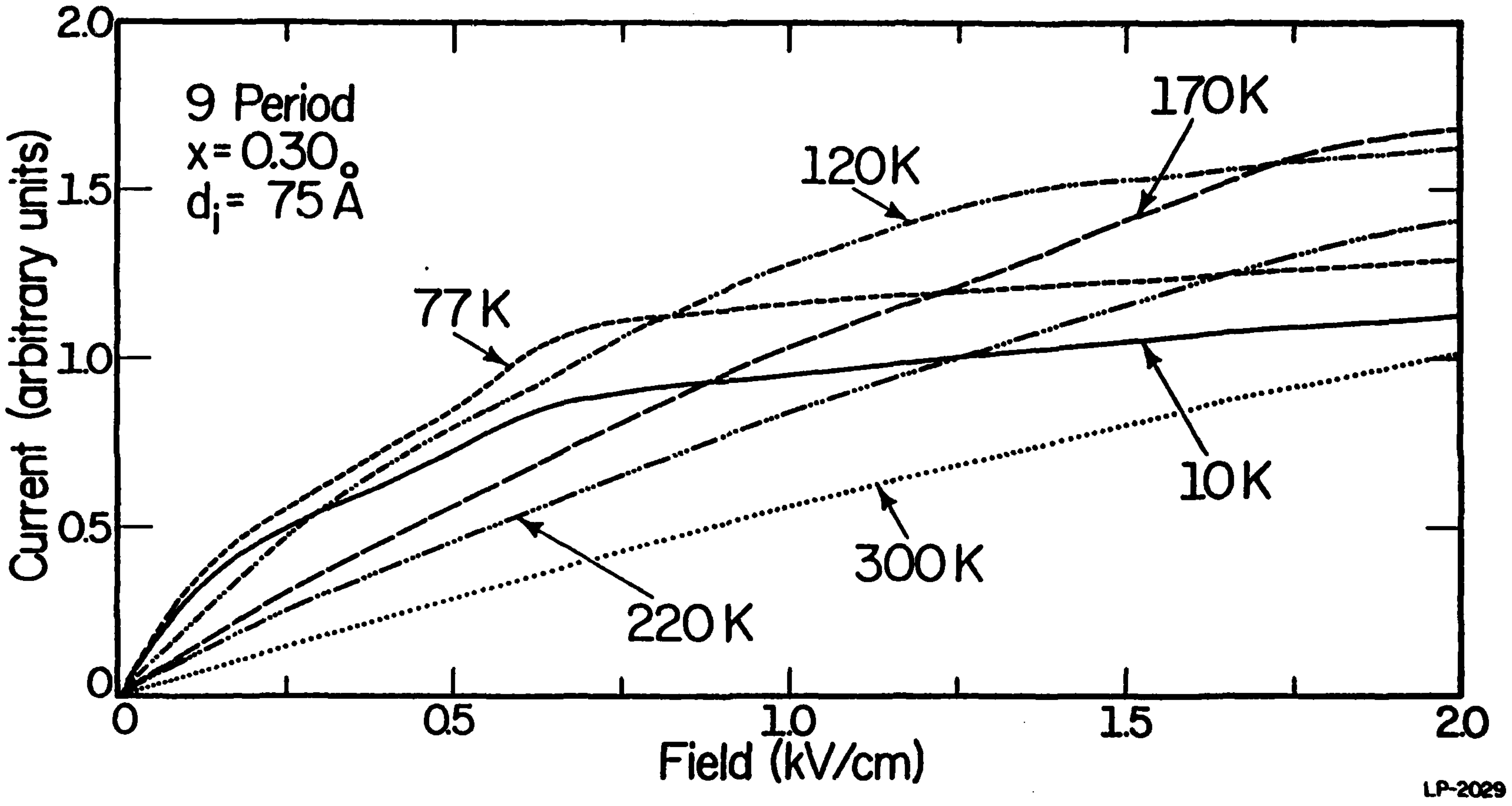

Fig. 4.15: Current-field characteristics for a nine-period heterostructure with x ≈ 0.30 and d_i = 75 Å. The undoped GaAs and doped AlGaAs layer thicknesses were 500 Å and 1250 Å, respectively.

grown at 680°C. Fig. 4.16 shows the current-field characteristics of a three-period structure grown at 680°C. The curves are well behaved at all temperatures and do not show any negative differential resistance; but in all cases the slope slowly decreases over the whole range of the electric fields investigated, as opposed to the slope of the single-period structure (Fig. 4.13) which remains essentially constant above 1 kV/cm. This illustrates that although the quality of the GaAs on AlGaAs interface has been improved, the mobility is still much lower than that of the AlGaAs on GaAs interface.

So it appears that even though higher growth temperatures have minimized the negative differential resistance effects associated with multiple-period structures, the single-period structures still appear to be superior for devices, both in terms of ease of preparation and in terms of moderate-field transport properties.

4.2 Low-Field Characteristics of Mobility

In the previous sections it was shown that strong nonlinearities in the current-field characteristics of high-mobility GaAs-$Al_xGa_{1-x}As$ heterostructures are present at low fields, especially at low temperatures. The unusually high mobilities measured by van der Pauw-Hall techniques (at electric field strengths near 5 V/cm and magnetic field strengths around 750 Gauss) are sustained only up to fields around 200 V/cm, above which the mobility drops very rapidly. As seen above, the features of the mobility drop are strongly dependent on the Al concentration x and the doping of the AlGaAs layers.

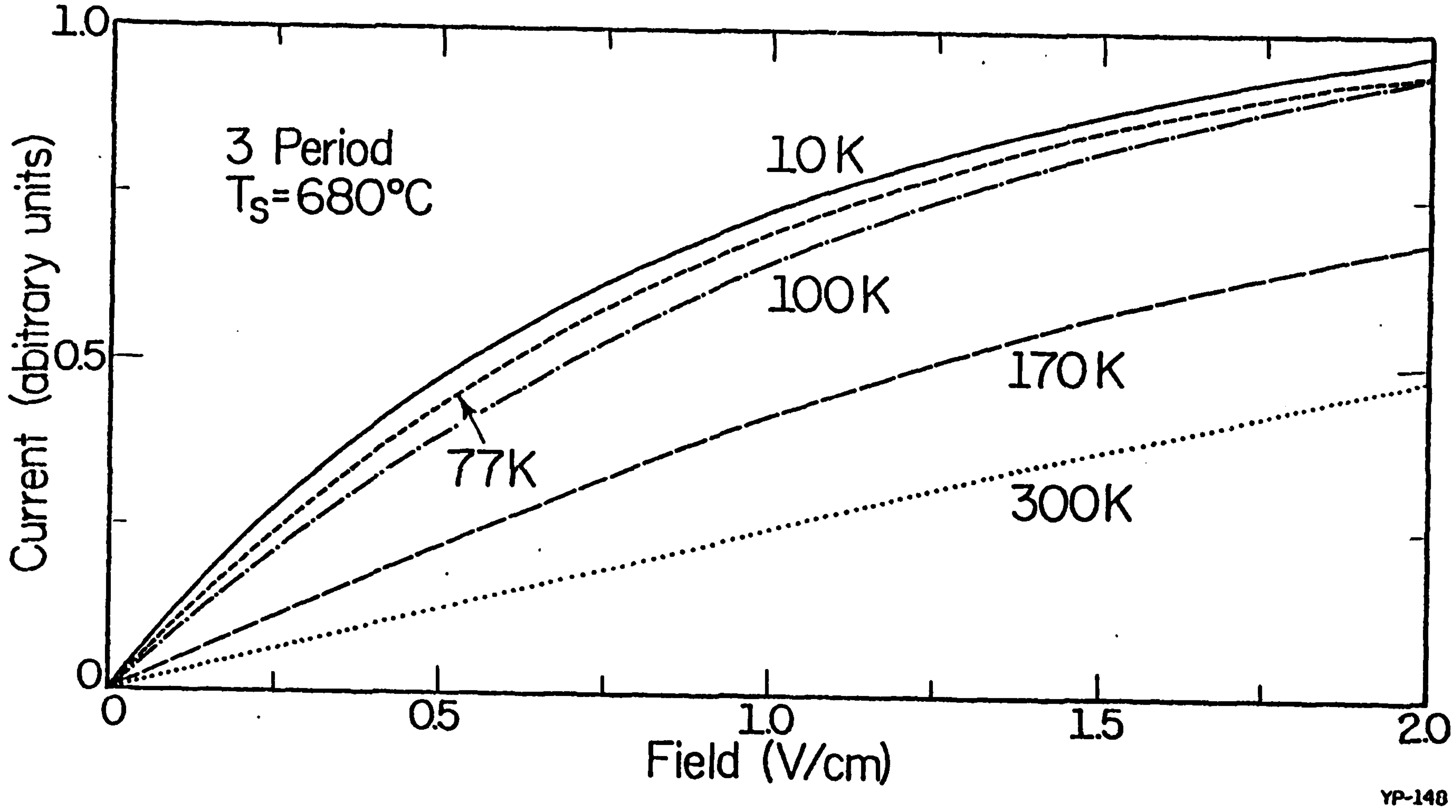

Fig. 4.16: Current-field characteristics at various temperatures for a three-period heterostructure grown with a substrate temperature of T_s = 680°C.

The sudden drop in mobility is thought to be due to a rapid increase in the average energy of the electrons to a point where polar optical phonon scattering becomes substantial. Higher initial mobilities would then lead to larger mobility drops at lower electric fields as was observed experimentally. The nature of mobility reduction certainly depends also on the subband population since the mobility is much reduced in higher subbands (as discussed in Section 2.4.2.3). The population of higher subbands together with the sudden onset of polar optical phonon scattering can reduce the mobility rapidly enough to cause negative differential resistances at very low electric fields as was seen in some of current-field curves of Section 4.1.

The first of the following subsections outlines the results of a theoretical calculation done by Hess to model the low-field dependence of the mobility. The subsequent subsections summarize the methods and results of experiments performed by the author to measure, more precisely, the electric field dependence of the mobility.

4.2.1 Theoretical Modeling of Mobility-Field Characteristics

Hess has calculated the mobility-field characteristics of modulation-doped GaAs-AlGaAs heterostructures using a two-dimensional model for the mobility [65-66]. Parts of this model were outlined earlier in Section 2.4.2.1. Since modulation-doped heterostructures combine the unique feature of high mobilities associated with large electron concentrations, the warm electron effects in these structures were treated with a model including strong electron-electron interactions. The simplest way of including electron-electron scattering is to assume a Fermi-distribution at an elevated electron temperature T_c for the spherically symmetric part of the distribution function. To calculate the carrier temperature, T_c, the power balance equation derived elsewhere [109] was used. This particular model involves scattering by acoustical phonons via deformation potential, polar optical phonons, remote donors, interface charges and background impurities. It does not, however, include subband repopulation and intersubband scattering.

Fig. 4.17 shows the experimental mobility-field curves for a very high mobility (200,000 cm^2/Vs at 10 K) three-period modulation-doped heterostructure in the field range 0 - 200 V/cm. A dashed curve representing the results of the theoretical calculation at 10 K is included in the figure for comparison.

In comparing experimental and theoretical results, two aspects are apparent. At very low fields the theory predicts a deviations from Ohm's law, which is steeper than the experimentally observed deviation. This discrepancy can be accounted for only by assigning a relatively large energy loss rate to interactions with phonons. In the model a deformation potential of 10 eV, which is rather large, was assumed. Therefore, an explanation seems to be possible only by additional phonon scattering processes, such as piezoelectric scattering and multiphonon emission.

At higher electric fields, the rate of decline in the electron mobility decreases, which may be an indication of a lower energy loss rate than what was used in this model. This type of difference between theory and experiment is typical for deviations of the distribution functions from the Fermi-shape, which was assumed [110].

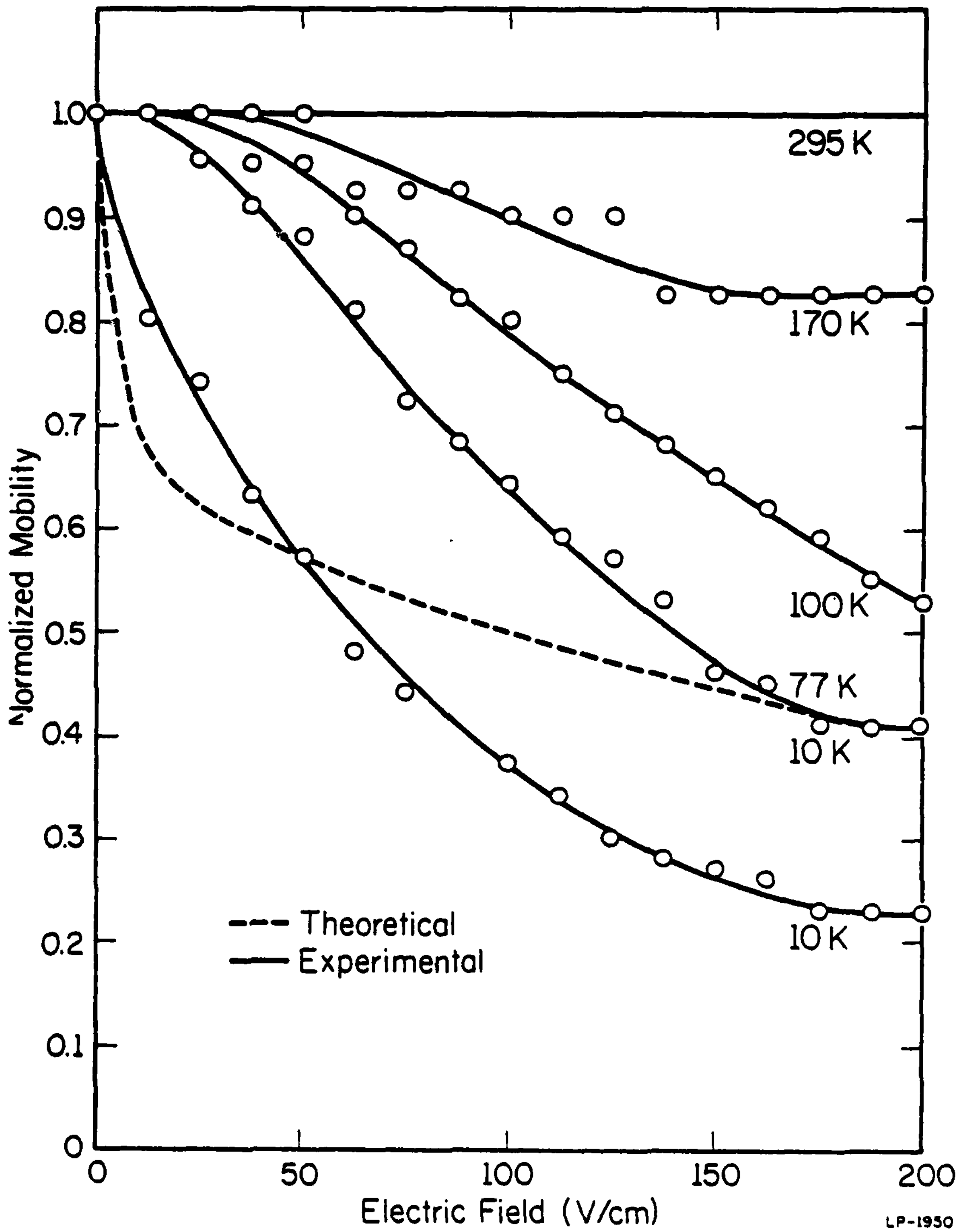

Fig. 4.17: Normalized mobility vs field curves for a high-mobility three-period heterostructure at several temperatures. The dashed curve represents the result from a theoretical calculation for T = 10 K.

4.2.2 Measuring Mobility from Corbino Resistance

Following the experimental discovery of a large conductivity drop at very low electric fields with current-field measurements, it seemed important to independently measure the mobility versus electric field characteristics in a more precise manner. In this section, a method will be described for determining how the mobility depends on electric field by measuring the "Corbino resistance" of special device shapes in a transverse magnetic field. The Corbino resistance is the "geometric" contribution to the magnetoresistance which can be quite large in certain device configurations.

In order to understand how the geometric contribution to magnetoresistance comes about, refer to Fig. 4.18. When a voltage is applied between the two closely-spaced ohmic contacts sketched in the figure, an electric field will be oriented as shown, from one contact to the other. However, when a magnetic field is applied, the trajectories of the electrons in the semiconductor are changed by the deflecting Lorentz force. The current lines and the direction of the electric field then form an angle different from zero. This angle is called the Hall angle θ_H if the magnetic field direction (into the page in Fig. 4.18) is perpendicular to the direction of the electric current. The relation between θ_H and the Hall mobility μ_H of the electrons is given by

$$\tan \theta_H = \mu_H B , \qquad (4.3)$$

where μ_H is defined as the ratio of the Hall coefficient R_H and the specific resistance ρ_B in a field with magnetic induction B:

$$\mu_H = R_H/\rho_B . \qquad (4.4)$$

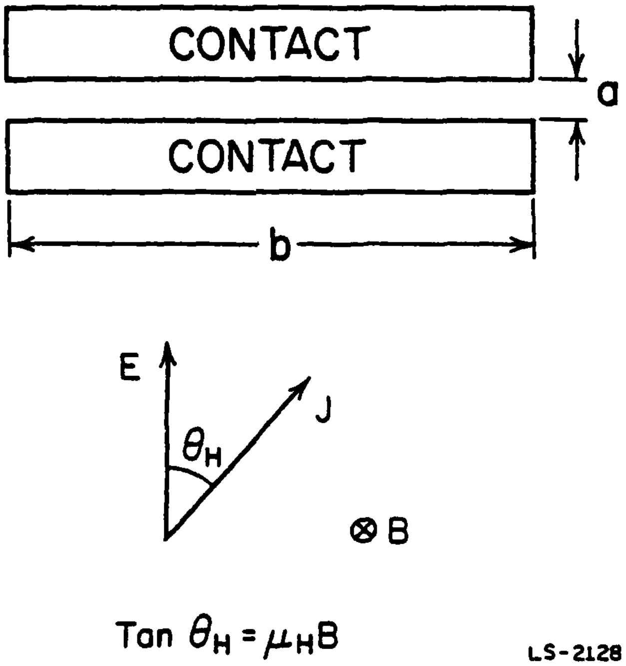

Fig. 4.18: Diagram illustrating the deflection of the current from the electric field direction by the Hall angle θ_H when a magnetic field of strength B is directed into the page.

As seen in Fig. 4.18, the path length of the current between contacts will be longer when there is an applied magnetic field. Hence, there is also an increase in the effective resistance between the contacts under these conditions. This increase in resistance is the "geometric contribution" to the magnetoresistance. For materials with a high electron mobility, this effect is very large and depends only on the Hall angle θ_H, and not on other material parameters of the semiconductor.

The geometrical shape of the sample is known to have an influence on the magnitude of the measured magnetoresistance. This shape influence is highly pronounced for large Hall angles, i.e., for materials with high electron mobilities. It has been reported that the magnetoresistance increases with a decreasing ratio of electrode separation to electrode width (a/b in Fig. 4.18) and approaches a limiting value. Calculations of the influence of the shape of the electrodes on the measured magnetoresistance have been made by Lippmann and Kuhrt (and were reported by Weiss [111]). Using a method of conformal mapping they found an integral which could be developed for small and large Hall angles. The transition region between small and large angles was calculated by numerical evaluation of the integrals. The results of these calculations, shown in Fig. 4.19, have corresponded quantitatively with the expermental results of other laboratories. The figure shows the ratio of resistances obtained with (R_B) and without (R_o) a magnetic field versus the product $\mu_H B = \tan \theta_H$ for various ratios of electrode separation to electrode width (a/b). It is seen that as a/b approaches small values the R_B/R_o ratio converges. According to these curves all electrode patterns such that a/b $\lesssim$ 0.05 would nearly give a maximum geometric contribution to magnetoresistance. The limiting value of

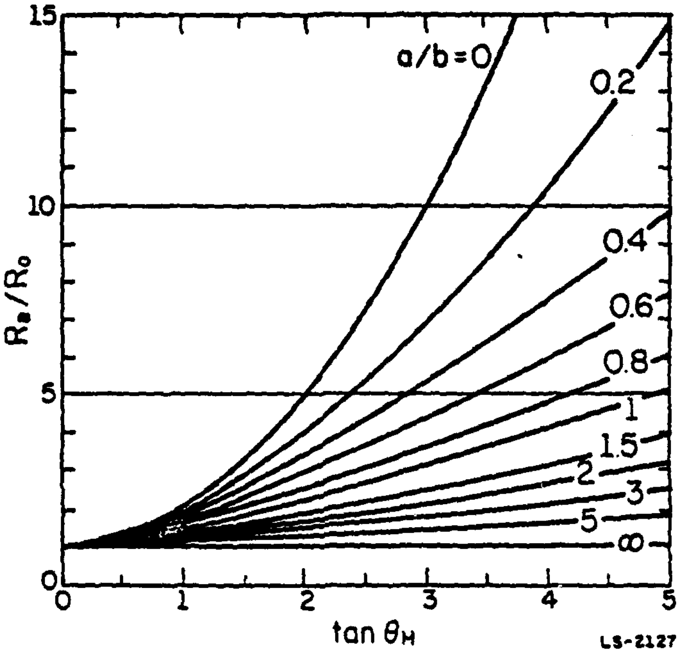

Fig. 4.19: Results of calculations by Lippmann and Kuhrt (after [111]) showing the influence of the electrode separation to width ration (a/b in Fig. 4.18) on the Corbino magnetoresistance.

R_B/R_o can be ideally obtained with a disk-shaped device (Corbino disk) with concentric inner and outer electrodes.

For an isotropic medium with an electrode configuration which allows a maximum geometric contribution to magnetoresistance the relative change in resistance upon applying a transverse magnetic field can be expressed by [112]

$$\frac{R_B-R_o}{R_o} \equiv \frac{\Delta R}{R_o} = \frac{\Delta\rho}{\rho_o} + \frac{\mu_H{}^2B^2}{1+\Delta\rho/\rho_o} . \tag{4.5}$$

Here $\Delta\rho/\rho_o$ is the relative change in specific resistivity as would be measured with a long filamentary sample of the same material. The second term on the right of Eq. (4.5) is the geometric contribution to $\Delta R/R_o$. For a high-mobility semiconductor $\Delta\rho/\rho_o$ is much smaller than $\mu_H{}^2B^2$ so Eq. (4.5) may be approximated by

$$\frac{\Delta R}{R_o} \approx \mu_H{}^2B^2 . \tag{4.6}$$

Measuring the relative change in resistance $\Delta R/R_o$ for a known magnetic field strength B at a particular electric field would thus allow one to evaluate the Hall mobility μ_H at that electric field from

$$\mu_H \approx \frac{1}{B}(\Delta R/R_o)^{1/2} . \tag{4.7}$$

It must be pointed out, however, that Eq. (4.7) approximates the mobility of an isotropic material where the mobility is assumed to be the same everywhere. In the case of a sample where conduction may take place through layers with different properties, the above equations must be modified. The modifications necessary to represent conduction through two layers (e.g., GaAs and AlGaAs) are outlined in the following section.

4.2.3 Mobility Determination with Two-Layer Conduction

In a one-period GaAs-AlGaAs structure, parallel conduction through both the AlGaAs and GaAs layers may occur. Let the Hall mobility, electron concentration, and conductive-layer cross sectional area of the AlGaAs(GaAs) layer be represented by μ_1, n_1, and A_1(μ_2, n_2, and A_2), respectively. Then the total current I flowing through the parallel layers due to an electric field E may be written as

$$I = I_1 + I_2 = (n_1\mu_1A_1 + n_2\mu_2A_2)\ eE\ . \tag{4.8}$$

Assuming the total number of electrons in the two layers remains constant one can write

$$n(A_1 + A_2) \equiv n_1A_1 + n_2A_2 \tag{4.9}$$

where n is the overall average charge concentration.

When there is no magnetic field the total resistance R_o of the two parallel layers is found from

$$\frac{1}{R_o} = \frac{1}{R_1} + \frac{1}{R_2}\ . \tag{4.10}$$

Similarly, when a magnetic field is applied perpendicular to the layers the total resistance R_B of the layers is found from

$$\frac{1}{R_B} = \frac{1}{R_1+\Delta R_1} + \frac{1}{R_2+\Delta R_2} \tag{4.11}$$

where ΔR_1 and ΔR_2 are the increase in the resistance of the AlGaAs and GaAs layers, respectively, due to the magnetic field. Using Eq. (4.6), the relative change in the resistance of each layer due to a perpendicular magnetic field B can be approximated by

$$\frac{\Delta R_1}{R_1} \approx \mu_1{}^2B^2 \quad \text{and} \quad \frac{\Delta R_2}{R_2} \approx \mu_2{}^2B^2 \ . \tag{4.12}$$

Eq. (4.10) and Eq. (4.11) may be used to express the relative change in resistance of both the layers as

$$\frac{R_B-R_o}{R_o} = \frac{\Delta R}{R_o} = R_B\left(\frac{1}{R_1}+\frac{1}{R_2}-\frac{1}{R_1+\Delta R_1}-\frac{1}{R_2+\Delta R_2}\right) \tag{4.13}$$

Using Eqs. (4.8), (4.9), and (4.13), one can obtain a third-order polynomial in μ_2 (see Appendix 1):

$$\left[\frac{A_2(1+\mu_1{}^2B^2)}{\mu_1A_1}+\frac{\Delta R}{R}\frac{K_2}{K_1}-\frac{K_2\mu_1{}^2B^2}{K_1}\right]\mu_2{}^3+\left[\frac{A_2I\mu_1{}^2B^2}{K_1}-\frac{\Delta R}{R}\frac{A_2I}{K_1}\right]\mu_2{}^2$$
$$+\left[\frac{\Delta R}{RB^2}\left\{\frac{K_2}{K_1}-\frac{A_2}{\mu_1A_1}(1+\mu_1{}^2B^2)\right\}-\frac{K_2\mu_1{}^2}{K_1}\right]\mu_2$$
$$+\left[\frac{A_2I\mu_1{}^2}{K_1}-\frac{\Delta R}{R}\frac{A_2I}{B^2K_1}\right] = 0 \tag{4.14}$$

where

$$K_1 = \mu_1A_1n(A_1+A_2)\,eE - A_1I \tag{4.15}$$

and

$$K_2 = A_2n(A_1+A_2)\,eE \ . \tag{4.16}$$

The mobility μ_2 in the GaAs may be calculated from the above third-order polynomial equation if the coefficients of the equation are evaluated. Measurements of current vs. electric field with and without a perpendicular magnetic field provide the values for I, E, $\Delta R/R_o$, and B. The average carrier concentration n is approximated from Hall measurements. The mobility μ_1 in the AlGaAs stays relatively constant with respect to temperature and is estimated to be in the range 1000 - 1500 cm^2/Vs. The value of A_1 is determined from the known AlGaAs layer width and the device dimensions. In order to calculate the conductive cross-sectional area A_2 in the GaAs, it is necessary to know the effective width of the high-mobility channel near the interface. This width has been calculated by Hsieh [113] based on the model of a triangular potential well at the interface. This data was used in combination with the device dimensions to calculate A_2.

The magnitude of μ_2 calculated from Eq. (4.14) will depend on the estimated values of μ_1 and n. It was found that a change in these parameters would shift the resulting mobility versus electric field curves up and down, but the shape of the curves would be preserved. Therefore, the mobility will be plotted in arbitrary units for the graphs presented in the following section. It is believed, however, that these mobility-field curves will illustrate in reasonably good detail the qualitative features of the GaAs mobility dependence on the electric field strength.

4.2.4 Experimental Determination of Low-Field Mobility Characteristics

Measurements have been made of the current-field characteristics at low temperatures in single-period GaAs-$Al_xGa_{1-x}As$ heterostructures like that shown in Fig. 4.20. Samples with AlAs mole fractions of $x = 0.16$ and 0.32 were tested using the pulsed-voltage techniques described previously. Two ohmic contacts of AuGe/Ni were diffused through the conducting epitaxial layers of the device. The width of the two contacts was 500 µm and their separation was either 10 µm or 20 µm. Thus, the ratio of electrode width to electrode separation was $a/b = 0.02$ or 0.04. This means that the geometric contribution of the magnetoresistance will be nearly maximized for all but the largest Hall angles. Note that when attempting to determine the

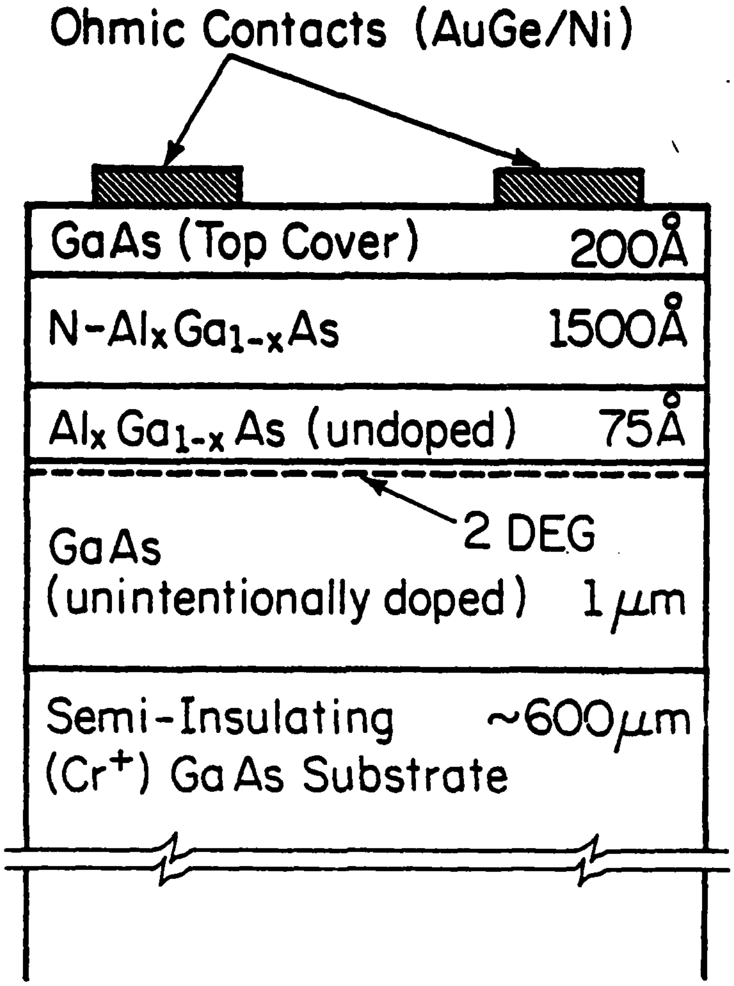

LP-2193

Fig. 4.20: Schematic diagram of the one-period heterostructure used for current-field measurements which led to a determination of the GaAs mobility. Measurements are reported for this structure with $x = 0.16$ and 0.32.

mobility characteristics in the electric field range (approximately 0 - 400 V/cm) where the low-temperature mobility becomes very high ($\mu_H \gtrsim 100{,}000$ cm^2/Vs), it is important that the magnetic field is not so high as to cause the Hall angle to exceed ~ 80° ($\mu_H B \sim 6$). However, when studying the mobility at higher electric fields where the mobility has decreased significantly, the use of higher magnetic fields (10 - 20 kG) will facilitate the measurements by increasing the resistance change. If the magnetic field is too large, however, Shubnikov-deHaas oscillations may occur. No such oscillations were observed for the range of magnetic fields used in making the measurements reported here.

Fig. 4.21 displays the results of current-field measurements made at 8 K on a sample with $x = 0.32$. The separation of the electrodes was 10 μm as depicted in the inset. The measurements were performed first with no magnetic field and then with a perpendicular magnetic field of 6 kG from an electromagnet. The relative change in resistance $\Delta R/R$ at a particular electric field strength was determined from the two values of current measured at the same electric field. Note in Fig. 4.21 that the slope of the I-E curve for $B = 0$ increases initially at very low fields. This feature signals an initial increase in mobility with increasing electric field which has not been experimentally reported previously.

A plot of the Hall mobility in the GaAs versus electric field strength is plotted in Fig. 4.22. Each data pont was calculated from Eq. (4.14) using $A_1 = 7.5 \times 10^{-7}$ cm^2, $A_2 = 3.6 \times 10^{-8}$ cm^2, $\mu_1 = 1500$ cm^2/Vs, and $n = 4.6 \times 10^{16}$ cm^{-3} along with values for I, E, and $\Delta R/R$ obtained from the current-field curves in Fig. 4.21. The data points are connected by a smooth line to facilitate viewing of the graph.

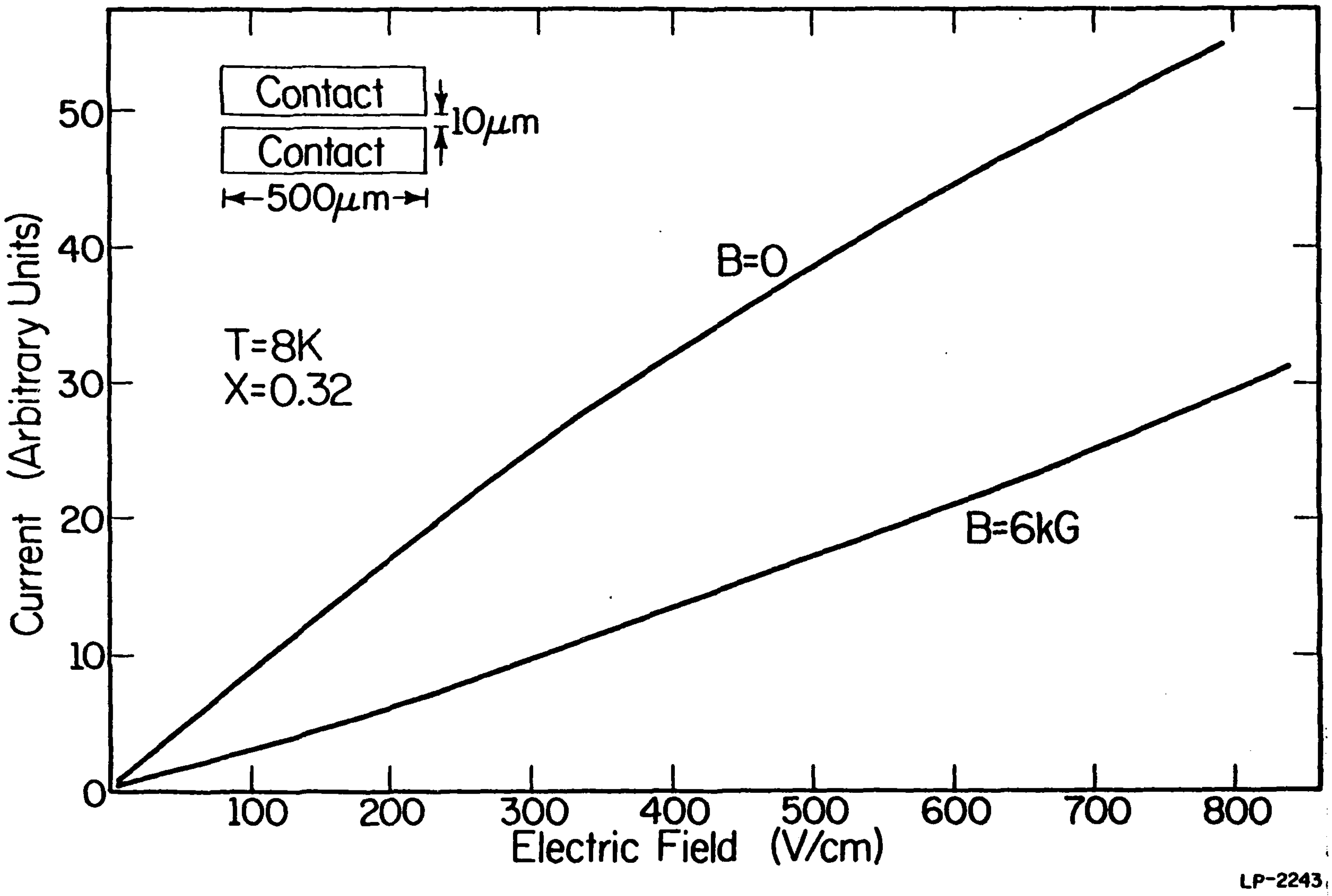

Fig. 4.21: Current-field characteristics at T = 8 K for the single-period heterostructure shown in Fig. 4.20 with x = 0.32. Measurements were made with and without a 6 kG perpendicular magnetic field.

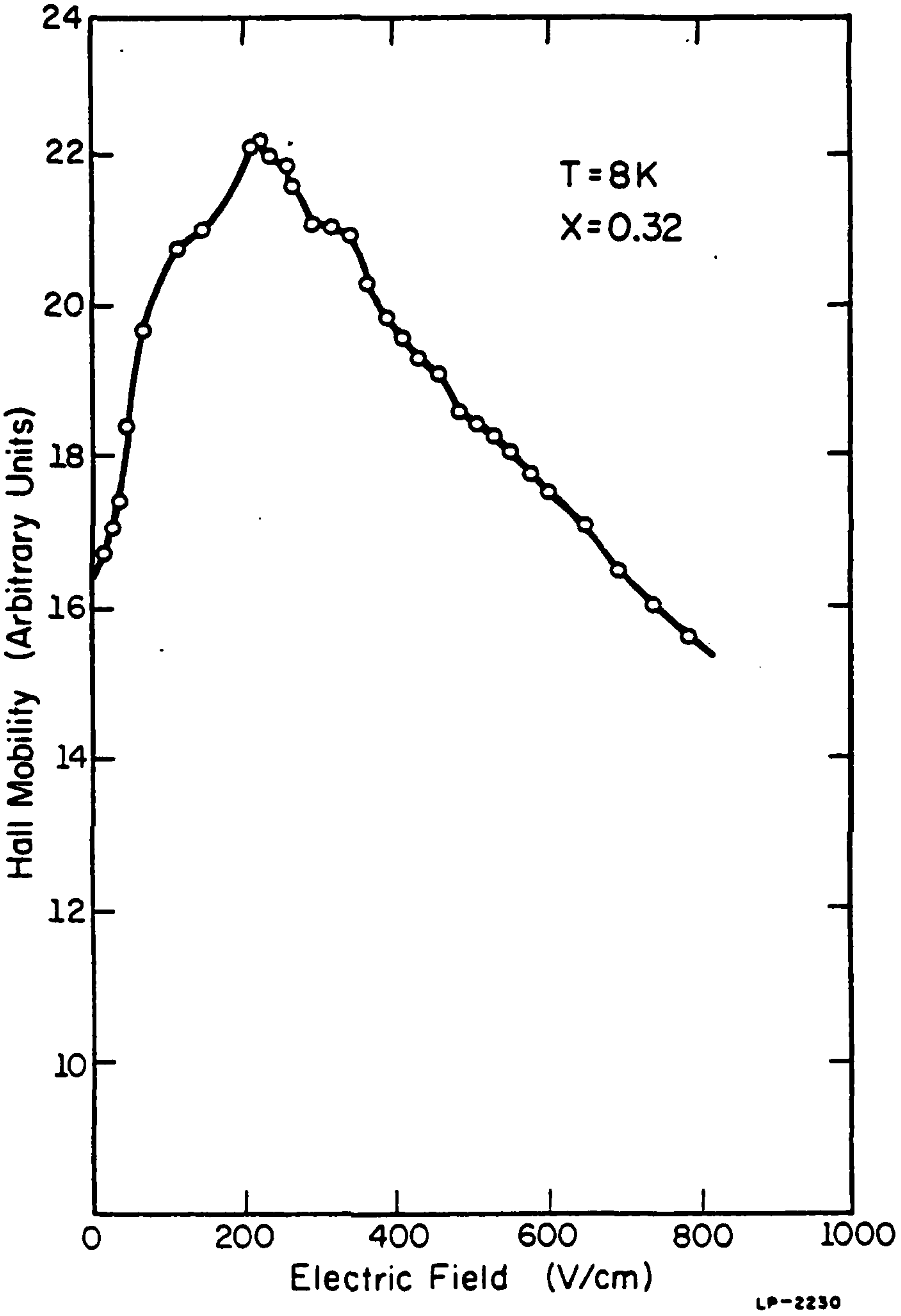

Fig. 4.22: Hall mobility vs electric field strength at T = 8 K using the data obtained from the current-field characteristics presented in Fig. 4.21. The mobility in the GaAs was calculated using Eq. (4.14) in the text.

The graph shows an initial increase in mobility as expected. Such an initial mobility increase with electric field has recently been predicted theoretically by Price [114]. He reported that the mobility might be expected to initially increase with electron temperature due to the temperature dependence of the screening constant for thermal electrons. The mobility increase is predicted to occur only until the electron temperature reaches a critical value, beyond which the mobility will start to decrease.

The GaAs mobility in the graph peaks near E = 200 V/cm and then decreases steadily for higher fields. The sharp mobility decrease is thought to be caused by the onset of polar optical phonon scattering which may become significant at these low electric fields due to the unusually high electron mobilities achieved in these modulation-doped heterostructures. Intersubband scattering may also contribute to the mobility decrease in this electric field range. Experimental evidence of mobility reduction due to intersubband scattering has already been reported in the literature [60,75,81] as was discussed in Section 2.4.2.3. It has been shown [81] that an electrode attached to the backside of a heterostructure sample can be used to vary the lateral electric field necessary to trigger a decrease in mobility due to intersubband scattering.

Fig. 4.23 shows the results of an identical calculation using data from I-E curves measured from another sample with the same structure as for the previous case. In this instance the current-field measurements were extended to electric fields that were twice as high. The low-field results appear nearly the same and the extended electric field range shows a continued steady decline in mobility.

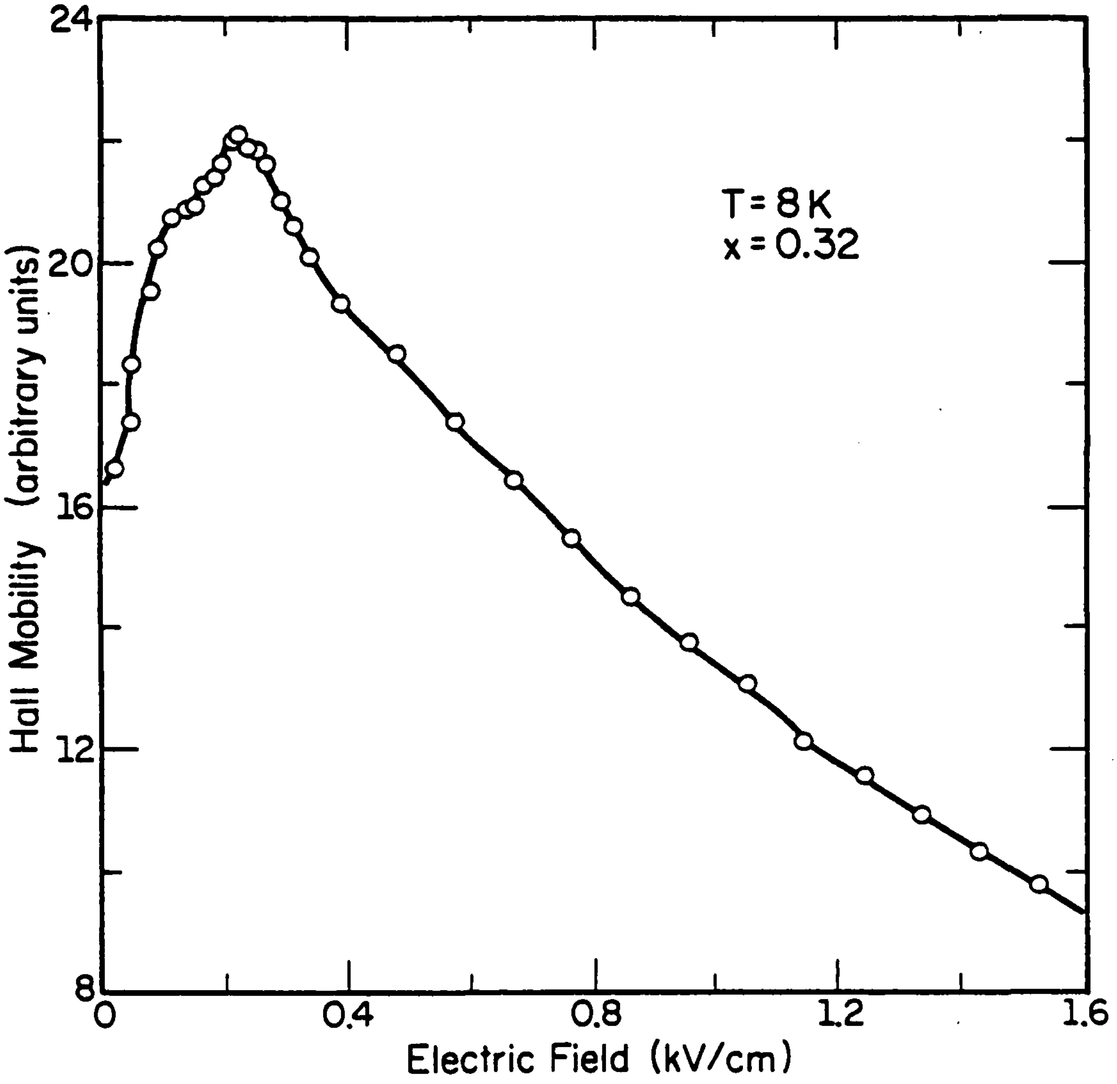

LP-2210

Fig. 4.23: Hall mobility in the GaAs versus electric field strength for another sample with the same structure as used in Fig. 4.22.

The results of current-field measurements made on a sample with the same structure, but with $x = 0.16$ instead of $x = 0.32$, is shown in Fig. 4.24. In this case the sample was immersed in liquid helium and higher magnetic fields were applied with a superconducting magnet. The contact separation in the conducting layers was again 10 μm. This sample had an electrode attached to the back substrate so that backside-gate voltages could be applied to shift the electron distribution nearer or farther from the heterojunction. The calculation of GaAs mobility versus electric field was performed using $A_1 = 7.5 \times 10^{-7}$ cm^2, $A_2 = 4.32 \times 10^{-8}$ cm^2, $n = 3.3 \times 10^{16}$ cm^{-3}, $\mu_1 = 1500$ cm^2/Vs, and $B = 9.4$ kG. Current-field data was included for the cases of backside-gate voltages of +60 V and −60 V. The results are plotted in Fig. 4.25.

As expected, the application of a positive backgate bias results in a slightly higher mobility at the higher fields since the carriers are pulled farther into the undoped GaAs and away from the scattering influences at the heterojunction. Similarly a negative bias acts to drive the electrons closer to the junction, subjecting them to a higher scattering rate which results in a lower mobility.

It is expected that when a positive backgate bias is applied to the structure, the population of the upper subband may increase causing the mobility drop due to intersubband scattering to occur at a lower electric field strength. It is not clear in Fig. 4.25 whether any shift in the curves due to intersubband scattering has taken place. This lack of change could have been caused for a variety of reasons which include: the intersubband scattering may be too small compared to the polar optical phonon scattering in this field range, the potential well at the interface

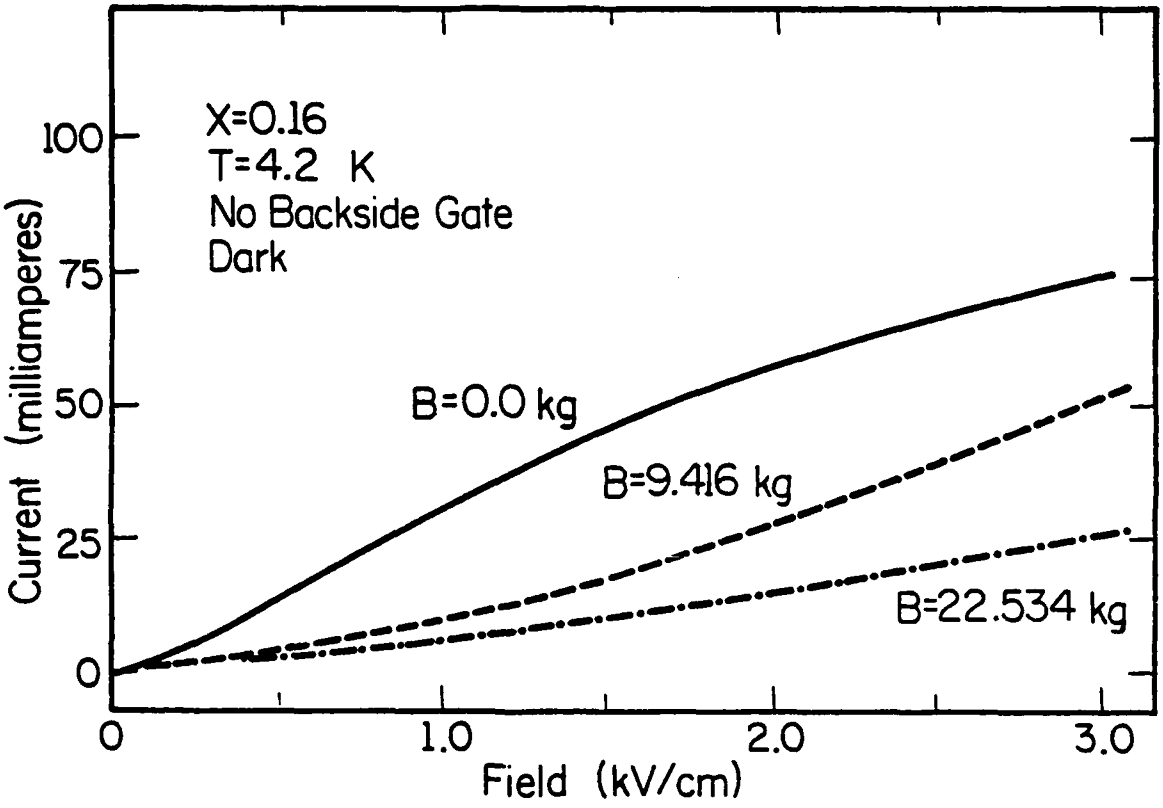

LP2200

Fig. 4.24: Results from current-field measurements made at 4.2 K on a single-period sample (Fig. 4.20) with x = 0.16. The characteristics were plotted for two magnetic field strengths in addition to the case with no magnetic field.

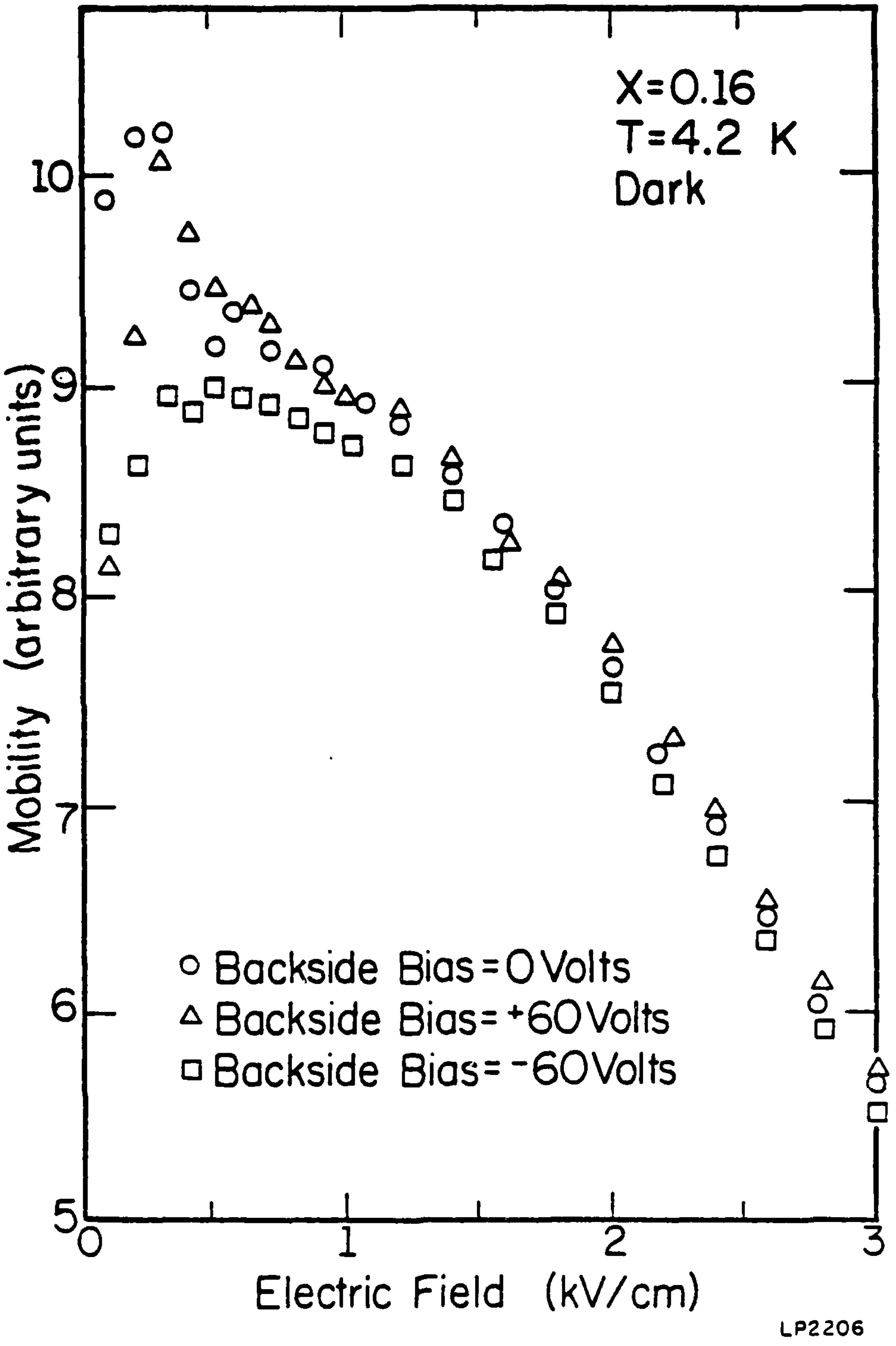

Fig. 4.25: GaAs mobility versus electric field characteristics for several backside gate voltages on the one-period sample measured in Fig. 4.24. Mobility values were calculated using the B = 9.4 kG and B = 0 current-field curves.

may not have been deep enough (for $x = 0.16$ and these particular band-bending characteristics) to contain an upper subband level, or the bias of 60 volts wasn't large enough to significantly change the intersubband scattering threshold.

Van der Pauw-Hall measurements on these structures (with $x = 0.16$ and $x = 0.32$) indicated that the very low-temperature peak mobility of the $x = 0.32$ structure was about 3/2 times that of the $x = 0.16$ structure. Since the magnetic field strength used for the mobility measurements of the $x = 0.16$ sample was about 3/2 times (9.4 kG vs. 6 kG) that used for the $x = 0.32$ sample, the peak $\mu_H B$ values of both samples were nearly equal. Then, since the layer structure and ohmic contact structure of both samples were also the same, it seems justifiable to make some qualitative comparisons of the features of Fig. 4.23 (with $x = 0.32$) and Fig. 4.25 (with $x = 0.16$).

The higher AlAs mole fraction sample ($x = 0.32$) reaches its peak mobility at a slightly lower electric field than the sample with $x = 0.16$. The GaAs mobility of the higher AlAs mole fraction sample also decreases more quickly with higher electric fields. The sample with $x = 0.32$ drops to one half of its peak mobility at $E \approx 1.4$ kV/cm whereas the sample with $x = 0.16$ doesn't drop to one half of its peak mobility until $E \gtrsim 3.0$ kV/cm.

These features could be explained by the fact that the larger mole fraction sample ($x = 0.32$) has a significantly higher low-field mobility. A higher mobility would allow the electrons to gain enough energy to spontaneously emit phonons at lower electric fields.

Fig. 4.26 displays the current-field measurements of a $x = 0.32$ sample measured with higher magnetic fields in the superconducting magnet. This

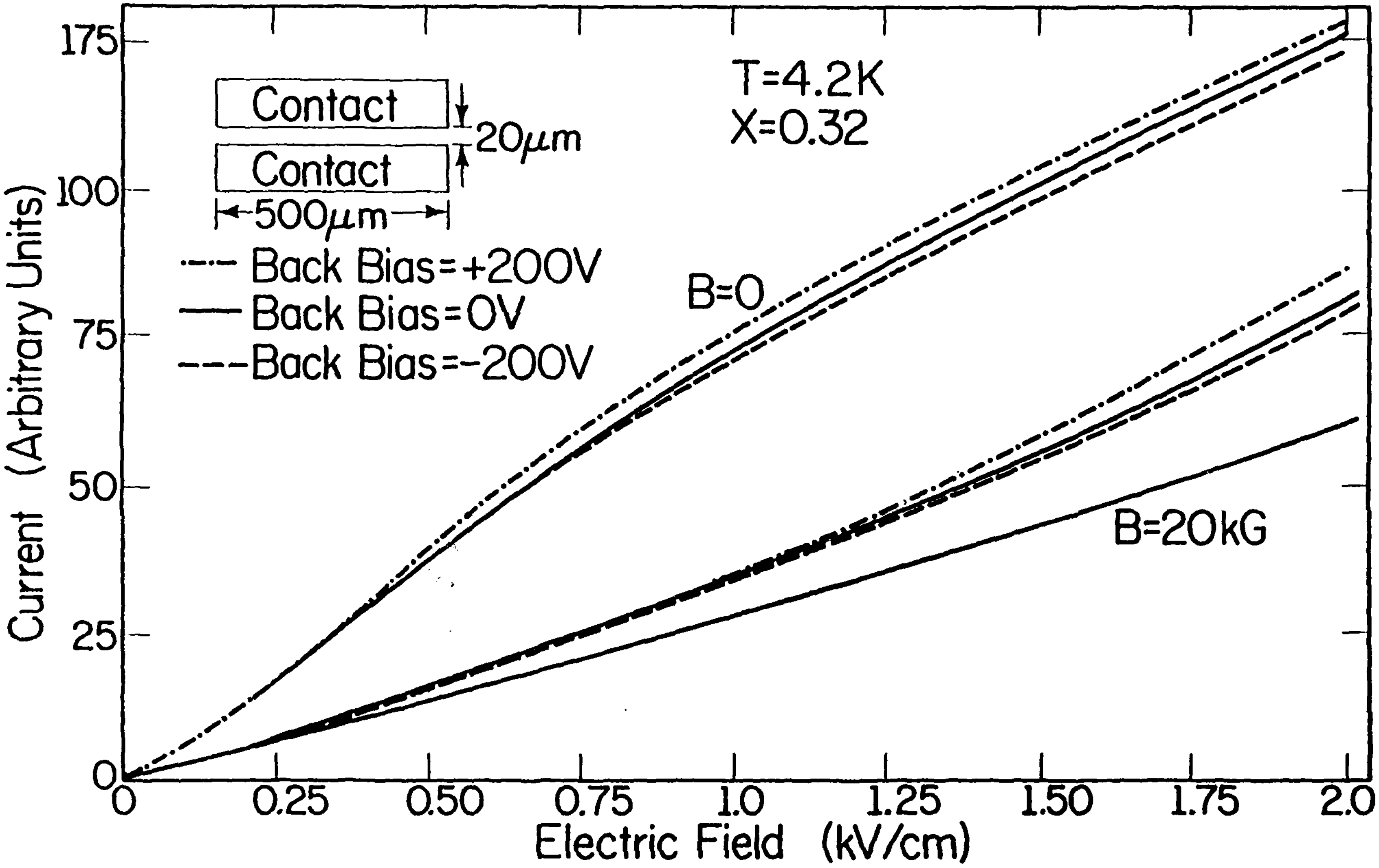

Fig. 4.26: Current-field data measured at 4.2 K with magnetic field strengths of B = 0, 10, and 20 kG. The single-period structure (shown in Fig. 4.20) had an AlAs mole fraction of x = 0.32.

device had a top-surface contact separation of 20 μm and also had a backside-gate electrode. Back bias voltages of +200 V and -200 V were included when measuring the current-field characteristics of this sample. The GaAs mobility was calculated as before using $A_1 = 7.5 \times 10^{-7}$ cm^2, $A_2 = 3.6 \times 10^{-8}$ cm^2, $n = 4.6 \times 10^{16}$ cm^{-3}, $\mu_1 = 1500$ cm^2/Vs, and B = 20 kG. The results are plotted in Fig. 4.27.

As before, a positive bias increases the mobility in the GaAs while a negative back bias lowers it. Although the bias voltages used here have been increased by more than a factor of three over the previously discussed sample, there is still no clear shift in the mobility drop that can be related to the onset of intersubband scattering. Therefore, it is not evident if intersubband scattering contributes significantly to the steady decrease in mobility.

A word of caution should be added here about placing very much emphasis on the high-mobility features in Fig. 4.27. Due to the large magnetic field used (20 kG), the bigger separation of the electrodes (20 μm) and the high mobility of this structure, it is possible that significant distortion of the deflected current paths may have occurred near the edges of the electrodes. This would shift the peak high-mobility characteristics toward higher electric fields and lessen the calculated values of the mobility (especially near the peak).

4.3 Low-Field Surface Acoustoelectric Effects

In one set of samples in which the AlGaAs layer was so highly doped that it became the main contribution to conduction, a sharp negative differential resistance was observed at very low electric fields. Fig. 4.28

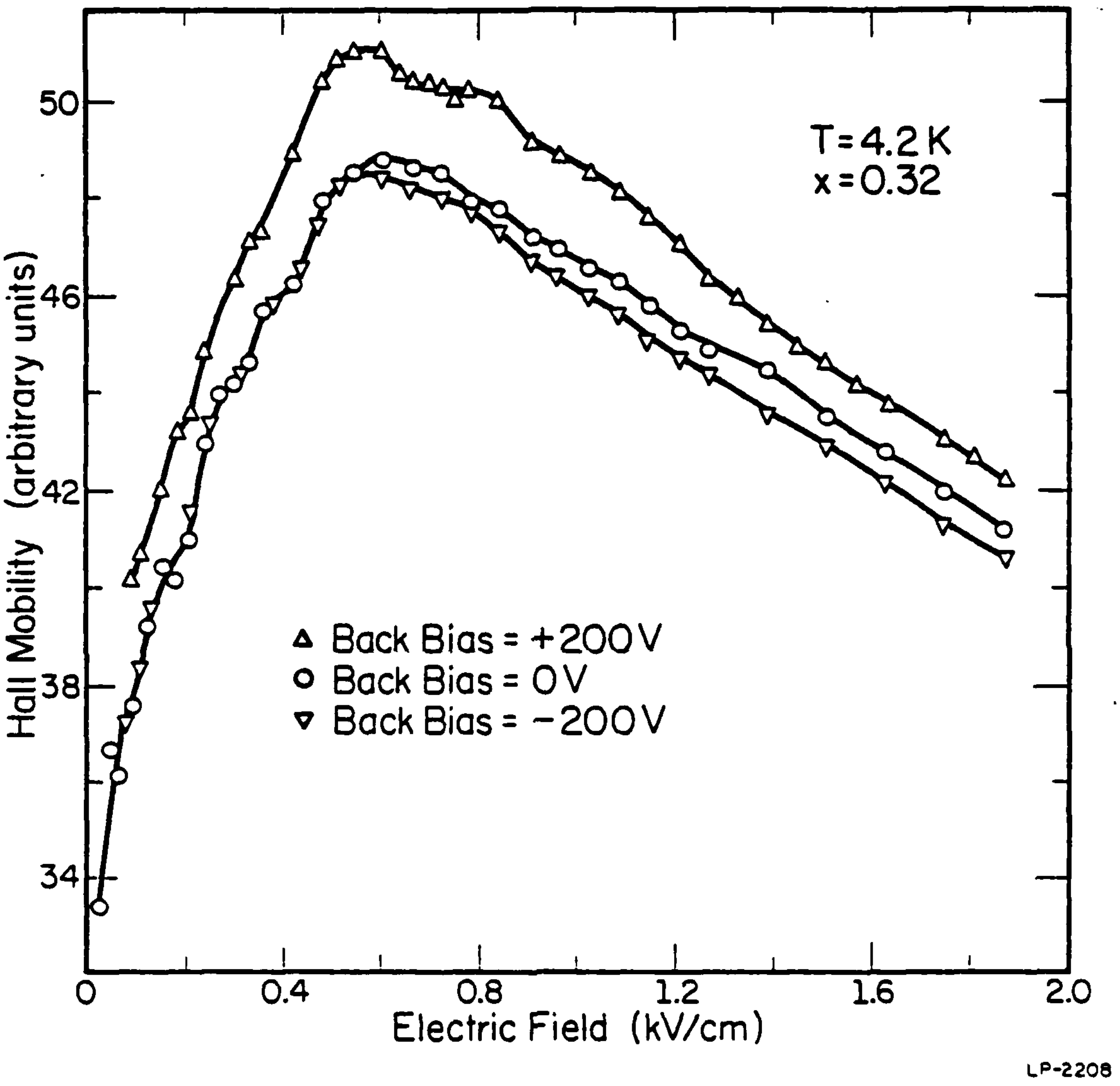

Fig. 4.27: A plot of GaAs mobility versus electric field for several values of backside gate voltages. The data was obtained using the B = 0 and 20 kG current-field curves in Fig. 4.26.

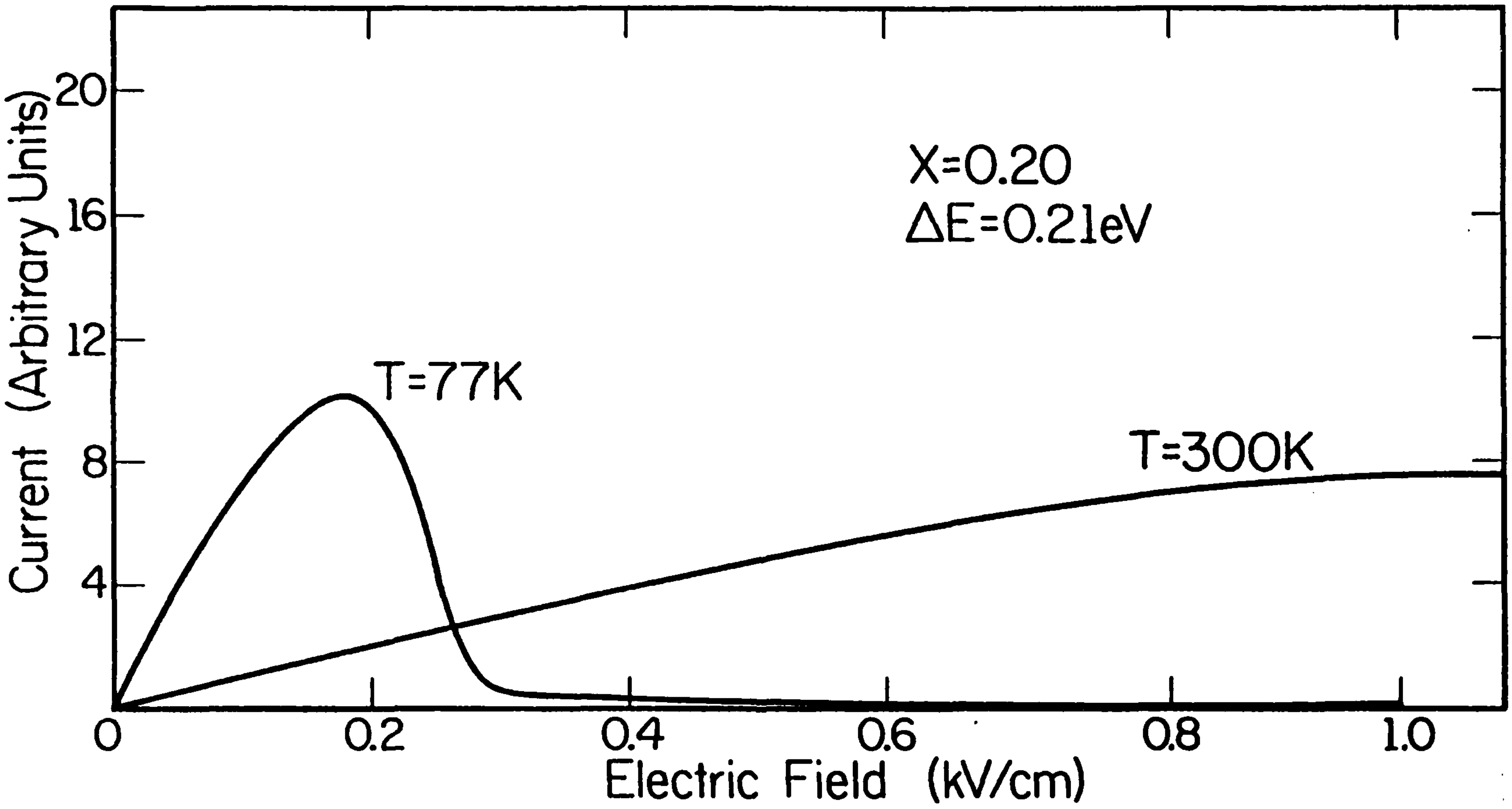

Fig. 4.28: Current-field characteristics at 77 K and 300 K for a single-period structure with x = 0.20. The sharp negative differential resistance at low fields at 77 K is thought to be caused by a surface acoustoelectric effect in the sample.

shows a representative example of this low-field negative differential resistance (NDR) which occurred only at low temperatures.

The MBE single-period structure consisted of a 1500 Å doped $Al_xGa_{1-x}As$ ($x = 0.20$) layer grown on top of a 1.6 μm undoped GaAs layer. Two ohmic contacts were diffused down through the semiconductor surface and the standard methods were employed to measure the current-field characteristics using 600 ns voltage pulses. The AlGaAs mobility of the samples was about $\mu = 1500\ cm^2/Vs$ so that $\mu E \simeq v_s$ at low fields, where v_s was the longitudinal sound velocity in the AlGaAs.

It was also seen that there was a slow time-dependent drop in the current pulses [35] that varied with electric field strength as shown in Fig. 4.29. These effects, together with the disappearance of the effect at 300 K, strongly suggest that this phenomenon is causes by a surface acoustoelectric effect.

Electrons traveling near the speed of sound through the AlGaAs layer amplify surface acoustic waves within ~ 1000 Å of the surface. This determines the frequency of the amplified surface waves to be ~ 10 GHz [115]. The unusually strong sound amplification slows and bunches the electrons causing the accompanying abrupt NDR. The effect does not occur at room temperature because the sample length was too short to compensate for the higher lattice losses at 300 K.

The peak-to-valley ratio and electric field threshold for the negative differential resistance varied considerably from one sample to another from the same wafer. Fig. 4.30 shows the I-E curves for a sample with a large peak-to-valley ratio and the NDR threshold near 300 V/cm. Fig. 4.31 shows the curves for another sample from the same wafer with a considerably

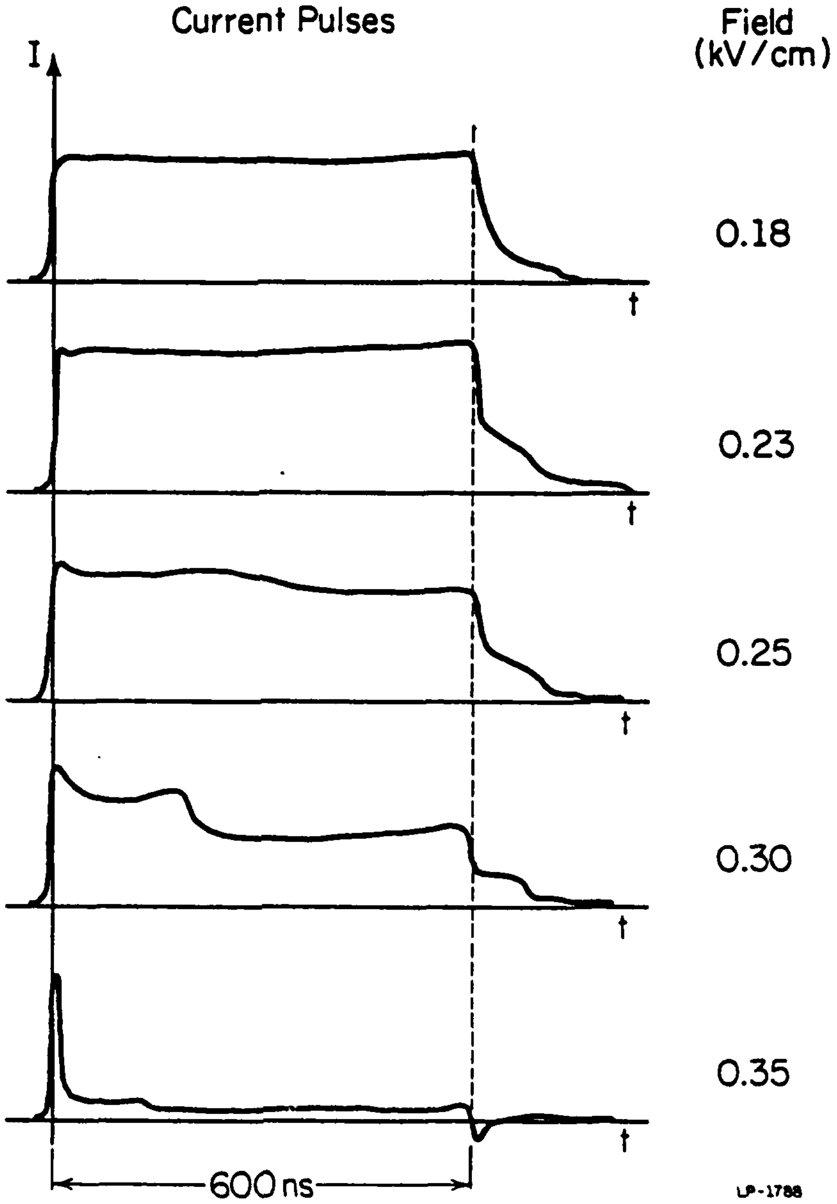

Fig. 4.29: Sketches of several 600 ns current pulses measured at various electric fields. The time-dependent drop in current magnitude on the bottom three pulses is probably caused by an acoustoelectric effect at low temperature.

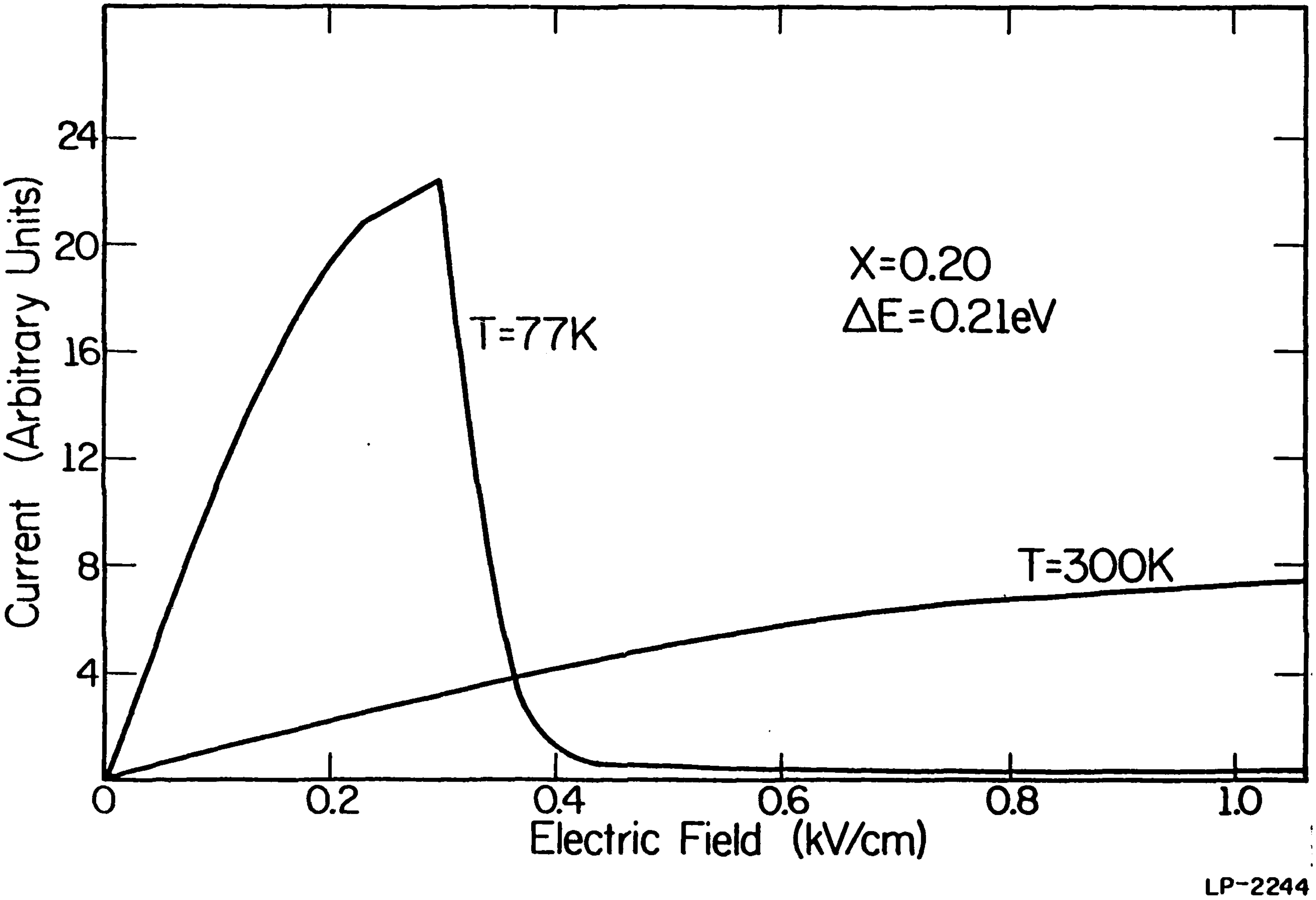

Fig. 4.30: Current-field data for 77 K and 300 K from another sample with the same structure as in Fig. 4.28. The negative differential resistance at 77 K is especially strong in this sample.

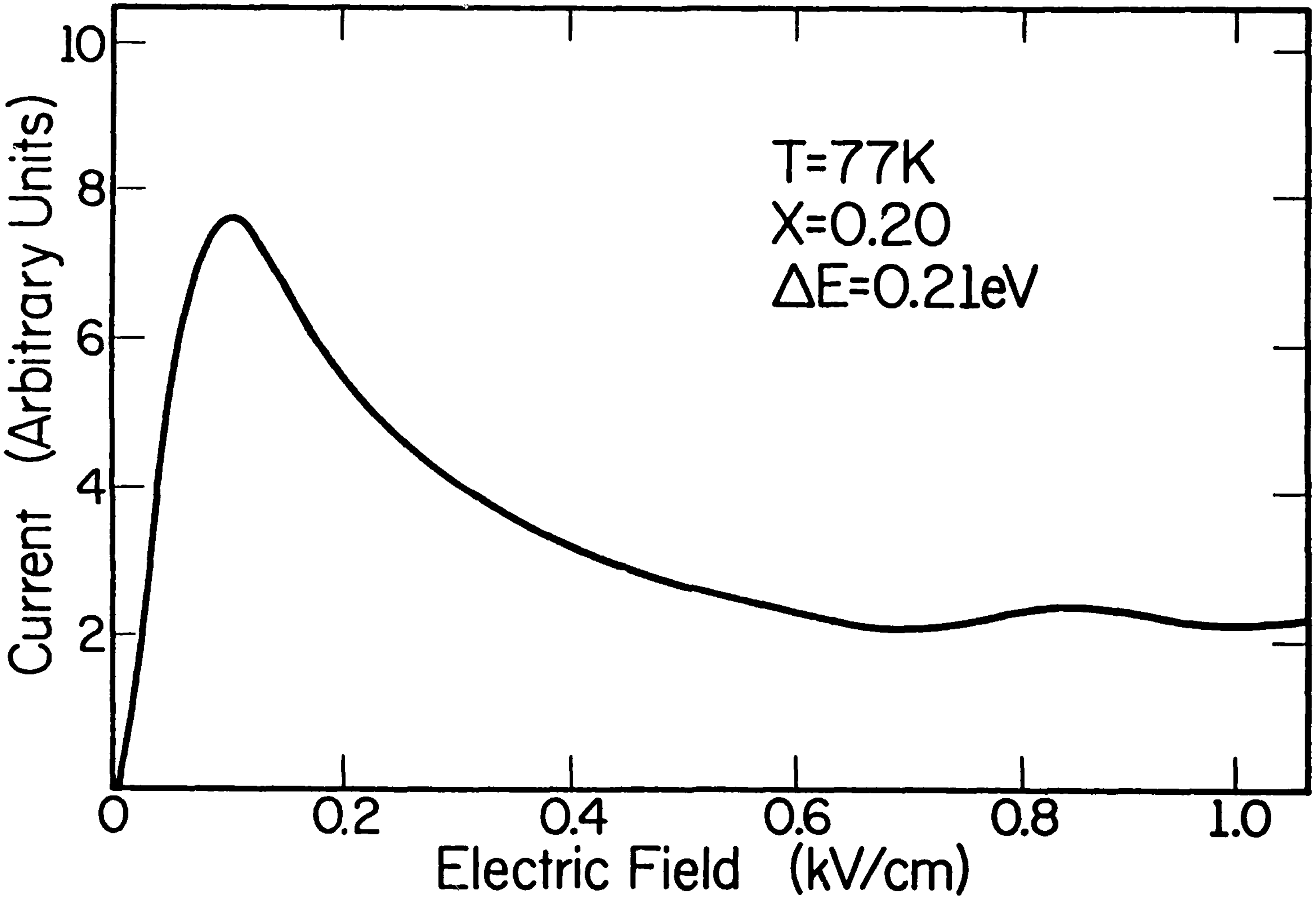

LP-2239

Fig. 4.31: Current-field characteristic at 77K for another sample with the same structure as the samples measured in Figures 4.28 and 4.30. The onset of the NDR occurs at a particularly low electric field near 100 V/cm.

smaller peak-to-valley ratio but the NDR occurs at a much smaller field of ~ 100 V/cm.

The effects reported here were observed only in the set of samples fabricated from one wafer and were not observed in any of the other sample structures studied during the course of this research. The discovery of this effect, however, suggests the possibility of direct generation of surface acoustic waves which might be far superior to the bulk acoustoelectric effect. This superiority is due to the versatility of the MBE growth process and the smallness of the structures, which can be made of the order of the coherence length of the generated sound. One could therefore avoid the incoherent amplification that is usually found in bulk material.

4.4 Summary

Measurements of the low-field electrical characteristics of GaAs-$Al_xGa_{1-x}As$ heterostructures have been reported. In all the samples tested, it was found that the very high mobilities measured at low temperatures with very low electric fields (such as with Hall measurements) decreased very rapidly with increasing electric field strengths. The mobilities were seen to drop significantly at electric fields below 500 V/cm.

The mobility decline as a function of electric field was seen to be very dependent on temperature. The largest mobility reductions occurred at low temperatures where the initial low-field mobility was the greatest. At higher temperatures (200 K to 300 K) there was comparatively little change in the mobility as a function of electric field for fields up to 2 kV/cm. In all cases it appeared as though the greater the magnitude of the peak low-field mobility, the faster was its rate of decline as the electric field was increased.

It was found that the low-field electron mobility at all temperatures in these samples increased with an increase in the AlAs mole fraction. Increasing the AlAs mole fraction x, which increases the conduction-band discontinuity, is thought to improve the mobility by reducing the Coulomb interaction between the spatially separated donors and electrons.

The intrinsic-layer width d_i was also found to be significant in determining the low-field mobilities and current-field characteristics of the heterostructures. There was found to be an optimum intrinsic-layer width for maximizing the low-field mobility that changed for different structures. The optimum value is obtained by balancing the mobility improvement due to decreased electron-donor interaction at larger separation, with the mobility decrease due to less electron transfer and screening when d_i is increased.

Current-field measurements on a variety of structures indicated that three- and nine-period heterostructures exhibit more cases of current saturation and instances of different temperature curves intersecting than do single-period samples. These more pronounced fluctuations in current would make the use of multiperiod heterostructures for FET applications more difficult. In fact, it has been seen in all our studies to date that the performance of single-period GaAs-AlGaAs structures are superior to multiple-period structures for FET applications.

If the doped AlGaAs layers are sufficiently thick or highly doped so as not to become depleted of electrons at low fields, then carrier freeze-out is thought to cause an initial reduction in the overall conductivity of the sample as it is cooled from room temperature. Mobility enhancement due to reduced electron-donor scattering, however, appears to dominate the sample conduction at lower cryogenic temperatures. It was also discovered that trapping states such as the resonant states at a sharp interface may cause noticeable negative differential resistance effects in the low-field current characteristics of a sample.

A study was made of the GaAs mobility dependence on the electric field strength in the modulation-doped structures. Results of measurements of the geometric contribution to the magnetoresistance were used in conjunction with an expression derived for two-layer conduction to calculate GaAs mobility vs. electric field characteristics for several samples. It was discovered that the electron mobility initially increases with electric field, reaches a peak for an electric field less than 500 V/cm, and then drops steadily for higher fields. The initial increase in mobility has been predicted theoretically by Price. The sharp drop in mobility after the peak is thought to be principally caused by the onset of polar optical phonon scattering. Significant phonon emission at such low fields would be due to the unusually high mobilities of the electrons as a result of modulation-doping effects.

The low-field characteristics summarized above certainly indicate that predictions of FET performance at moderate electric fields near 2 kV/cm cannot be based solely on extrapolations from zero-field mobilities obtained from Hall measurements at cryogenic temperatures. The extremely high mobilities reported by various laboratories for modulation-doped GaAs-$Al_xGa_{1-x}As$ heterostructures will not scale up with electric field strength as device dimensions are reduced. The low-field characteristics presented in this chapter are very important for design considerations of heterostructure devices using lateral electric fields to control electron transport.

As will be shown in the following chapter, velocity-saturation effects and negative differential resistances commonly occur for still higher fields above 2 kV/cm. This will limit even more the performance of devices depending on the lateral high-mobility transport properties of modulation-doped heterostructures.

5. HIGH-FIELD MEASUREMENTS

5.1 Real-Space Electron Transfer

5.1.1 Introductory Discussion

The important characteristics of modulation-doped GaAs-$Al_xGa_{1-x}As$ structures which were described in detail in Chapter 2 are displayed in Fig. 5.1. Only the AlGaAs is intentionally doped, leaving the GaAs layers relatively free of impurities. This allows a large reduction in ionized-donor scattering for electrons in the GaAs and as a result, the mobility in the GaAs is much higher than that in the AlGaAs, especially at low temperatures. Due to the lower band gap of the GaAs, the free electrons in the doped AlGaAs leave their donors and transfer to the GaAs layer. Under low-field conditions the electrons are trapped in the GaAs by the conduction-band discontinuity ΔE_c at the interface.

The width of the potential well holding the electrons depends on the band-bending characteristics as well as the GaAs layer width as can be seen in Fig. 5.2. When the band bending is not very large, as in Figs. 5.2(a) and (b), the potential well containing the bound states is the same width as the GaAs layer. When the band-bending is sufficiently large, however, the electrons are confined to a thinner quasi-triangular potential well as shown in Fig. 5.2(c) and a two-dimensional electron gas (2DEG) forms at the interface. The undoped AlGaAs layers of width d_i in Fig. 5.2 are used to increase the mobility in the GaAs material near the interface. The influence of these "intrinsic" AlGaAs layers was explained thoroughly in

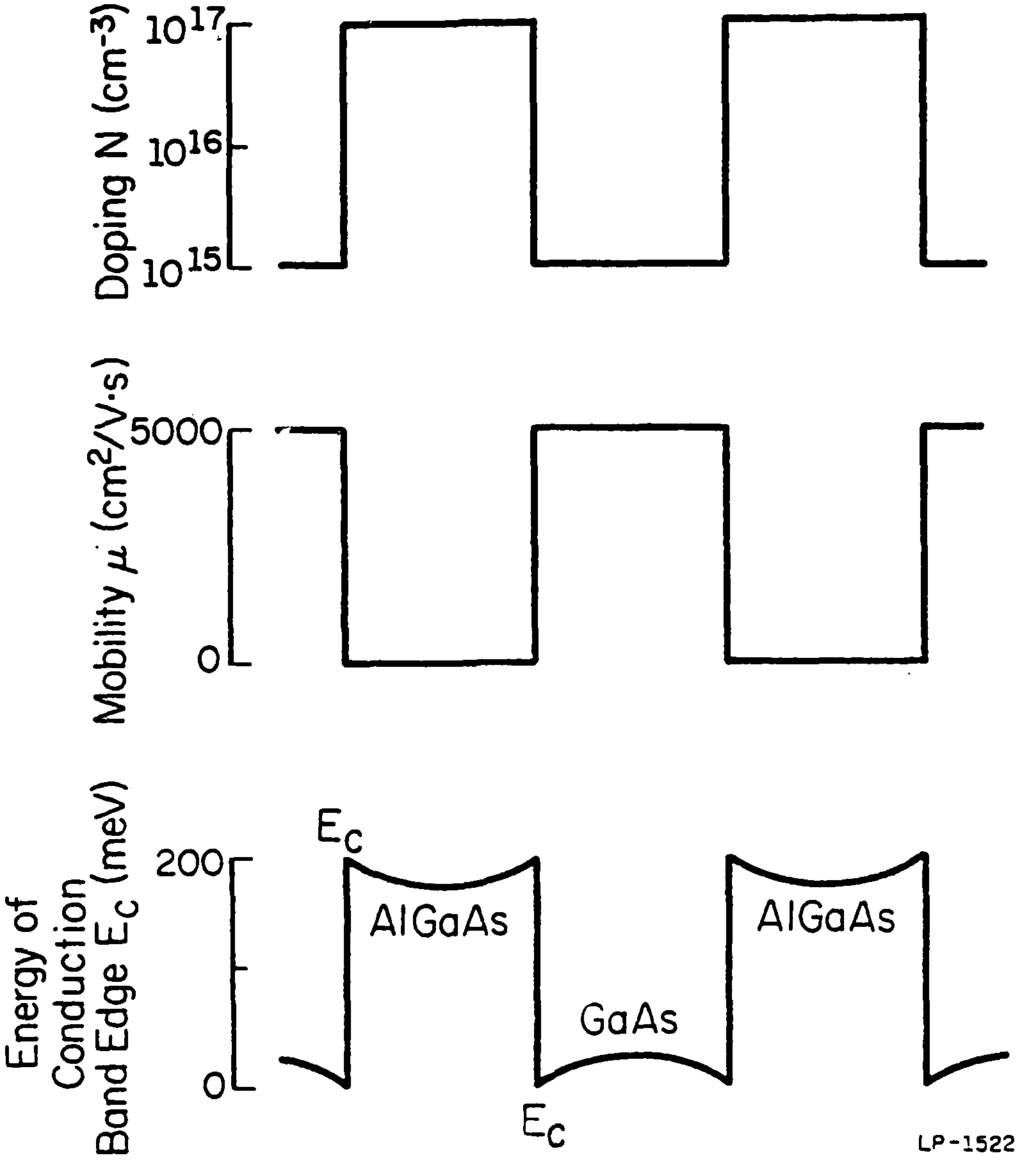

Fig. 5.1: Schematic diagram displaying the doping profile, general locations of higher mobility, and the simplified conduction-band configuration of a modulation-doped GaAs-$Al_xGa_{1-x}As$ heterostructure [26].

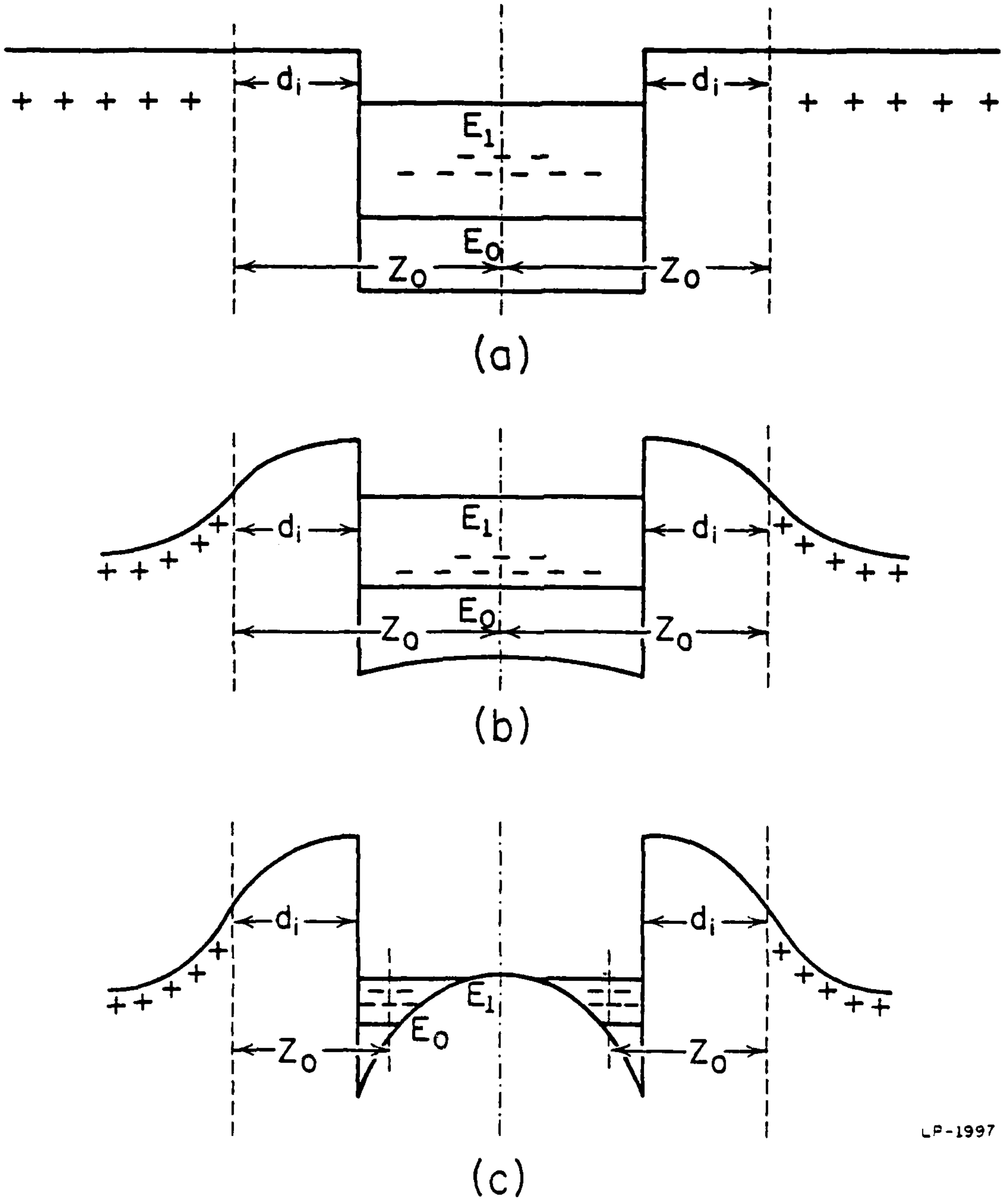

Fig. 5.2: Schematic conduction-band diagram illustrating the influence of band bending on the width of the potential well for the cases of (a) no band bending, (b) moderate band bending, and (c) strong band bending [67].

Chapter 2.

When a large electric field is applied parallel to the heterojunction interfaces, the electrons in the GaAs are heated to energies far above their thermal equilibrium values. Since the power absorbed by the electrons is proportional to their mobility, the high-mobility electrons in the GaAs are heated much more than the electrons in the low-mobility AlGaAs. If the electric field is large enough, the electron energies in the GaAs can become comparable to the conduction-band discontinuity ΔE_c and the electrons can propagate into the adjacent AlGaAs layer as shown in Fig. 5.3. These electrons acquire the momentum to cross the interface either by being scattered out of the GaAs or through the strong Coulomb attraction of the donors in the AlGaAs layer. Note that the conduction-band discontinuity ΔE_c must be low enough ($\Delta E_c \lesssim 0.32$) so that the electrons transfer out of the GaAs before they transfer in k-space to the L satellite minima (causing the Gunn effect).

When the hot electrons transfer in real space from the high-mobility GaAs to the low-mobility AlGaAs layer a negative differential resistance (NDR) can occur as proposed by Hess in 1979 [26]. The NDR caused by real-space transfer is analogous to the Ridley-Watkins-Hilsum (RWH) mechanism associated with the Gunn effect. In the RWH effect, the electrons transfer in k-space from the high-mobility central valley to the low-mobility satellite minima. The NDR mechanism of real-space transfer, however, is much more versatile than that of the RWH effect. All the characteristics of the real-space transfer NDR, including the threshold electric field, can be altered by changing the Al concentration x (which changes ΔE_c), the doping in the $Al_xGa_{1-x}As$, or the other growth parameters such as layer widths.

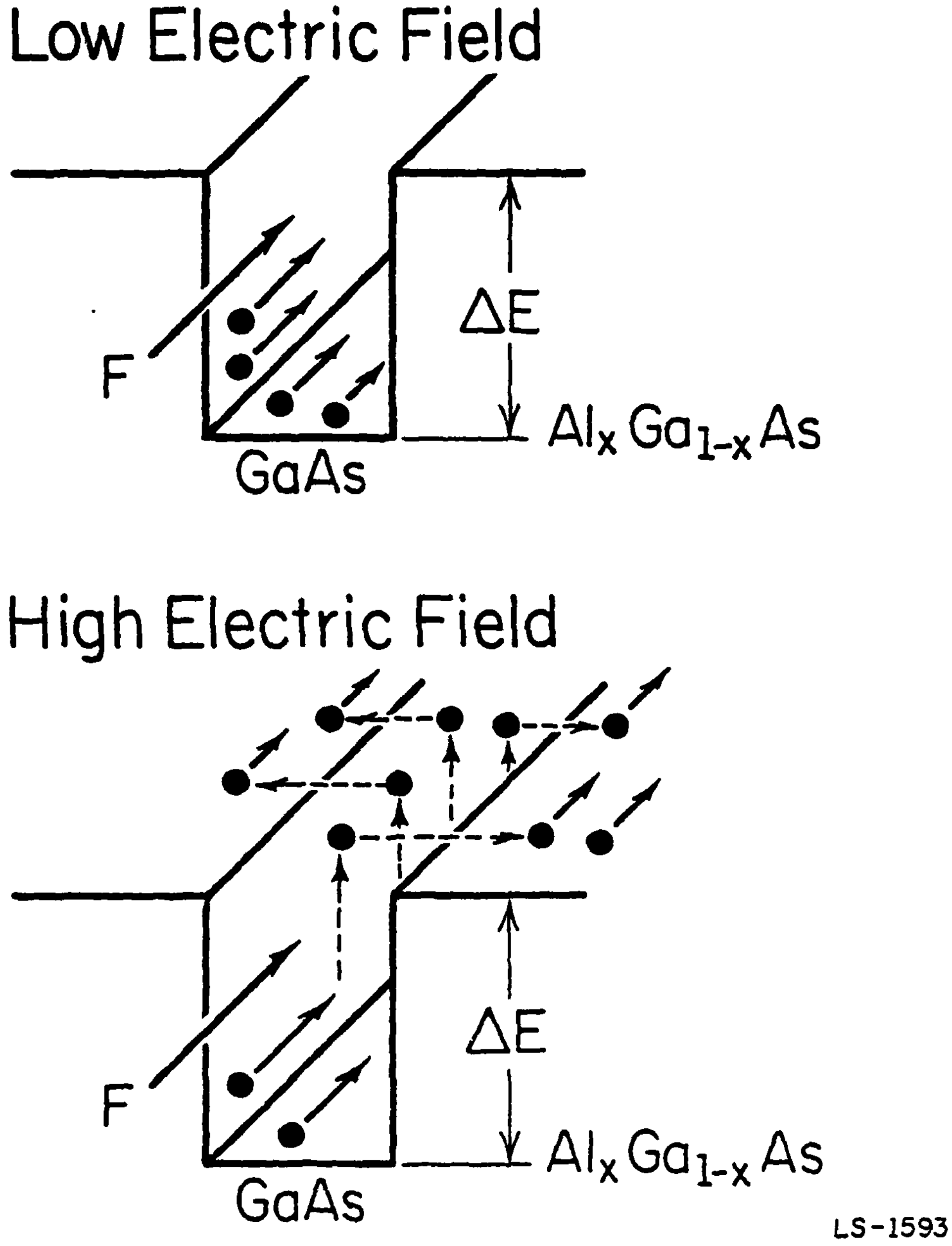

Fig. 5.3: Schematic diagram of the conduction band, illustrating the thermionic emission of hot electrons out of the GaAs potential well when a high electric field is applied parallel to the layers.

Thus the characteristics of the negative differential resistance can be engineered to meet the needs of various device applications.

In order to obtain a large NDR it is necessary to both have a large mobility difference between the GaAs and AlGaAs layers, and also to have the AlGaAs nearly depleted of electrons at low fields. The mobility in the AlGaAs may be lowered by using a higher doping concentration but this can also result in more electrons being left in the AlGaAs to contribute to conduction at low fields. When both layers conduct at low fields, the current reduction will be smaller when the electrons initially in the GaAs transfer back to the AlGaAs. Such cases of parallel (two-layer) conduction can totally eliminate any NDR effect. In order to have the impurity concentration high in the AlGaAs (to obtain low mobility) and at the same time still deplete the AlGaAs completely at low fields, it may be necessary to compensate the AlGaAs. In single-period structures with the doped AlGaAs layer on top, pinning of the Fermi level below the AlGaAs conduction band at the top surface may also help deplete the AlGaAs of electrons at low fields.

Once an electron has escaped from the GaAs layer it can be recaptured in the GaAs potential well only by losing energy through some inelastic process. The strongest inelastic process is optical-phonon scattering. When x is high enough so that intervalley deformation potential scattering is important, the scattering is very strong and electrons can be easily collected in wells 100 Å thick or less. When x is small, however, only polar optical scattering, which occurs at an almost constant rate of $\sim 10^{13}\ s^{-1}$, is possible. Then an electron injected into the GaAs just below the L minima may travel about 1000 Å without substantial energy losses. However, after emitting one phonon the electrons are essentially captured because the emission of another phonon is much more probable than phonon absorption.

The details of real-space transfer are fairly complicated and cannot be derived analytically. However, the transfer speed between layers can be estimated as discussed below and a few of the results of Monte Carlo calculations performed by Glisson et al. [116] will be presented in the following section.

To calculate the switching speed, observe that the potential wells in Fig. 5.2 are similar to the step-like wells in charge-coupled devices, where electrons move by diffusion from one gate to another. Using this analogy, one can obtain the time t_s which the electrons need to fall back into the GaAs layer after switching off the "heating" field [26]:

$$t_s \approx 4L_2{}^2/\pi^2 D \tag{5.1}$$

where L_2 is the thickness of the $Al_xGa_{1-x}As$ layer, and D is the diffusion constant in the $Al_xGa_{1-x}As$. This formula is valid only as long as the diffusion concept applies and the mean free path for phonon emission λ_{ph} is smaller than L_1, the thickness of the GaAs layer. If λ_{ph} is longer than L_1, the probability of an electron being captured in the well is reduced by L_1/λ_{ph}. Eq. (5.1) then becomes

$$t_s \approx 4L_2{}^2\lambda_{ph}/\pi^2 DL_1 \ . \tag{5.2}$$

For typical values such as $L_1 = L_2 = 400$ Å, $\lambda_{ph} \lesssim 10^{-5}$ cm, and $D = 1$ cm^2/s, one obtains $t_s < 1.62 \times 10^{-11}$ s, which is an attractively short time for a variety of applications. Of course, one must add the time required for heating and cooling of the electrons, about 5×10^{-12} s, to t_s. In deriving

Eq. (5.2) it was assumed that there is no potential barrier as seen in Fig. 5.4. caused by the ionized donors in the $Al_xGa_{1-x}As$. The potential barrier ψ_2 created by such donors is comparable to kT_L/e for an $Al_xGa_{1-x}As$ layer width of 600 Å, a net doping concentration of 10^{16} cm^{-3}, and T_L = 300 K. Here T_L is the temperature of the crystal lattice.

If the layers are very thin and the potential barrier created by the donors is high, the diffusion concept breaks down and the back transfer will be "thermionic emission" limited. The principles of the thermionic emission current are well known and one can obtain the back-transfer time [117]:

$$t_s \approx \frac{eN_c L_1 m_o}{A^* T_L^2 m^*} \exp\left(\frac{e\psi_2}{kT_L}\right) \qquad (5.3)$$

where A^* is the Richardson constant, m^* is the effective mass, m_o is the free-electron mass, ψ_2 is the potential barrier created by the donors in the $Al_xGa_{1-x}As$, and N_c is the effective density of states in the $Al_xGa_{1-x}As$. For $e\psi_2/kT_L \lesssim 2$, t_s is about 10^{-12} s, and therefore the transfer speed is also determined by the heating and cooling time and the time needed to resupply electrons with high enough kinetic energy to overcome the barrier. Both time constants are determined by collision rates and are about 5×10^{-12} s. The correctional factor of L_1/λ_{ph} must again be included for $\lambda_{ph} > L_1$.

The transfer out of the GaAs is also dominated by the time constant in Eq. (5.3). One need only replace ψ_2 by the band-edge discontinuity ΔE_c and the lattice temperature T_L by the actual temperature of the carriers T_c, which is much larger than T_L for high fields. The results of several calculations using Eq. (5.3) will be discussed in Section 5.3.

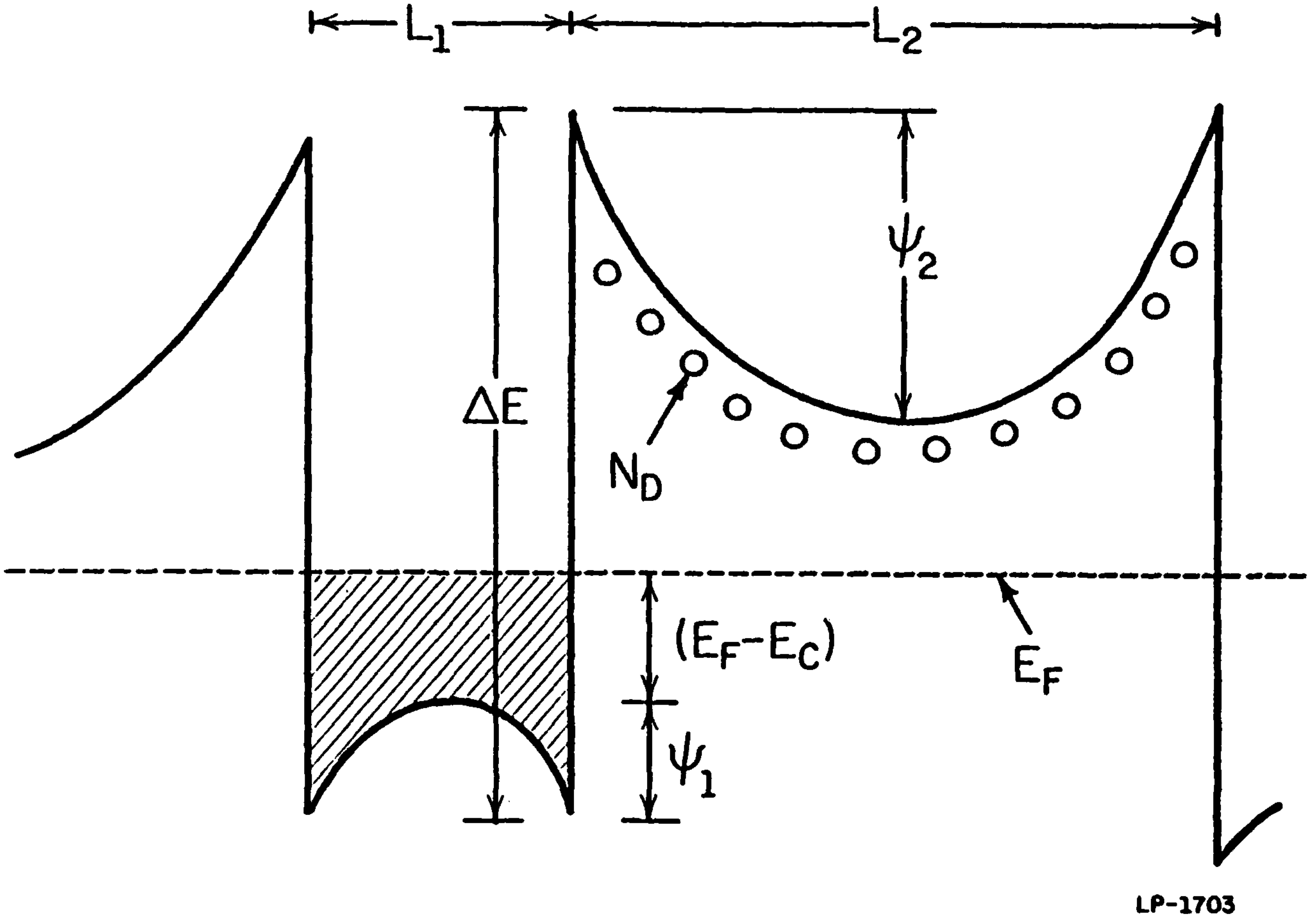

Fig. 5.4: Schematic drawing of the heterostructure conduction band with significant band-bending effects. Note the potential barriers formed in the AlGaAs layer due to the ionized donors.

5.1.2 Review of Monte Carlo Calculations

Monte Carlo studies of real-space transfer in GaAs-AlGaAs layered heterostructures have been performed by Glisson, Shichijo, and co-workers [116]. They found that the Monte Carlo calculations predicted a negative differential resistance (NDR) for properly chosen heterostructures. Calculations also indicated that the peak-to-valley ratio of the NDR could be controlled by the layer width and mobility ratio, the onset of the NDR could be controlled by the AlAs mole fraction (barrier height), and the speed of the device could be controlled by the layer thicknesses. The simulations also indicated that the real-space transfer (RST) effect occurred well before the k-space transfer (Gunn effect) for junction barrier heights of approximately 200 meV.

The Monte Carlo method was applied to the material/device configuration shown in Fig. 5.5. The GaAs and AlGaAs layer widths were denoted by d_1 and d_2, respectively. The model assumed an abrupt potential barrier of height ΔE in the GaAs, and band-bending effects were neglected. The electric field created by the ionized donors in the space-charge region of the heterojunction was also neglected. This field ends to attract energetic electrons from the GaAs into the $Al_xGa_{1-x}As$. Hence, it would enhance the transfer out of the well and impede transfer back into the well. This would enhance the negative resistance effect reported here.

The electrons drift in a uniform electric field applied in the y-direction parallel to the heterojunction interface. The one electron simulation begins by releasing an electron from the center of the GaAs well with thermal (T = 300 K) energy and in a randomly-selected direction. the electron then undergoes scattering interactions in the normal Monte Carlo

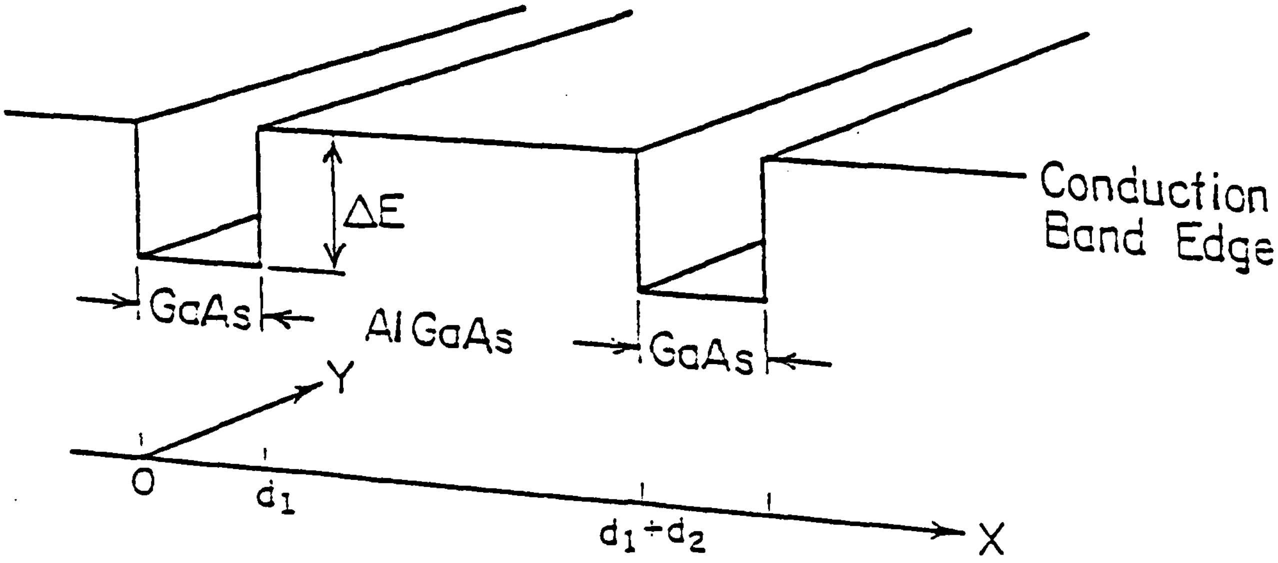

Fig. 5.5: Heterostructure material configuration used for Monte Carlo simulation of real-space transfer.

framework. The scattering mechanisms considered in these calculations include acoustic phonon scattering, optical phonon scattering, piezoelectric scattering, equivalent and non-equivalent intervalley scattering, ionized-impurity scattering, and random potential alloy scattering in the $Al_xGa_{1-x}As$. In the calculations reported here only the $\Gamma(000)$ and L(111) conduction bands were considered for GaAs, and only the $\Gamma(000)$ conduction band was considered in the $Al_xGa_{1-x}As$. This represented adequate band-structure details to illustrate the essential features of real-space transfer in GaAs/AlGaAs heterostructures.

Carrier compensation was utilized in the simulation in order to vary the mobility of electrons in the AlGaAs. The free electron density in the scattering rate for ionized-impurity scattering was taken to be 10^{17} cm^{-3}, while the net ionized-impurity density was allowed to vary from 10^{17} cm^{-3} to 10^{20} cm^{-3}. This varied the electron mobility in the AlGaAs from about 4000 cm^2/Vs to 50 cm^2/Vs. The 300 K low-field mobility in the GaAs was held constant at about 8000 cm^2/Vs by taking the ionized-impurity density in the GaAs to be zero.

The model and procedures described above were used to simulate the electron transport in GaAs/AlGaAs heterostructures at 300 K with various device thicknesses, barrier heights, and other AlGaAs material parameters. Fig. 5.6 shows the steady state drift velocity of such a structure for the case where the low-field mobility of the GaAs is 8000 cm^2/Vs and that in the AlGaAs is about 50 cm^2/Vs. Here, the ionized-impurity density in the AlGaAs is 10^{20} cm^{-3} and the barrier height is 0.2 eV. In this figure the drift velocity in the device structure is compared to that for bulk GaAs and AlGaAs. The transport in the AlGaAs remains essentially ohmic for the range

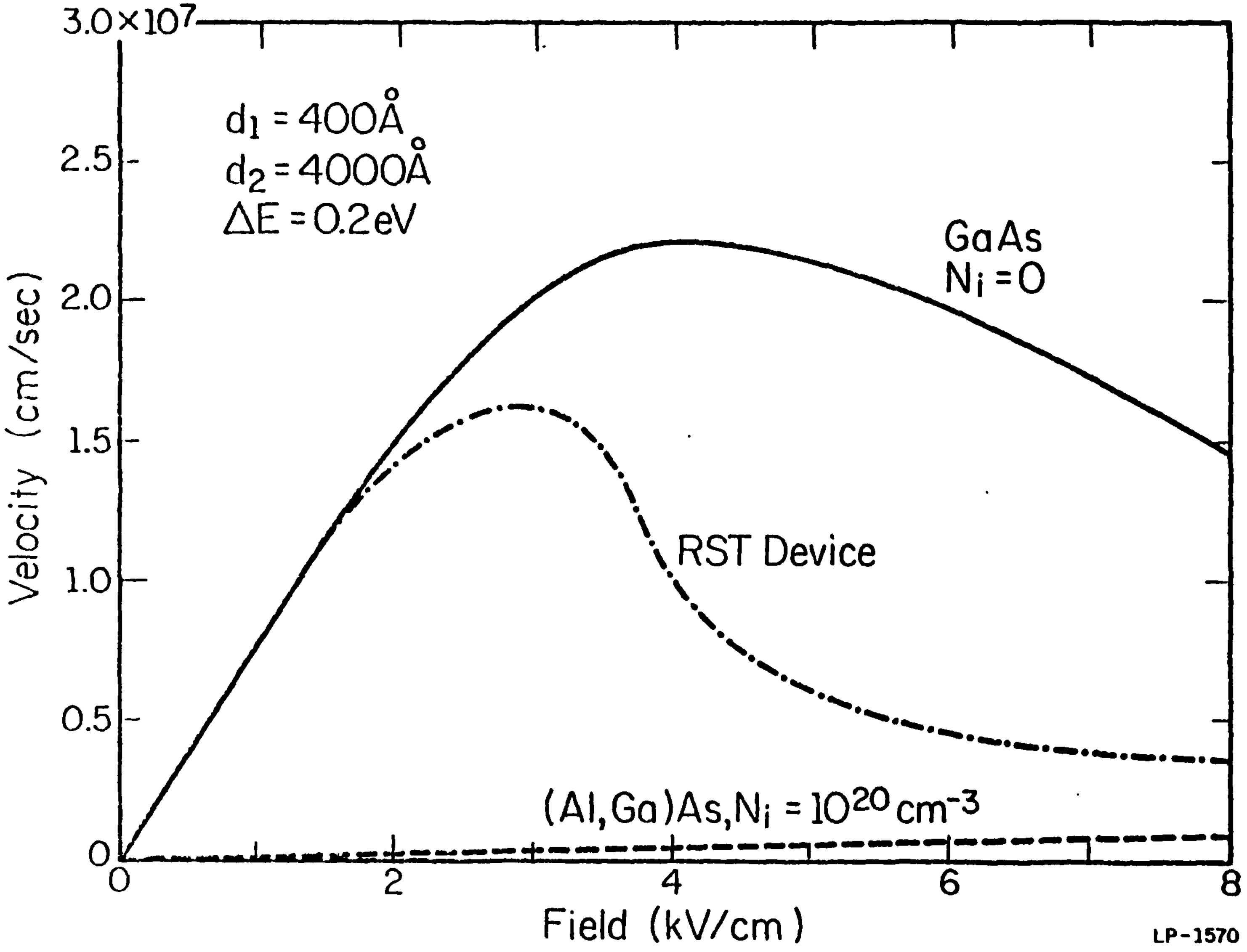

Fig. 5.6: Velocity-field characteristic at 300 K for real-space transfer device as compared to those of bulk GaAs and AlGaAs. The GaAs and AlGaAs electron mobilities were 8000 cm^2/Vs and 50 cm^2/Vs, respectively with $\Delta E_c = 0.2$ eV. The AlGaAs impurity concentration was 10^{20} cm^{-3} [116].

of electric fields shown in Fig. 5.6, although at fields near 15kV/cm the transport in the AlGaAs would become non-linear and would eventually exhibit velocity saturation. The peak velocity for the real-space transfer structure is 1.6 x 10^7 cm/s and the threshold field is about 2.8 kV/cm. The onset of electron transfer to the AlGaAs layers occurs at a field of about 2 kV/cm, as can be seen in Fig. 5.7. This figure, which shows the relative number of electrons in the two adjacent materials, illustrates that for the material thicknesses and barrier height used a substantial number of electrons remain in the GaAs, even for fields well above threshold. The ratio of electrons in the two materials largely determines the peak-to-valley ratio of the real-space transfer device [26].

Fig. 5.8 shows a velocity-field characteristic at 300 K when the AlGaAs mobility is 4000 cm^2/Vs. Here, a substantial number of electrons remain in the GaAs for fields well above 8 kV/cm, and the two materials are equally important in determining the drift velocity in the heterostructure for fields above the threshold field of GaAs. This figure serves to illustrate that a layered heterostructure device might be used to achieve an adjustable velocity-saturation mechanism with very small or negligible negative differential resistance where the saturation velocity at 300 K is well above the value normally obtained in silicon or indirect band gap AlGaAs ternary systems. It is worth noting that in Fig. 5.8 there is a slight negative differential conductivity in the AlGaAs even though only the central valley was used in the simulation. This is due to the nonparabolic nature of the central conduction band.

Note that since compensated AlGaAs material was unattainable for experimental study during the span of this research, doping levels near

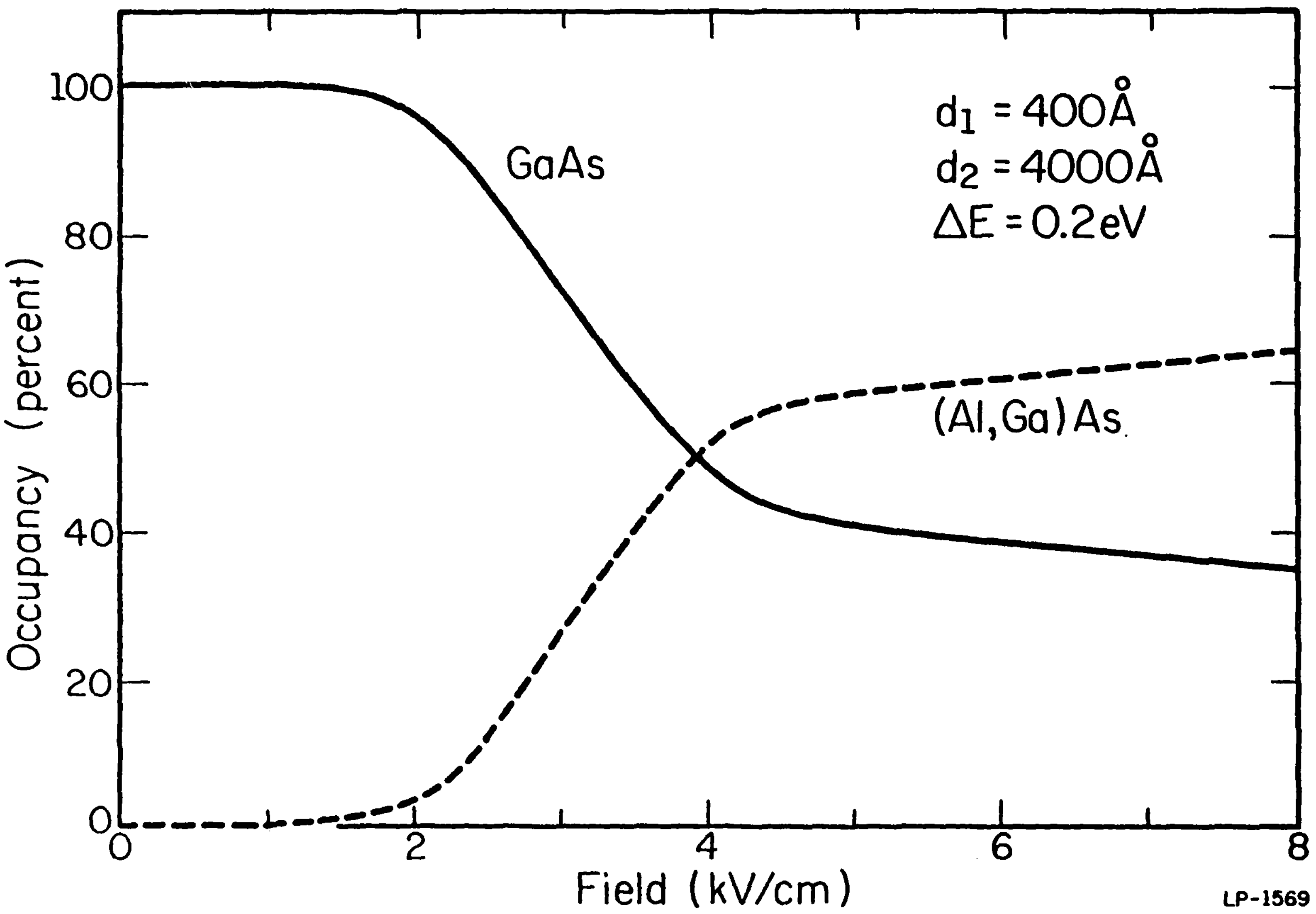

Fig. 5.7: Relative occupancy of electrons in the GaAs and AlGaAs layers versus electric field strength for the same parameters as given in Fig. 5.6 [116].

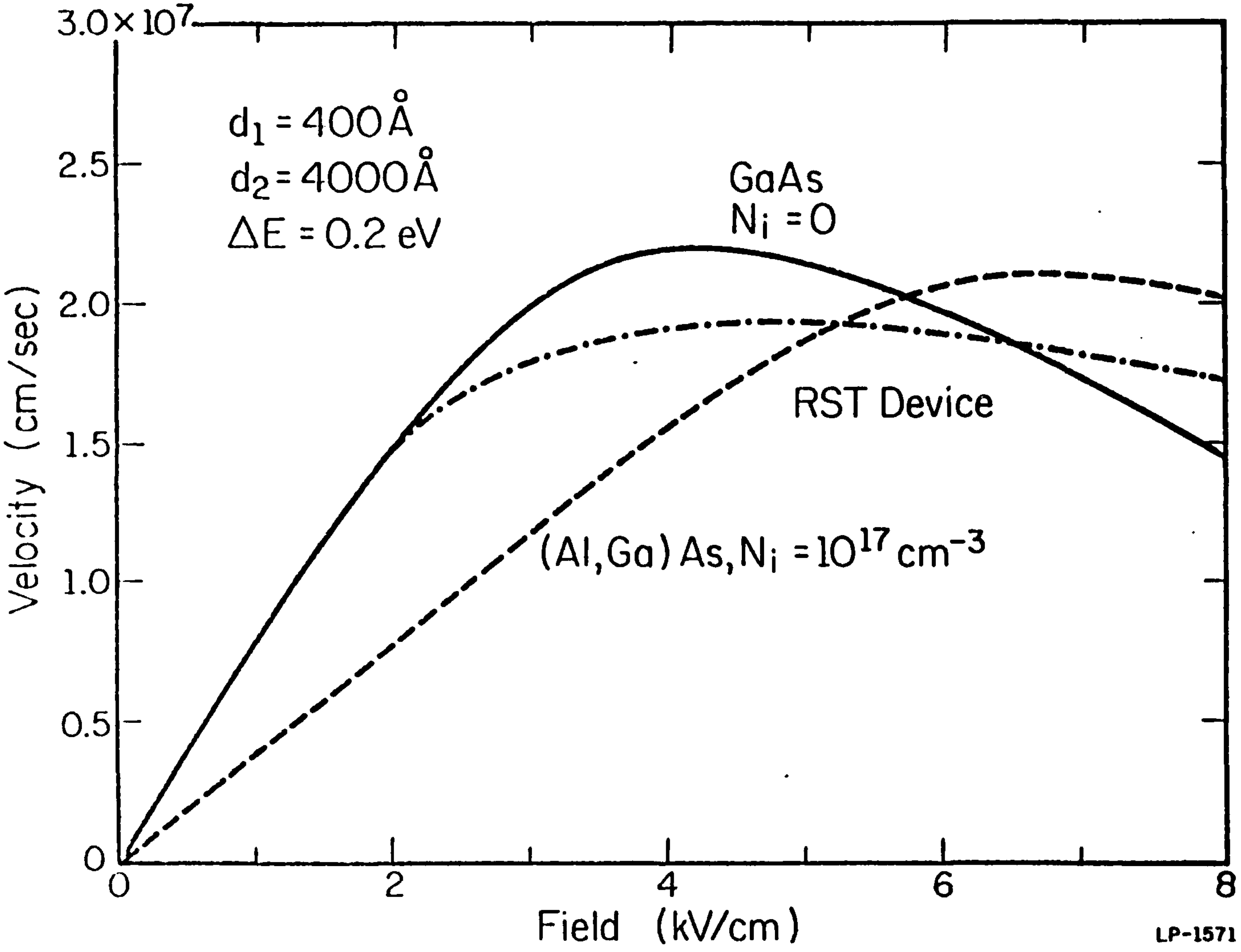

Fig. 5.8: Velocity-field characteristic at 300 K for real-space transfer device as compared to bulk GaAs and AlGaAs. The donor concentration in the AlGaAs was 10^{17} cm^{-3} with mobilities of 4000 cm^2/Vs and 500 cm^2/Vs in the GaAs and AlGaAs, respectively [116].

$10^{17} cm^{-3}$ were used for the experimental measurements so that the AlGaAs could be nearly depleted of electrons at low fields. Thus, the RST device curve in Fig. 5.8 indicates the type of result that may be typically expected for the experimental 300 K current-field curves presented in the following section.

5.1.3 Current-Field Characteristics

High-field measurements were performed on modulation-doped heterostructures of the general type shown in Fig. 5.9. The AlGaAs layers were usually doped in the range of 10^{17} cm^{-3} and the GaAs layers were not intentionally doped. Most of the results reported in this section were from one- or two-period structures with the AlGaAs layer width being 1000 Å. Some samples contained undoped AlGaAs spacer layers and/or a top GaAs cap layer of the sort described previously. The AlAs mole fraction x was 0.17 for most of the data reported here, but higher x samples were also studied. The ohmic contacts were most frequently made with the AuGeNi compound as discussed in Chapter 3. The contacts were alloyed in flowing H_2 at 450°C and turned out to be ohmic in most cases.

When studying real-space transfer effects, most of the current-field measurements were performed with the simple two-contact device structure shown in Fig. 5.9. This contact configuration was the easiest to construct and use for testing. Other multiple-contact devices were also tested at high fields, however. One such structure (etched-Hall pattern) was described in Chapter 4 and another configuration will be introduced in Section 5.3. All high-field characteristics were measured using short voltage pulses and the sampling-oscilloscope circuit arrangement presented in Chapter 3.

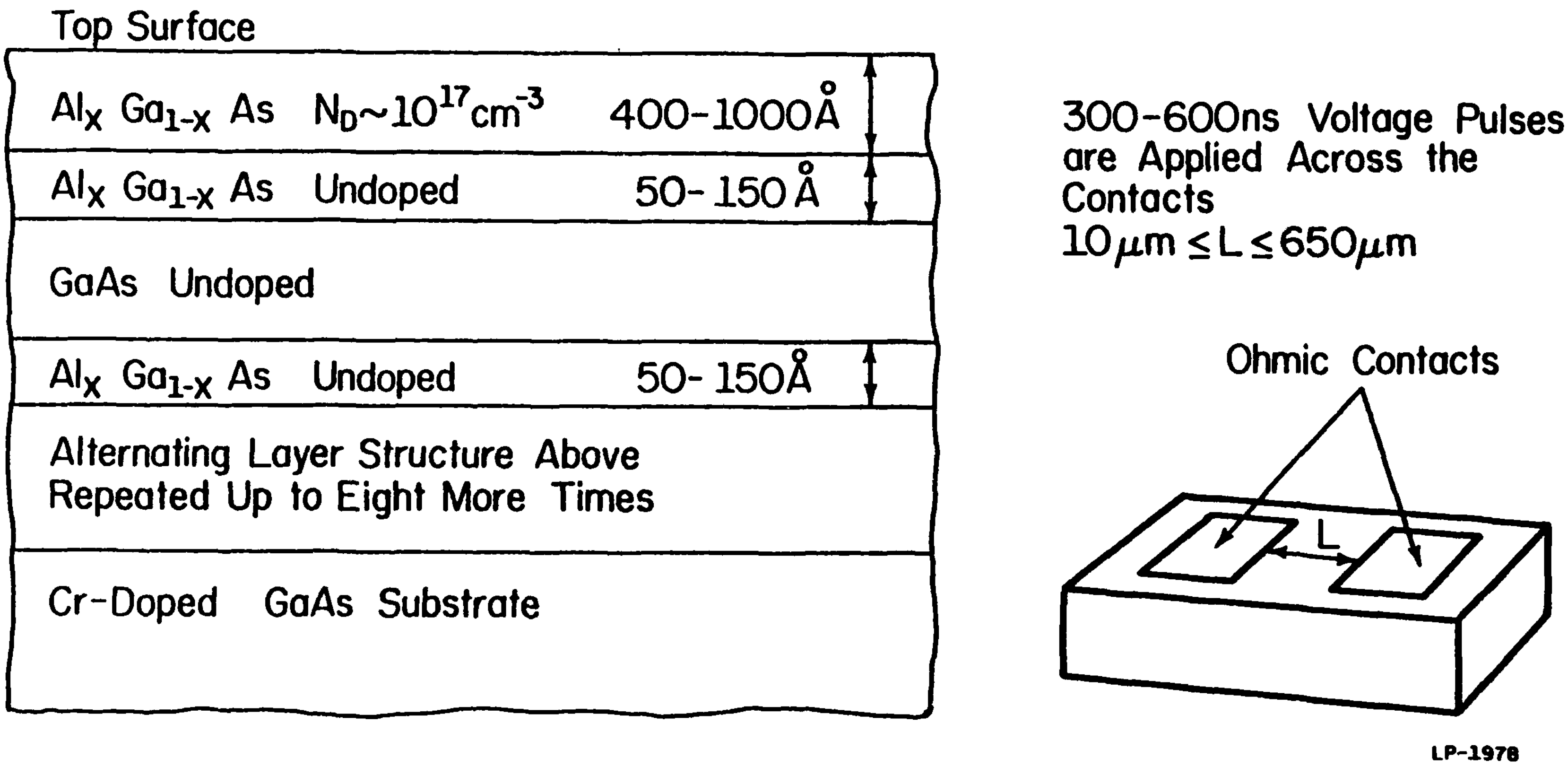

Fig. 5.9: Sketch of the general modulation-doped sample layer cross section used for experimental measurements. The simple two-electrode device was used for measuring the lateral current-field characteristics associated with real-space electron transfer.

The current-field characteristics presented in Fig. 5.10 were measured at 300 K and were representative of the data obtained from many MBE and MOCVD wafers and device geometries. The AlAs mole fraction was $x = 0.17$ so that the potential barrier height for electron emission from the GaAs was approximately 0.2 eV. The curves exhibit small NDR effects or current saturation of the form predicted by the Monte Carlo simulations for equivalent doping ($\sim 10^{17}$ cm^{-3}) in the AlGaAs. The onset of NDR occurred in the range of 2 - 4 kV/cm and there was no evidence of any Gunn-type oscillations.

Extremely close matching of experimental and theoretical characteristics were found in several instances. Fig. 5.11 shows an experimentally measured current-field curve (solid line) superimposed over the Monte Carlo RST curve (dashed line) for $N_D \approx 10^{17}$ cm^{-3} that was shown in Fig. 5.8. The characteristics are seen to compare quite closely.

Fig. 5.12 shows a typical result obtained for MBE samples which were made with a single layer of doped $Al_xGa_{1-x}As$ on top of a not intentionally doped layer of GaAs. The AlGaAs layer was initially 1000 Å thick and was somewhat highly doped ($\sim 6 \times 10^{17}$ cm^{-3}) so that the AlGaAs was not fully depleted of electrons at low fields. As a result, the curves measured at both 77 K and 300 K showed little evidence of a negative differential resistance at high fields. The samples were then placed in an etching solution of known etch rate and approximately 500 Å of AlGaAs was etched from the top surface of the sample. The ohmic contacts were protected by a covering of black wax during the etch so that the contact properties would not be affected by the etch.

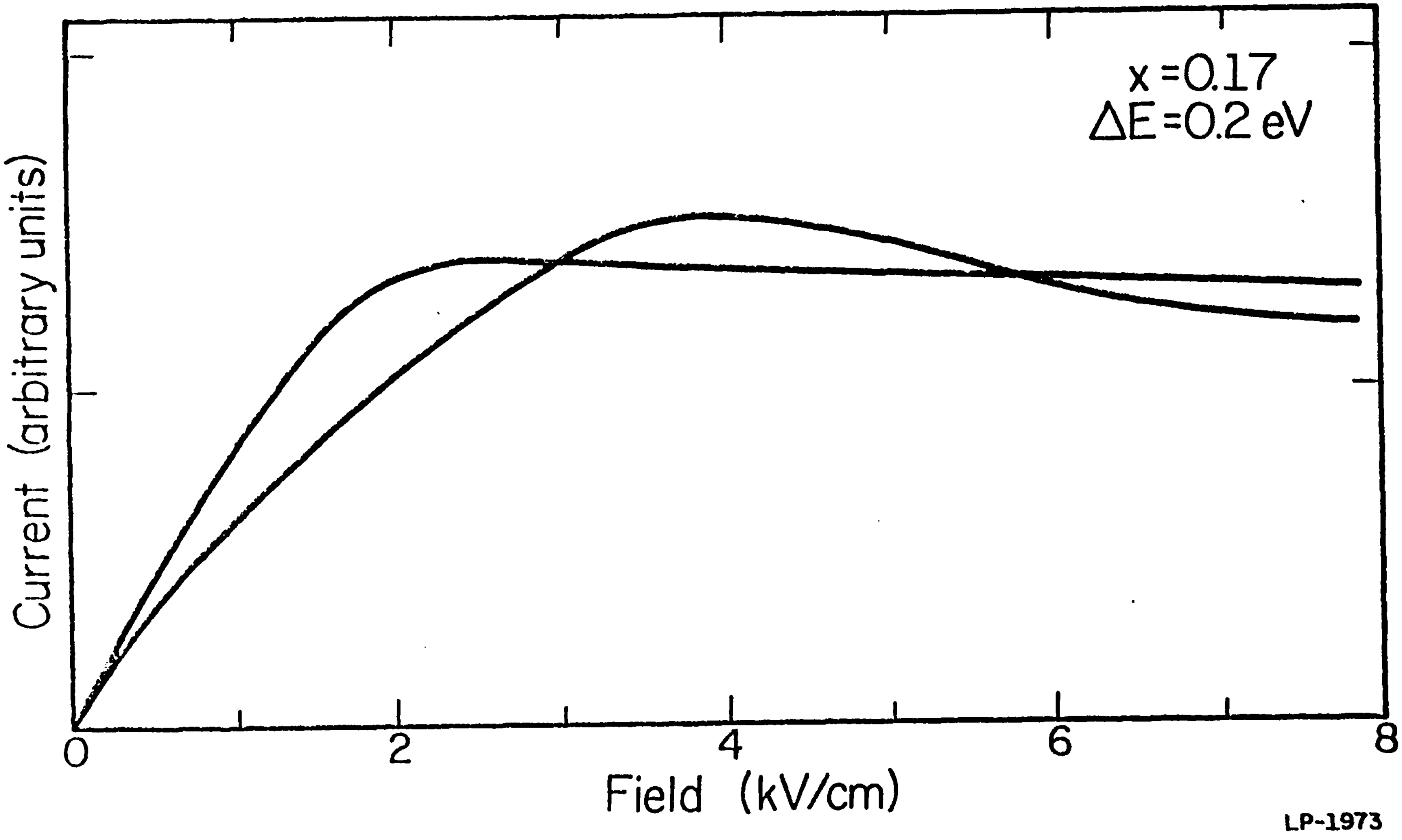

Fig. 5.10: Current-field characteristics measured at 300 K from two typical heterostructures that exhibited real-space transfer effects. These curves are representative of data obtained from many MBE and MOCVD wafers and device geometries.

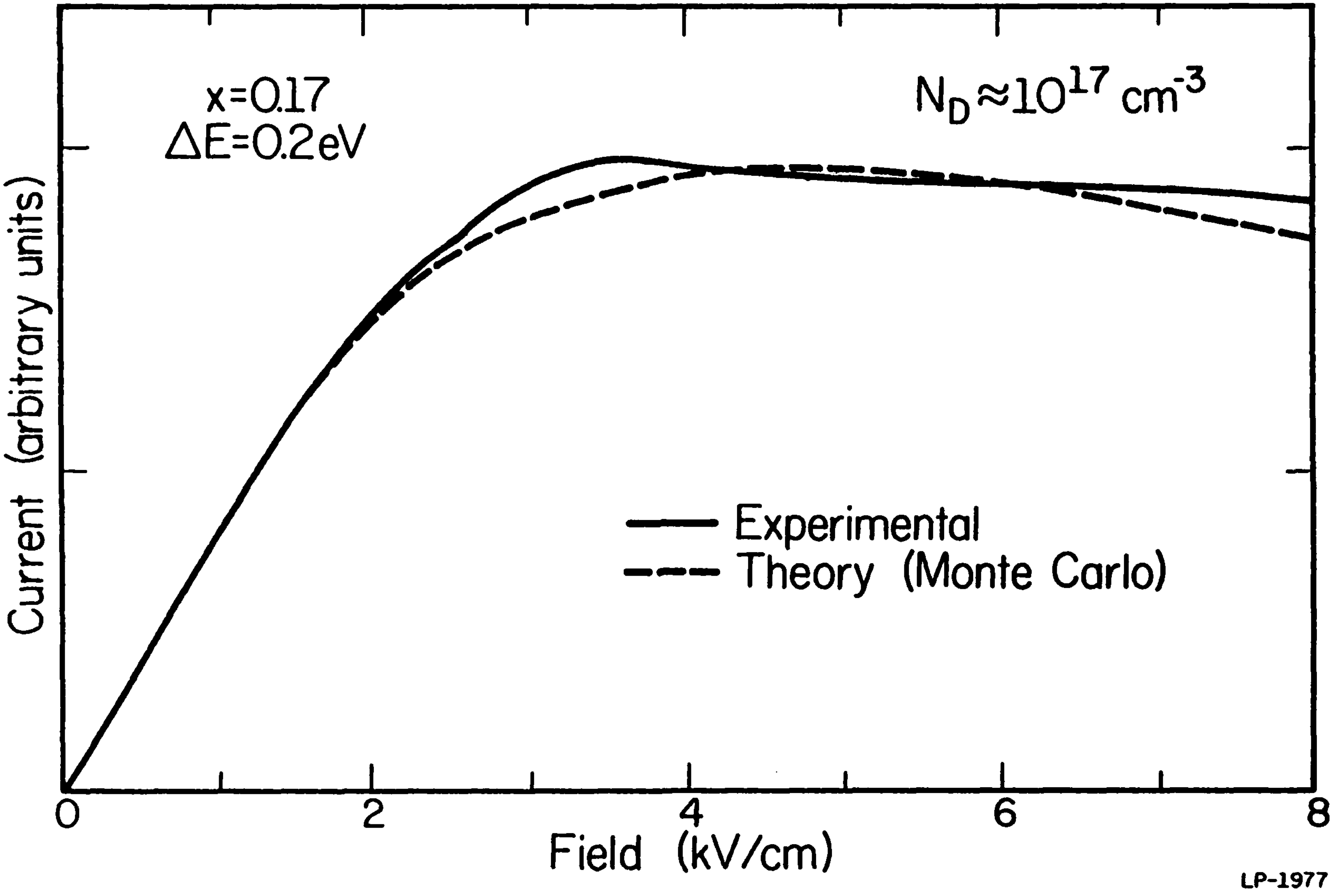

Fig. 5.11: Current-field characteristics at 300 K exhibiting close agreement between theoretical and experimental results. The concentration of donors in the AlGaAs was $N_D \approx 10^{17}$ cm^{-3} in both instances.

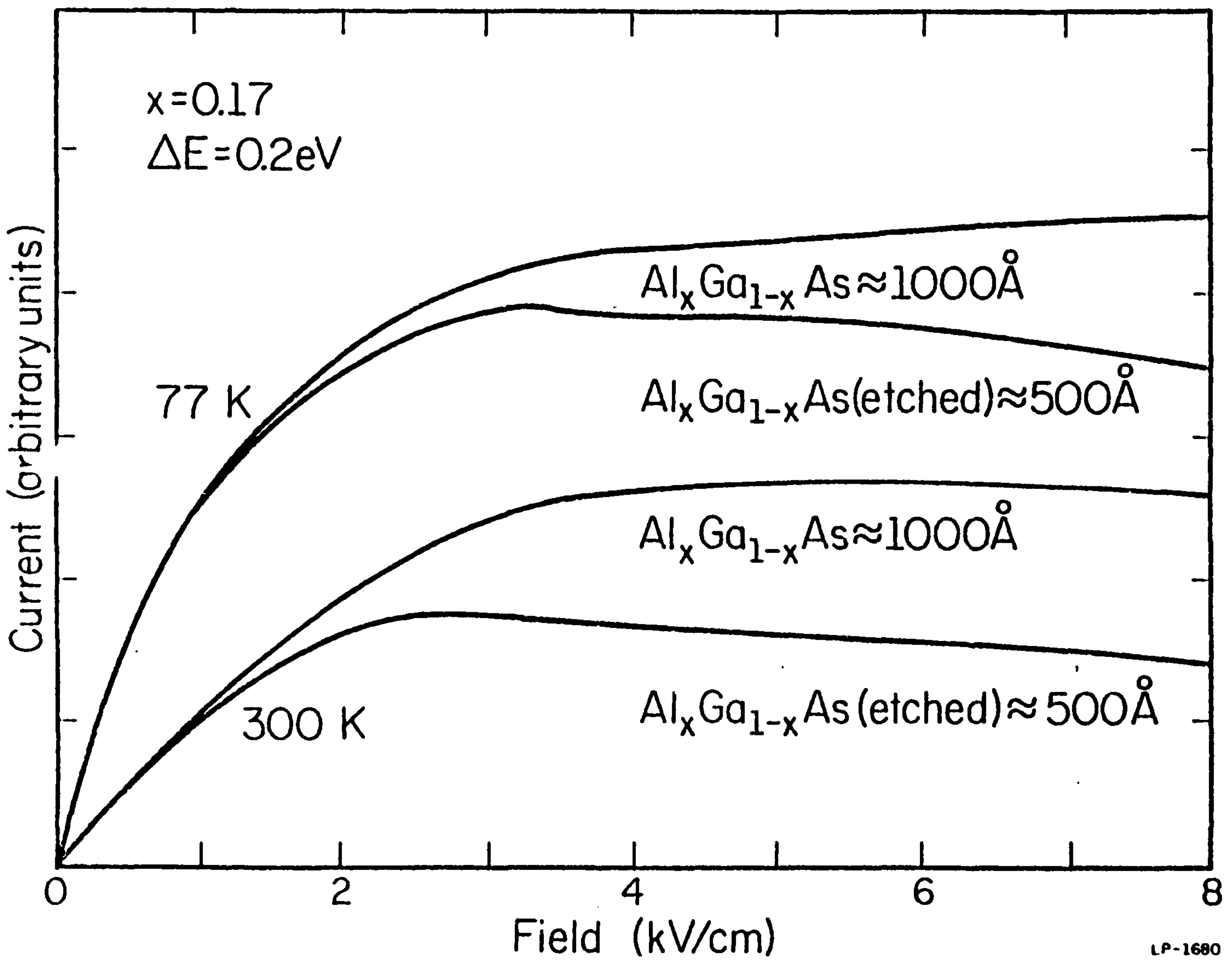

Fig. 5.12: Current-field characteristics showing the occurrence of negative differential resistance at 300 K and 77 K when the Al$_x$Ga$_{1-x}$As layer thickness was reduced from 1000 Å to 500 Å.

It is seen in Fig. 5.12 that after etching away half of the top AlGaAs layer the current-field characteristics exhibited an enhanced negative differential resistance at both 77 K and 300 K. This indicates that the etching has caused a more thorough depletion of the AlGaAs at low fields which causes a greater reduction in current when real-space transfer occurs. This experiment provides a very strong argument for the existence of electron transfer into the AlGaAs at high fields. If the NDR effects were due to something like k-space transfer in the GaAs, the etching of the AlGaAs would not have been expected to cause the observed changes.

One should also observe in Fig. 5.12 that decreasing the sample temperature from 300 K to 77 K caused a very large increase in the low-field conductivity as is expected with modulation-doped structures. In addition, it is seen that the 77 K curve after etching also exhibits a larger negative differential resistance than the corresponding 300 K curve. This effect is expected for the real-space transfer mechanism since the AlGaAs mobility changes little with temperature while the GaAs mobility increases significantly for lower temperatures. Therefore lowering the temperature causes the difference between the GaAs and AlGaAs mobilities to increase and enhances the NDR due to real-space transfer.

The etching experiment discussed above, which was performed on a number of wafers, also gave another indication of the doping values by using the known depletion width obtained from the calibrated etching rate [28].

Generally, the variety of changes in the current-field characteristics which were observed in samples with different doping make it appear that real-space transfer effects occur in these structures and that the negative differential resistances and current saturations observed are not merely caused by the Gunn effect in the GaAs layer. Although it is difficult to exactly determine the threshold field for the onset of the NDR due to contact effects, it was seen from the many samples tested that in general, the samples with higher x (higher potential barriers) also tended to have a higher NDR threshold field if other wafer parameters were similar. This supports the real-space transfer concept since the threshold field for NDR due to k-space transfer should not be so dependent on the value of x in the $Al_xGa_{1-x}As$ layers.

In the current-field measurements described above, inhomogeneities in the electric field can mask the true microscopic characteristics in the field range of the negative differential resistance. This effect is difficult to evaluate because the continuum approximation for the impurity charge and the band bending is not very good (the impurity spacing is of the order of the layer width). It was mentioned previously that the characteristics of the current-field measurements depend sensitively on whether or not the AlGaAs layers are entirely depleted of free charge carriers. This is shown again unmistakenly in Fig. 5.13 as described below.

The current-field characteristics of MBE-grown samples from two different three-period wafers were measured at temperatures of 77 K and 300 K. The two wafers had identically grown structures except that one wafer had the AlGaAs layers moderately doped ($N_D \approx 7 \times 10^{16}$ cm^{-3}) whereas the other was highly doped ($N_D > 1 \times 10^{17}$ cm^{-3}). It is seen in Fig. 5.13 that the current of the moderately-doped sample (dashed lines) tended to saturate around E = 2 kV/cm. The current of the highly-doped sample (solid lines), however, rose steeply throughout the measured field range with only a region of inflection at higher fields to indicate the presence of real-

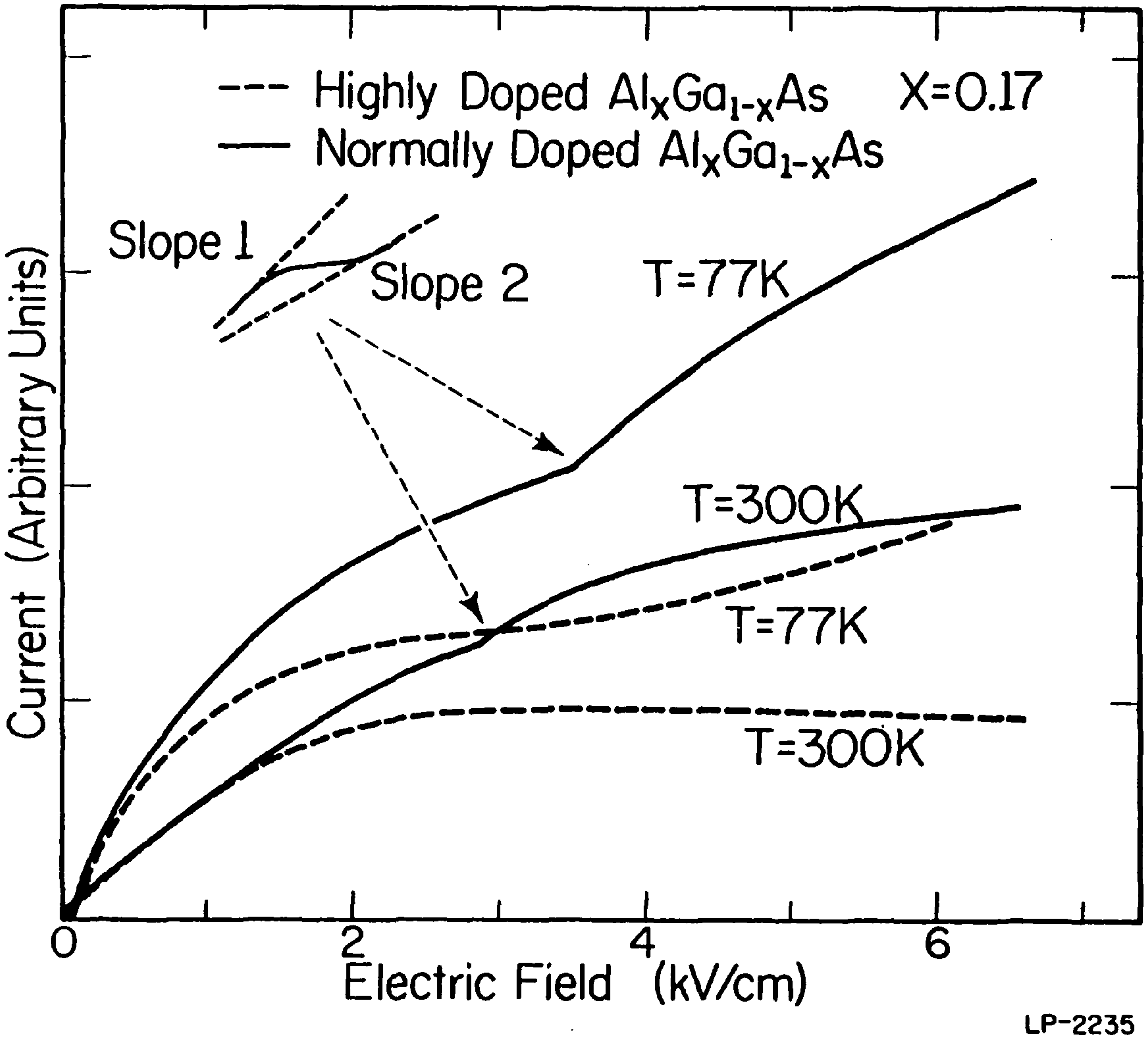

Fig. 5.13: Current-field characteristics of two similar samples at 77 K and 300 K. When the AlGaAs layer is not depleted at low fields (solid lines) the current does not saturate or decrease at higher fields.

space transfer. The solid curves indicate the current-field schematic that can occur when the AlGaAs as well as the GaAs layers are significantly populated with carriers at low fields. This implies that by examining the I-E curves, one can determine if electrons populate the AlGaAs in addition to the GaAs layers. The ratio of slopes near the inflection (as shown in the inset of Fig. 5.13) is given by [42]:

$$\frac{m_1}{m_2} \equiv \frac{\text{Slope 1}}{\text{Slope 2}} = \frac{n_{GaAs}\mu_{GaAs} + n_{AlGaAs}\mu_{AlGaAs}}{(n_{GaAs} + n_{AlGaAs})\,\mu_{AlGaAs}} \quad . \tag{5.4}$$

In all of the samples measured during the course of this research we have never observed Gunn-type oscillations. The reason for this is not entirely understood, but it may be due to the lack of a local microscopic NDR in the heterostructure at the electric fields at which real-space transfer effects occur. Accumulation (and therefore dipole) domains cannot be formed because accumulating electrons would be emitted out of the GaAs. In addition, there is no local microscopic NDR in the AlGaAs at the electric fields considered. The total lack of any kind of instability, however, does not follow from these arguments. The lack of instability may instead [67] be connected with fixed interface inhomogeneities at which the electrons spill out first and with the fact that the layers are very thin (Gunn instability is sensitive to the dimensionality).

The experimental verification of real-space transfer, as discussed in this section, will have a profound influence on all devices using high-field lateral electron transport in GaAs-AlGaAs heterostructures. Consider, for instance, the heterostructure MESFET-type device and MISFET-type device sketched in Figs. 5.14 and 5.15, respectively. In Fig. 5.14, a Schottky barrier is formed by depositing Al on the doped AlGaAs surface to create the

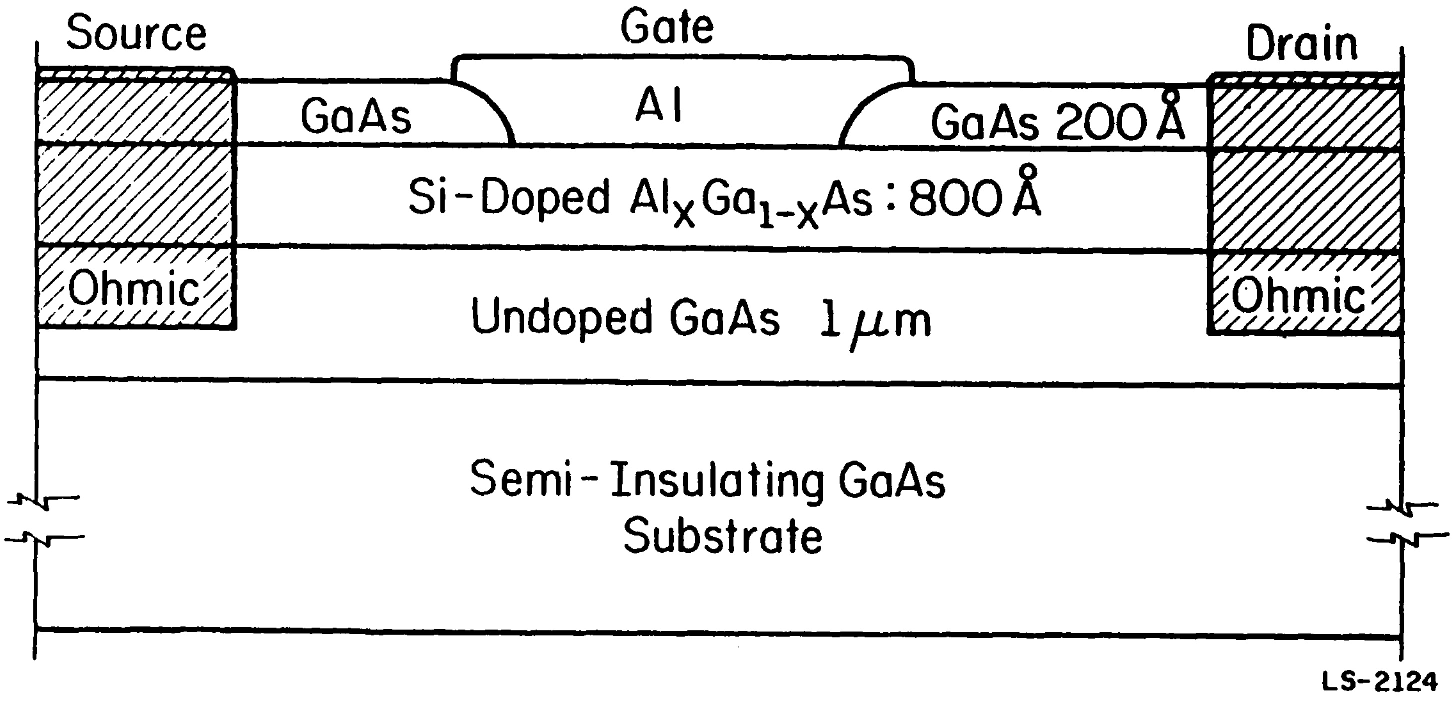

Fig. 5.14: Sketch of $Al_xGa_{1-x}As$-GaAs heterostructure FET with a Schottky-barrier gate formed by depositing Al on the doped AlGaAs layer.

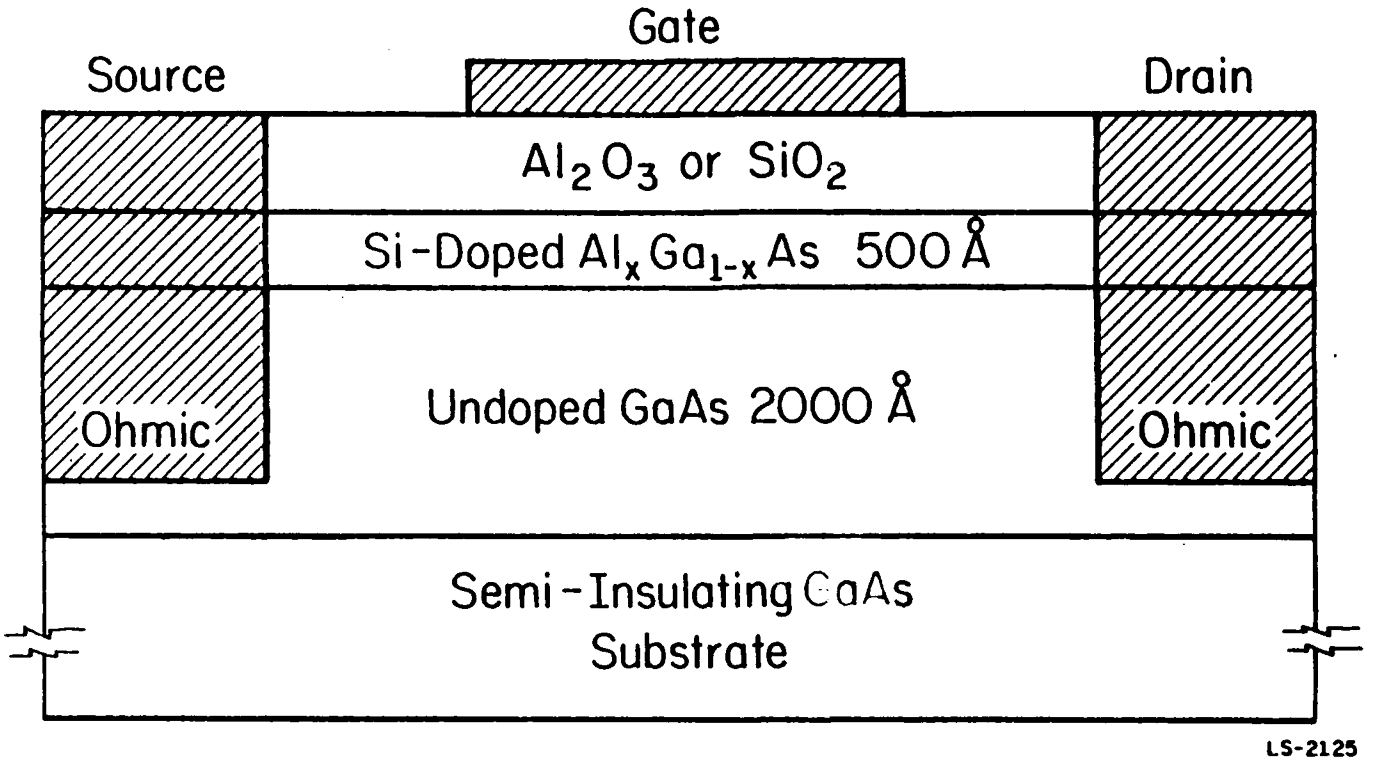

Fig. 5.15: Diagram of $Al_xGa_{1-x}As$-GaAs heterostructure FET with a metal-insulator gate configuration.

gate. In Fig. 5.15, an insulator such as Al_2O_3 or SiO_2 is grown between the gate metal and the doped AlGaAs layer to form a rectifying gate contact. In both structures a high-mobility channel will be formed in the GaAs layer next to the heterojunction. The performance of the FET will depend very sensitively on the conduction through this high-mobility channel. When the electric field between the source and drain contacts becomes sufficiently large (as can occur easily in a small FET) the electrons in the high-mobility channel can be thermionically emitted into the low-mobility AlGaAs layer. A large reduction in device performance would then obviously result due to the occurrence of this real-space transfer effect.

Similar effects have been known to occur in Si-MOSFETs for many years. Ning [118] has shown that in the MOS system, high electric fields can cause electrons to be emitted from the Si into the SiO_2 over large potential barriers of ~ 3 eV. Only a few electrons can overcome such a high barrier at the Si-SiO_2 interface but, nevertheless, this effect is important over extended periods of time for device stability considerations. Electrons emitted into the SiO_2 become trapped there and contribute to the accumulating space charge which causes an unwelcome change in the interface potential leading to instabilities in the MOS device performance. Fig. 5.16 shows the drain current versus drain voltage characteristics measured by Hess [119] for a Si-MOSFET with a high concentration of oxide charges ($Q_o = 6 \times 10^{11}$ e/cm^2) at the interface. Negative differential resistances were seen to occur for temperatures ranging from 4.2 to 240 K. Note that at 10 K a strong hysteresis took place.

Since the above described effects occur in Si-MOSFETs where the electrons must overcome potential barriers as high as 3 eV, similar effects

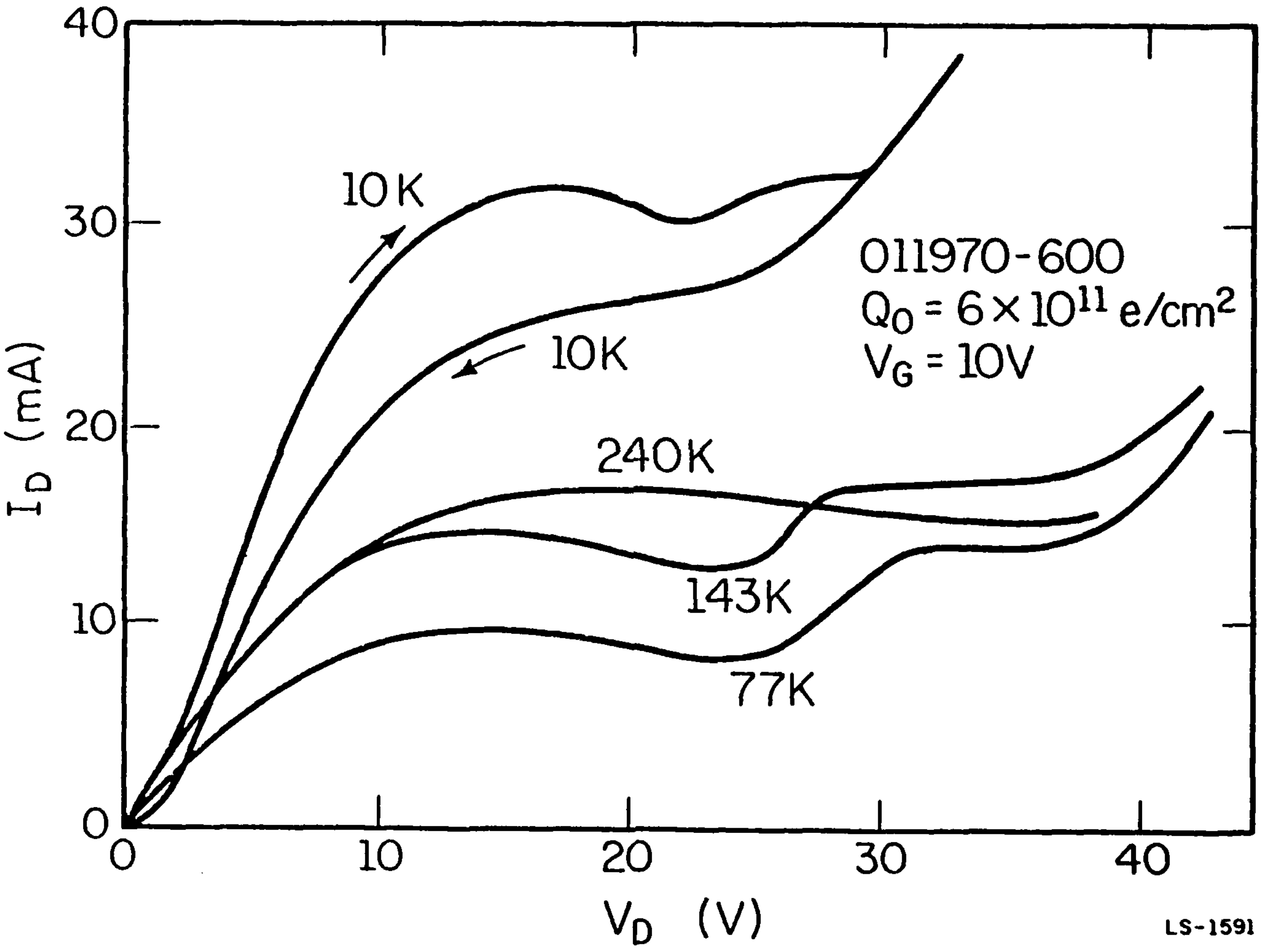

Fig. 5.16: Drain current vs drain voltage characteristics at several temperatures for a Si-MOSFET with a high concentration of oxide charges ($Q_0 = 6 \times 10^{11}$ e/cm^2) at the interface. Note the strong 10 K hysteresis effect [119].

can occur more easily in GaAs-Al$_x$Ga$_{1-x}$As heterostructure FETs where the GaAs-Al$_x$Ga$_{1-x}$As interface potential is less than 0.5 eV. Therefore, real-space transfer effects must be carefully considered when designing transport devices of this type so as to minimize carrier loss from the high-mobility regions.

Real-space transfer effects can also have positive applications in new and innovative devices. Two of these novel device applications (a high frequency oscillator and a fast switching and storage device) which rely totally on the real-space transfer mechanism will be examined in the following two sections.

5.2 Tunable Frequency Oscillation

In the previous section it was demonstrated that a lateral high electric field causes electrons to transfer in real space from a high-mobility GaAs layer to a low-mobility AlGaAs layer. In this section, it is demonstrated that if a dc plus ac electric field is applied parallel to the layered interfaces, a new type of conduction-current oscillator, making use of this real-space transfer of electrons, can be created. The applied fields cause dc and ac heating of the electrons in the low-resistance GaAs layers, moving the carriers between the GaAs layers and high-resistance AlGaAs layers. This results in the ac current being 180° out of phase with the ac voltage and causes power generation. Measurements of the oscillation behavior of normally-fabricated samples with two ohmic contacts were done in collaboration with Coleman [30] and are described below.

The three-period GaAs/nAl$_x$Ga$_{1-x}$As heterostructure used in the experiments is shown in Fig. 5.17. This structure had a 150 Å undoped

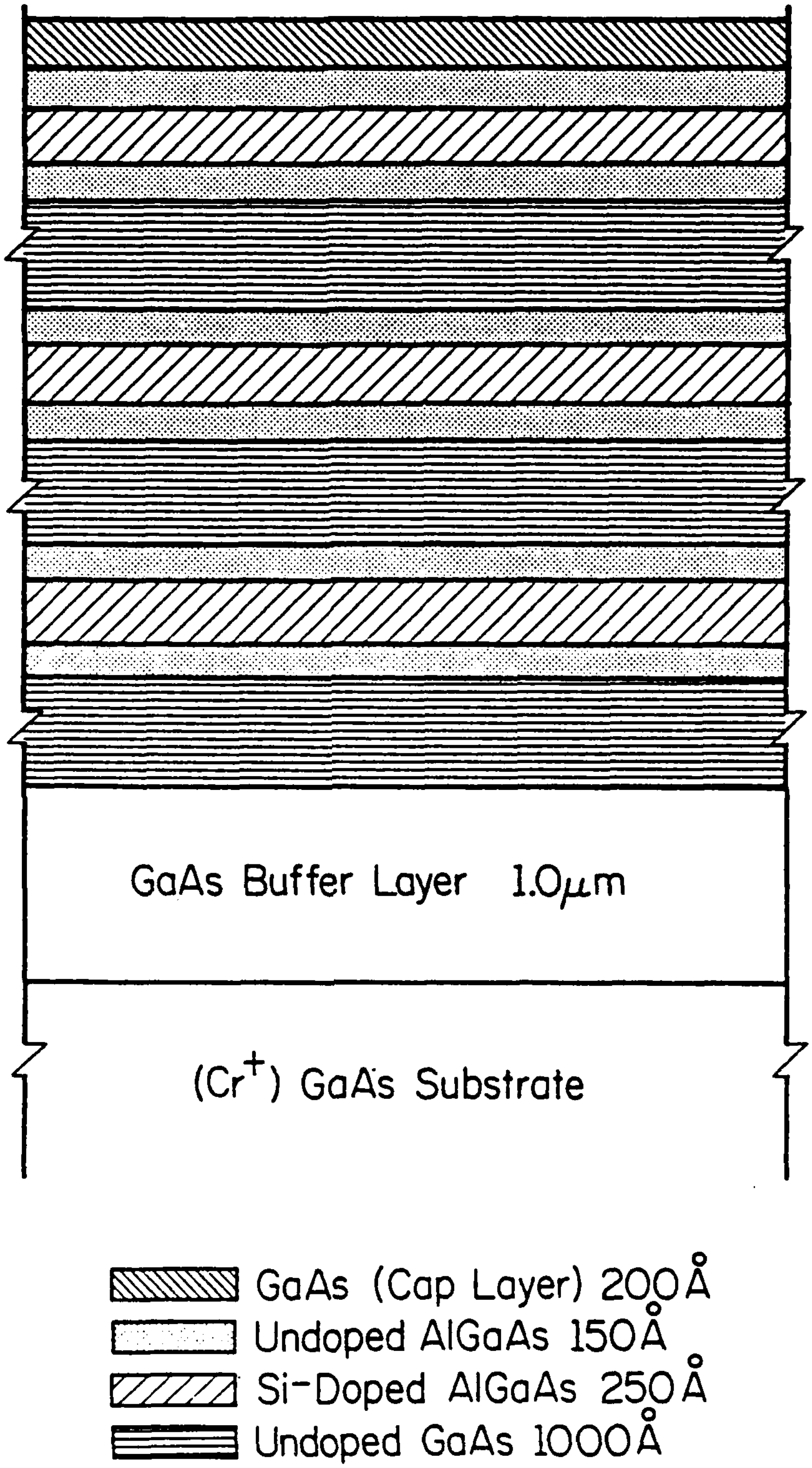

LP-2226

Fig. 5.17: Schematic representation of the three-period heterostructure used in the fabrication of a tunable frequency real-space transfer oscillator. The AlAs mole fraction was $x = 0.20$.

$Al_xGa_{1-x}As$ spacer layer to further enhance the mobility in the GaAs, but it is believed that this is not necessary for the oscillator application. The oscillator work reported here is in its initial phase with an optimum heterostructure design as yet to be determined.

The oscillator principle demonstrated in this section is believed to be due to real-space electron transfer and not a Gunn effect. Here the frequency of oscillation did not depend upon the transit time (i.e., separation distance) between ohmic contacts and no domain formation phenomena was observed.

A tunnel diode rf circuit, shown in Fig. 5.18, was used to study the oscillator behavior in the 2 - 25 MHz range. This frequency range was chosen to facilitate the oscilloscope measurements. The heterostructure was mounted in a TO-18 transistor header which was placed in liquid nitrogen. Pulse voltages in the 1 - 5 μsec range at low repetition rates of 60 - 100 Hz were employed to avoid heating the device appreciably. The heterostructure sample dimensions were 1 mm in width with a 50 μm spacing between the ohmic contacts. Normal pulsed-voltage methods were used to measure an I-E curve of the three-period sample as shown in Fig. 5.19. It is seen that the 77 K current saturated around 2 kV/cm and displayed a slight negative slope for fields above 2 kV/cm.

Measurements were made of the oscillator behavior using an oscilloscope when the LC circuit was tuned to 2 MHz and 25 MHz. It was observed that as the pulsed bias voltage was increased, one first saw a small highly damped ringing of the LC circuit at the start of the oscilloscope trace. Then, as the NDR threshold was approached, the damping decreased, the ringing increased, and steady-state oscillation was achieved with a further increase

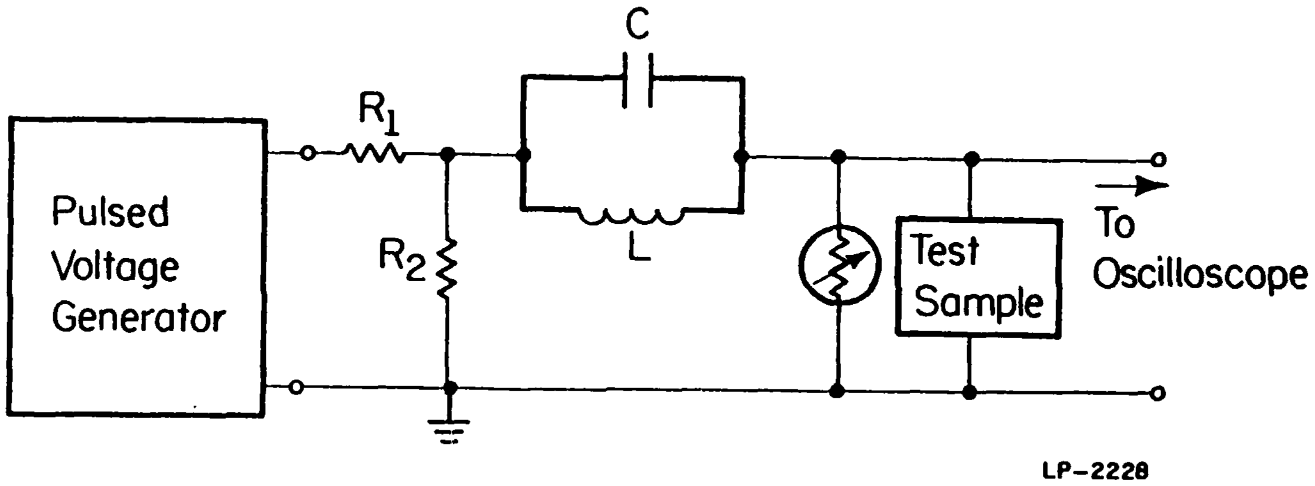

Fig. 5.18: Diagram of the tunable frequency rf tunnel diode circuit used to study the real-space transfer oscillator behavior in the 2 - 25 MHz range. Pulsed voltages in the 1 - 5 μs range at low repetition rates of 60 - 100 Hz were employed to avoid heating the sample [30].

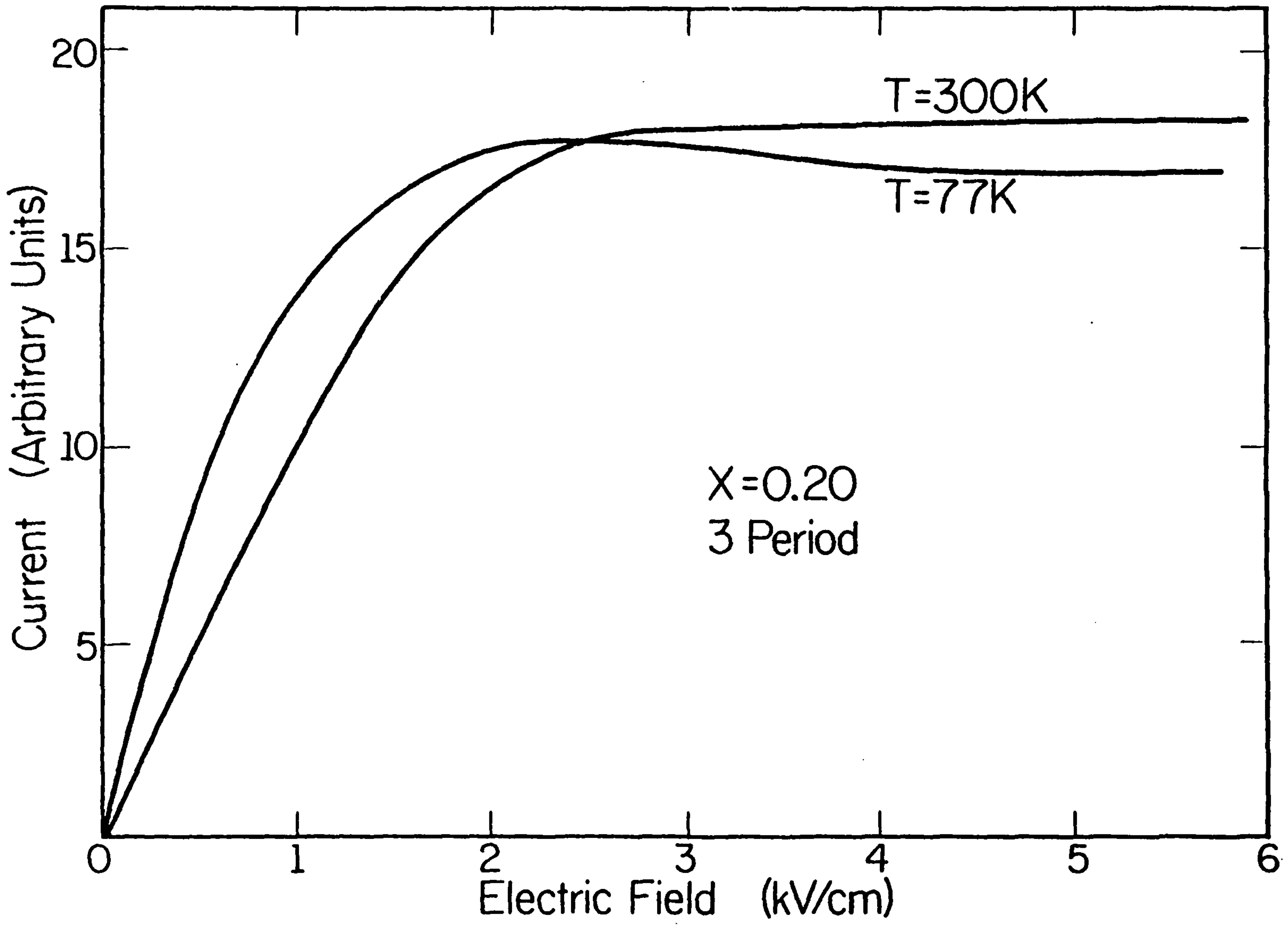

Fig. 5.19: Current-field characteristics at 77 K and 300 K for the three-period structure shown in Fig. 5.17.

in bias. The behavior at 25 MHz is shown in the inset of Fig. 5.20 with the bias field near 2.6 kV/cm and the peak rf voltage near 3 V. The 77 K current-field curve is repeated in Fig. 20 for reference. It was found that increasing the dc bias beyond 2.6 kV/cm did not appreciably increase the peak rf voltages.

The real-space transfer oscillator characteristics described here are different from those of a Gunn oscillator. In a traveling dipole-domain mode ($nl > 2 \times 10^{12}$ cm^{-2}) a Gunn oscillator shows little response to circuit tuning [120]. The real-space oscillator, on the other hand, could be readily tuned in the 2 - 25 MHz range by means of the LC circuit. Increasing the dc voltage of our oscillator above threshold did not significantly increase the power output. For the Gunn oscillator, however, an almost linear dependence of the output with the dc input voltage has been demonstrated. The field threshold for the real-space transfer device reported here was about 2 kV/cm which is less than the 3.4 kV/cm threshold usually associated with a Gunn device. Dipole domain formation in the heterostructure appears to be prevented by the electrons transferring from the GaAs to the AlGaAs layers as has been discussed previously. Since the electrons move from one semiconductor to another, the oscillator does not violate Schockley's theorem which states that a homogeneous semiconductor with a negative differential mobility and a well-behaved cathode contact has a positive differential conductance.

The experiment discussed above, while preliminary in nature, demonstrates a new type of oscillator which uses real-space electron transfer effects and whose frequency can be readily tuned by an external circuit. The frequency limitation of the oscillator appears to be

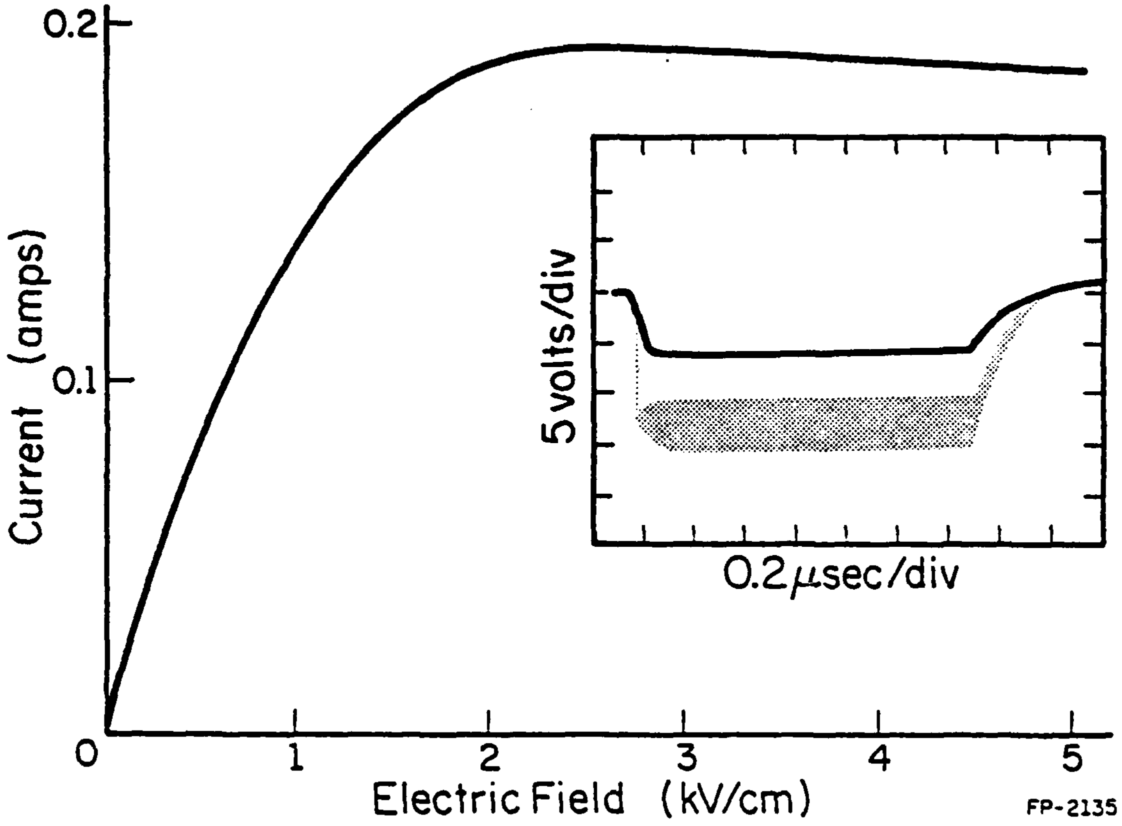

Fig. 5.20: The current-field characteristic at 77 K is repeated from Fig. 5.19 with the addition of the oscillation behavior at 25 MHz shown in the inset. The peak rf voltage is about 3 V.

associated only with the transverse dimensions of the structure. Since the transfer time between layers is predicted to be less than 10^{-11} s for $L_1 = L_2 = 400$ Å (as discussed in Section 5.1.1), it may be possible to extend the frequency of the oscillator high into the GHz range. In addition, since the current flowing through the device can be increased by simply adding more conducting layers to the oscillator, the power output at high frequencies could be made quite large. Very high frequency operation, however, has not yet been attempted.

5.3 Fast Switching and Storage Effects

In this section, experimental results will be described that demonstrate the existence of fast electron switching and storage effects in GaAs-$Al_xGa_{1-x}As$ heterostructures when electric fields are applied separately to different layers.

It has been demonstrated that when a high electric field is applied parallel to the layer interfaces, the high-mobility electrons in the GaAs layers will be heated to energies far above their thermal equilibrium values. When these high-field induced electron energies are comparable to the GaAs-$Al_xGa_{1-x}As$ conduction-band discontinuity ΔE_c, the electrons can propagate into the adjacent $Al_xGa_{1-x}As$ layers. Suppose, however, there are also nearby GaAs layers containing no applied electric field. The electrons scattered into an $Al_xGa_{1-x}As$ layer from a high-field GaAs layer on one side may then enter the low-field GaAs layer on the other side. The energetic electrons entering the low-field GaAs region can lose energy through phonon emission and as a result, they become trapped in this GaAs layer if the temperature is not high enough for them to escape by thermal emission. Fig. 5.21 depicts this transfer of electrons from a GaAs layer, with an

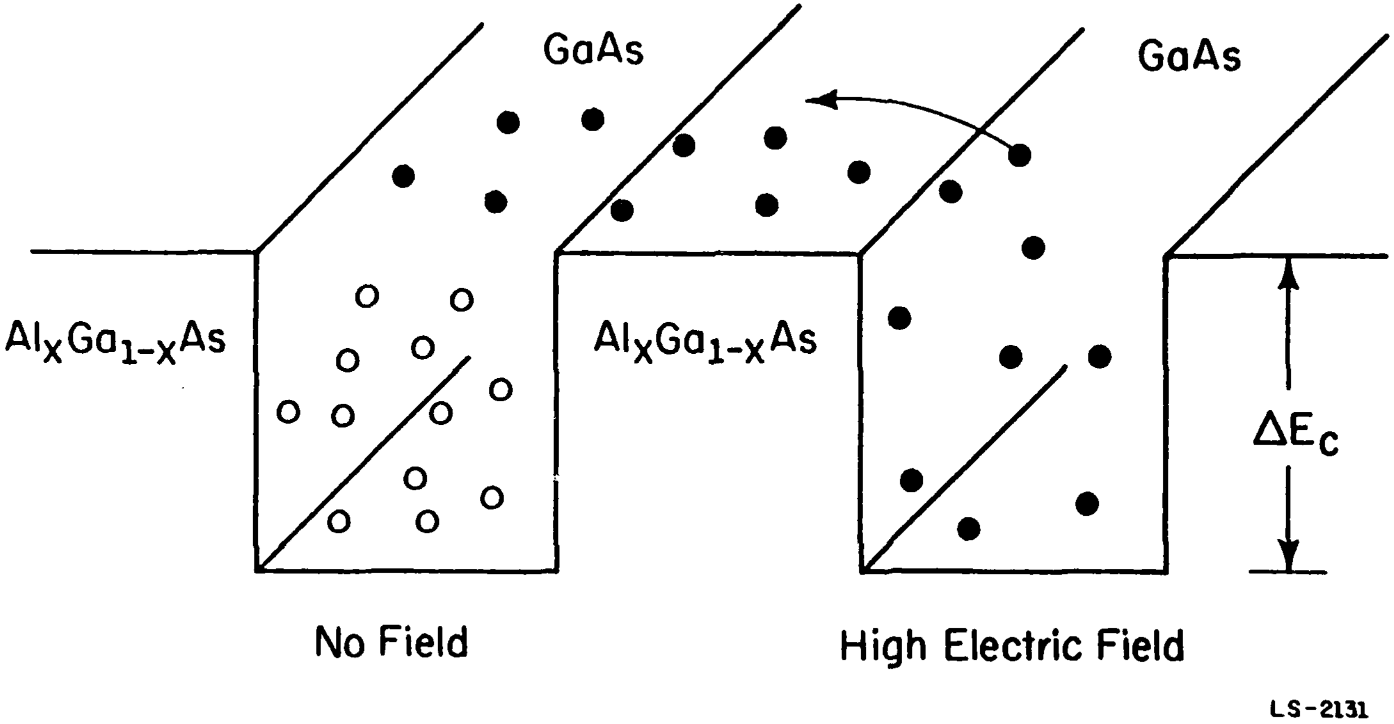

Fig. 5.21: Hot electrons (closed circles) propagate from a GaAs layer with an applied electric field through the intermediate $Al_xGa_{1-x}As$ layer to a GaAs layer with no applied field. The electrons then lose energy (through phonon emission) and become trapped in the "cold" GaAs layer (open circles).

applied high electric field, through the adjacent $Al_xGa_{1-x}As$ layer to the neighboring GaAs layer where the electrons lose energy and become trapped. The high energy (hot) electrons are represented by closed circles whereas the open circles represent the electrons that have lost energy and can no longer escape from the GaAs well. Thus it is predicted that the application of an electric field only in selected GaAs layers should allow one to intentionally control the switching and storage of groups of electrons in the heterostructure.

To calculate the switching time, one can use the well known principles of thermionic emission. The transfer time out of the GaAs can be expressed by [117]

$$t_s \approx \frac{eN_c L m_o}{A^* T_c^2 m^*} \exp\left(\frac{\Delta E_c}{kT_c}\right) \qquad (5.5)$$

where A^* is the Richardson constant (120 A/cm^2K^2), m^* is the effective mass in the GaAs, m_o is the free electron mass, N_c is the effective density of states the GaAs, ΔE_c is the barrier height (conduction-band discontinuity), and T_c is the actual temperature of the carriers. Assuming the applied electric field is such that $kT_c = \Delta E_c = 0.20$ eV in a GaAs layer of width L = 500 Å, one obtains $t_s \approx 2.5 \times 10^{-14}$ sec. However, the time required for heating of the electrons is about 5×10^{-12} sec. The electrons that propagate toward the zero-field GaAs layer will transverse a thin $Al_xGa_{1-x}As$ layer (L $\cong$ 500 Å) in less than 10^{-12} s so the switching time of this structure is determined by the heating time of the electrons, namely $\sim 5 \times 10^{-12}$ sec.

The storage time of electrons that reach the cold (no applied field) GaAs layer can also be expressed by the thermionic-emission equation above.

When there is no electric field the electron temperature will be equal to the lattice temperature of the sample. Thus the electron storage times in the cold layer (using Eq. (5.5)) become $t_s \approx 10^{-9}$ s at T = 300 K, $t_s \approx 100$ s at T = 77 K, and $t_s \approx$ years at T = 10 K for the same barrier height of $\Delta E_c = 0.20$ eV. These times make the storage effect rather attractive for high-speed, low-power, low-temperature applications. Notice that the band-edge discontinuity enters exponentially into the equation for t_s. It is therefore conceivable that for high x and high ΔE_c reasonably long storage times can even be achieved at room temperature (e.g., x = 1, $\Delta E_c = 1.06$ eV, and $t_s \approx 3.3 \times 10^5$ s $\approx$ days).

Sample configurations of the type sketched in Fig. 5.22 were used to test for switching and storage effects. These devices were fabricated from GaAs-$Al_xGa_{1-x}As$ heterostructures grown by metal organic chemical vapor deposition (MOCVD) or molecular beam epitaxy (MBE). The results to be reported here were measured from a MOCVD sample consisting of nine alternate pairs (periods) of $Al_xGa_{1-x}As$ and GaAs layers, each 500 Å thick. The AlAs mole fraction in the $Al_xGa_{1-x}As$ was 0.21 so that $\Delta E_c \approx 0.22$ eV. Hall measurements on independently grown layers under similar conditions were used to determine carrier concentrations and mobilities. The $Al_xGa_{1-x}As$ layers were doped with Se to achieve $n \sim 1 \times 10^{17}$ cm^{-3} with a mobility of $\mu_n \sim 80$ cm^2/Vs. The GaAs layers had an unintentional doping of $n \sim 2 \times 10^{15}$ cm^{-3} with a room temperature mobility of $\mu_n \sim 6000$ cm^2/Vs.

The test structure (Fig. 5.22) was fabricated using standard photolithographic and chemical etching techniques. Four ohmic contacts were formed by vacuum evaporation of AuGeNi and subsequent alloying at 450°C for 10 s in flowing H_2. The resulting structure had a dumbbell shaped center

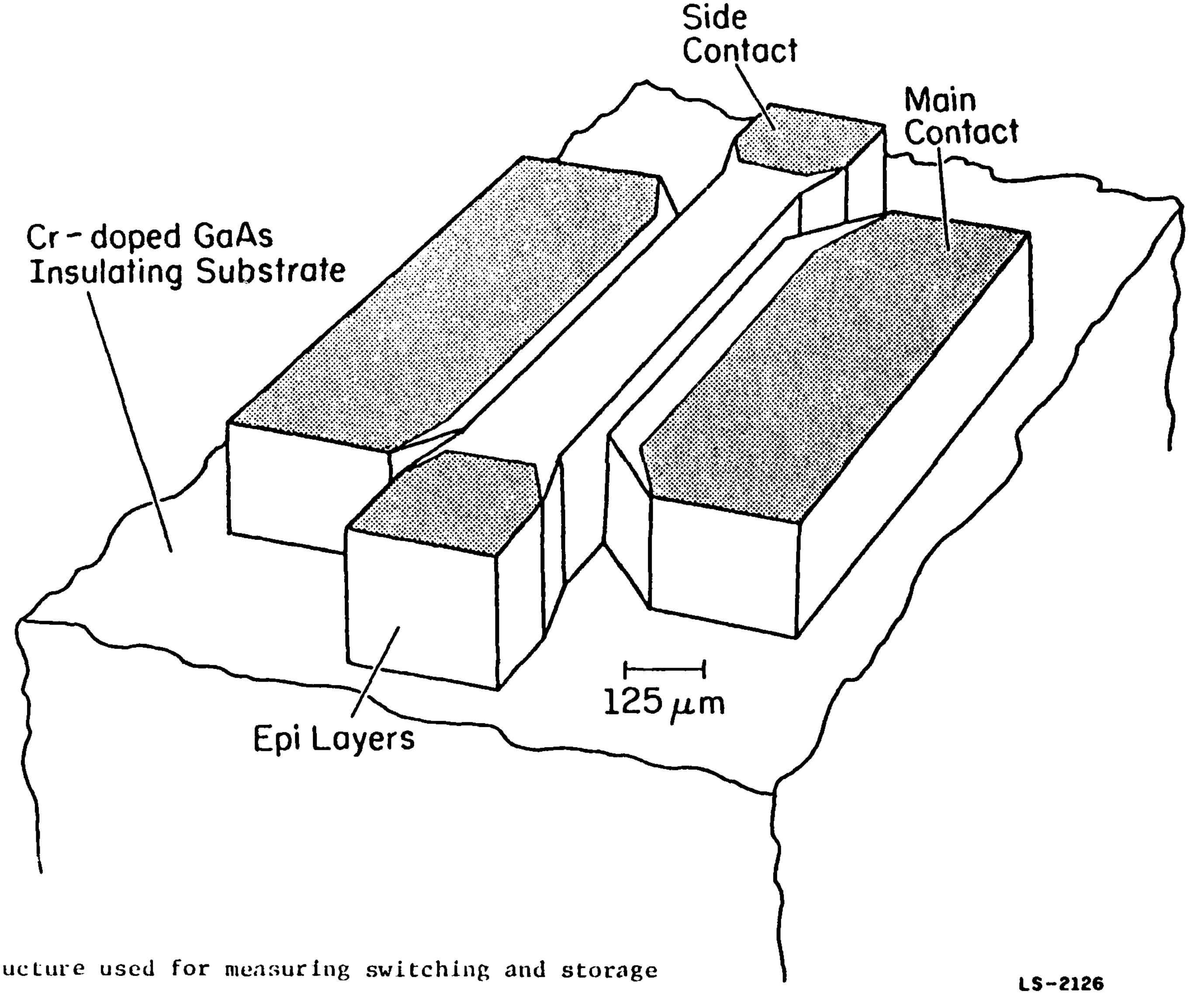

Fig. 5.22:
Device structure used for measuring switching and storage effects in the heterostructure. When a high electric field is applied only between the main contacts, hot electrons can propagate from the bottom high field layers to the upper electrically isolated layers in the bridge connecting the side contacts.

region containing all nine heterostructure periods contacted at each end by an ohmic contact (labelled side contact in Fig. 5.22) that was diffused down through the top two or three periods. The diffusion depths of the contact constituents after alloying were measured in similarly prepared samples using secondary ion mass spectrometry (SIMS) and a calibrated Sloan Dektak stylus instrument as described in Chapter 3. The areas containing the main contacts (see Fig. 5.22) were etched down so that the top three GaAs-$Al_xGa_{1-x}As$ layer pairs were removed leaving only the lower six period contacted by the alloyed main contacts.

If the voltages are applied only to the main contacts (no applied voltage on side contacts) then only the GaAs layers in the bottom six periods will have high electric fields. Some of the electrons that escape from the GaAs layers under high-field conditions in these bottom periods can propagate into the upper electrically isolated layers nearer the surface in the dumbbell bridge. If the sample is cooled to cryogenic temperatures, the electrons that lose energy in these top isolated layers will become trapped in the GaAs regions and will not be able to gain enough energy from the crystal lattice or fringing low electric fields to escape by thermionic emission. Thus, as soon as the electric field between the main contacts becomes high enough to cause electrons to be emitted from the lower GaAs layers, a fraction of these electrons can propagate to the upper isolated GaAs layers where they are trapped. The resulting current between the main contacts will then be reduced for all following measurements of the current at lower fields.

Suppose a voltage is then applied only to the side contacts so that the resulting electric field in the dumbbell bridge region is high enough to allow thermionic emission of the electrons in the upper GaAs layers above the main contacts. The initially higher concentration of electrons stored in the top three periods will then be redistributed to the lower layers, thus returning the carrier concentration in the region between the main contacts to values near those existing before any voltages were applied. The current between the main contacts at low fields will then also return to values very near or perhaps even slightly above the original values.

The results of current-field measurements between the main contacts on a sample cooled to 77 K are shown in Fig. 5.23. Measurements were performed using 700 ns voltage pulses at low repetition rates to reduce sample heating. Measurements of the current vs. field shown in the graphs were taken at 600 ns after the beginning of each pulse although no time dependence was observed in the pulses between 10 and 700 ns. A slight ringing during approximately the first 10 ns of the current pulse (due to small impedance mismatch reflections) prevented a precise measurement of the transfer time. The sample was mounted on a temperature-controlled cold finger in an evacuated sample chamber and standard 50-Ω sampling oscilloscope and x-y recorder techniques were used. All measurements were performed with the sample in the dark. The upper solid line in Fig. 5.23 shows the virgin current-field characteristics between the main contacts when the first voltage was initially applied to the main contacts (no voltage between side contacts). After the electric field exceeded a threshold value necessary to cause a real-space transfer of electrons, the voltage was returned smoothly to zero resulting in the lower solid curve. The exact value of the threshold field was difficult to determine since it can be influenced by the contact potential drops. The significantly lower

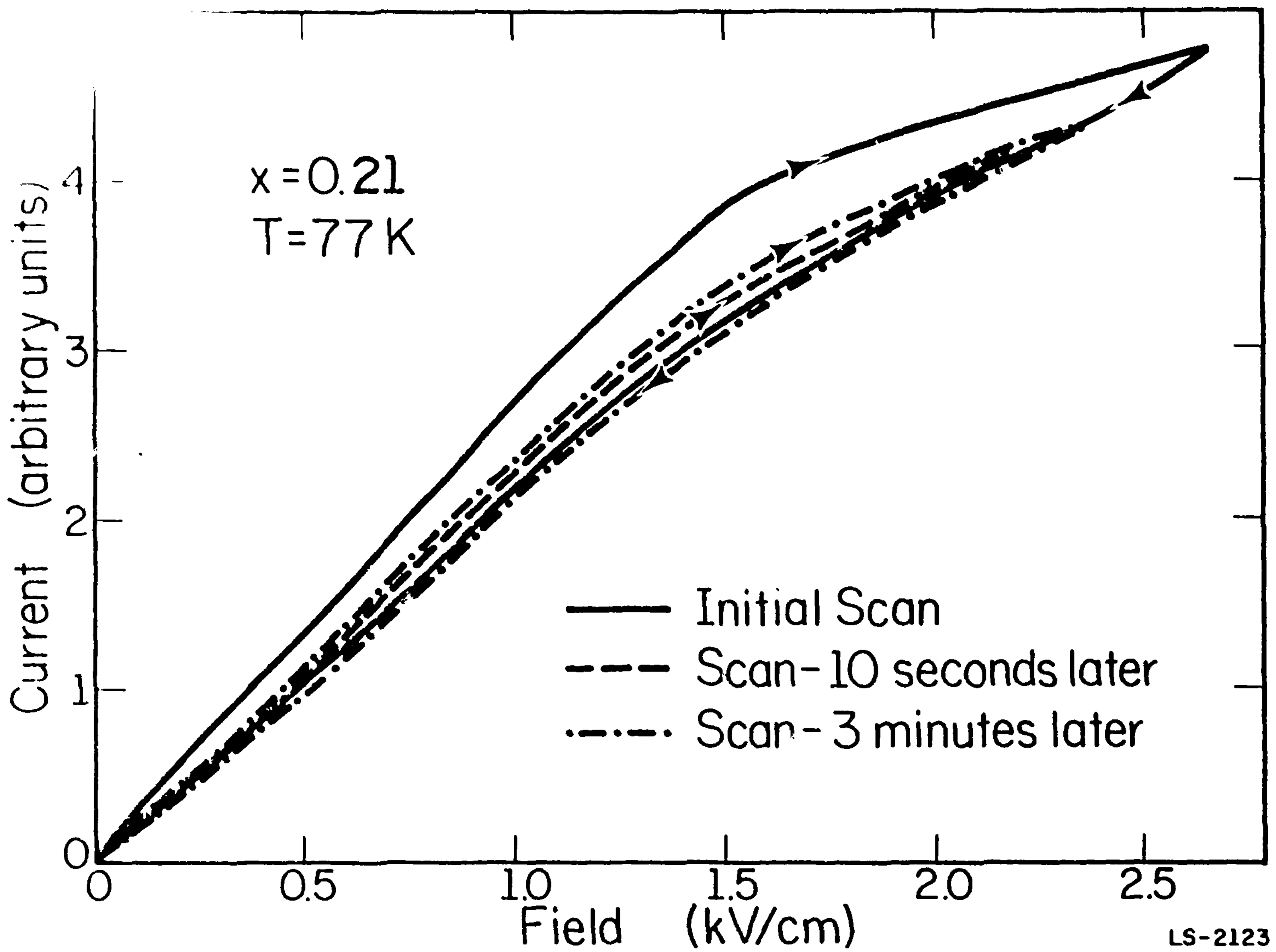

Fig. 5.23: Current-field characteristics measured between the main contacts at 77 K. Current reduction following the initial (virgin) voltage scan is due to electron switching and storage. Applying a voltage to the side contacts restores virgin conditions.

current values measured as the voltage was returned to zero indicates that a fraction of the electrons have been transferred and stored and can no longer contribute to the current. Repeating the same voltage scan several seconds later (dashed curve in Fig. 5.23) revealed only a slight change in the reduced current. The dashed curve coincided with the lower solid curve during the decreasing portion of the voltage scan. Another scan of the voltage several minutes later (dot-dashed curve) exhibited only a small further increase in the reduced current, indicating the number of stored electrons has changed very little. Immediately thereafter, a high field was applied between the side contacts (no applied voltage on main contacts) to redistribute the stored electrons. A following voltage scan between the main contacts nearly resulted in a retracing of the initial virgin solid-line current-field curve.

The same sequence of current-field measurements were repeated with the sample at a temperature of 10 K (Fig. 5.24). The first increase and decrease of voltage between the main contacts resulted in a current reduction (solid curve) that was larger than that seen at 77 K. Repeating the voltage scan several minutes later (dot-dashed line) again exhibited only a small change in the reduced current between the main contacts. After applying a high field through the upper three periods using the side contacts, the current-field characteristics between the main contacts returned to nearly their original values. The above pattern of voltage applications was repeated several times with the same results.

Measurements of the main contact current-field characteristics at room temperature, however, exhibited no evidence of current reduction (electron storage) on the time scales of our measurements.

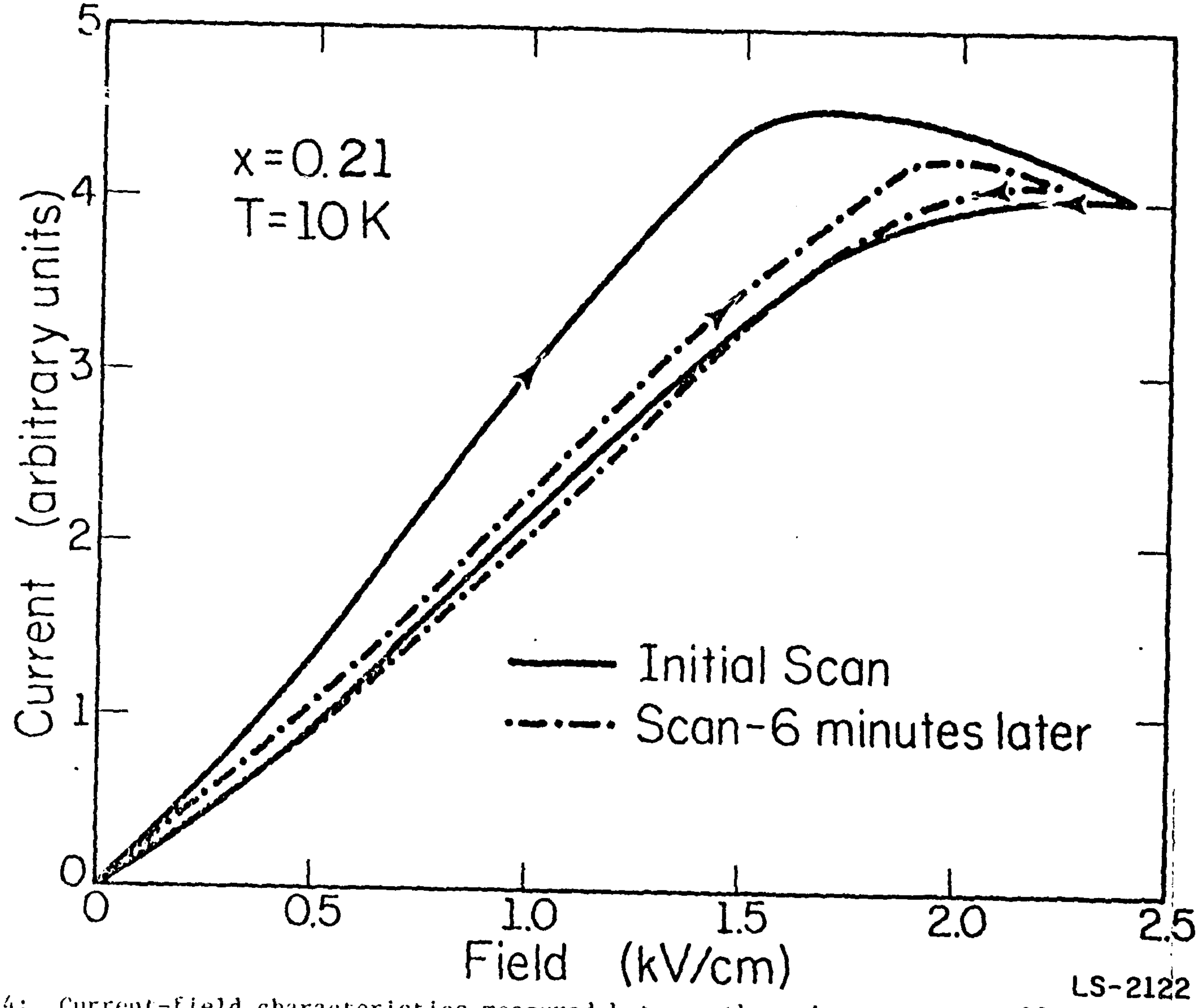

Fig. 5.24: Current-field characteristics measured between the main contacts at 10 K. The prolonged reduction in current following the initial voltage scan is due to the switching and storage of electrons. The initial scan (virgin) characteristics are restored by applying a high field between the side contacts.

The results reported above seem to verify that the storage effects outlined at the beginning of this section do indeed occur. It is evident that electrons may be switched very quickly to preselected regions of the heterostructure at will (using selected pairs of ohmic contacts) and that the length of time the electrons remain stored depends upon temperature in the manner expected. The switching time of the electrons between layers could not be determined with the present experimental arrangement, but the effect was seen to occur in much less than 10 ns.

The sample preparation and contact diffusion were aimed at an electrical separation of the two sets of layers. However, the degree of separation under high-field conditions (short pulses) is hard to determine. One therefore cannot entirely rule out the participation of interface and surface trapping in these heterostructures. It is unlikely, however, that the trapping of electrons in surface states would be totally responsible for the observed storage phenomena reported here. One would not expect the alternate electric field applications of nearly equal strengths through the two sets of contacts to cause repeated trapping and emission of carriers from these states in such a manner as to result in the reproducible storage effects described above.

In addition, surface depletion effects probably hampered the spreading of electrons to the surface and may have decreased the space available for electron storage in the layers close to the surface. Any trapping of electrons in surface states which does occur under high field conditions, serves to reinforce the concept of real-space transfer of hot electrons from the high mobility GaAs (to the surface in this case) when an electric field of sufficient strength is applied parallel to the layers.

The experiments reported in this section have experimentally demonstrated the use of real-space electron transfer to obtain electron switching and storage effects in GaAs-Al$_x$Ga$_{1-x}$As heterostructure devices. electric fields were selectively applied to separately contacted layers to induce the transfer of electrons from one set of GaAs layers to another nearby set of "cold" (no applied field) GaAs layers. The switching effects were shown to be reversible and repeatable, and the storage times of the electrons in the cold layers were shown to be dependent on temperature. Switching times were proven to be much less than 10 ns and are predicted to be about 10^{-11} sec.

5.4 Photoconductive Effects

The results presented in the above sections were obtained from measurements performed with the heterostructure samples in the dark. It was found, however, that some of the wafers displayed significant light-sensitive effects such as enhanced conduction when illuminated with various sources of light including room light. In most samples, this photoconductivity was significant only as long as the light source was present and was directly related to the intensity of the light. In samples from a few special wafers, however, the enhanced conductivity was found to persist long after the source of light was removed. The normal and persistent photoconductive effects found in our GaAs-Al$_x$Ga$_{1-x}$As samples will be discussed in the following two subsections.

5.4.1 Normal Photoconductive Effects

All semiconductors exhibit some increase in conductivity when irradiated with light of sufficiently high energy ($h\nu > E_G$). This is a consequence of the generation of electron-hole pairs as well as the ionization of impurity and defect levels located within the band gap. In the case of GaAs-$Al_xGa_{1-x}As$ heterostructures the absorption of optical energy can also empty traps in the AlGaAs and provide the electrons with sufficient energy to overcome the interfacial barrier and spill into the GaAs layer. A conductivity increase will then result due to these additional free electrons residing in the 2DEG.

Fig. 5.25 shows the I-E curves at 300 K for a three-period MBE-grown structure ($x = 0.17$) when the sample is illuminated with normal room light and when it is in the dark. The room light increases the conductivity of the sample throughout the midfield range. At very high fields ($E \gtrsim 5$ kV/cm) the current with illumination merges with that from the dark. This may be due to the trapping of electrons in the AlGaAs that have transferred (real-space transfer) from the GaAs. The merging of light and dark curves could also be at least partially due to the low mobility in the AlGaAs which greatly reduces the contribution to the current from the extra carriers that transfer into the AlGaAs while the sample is illuminated.

The presence of the light clearly enhances the negative differential resistance in the current-field characteristic of this sample. This was seen to occur in nearly all of the many light-sensitive samples tested. Usually the enhancement in conduction and NDR while the illumination was present was virtually eliminated immediately after the light source was removed.

Increasing the intensity of the illumination increased the photoconduction in most cases, and often improved the peak-to-valley ratio of the NDR. Fig. 5.26 displays the I-E curves measured at 300 K for a sample

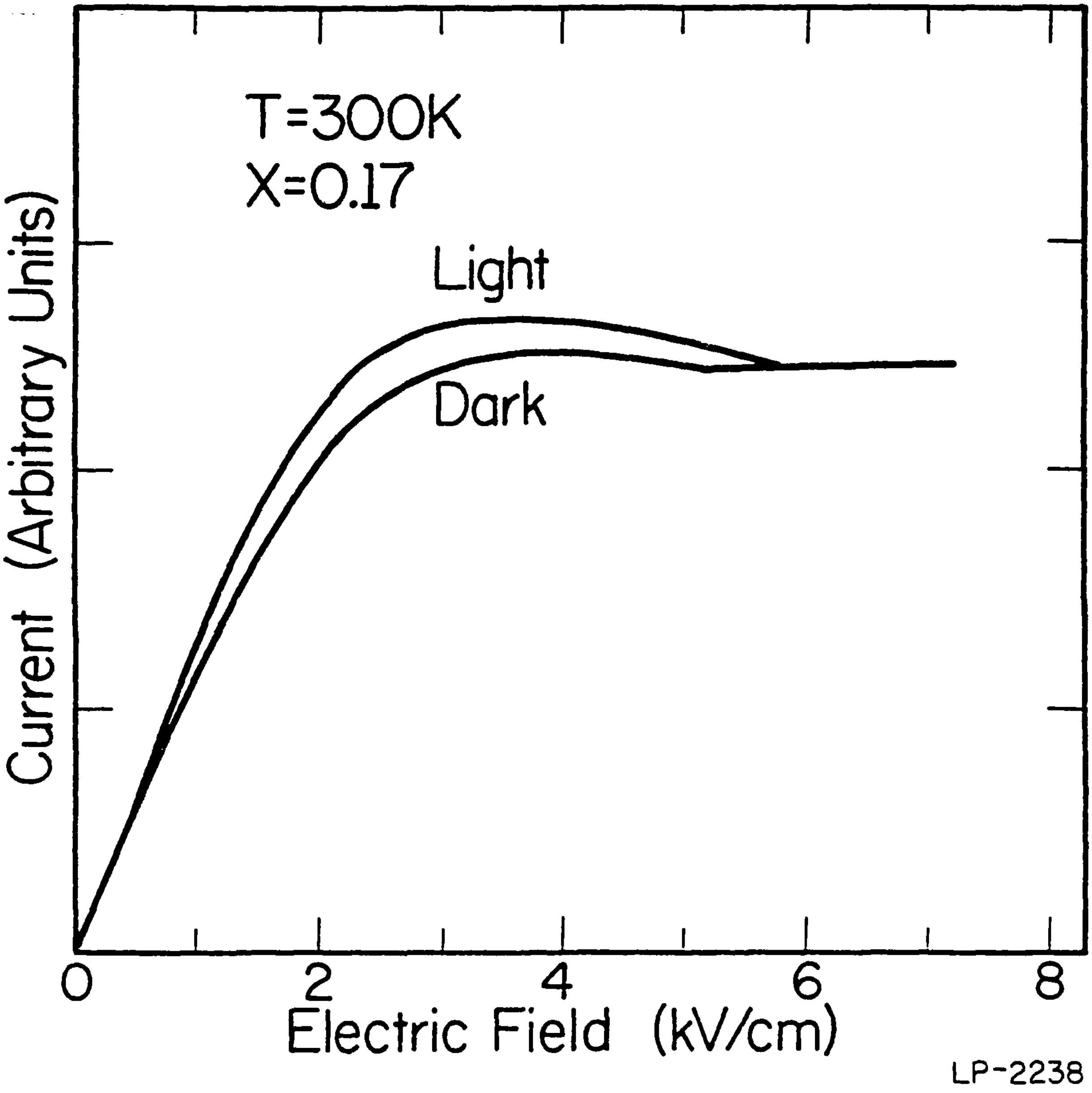

Fig. 5.25: Current-field characteristics of a three-period heterostructure (x = 0.17) at 300 K. Measurements were taken with the device in the dark and exposed to normal roomlight.

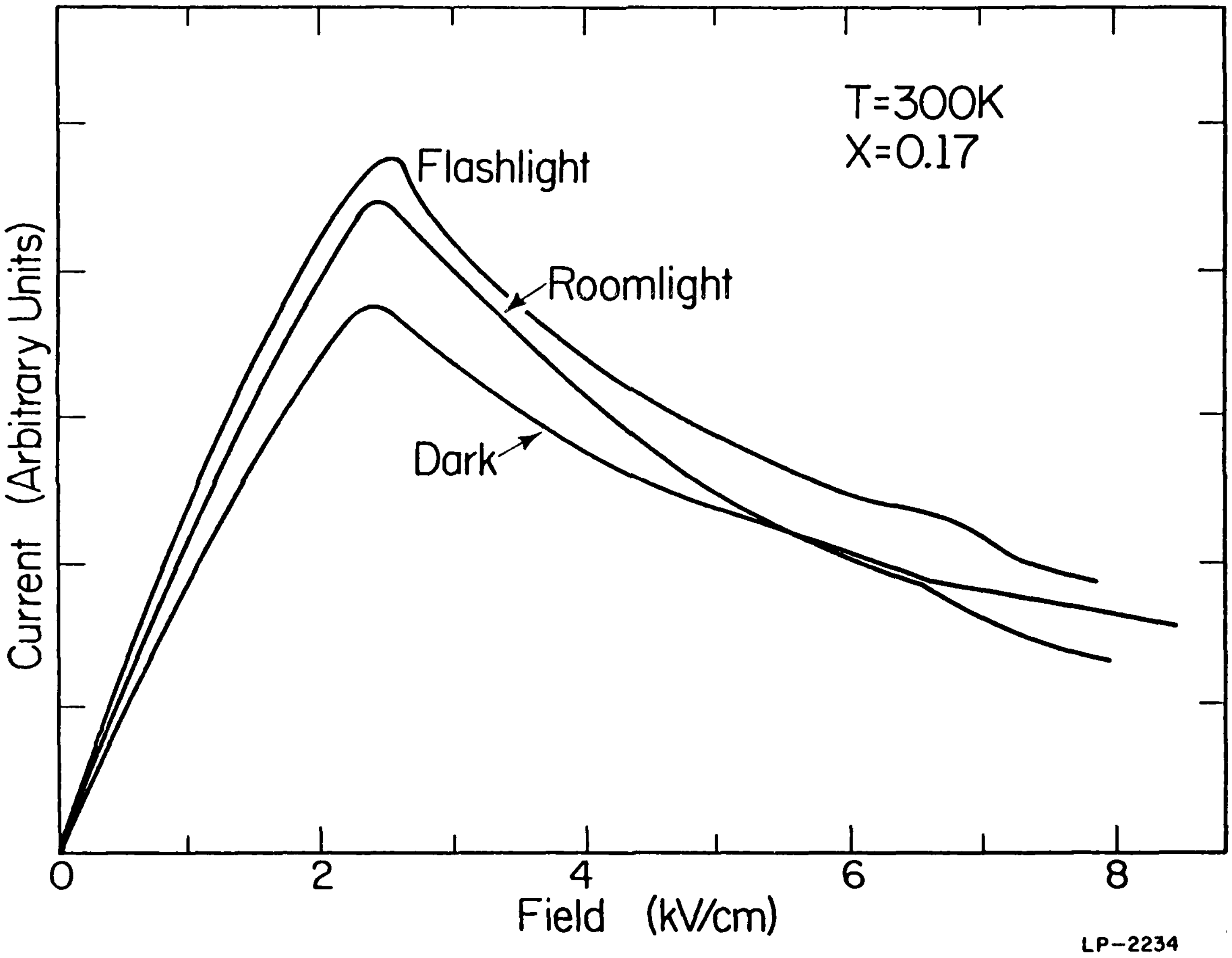

Fig. 5.26: Results of current-field measurements at 300 K on a single-period structure in the dark, exposed to roomlight, and illuminated by a flashlight.

exposed to different intensities of illumination. The sample was grown by MBE and contained a 1000 Å Si-doped $Al_xGa_{1-x}As$ ($x = 0.17$) layer on top of an undoped GaAs layer, 1 μm thick. When the light from a standard two-cell flashlight was added to the background room light, the conduction was improved significantly at all measured field strengths as shown in Fig. 5.26. Similarly it was found that the current conduction was still further improved when the sample was illuminated with a high intensity lamp (not shown in the figure).

Very large peak-to-valley ratios have been obtained for the negative differential resistances caused by real-space transfer in GaAs-AlGaAs heterostructures when the samples were illuminated. The current-field characteristic of an illuminated sample (with the same structure as the sample in Fig. 5.26) is shown in Fig. 5.27. The peak-to-valley ratio of the NDR in this case is approximately 3 to 1, which is higher than that attained with k-space transfer in GaAs. Thus, sample characteristics may be adjusted to meet special device needs by carefully controlling the illumination.

Fig. 5.28 displays the curious characteristics of a three-period MBE-grown sample measured in the dark and in the light. Just as in Fig. 5.13 there are points of inflection in the current in the dark that are possibly caused by conduction in the AlGaAs at low fields (AlGaAs not depleted). Shining room light on the sample increased the low-field conduction while the very high-field curves were not noticeably affected. It is seen that at 300 K the light eliminates the inflection in the current-field characteristics while at 77 K the inflection is shifted to higher values.

A form of hysteresis has sometimes been measured at low temperatures for a sample measured in the dark after it has been illuminated. An example

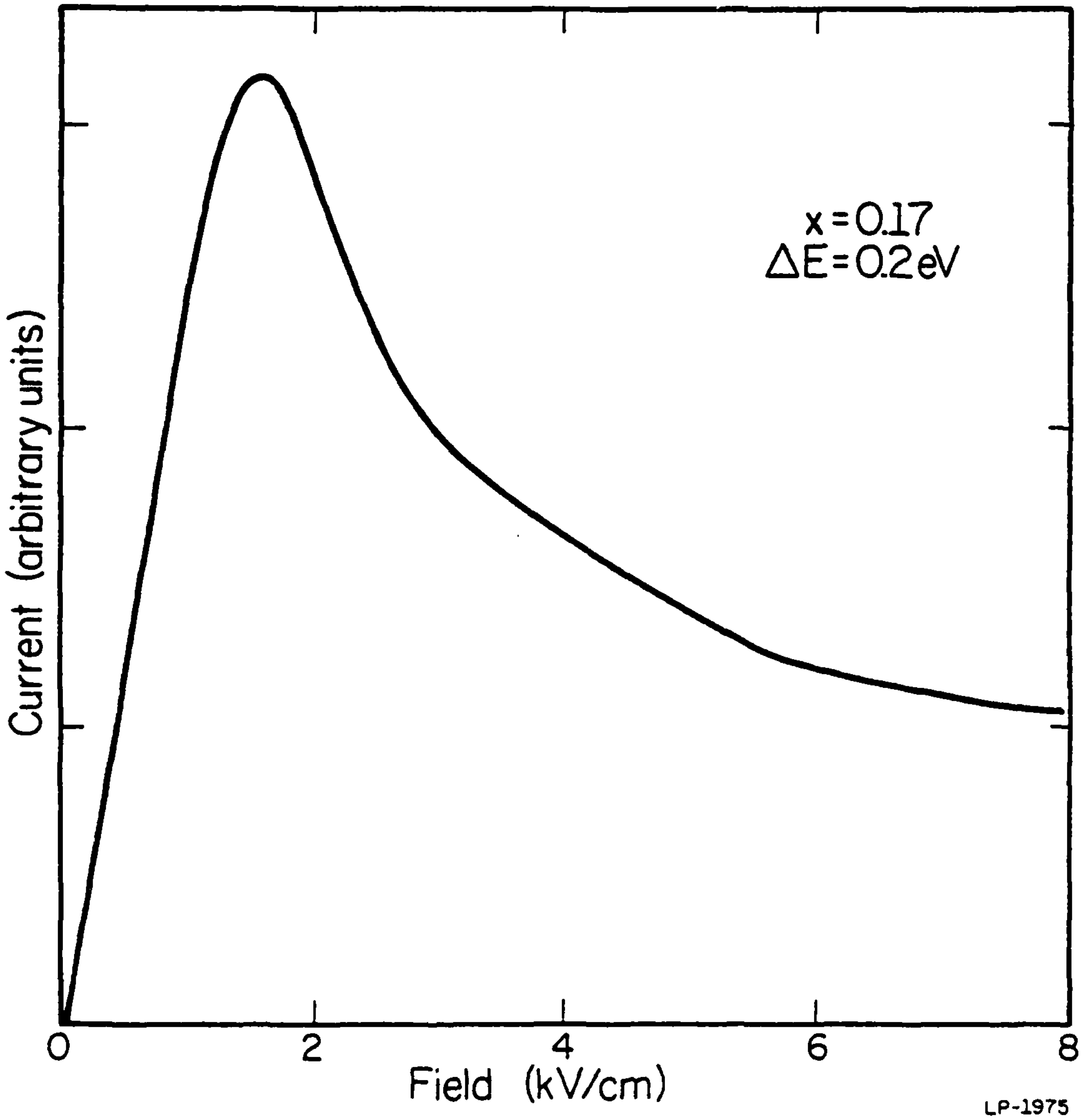

Fig. 5.27: Results of a current-field measurement at 300 K on a single-period structure (x = 0.17) which displayed a very large peak-to-valley ratio when exposed to roomlight.

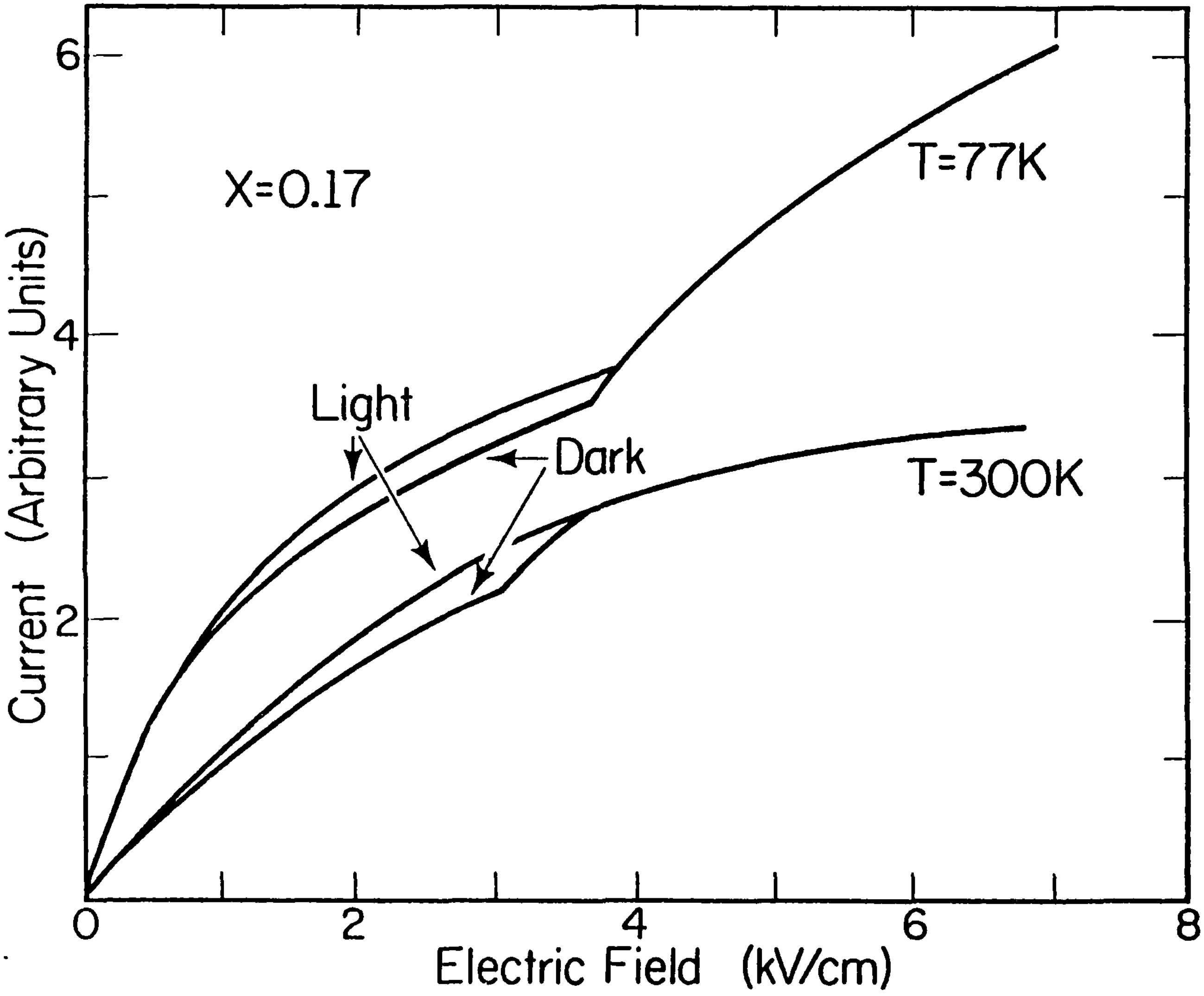

Fig. 5.28: Current-field characteristics measured at 77 K and 300 K for a three-period heterostructure ($x = 0.17$). The curious points of inflection in the current in the dark were shifted when the sample was exposed to roomlight.

of the hysteresis is shown in Fig. 5.29. The sample being measured had one period ($x = 0.32$) grown by MBE with a 200 Å GaAs cap layer. Little or no hysteresis was observed in the dark curve when the electric field was kept below 4 kV/cm. Since most of the current in this sample ($\Delta E_c \approx 0.34$ eV) is carried in the GaAs layer in this field range, the hysteresis effect observed at higher fields is most likely due to the trapping of transferred electrons in the AlGaAs.

In order to determine whether the observed photoconductivity is due mainly to electron-hole pair generation or excitation from trap levels, the same sample was illuminated by passing the incident light through a Ge filter, which has a bad gap of 0.67 eV compared to 1.43 eV for GaAs. The resulting I-E characteristics exhibited little change from previous light measurements so it is concluded that the photoconductivity observed in this sample is primarily due to carrier emission from traps in the AlGaAs layer.

Measurements made at 77 K and 300 K on the same single-period structure with a less intense light source are displayed in Fig. 5.30. The dashed lines represent the curves measured in the dark before the sample was exposed to light. At 77 K the dashed lines show a slight hysteresis, which indicates a small amount of trapping (probably in the AlGaAs or at the interface). At 300 K there is no hysteresis and the "dark before light" (dashed) curve and "dark after light" (solid) curve nearly coincide. The dark after light characteristic at 77 K, however, shows a significant hysteresis similar to that just seen in Fig. 5.29. The room light curve at 77 K shows no hysteresis as expected.

In some wafers the low-temperature hysteresis was found to be quite large. For example, the current-field characteristics shown in Fig. 5.31

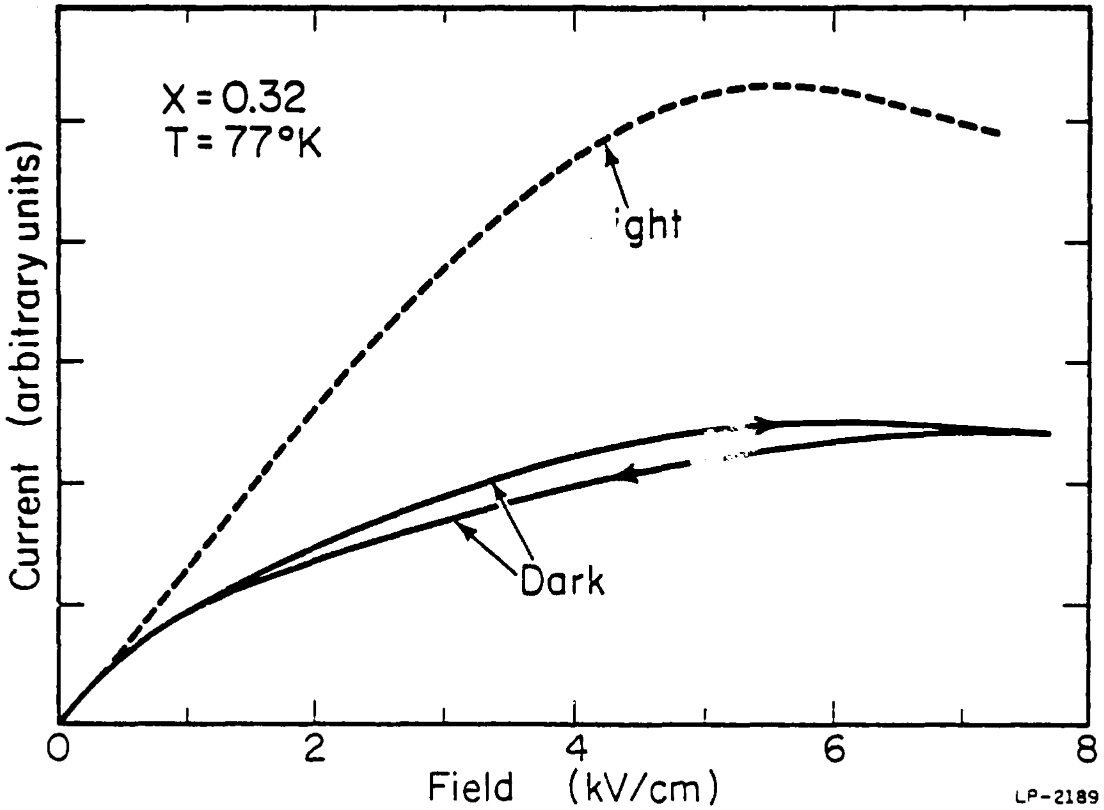

Fig. 5.29: Typical current-field characteristics of a single-period structure (x = 0.32) which exhibited a hysteresis effect when the sample was measured in the dark at 77 K after having been illuminated.

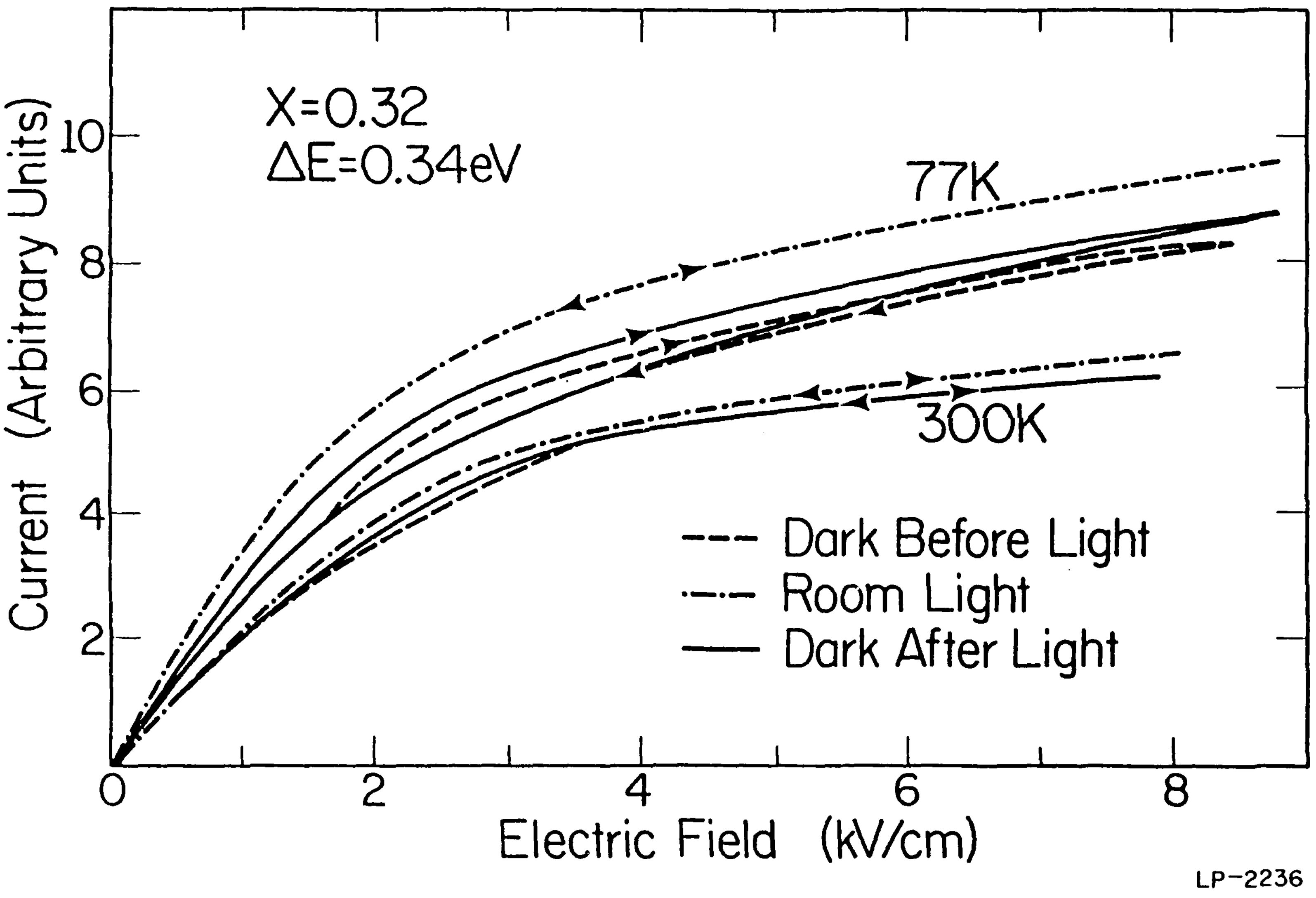

Fig. 5.30: Results of current-field measurements made on the same single-period heterostructure as in Fig. 5.29 with a less intense light source. A hysteresis appears (solid line) only at 77 K.

AD-A125 858 EXPERIMENTAL STUDIES OF LATERAL ELECTRON TRANSPORT IN 3/3
GALLIUM ARSENIDE-AL..(U) ILLINOIS UNIV AT URBANA
COORDINATED SCIENCE LAB M R KEEVER DEC 82 R-975
UNCLASSIFIED N00014-76-C-0806 F/G 20/12 NL

END

FILMED

DTIC

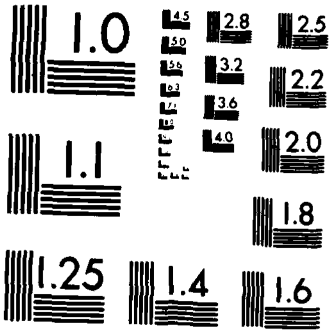

MICROCOPY RESOLUTION TEST CHART
NATIONAL BUREAU OF STANDARDS-1963-A

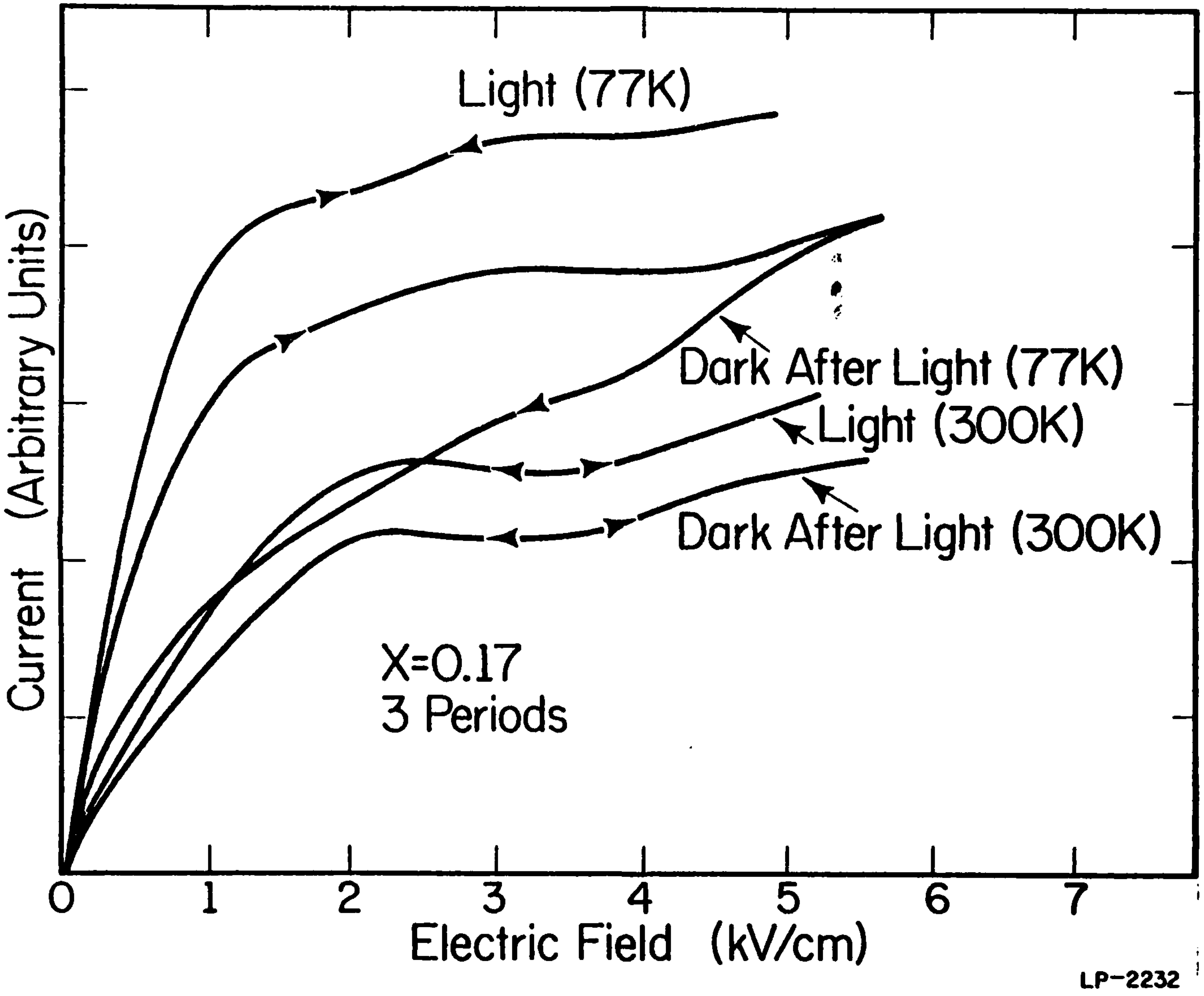

Fig. 5.31: Current-field characteristics at 77 K and 300 K of a three-period device with x = 0.17. The low temperature hysteresis was very large, indicating that a large fraction of the electrons were captured in traps at high fields.

exhibit a very substantial reduction in current at 77 K (dark after light) when the field is reduced. It is evident that a large fraction of the electrons were captured in traps at high fields. This MBE sample structure contained three periods with x = 0.17.

Similar effects have been seen as well in MOCVD-grown heterostructures. The nine-period sample (x = 0.21) measured for Fig. 5.32 was grown by MOCVD and exhibited especially large photoconductivity. The current at both 300K and 77 K when illuminated by a flashlight was twice the dark current value. The dark after light curve once again shows a large hysteresis as was seen in the MBE samples.

The above measurements have shown that in various samples, there are significant concentrations of trapping centers in the AlGaAs or at the interface that can be emptied by optical stimulation. An enhanced conductivity then results as the energetic electrons transfer to the high-mobility GaAs. When the electrons are transferred by high fields back to the vicinity of the traps they can be recaptured. This may result in a large hysteresis in the dark at low temperatures, since under these conditions it is very difficult for the electrons to regain enough energy to escape from the trapping states in the AlGaAs.

The photoconductivity of the samples at low temperatures exhibited various degrees of persistence after the source of illumination was removed. In most cases the increased conductivity decreased significantly within a few minutes, but in some cases it would persist for much longer times. In the following section, measurements will be presented for a set of samples which displayed a persistent photoconductive effect that lasted for many hours at 'ow temperatures.

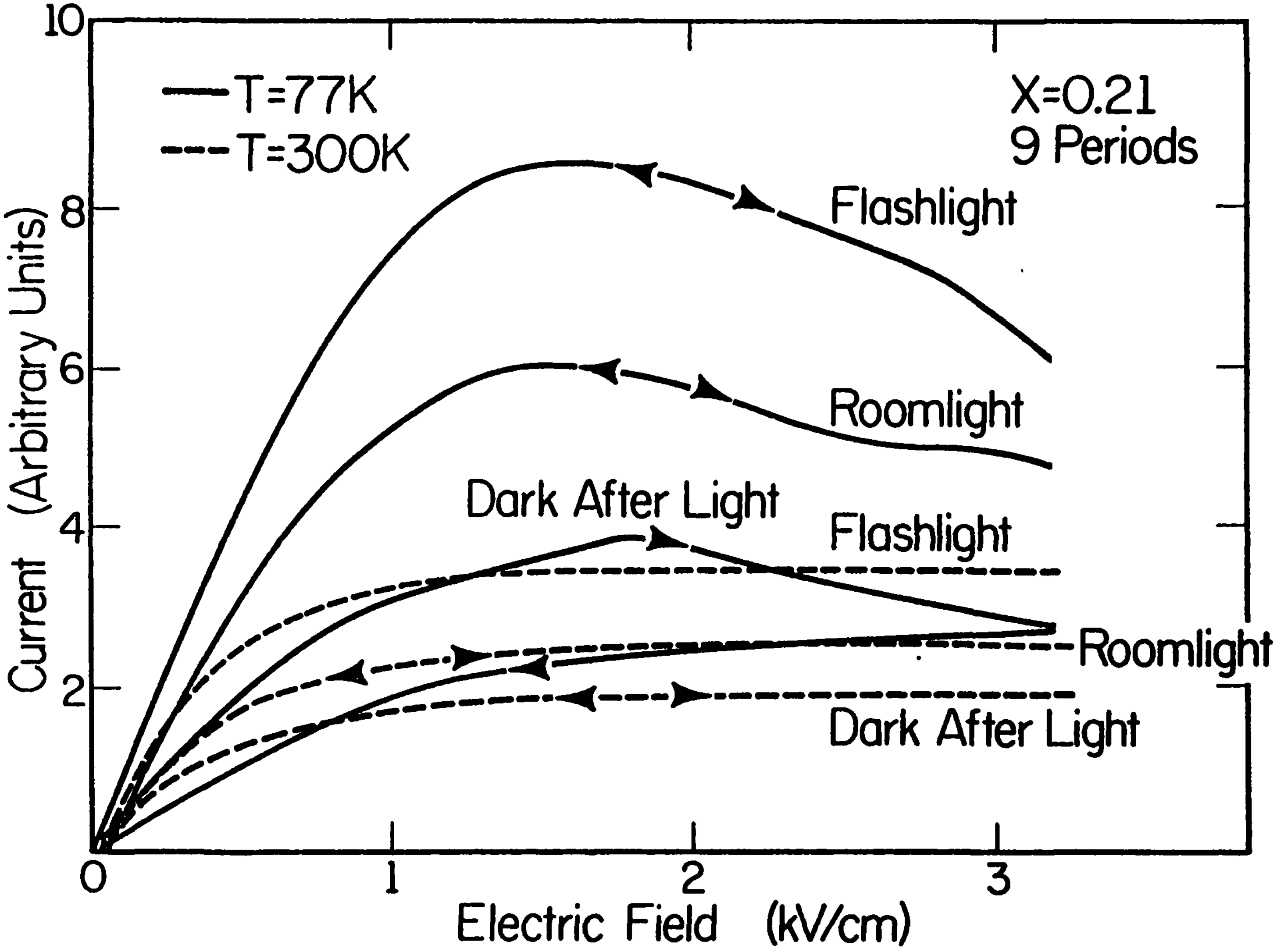

LP-2237

Fig. 5.32: Results of current-field studies of a nine-period MOCVD sample (x = 0.21) at 77 K and 300 K. The dark after light curve exhibits a large low-temperature hysteresis just as was seen for the MBE samples in Figures 5.29 - 5.31.

5.4.2 Persistent Photoconductive Effects

The set of single-period samples investigated in this section were characterized by a dramatic photoconductivity which persisted for long periods after the illuminating source was removed. The persistence of the photoeffect had a time constant on the order of days and was quenched only by heating the sample above some characteristic temperature. The origin of the effect is not yet settled but may likely be related to the so-called DX center [121], which is thought to be present in the AlGaAs layer. This model and other models for the origin of the effect will be discussed later in this section.

The sample being studied consisted of a single-period MBE-grown structure with $x = 0.16$. A schematic diagram of the structure is repeated in Fig. 5.33. Two ohmic contacts separated by 10 or 20 μm were alloyed down through the conducting layers from the top surface of the sample. The sample was mounted on a TO-18 header which was attached to the temperature-controlled cold finger of closed-cycle helium cryostat. An optical window on the cryostat was fitted with a Ge filter and the sample was irradiated with an appropriate light source.

The temperature dependence of the persistent photoeffect was measured with the assistance of B. Bereznak to determine its thermal threshold. At a constant temperature, current versus field scans were recorded, first in the dark, next with the sample illuminated and then once again in the dark after the light was removed. Measurements were performed in a sequence from high to low temperatures. Representative data in the critical range of thermal activation ($100\ K \leq T \leq 130\ K$) is shown in Fig. 5.34. These results show that persistent photoconductivity is strongly activated below 130 K.

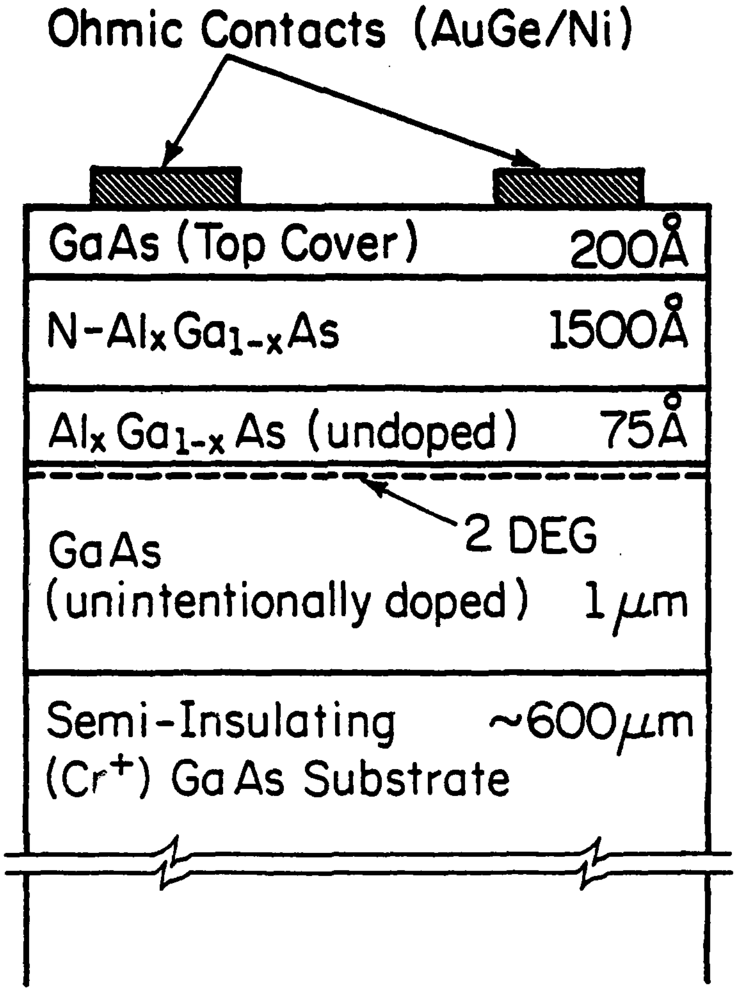

LP-2193

Fig. 5.33: Schematic diagram of the cross section of the single-period modulation-doped heterostructure with $x = 0.16$ which exhibited a long-lifetime, low-temperature persistent photoconductivity.

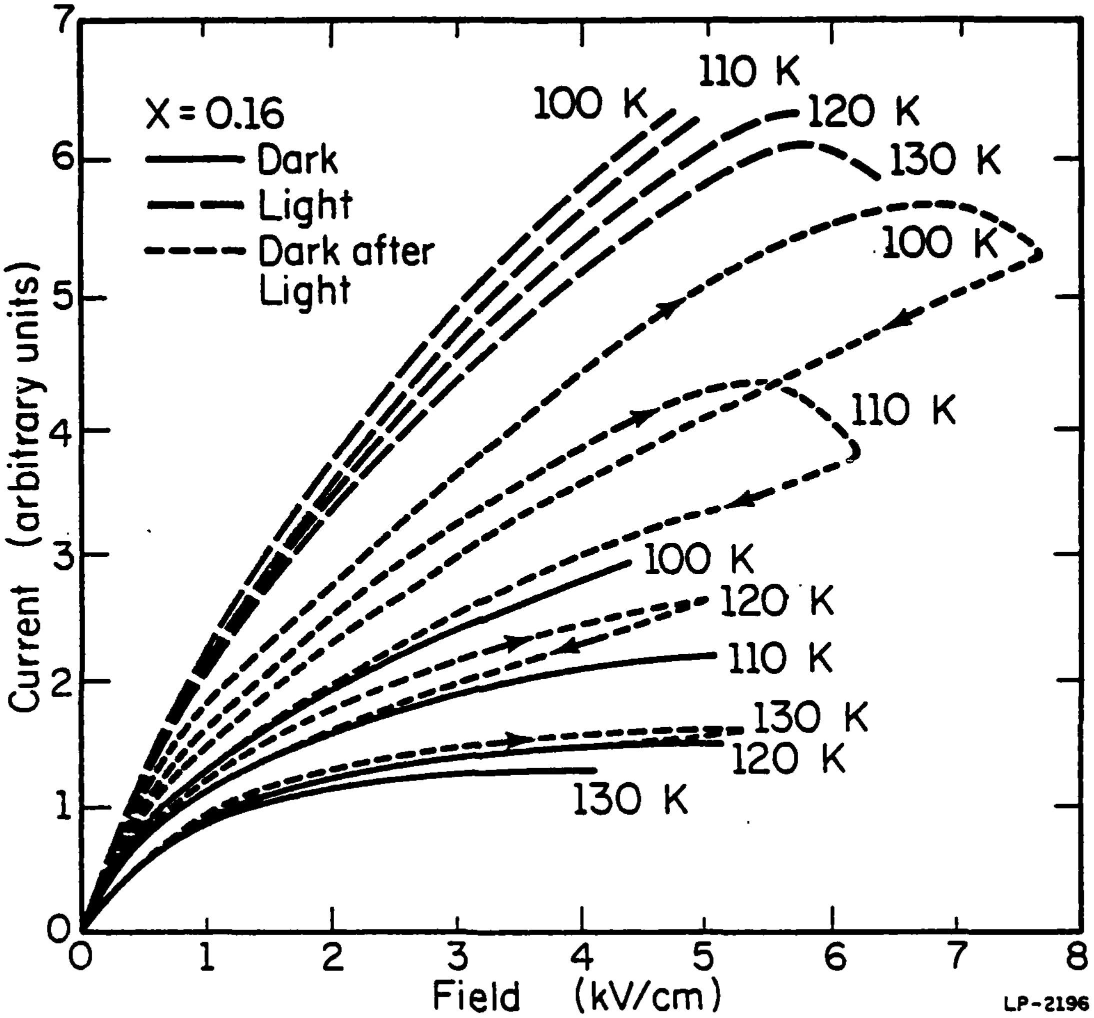

Fig. 5.34: Current-field characteristics of the heterostructure shown in Fig. 5.33 showing the temperature dependence of the persistent photoconductive effect. To avoid confusion only the forward characteristic of the dark curves is shown (the reverse hysteresis has been omitted).

There are other revealing features in the "dark after light" traces of Fig. 5.34. It was observed that sample photoconductivity decreased, gradually and without an additional increment in the electric field, once a certain field strength was reached. Evidently the photoconducting state was being quenched by the high electric field since the current loss experienced did not recover after returning to low fields. Instead, subsequent voltage sweeps repeatedly produced conductivity losses at high fields. This is the reason why the dark curves follow the reverse characteristic of the dark after light traces of the previous temperatures.

Since the initial conductivity of the dark after light curves are always lower than the light curves it is apparent that only a small fraction of the light-induced conductivity is due to electrons that do not recombine quickly with trapping centers or holes when the light is removed. These remaining carriers, however, persist in contributing to the current for very long periods of time after the light is removed and are evidently associated with a special type of trapping center.

An experiment designed to measure the optical activation energy of the trapping center responsible for persistent photoconductivity was performed. The experiment consisted of directing light from a quartz halogen bulb, which provides an excellent source of infrared radiation, onto a selective diffraction grating. The diffraction grating acts to separate out the various wavelength components of incident radiation, depending on the angle at which the source strikes it. This angle was adjusted to select a specific wavelength which was then focused onto the sample surface. Sample resistance was monitored while the wavelength was being swept from lower to higher energies. A typical result is given in Fig. 5.35 where the sample

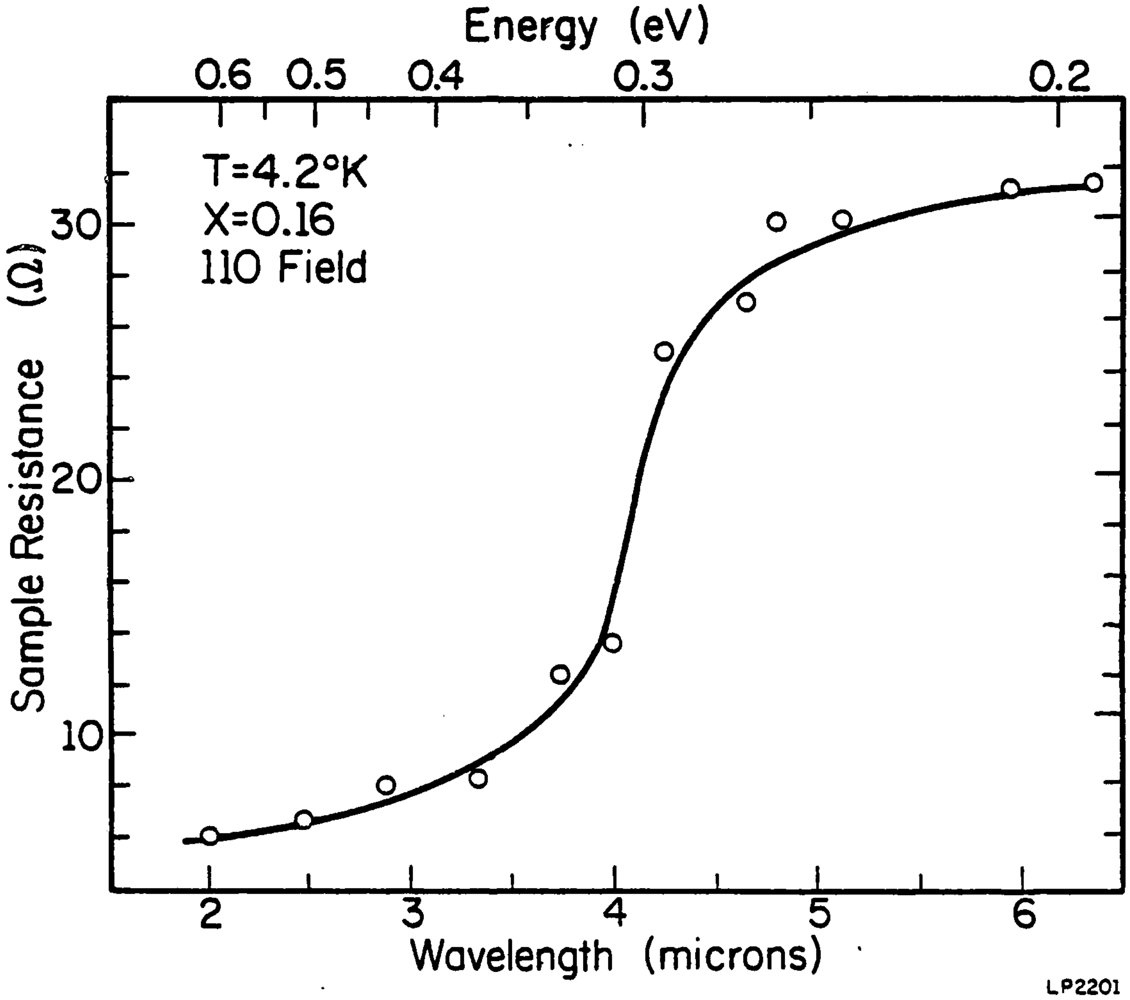

Fig. 5.35: Plot of sample resistance as a function of light energy and wavelength for the structure shown in Fig. 5.33 with x = 0.16. The abrupt change in resistance marks the onset of persistent photoconductivity and is a measure of the optical trap depth.

resistance of the one-period structure is plotted versus the wavelength of the incident light. It is seen that the onset of trap activated photoconductivity is marked by the dramatic drop in sample resistance at a wavelength of approximately 4.05 μm (about 0.310 eV). This value differs with a reported thermal ionization energy of 0.107 eV as measured by double-pulse experiments [122]. A large difference between the thermal and optical activation, i.e., a large Stokes shift, has also been reported by Lang et al. [121,123] and Nelson [124] in connection with persistent photoconductivity in Te-doped $Al_xGa_{1-x}As$. They described a defect having a thermal ionization energy 0.12 eV while the optical ionization energy was 1.1 eV.

The Stokes shift is also manifested in the inability to quench the photoconducting state optically, i.e., by freeing holes in the valence band and exciting them to empty defect levels [125]. We stimulated the sample directly with the 6328 Å (1.96 eV) line of a He-Ne laser and could not observe any photocurrent loss from previous measurements. If an optical quenching path were present we would expect light of this energy to diminish the photoconductivity ($E_G \approx 1.72$ eV at $T = 4.2$ K for $x = 0.16$). Evidently the transition is shifted to an energy larger than the band gap.

Although the origin of the persistent photoconductivity effect is not well understood, its temperature dependence and optical properties have been best explained up to now by a large lattice relaxation model involving a trap complex called a "DX" center in the AlGaAs layer. From studies on the donor doping dependence of the center [121,123,124], a complex involving a donor and anion vacancy was proposed.

This model has been shown in the literature to be qualitatively consistent with the dominant features of persistent photoconductivity: the very small capture cross section, the differences between the thermal and optical ionization energies, and the inability to optically quench the photocurrent.

The trap complex model was first associated with Te-doped AlGaAs where at temperatures below about 110 K, lattice relaxation produces a potential barrier of about 180 meV to electron capture, thus causing a long lifetime photoconductivity effect. However, it was recently reported by Drummond et al. [126] that the strong correlation between the temperature dependence of electron density as measured by Nelson for Te-doped AlGaAs and that measured in Si-doped AlGaAs grown by MBE indicate that the trap is not sensitive to the substitution of Si for Te as the donor dopant. Thus the DX center model should apply equally well to the Si-doped AlGaAs structures that are being investigated here.

A second model proposes that a doubly-charged defect center, which is strongly coupled to the indirect L or X minima of the Brillouin zone, is responsible for the persistence effect in n-type $Al_xGa_{1-x}As$. On photoexcitation, electrons released to a higher conduction-band minima would rapidly thermalize to the lowest energy state at Γ, leaving the center in a singly-charge state. Carrier capture is inhibited by the Coulombic barrier of the still negatively-charged center. Saxena [127] has observed a trap center having a thermal activation energy of 0.210 eV in intentionally undoped $Al_xGa_{1-x}As$ with mole fraction $x = 0.32$. From hydrostatic-pressure experiments he concluded that this deep level was primarily associated with the L conduction-band minima. We feel, however, that this model is somewhat inadequate since no systematic trends with alloy composition were observed in our data. In addition, experimental results of Nelson [124] on $Al_xGa_{1-x}As$ indicated that the capture properties were rather insensitive to changes in x. However, due to the complex nature of the trap and its strongly activated temperature dependence it is conceivable that such a center would most likely be formed away from the symmetric zone center at Γ. Therefore, we do not rule out the possibility that the defect levels may be associated with non-Γ minima.

A third proposal suggests that photoexcited electrons residing in the 2DEG at the interface are prevented from recombining by a macroscopic potential barrier (junction, surface barriers, band bending due to inhomogeneities, etc.). In fact, recent evidence shows that persistent photoconductivity in thin (less than 5 μm) epitaxial GaAs is a direct consequence of the epi-substrate interface junction [128].

However, there are several valid reasons for discounting the universal acceptance of this model. First of all, if the predominant cause of persistent photoconductivity was band bending at a conduction-band discontinuity then we would expect the effect to be widespread in all modulation-doped heterostructures. This is simply not the case. Moreover, this effect is readily observed in materials that do not have gross macroscopic barriers, i.e., bulk III-V ternary alloys. A distinction between results for thin epitxial layers and those for heterostructures grown by MBE must be maintained. It is reasonable to believe that band bending contributes to, and exaggerates the overal persistence effect described in this chapter, but it is probably not the most determining factor.

5.5 Summary

In this chapter, measurements of the high-field effects in GaAs-$Al_xGa_{1-x}As$ have been presented for a wide variety of device structures. The major emphasis has been placed on the experimental verification of real-space electron transfer in the heterostructures.

Monte Carlo simulations by others have predicted the effect of important parameters such doping concentration and AlAs mole fraction on the characteristics of the negative differential resistance (NDR) that can occur when real-space transfer (RST) takes place. The experimental results were found to match closely to these Monte Carlo calculations in many instances.

The growth parameters of a heterostructure were found to be very important for determining the threshold field and magnitude of a RST-induced negative differential resistance. Increasing the AlAs mole fraction x (which increased ΔE_c) tended to increase the threshold field for the onset of NDR in addition to altering the shape of the NDR itself. The magnitude of doping in the $Al_xGa_{1-x}As$ also significantly affects the characteristics of the NDR. It was found that if the AlGaAs was too highly doped to be depleted of electrons at low fields, the NDR effect could be eliminated completely.

It was discovered that the NDR due to real-space transfer could be significantly changed in many samples by illuminating the sample with light of various intensities. Very high peak-to-valley ratios were otained experimentally by illuminating the surface of the heterostructure.

The above findings suggest that the NDR due to RST can be "engineered" to meet necessary device requirements by controlling the growth parameters and device environment. It is thus more versatile than the analogous NDR caused by k-space transfer in GaAs, which has most of its NDR characteristics nearly fixed.

Our investigations have demonstrated that the high-field RST mechanism can be employed to create novel devices with attractive properties. It is possible to create a high-frequency oscillator using RST effects where the frequency of oscillation is controlled by the external circuit, not by the length of the device. Since the ultimate frequency is limited only by the carrier transfer times between layers (estimated to be less than 10^{-11} s), the device is expected to be operable well into the GHz range. In addition, the power of the oscillator may be increased by adding additional layer pairs to the device cross section without changing the frequency of oscillation.

The fast transfer times of carriers between layers can be used to advantage in devices for switching and storage applications. It was shown in this chapter that switching and storage devices can be constructed by contacting groups of layers separately so that electric fields can be applied selectively to only some of the layers. The storage times are determined by the AlAs mole fraction of the AlGaAs and the lattice temperature of the heterostructure. Storage times from the nanosecond range to a period of years should be attainable.

In addition to the normal photoconductivity present in many of the samples, a persistent photoconductive effect was found to exist in a limited number of the heterostructures. The persistent photoeffect appeared at temperatures below 130 K and had a time constant of days. The optical ionization energy was measured to be 0.31 eV which was significantly higher than the thermal ionization energy of 0.11 eV measured by Bereznak [122]. The origin of the persistent photoconductivity is not well established, but one prominent model proposes that it is due to a trap complex involving a donor and anion vacancy.

6. SUMMARY AND CONCLUSIONS

In the past several years modulation-doped GaAs-$Al_xGa_{1-x}As$ heterostructures have been receiving considerable attention because of their very high electron mobilities which have been measured at low temperatures using low electric fields. The purpose of the research reported in this dissertation has been to experimentally measure the electron-transport properties of these structures over a broad range of laterally-applied electric field strengths using a diverse set of device structures and temperatures. Many interesting transport characteristics have been revealed at both low and high electric fields.

It was discovered that the electron mobility in these structures increased initially as the electric field was increased from zero, possibly due to the electron-temperature dependence of the electron screening. The low-field mobility then usually reached a maximum at low fields (200 - 400 V/cm for the structures studied) and dropped quickly for increasingly higher electric fields. The mobility decline as a function of electric field was seen to be very dependent on device temperature. The largest mobility reductions occurred at low temperatures where the peak low-field mobility was the largest. At higher temperatures (200 to 300 K) there was comparatively little change in the mobility for electric fields up to 2 kV/cm [34,92].

The sharp drop in mobility after the peak is most likely due to the onset of polar optical phonon scattering. Intersubband scattering for the 2DEG may also contribute considerably to the mobility decrease after the peak. An attempt was made to determine the influence of intersubband scattering on the observed mobility versus field characteristics of the structures using a back-side gate electrode. The results were inconclusive, however, and it is recommended that further research be done in this area to assess the relative strengths of intersubband scattering and polar optical phonon scattering.

One isolated set of samples from one wafer exhibited a very steep negative differential resistance (NDR) that occurred at very low fields. The observed characteristics were indicative of a low-temperature surface acoustoelectric effect [35]. The effect did not occur at room temperature because the sample length was too short to compensate for the higher lattice losses at 300 K.

At higher fields (above 2 kV/cm) a variety of other effects were observed in the modulation-doped heterostructures. When the fields were sufficiently high, the high-mobility electrons in the GaAs could obtain enough energy to be thermionically emitted over the conduction-band discontinuity into the low-mobility AlGaAs [26,27]. This real-space transfer of electrons was seen to cause current saturations or various degrees of negative differential resistance [28] in the experimental samples being studied. The real-space transfer effect is thought to be analogous to k-space transfer in bulk GaAs. However, the characteristics of real-space transfer (unlike k-space transfer) were found to be adjustable by varying the growth parameters such as the AlAs mole fraction, doping concentrations, and layer widths. These same growth parameters were also seen to be influential in changing the mobility characteristics at low fields.

It was also observed that the NDR due to real-space transfer could be significantly enhanced in many samples by illuminating the surface of the heterostructure. In a few of the structures the increase in conductivity due to the photoconductive effect was found to persist after the source of illumination was removed. The persistent photoconductivity occurred only at low temperatures ($T < 130$ K) and could be quenched by heating the sample. Although various models have been proposed which qualitatively explain various characteristics of this effect, the origin of the persistent photoconductivity is still not settled and there is a great need for further research on this phenomenon.

The occurrence of a negative differential resistance due to the real-space transfer of electrons out of the high-mobility GaAs layer can greatly limit the performance of a GaAs-AlGaAs heterostructure FET. Devices such as these, which depend on high-speed electron transport, must be designed very carefully so as to reduce internal high electric fields and minimize real-space transfer effects.

Real-space transfer effects have many positive applications as well in novel new devices. It was demonstrated that real-space transfer at high fields could be easily utilized to create a variable frequency oscillator [30]. The frequency was controlled by an external circuit and was not dependent on the sample length. Since the transfer of electrons between layers is very fast (theoretically near 5×10^{-12} s) it may be possible to push this oscillator to frequencies well into the GHz range with a substantial power output. Further investigation of the high-frequency properties of GaAs-AlGaAs heterostructure devices is being pursued by others at this time.

Very fast electron switching speeds also make the real-space transfer mechanism attractive for switching and storage applications. It was demonstrated that useful switching and storage devices could be constructed with GaAs-AlGaAs heterostructures by electrically contacting groups of layers separately so that electric fields could be applied selectively to only some of the layers [32]. Electrons could then be transferred and stored for varying lengths of time (determined by the temperature and AlAs mole fraction) in different GaAs layers in the heterostructure. It was predicted that storage times from nanoseconds to years could be attainable.

More sophisticated and efficient switching and storage devices can be easily constructed using present day crystal-growth systems with a rotating mask or substrate holder in the crystal-growth chamber. This will increase the ease with which additional sets of layers can be contacted separately and will also increase the fraction of the electrons in the device that can contribute to the switching and storage effects. Further research in this area will undoubtedly result in considerable improvement in the switching characteristics and storage capabilities of this novel device.

In closing, it is pointed out that all of the effects described above are consequences of the complicated boundary conditions that can be imposed on these heterostructures. Many of the important transport characteristics that result from various boundary conditions have been investigated and reported here, but many more effects undoubtedly still remain to be discovered and explored in the future. It is this large variability of the boundary conditions of GaAs-$Al_xGa_{1-x}As$ heterostructures [129] which make them so attractive for transport applications such as those investigated here as well as for use in optoelectronics [129-133].

APPENDIX

Determination of GaAs Mobility with Two-Layer Conduction

In this appendix, the formula (Eq. (4.14)) used to calculate the mobility μ_2 in the GaAs layer is derived.

It is assumed that the total number of carriers in the GaAs and AlGaAs layers stays constant. This may be represented by

$$n(A_1 + A_2) = n_1 A_1 + n_2 A_2 \tag{A.1}$$

where n_1 and A_1 (n_2 and A_2) are the carrier concentration and conductive-layer cross section of the AlGaAs (GaAs). n is the overall average charge density of the conducting layers.

By defining $x = n_2/n_1$, one may use Eq. (A.1) to obtain

$$n_2 = \frac{xn(A_1+A_2)}{A_2 x + A_1}, \quad n_1 = \frac{n(A_1+A_2)}{A_2 x + A_1}. \tag{A.2}$$

The total current I flowing through the AlGaAs (subscript 1) and GaAs (subscript 2) layers due to an electric field E may be written as

$$I = I_1 + I_2 = (n_1\mu_1 A_1 + n_2\mu_2 A_2)\, eE . \tag{A.3}$$

Substituting Eq. (A.2) into Eq. (A.3) and solving for x yields

$$x = \frac{\mu_1 A_1 n(A_1+A_2)eE - A_1 I}{A_2 I - \mu_2 A_2 n(A_1+A_2)eE} = \frac{K_1}{A_2 I - K_2\mu_2} \tag{A.4}$$

where

$$K_1 = \mu_1 A_1 n(A_1 + A_2)\, eE - A_1 I \tag{A.5}$$

and

$$K_2 = A_2 n(A_1 + A_2)\, eE . \tag{A.6}$$

When there is no magnetic field, the total resistance R_o of the two parallel layers is obviously found from

$$\frac{1}{R_o} = \frac{1}{R_1} + \frac{1}{R_2} . \tag{A.7}$$

Let the AlGaAs (GaAs) layer increase in resistance by ΔR_1 (ΔR_2) when a magnetic field of strength B is applied perpendicular to the layers. Then the total parallel resistance R_B of the layers when the transverse magnetic field of strength B is applied is found from

$$\frac{1}{R_B} = \frac{1}{R_1+\Delta R_1} + \frac{1}{R_2+\Delta R_2} . \tag{A.8}$$

The total relative change in resistance with the magnetic field is

$$\frac{\Delta R}{R_o} = \frac{R_B-R_o}{R_o} = R_B \left(\frac{1}{R_o} - \frac{1}{R_B} \right) \tag{A.9}$$

It was found in Chapter 4 (Eq. (4.12)) that

$$\frac{\Delta R_1}{R_1} \approx \mu_1{}^2 B^2 , \quad \frac{\Delta R_2}{R_2} \approx \mu_2{}^2 B^2 . \tag{A.10}$$

Substituting Eqs. (A.7) and (A.8) into Eq. (A.9) gives

$$\frac{\Delta R}{R_o} = \frac{(R_1+\Delta R_1)(R_2+\Delta R_2)}{R_1+R_2+\Delta R_1+\Delta R_2} \left[\frac{\Delta R_1}{R_1(R_1+\Delta R_1)} + \frac{\Delta R_2}{R_2(R_2+\Delta R_2)} \right] . \tag{A.11}$$

By substituting Eq. (A.10) into Eq. (A.11) and simplifying, one can find

$$\begin{aligned} \frac{\Delta R}{R_o} &= B^2 \left[\frac{(R_2+\Delta R_2)\mu_1{}^2 + (R_1+\Delta R_1)\mu_2{}^2}{R_1+R_2+\Delta R_1+\Delta R_2} \right] \\ &= B^2 \left[\frac{R_2(1+\mu_2{}^2B^2)\mu_1{}^2 + R_1(1+\mu_1{}^2B^2)\mu_2{}^2}{R_1(1+\mu_1{}^2B^2) + R_2(1+\mu_2{}^2B^2)} \right] . \end{aligned} \tag{A.12}$$

Note that

$$\frac{R_1}{R_2} = \frac{n_2\mu_2A_2}{n_1\mu_1A_1} = x\,\frac{\mu_2A_2}{\mu_1A_1} \quad . \tag{A.13}$$

Then using Eq. (A.13) in Eq. (A.12) gives

$$\frac{\Delta R}{R} = B^2\left[\frac{\frac{1}{x}\,(1+\mu_2{}^2B^2)\;\mu_1{}^2 + \frac{A_2}{\mu_1A_1}\,(1+\mu_1{}^2B^2)\;\mu_2{}^3}{\frac{A_2}{\mu_1A_1}\,(1+\mu_1{}^2B^2)\;\mu_2 + \frac{1}{x} + \frac{1}{x}\,B^2\mu_2{}^2}\right] \quad . \tag{A.14}$$

To obtain a third order polynomial in μ_2, one can substitute Eq. (A.4) for x into (A.14) and then put the entire equation over a common denominator and combine like powers of μ_2. The final expression, which is the same as Eq. (4.14), then becomes

$$\left[\frac{A_2(1+\mu_1{}^2B^2)}{\mu_1A_1} + \frac{\Delta R}{R}\,\frac{K_2}{K_1} - \frac{K_2\mu_1{}^2B^2}{K_1}\right]\mu_2{}^3 + \left[\frac{A_2I\mu_1{}^2B^2}{K_1} - \frac{\Delta R}{R}\;\frac{A_2I}{K_1}\right]\mu_2{}^2$$

$$+ \left[\frac{\Delta R}{RB^2}\left(\frac{K_2}{K_1} - \frac{A_2}{\mu_1A_1}\,(1 + \mu_1{}^2B^2)\right) - \frac{K_2\mu_1{}^2}{K_1}\right]\mu_2$$

$$+ \left[\frac{A_2I\mu_1{}^2}{K_1} - \frac{\Delta R}{R}\,\frac{A_2I}{B^2K_1}\right] = 0 \tag{A.15}$$

where K_1 and K_2 are given by Equations (A.5) and (A.6), respectively.

This third-order polynomial (Eq. (A.15)) was used to calculate the mobility in the GaAs as described in detail in Chapter 4.

REFERENCES

1. H. Rupprecht, J. M. Woodall, and G. D. Petit, "Efficient visible electroluminescence at 300 K from Ga$_{1-x}$Al$_x$As p-n junctions grown by liquid-phase epitaxy," Appl. Phys. Lett., vol. 11, pp. 81-83, 1967.

2. H. M. Manasevit, "The use of metal-organics in the preparation of semiconductor materials: III. Studies of epitaxial III-V aluminum compound formation using trimethylaluminum," J. Electrochem. Soc., vol. 118, pp. 647-650, 1971.

3. A. Y. Cho, "Growth of periodic structures by the molecular-beam method," Appl. Phys. Lett., vol. 19, pp. 467-468, 1971.

4. A. Y. Cho and J. R. Arthur, "Molecular beam epitaxy," Progress in Solid State Chemistry, edited by G. Somerjai and J. McCaldin. Pergamon, New York, 1975, vol. 10, pp. 157-191.

5. R. Dingle, H. L. Störmer, A. C. Gossard, and W. Wiegmann, "Electron mobilities in modulation-doped semiconductor heterojunction superlattices," Appl. Phys. Lett., vol. 33, pp. 665-667, 1978.

6. H. L. Störmer , R. Dingle, A. C. Gossard, W. Wiegmann, and M. D. Sturge, "Two-dimensional electron gas at a semiconductor-semiconductor interface," Solid State Commun., vol. 29, pp. 705-709, 1979.

7. H. L. Störmer, R. Dingle, A. C. Gossard, W. Wiegmann, and M. D. Sturge, "Two-dimensional electron gas at differentially doped GaAs-Al$_x$Ga$_{1-x}$As heterojunction interface," J. Vac. Sci. Technol., vol. 16, pp. 1517-1519, 1979.

8. S. Mori and T. Ando, "Electronic properties of a semiconductor superlattice, II. Low temperature mobility perpendicular to the superlattice," J. Phys. Soc. Jpn., vol. 48, pp. 865-873, 1980.

9. S. Mori and T. Ando, "Electronic properties of a heavily-doped n-type GaAs-Ga$_{1-x}$Al$_x$As superlattice," Surface Sci., vol. 98, pp. 101-107, 1980.

10. H. Morkoç, L. C. Witkowski, T. J. Drummond, C. M. Stanchak, A. Y. Cho, and B. G. Streetman, "Growth conditions to achieve mobility enhancement in Al$_x$Ga$_{1-x}$As-GaAs heterojunctions by M.B.E.," Electron. Lett., vol. 16, pp. 753-754, 1980.

11. T. Mimura S. Hiyamizu, T. Fujii, and K. Nanbu, "A new field-effect transistor with selectively doped GaAs/n-Al$_x$Ga$_{1-x}$As heterojunctions," Jpn. J. Appl. Phys., vol. 19, pp. L225-L227, 1980.

12. D. Delagebeaudeuf, P. Delescluse, P. Etienne, M. Laviron, J. Chaplart, and N. T. Linh, "Two-dimensional electron gas MESFET structure," Electron. Lett., vol. 16, pp. 667-668, 1980.

13. D. Delagebeaudeuf and N. T. Linh, "Charge control of the heterojunction two-dimensional electron gas for MESFET application," IEEE Trans. Electron. Devices, vol. ED-28, pp. 790-795, 1981.

14. S. Judaprawira, W. I. Wang, P. C. Chao, C. E. C. Wood, D. W. Woodard, and L. F. Eastman, "Modulation-doped MBE GaAs/n-Al$_x$Ga$_{1-x}$As MESFETs," IEEE Electron Dev. Lett., vol. EDL-2, pp. 14-15, 1981.

15. D. C. Tsui, A. C. Gossard, G. Kaminsky, and W. Wiegmann, "Transport properties of GaAs-Al$_x$Ga$_{1-x}$As heterojunction field-effect transistors," Appl. Phys. Lett., vol. 39, pp. 712-714, 1981.

16. P. Delescluse, M. Laviron, J. Chaplart, D. Delagebeaudeuf, and N. T. Linh, "Transport properties in GaAs-Al$_x$Ga$_{1-x}$As heterostructures and MESFET application," Electron Lett., vol. 17, pp. 342-344, 1981.

17. H. Morkoç, "Current transport in modulation-doped (Al,Ga)As/GaAs heterostructures: Applications to high-speed FETs," IEEE Electron. Dev. Lett., vol. EDL-2, pp. 260-262, 1981.

18. M. Laviron, D. Delagebeaudeuf, P. Delescluse, J. Chaplart, and N. T. Linh, "Low-noise two-dimensional electron gas FET," Electron. Lett., vol. 17, pp. 536-537, 1981.

19. W. Kopp, H. Morkoç, T. J. Drummond, and S. L. Su, "Characteristics of submicron gate GaAs FETs with Al$_{0.3}$Ga$_{0.7}$As buffers: Effects of interface quality," IEEE Electron. Dev. Lett., vol. EDL-3, pp. 46-48, 1982.

20. K. Kodama, M. Ozeki, and A. Shibatomi, "Breakdown mechanism of buffer layers in vapor phase epitaxial GaAs for metal-semiconductor field-effect transistors," Appl. Phys. Lett., vol. 41, pp. 249-250, 1982.

21. D. Delagebeaudeuf, M. Laviron, P. Delescluse, P. N. Tung, J. Chaplart, and N. T. Linh, "Planar enhancement mode two-dimensional electron gas FET associated with a low AlGaAs surface potential," Electron. Lett., vol. 18, pp. 103-105, 1982.

22. T. J. Maloney, R. R. Saxena, and Y. G. Chai, "AlGaAs/GaAs JFETs by organo-metallic and molecular beam epitaxy," Electron. Lett., vol. 18, pp. 112-113, 1982.

23. T. J. Drummond, W. Kopp, R. E. Thorne, R. Fischer, and H. Morkoç, "Influence of $Al_xGa_{1-x}As$ buffer layers on the performance of modulation-doped field-effect transistors," Appl. Phys. Lett., vol. 40, pp. 879-881, 1982.

24. W. Kopp, R. Fischer, R. E. Thorne, S. L. Su, T. J. Drummond, H. Morkoç, and A. Y. Cho, "A new $Al_{0.3}Ga_{0.7}As$/GaAs modulation-doped FET," IEEE Electron Dev. Lett., vol. EDL-3, pp. 109-111, 1982.

25. C. Y. Chen, A. Y. Cho, A. C. Gossard, and P. A. Garbinski, "Offset channel insulated gate field-effect transistors," Appl. Phys. Lett., vol. 41, pp. 360-362, 1982.

26. K. Hess, H. Morkoç, H. Shichijo, and B. G. Streetman, "Negative differential resistance through real-space electron transfer," Appl. Phys. Lett., vol. 35, pp. 469-471, 1979.

27. H. Shichijo, K. Hess, and B. G. Streetman, "Real-space electron transfer by thermionic emission in GaAs-$Al_xGa_{1-x}As$ heterostructures: Analytical model for large layer widths," Solid-State Electron., vol. 23, pp. 817-822, 1980.

28. M. Keever, H. Shichijo, K. Hess, S. Banerjee, L. Witkowski, H. Morkoç, and B. G. Streetman, "Measurements of hot-electron conduction and real-space transfer in GaAs-$Al_xGa_{1-x}As$ heterojunction layers," Appl. Phys. Lett., vol. 38, pp. 36-38, 1981.

29. K. Hess, "Hot-electron and phonon effects in layered semiconductor structures and heterostructures," Comments Solid State Phys., vol. 10, pp. 67-84, 1981.

30. P. D. Coleman, J. Freeman, H. Morkoç, K. Hess, B. G. Streetman, and M. Keever, "Demonstration of a new oscillator based on real-space transfer in heterojunctions," Appl. Phys. Lett., vol. 40, pp. 493-495, 1982.

31. H. Shichijo, "Theoretical studies of high field transport in III-V semiconductors," Ph.D. dissertation, University of Illinois at Urbana-Champaign, 1980. Also Coordinated Science Laboratory Report R-893, UILU-ENG 80-2225.

32. M. Keever, K. Hess, and M. Ludowise, "Fast switching and storage in GaAs-Al$_x$Ga$_{1-x}$As heterojunction layers," IEEE Electron Dev. Lett., vol. EDL-3, pp. 297-300, 1982.

33. T. J. Drummond, M. Keever, W. Kopp, H. Morkoç, K. Hess, and B. G. Streetman, "Field dependence of mobility in Al$_{0.2}$Ga$_{0.8}$As/GaAs heterojunctions at very low fields," Electron. Lett., vol. 17, pp. 545-547, 1981.

34. M. Keever, W. Kopp, T. J. Drummond, H. Morkoç, and K. Hess, "Current transport in modulation-doped Al$_x$Ga$_{1-x}$As/GaAs heterojunction structures at moderate field strengths," Jpn. J. Appl. Phys., to be published.

35. M. Keever, T. J. Drummond, K. Hess, H. Morkoç, and B. G. Streetman, "Time dependence of current at high electric fields in Al$_x$Ga$_{1-x}$As-GaAs heterojunction layers," Electron. Lett., vol. 17, pp. 93-94, 1981.

36. R. Dingle, "Confined carrier quantum states in ultrathin semiconductor heterostructures," Festkörperprobleme XV (Advances in Solid State Physics). Pergamon-Vieweg, Brainschwieg, 1975, pp. 21-48.

37. J. R. Arthur, "Abstract: Fundamentals of MBE," J. Vac. Sci. Technol., vol. 16, pp. 273-274, 1979.

38. A. Y. Cho, "Recent developments in moleclar beam epitaxy (MBE)," J. Vac. Sci. Technol., vol. 16, pp. 275-284, 1979.

39. A. C. Gossard, P. M. Petroff, W. Wiegmann, R. Dingle, and A. Savage, "Epitaxial structures with alternate-atomic-layer composition modulation," Appl. Phys. Lett., vol. 29, pp. 323-325, 1976.

40. J. J. Coleman, P. D. Dapkus, D. E. Thompson, and D. R. Clarke, "The growth and characterization of metalorganic chemical vapor deposition (MOCVD) quantum well transport structures," J. Cryst. Growth, vo.l 55, pp. 207-212, 1981.

41. J. J. Coleman, P. D. Dapkus. and J. J. J. Yang, "Single-interface enhanced mobility structures by metalorganic chemical vapor deposition," Electron. Lett., vol. 17, pp. 606-608, 1981.

42. M. Kaever, T. J. Drummond, H. Morkoç, K. Hess, B. G. Streetman, and M. Ludowise, "Hall effect and mobility in heterojunction layers," J. Appl. Phys., vol. 53, pp. 1034-1036, 1982.

43. E. J. Thrush and J. E. A. Whiteaway, "Preparation and performance of GaAs/(GaAl)As double heterostructure lasers grown by the MOCVD process," *Int. Symp. on GaAs and Related Compounds, 1980*, Inst. Phys. Conf. Ser. 56, London, 1981, pp. 337-346.

44. R. D. Dupuis, L. A. Moudy, and P. D. Dapkus, "Preparation and properties of Ga$_{1-x}$Al$_x$As-GaAs heterojunctions grown by metallorganic chemical vapour deposition," *Int. Symp. on GaAs and Related Compounds, 1978*, Inst. Phys. Conf. Ser. 45, London, 1979, pp. 1-9.

45. H. C. Casey, Jr. and M. B. Panish, *Heterostructure Lasers, Part A*. Academic, New York, 1978.

46. D. Ankri and A. Scavennec, "Design and evaluation of a planar GaAlAs-GaAs bipolar transistor," *Electron. Lett.*, vol. 16, pp. 41-42, 1980.

47. H. Beneking and L. M. Su, "Double heterojunction NpN GaAlAs/GaAs bipolar transistor," *Electron. Lett.*, vol. 18, pp. 25-26, 1982.

48. D. Ankri, A. Scavennec, C. Besombes, C. Courbet, F. Heliot, and J. Riou, "Diffused epitaxial GaAlAs-GaAs heterojunction bipolar transistor for high-frequency operation," *Appl. Phys. Lett.*, vol. 40, pp. 816-818, 1982.

49. Y. Z. Liu, R. J. Anderson, I. Deyhimy, and L. R. Tomasetta, "Proton-bombardment isolated GaAlAs/GaAs charge-coupled devices," *Electron. Lett.*, vol. 16, pp. 327-328, 1980.

50. Y. Z. Liu, I. Deyhimy, R. J. Anderson, R. A. Milano, M. J. Cohen, J. S. Harris, Jr., and L. R. Tomasetta, "A backside-illuminated imaging AlGaAs/GaAs charge-coupled device," *Appl. Phys. Lett.*, vol. 37, pp. 803-805, 1980.

51. Y. Z. Liu, R. J. Anderson, R. A. Milano, and M. J. Cohen, "Effect of heterojunction spike on the quantum efficiency of an AlGaAs/GaAs heterojunction charge-coupled device," *Appl. Phys. Lett.*, vol. 40, pp. 967- 969, 1982.

52. D. C. Tsui and R. A. Logan, "Observation of two-dimensional electrons in LPE-grown GaAs-Al$_x$Ga$_{1-x}$As heterojunctions," *Appl. Phys. Lett.*, vol. 35, pp. 99-101, 1979.

53. R. W. Glew, "Hall mobility enhancement in GaAs-GaAlAs multilayer structures," *Phys. Stat. Sol.*, vol. 59A, pp. K179-K182, 1980.

54. R. W. Glew and M. Halberstadt, "Modulation-doped GaAs-GaAlAs multilayer structures," Int. Symp. on GaAs and Related Compounds, 1980, Inst. Phys. Conf. Ser. 56, London, 1981, pp. 731-740.

55. C. M. Garner, Y. D. Shen, J. S. Kim, G. L. Pearson, and W. E. Spicer, "Auger profiling of abrupt LPE $Al_xGa_{1-x}As$-GaAs heterojunctions," J. Appl. Phys., vol. 48, pp. 3147-3149, 1977.

56. A. Chandra and L. F. Eastman, "Rectification at n-n GaAs:(Ga,Al)As heterojunctions," Electron. Lett., vol. 15, pp. 90-91, 1979.

57. C. M. Garner, C. Y. Su, Y. D. Shen, C. S. Lee, G. L. Pearson, and W. E. Spicer, "Interface studies of $Al_xGa_{1-x}As$-GaAs heterojunctions," J. Appl. Phys., vol. 50, pp. 3383-3388, 1979.

58. R. Dingle, W. Wiegmann, and C. H. Henry, "Quantum states of confined carriers in very thin $Al_xGa_{1-x}As$-GaAs-$Al_xGa_{1-x}As$ heterostructures," Phys. Rev. Lett., vol. 33, pp. 827-830, 1974.

59. R. Dingle, H. L. Störmer, A. C. Gossard, and W. Wiegmann, "Electronic properties of modulation-doped GaAs-AlGaAs heterojunction superlattices," Int. Symp. on GaAs and Related Compounds, 1978, Inst. Phys. Conf. Ser. 45, London, 1979, pp. 248-255.

60. S. Hiyamizu, T. Mimura, T. Fujii, and K. Nanb, "High mobility of two-dimensional electrons at the GaAs/n-AlGaAs heterojunction interface," Appl. Phys. Lett., vol. 37, pp. 805-807, 1980.

61. W. I. Wang, C. E. C. Wood, and L. F. Eastman, "Extremely high electron mobilities in modulation-doped GaAs-$Al_xGa_{1-x}As$ heterojunction superlatices," Electron. Lett., vol. 17, pp. 36-37, 1981.

62. R. Dingle, H. L. Störmer, A. C. Gossard, and W. Wiegmann, "Electronic properties of the GaAs-AlGaAs interface with applications to multi-interface heterojunction superlattices," Surface Sci., vol. 98, pp. 90-100, 1980.

63. D. C. Tsui, H. L. Störmer, A. C. Gossard, and W. Wiegmann, "Two-dimensional electrical transport in GaAs-$Al_xGa_{1-x}As$ multilayers at high magnetic fields," Phys. Rev. B, vol. 21, pp. 1589-1595, 1980.

64. H. L. Störmer and W. T. Tsang, "Summary abstract: Two-dimensional hole gas at a semiconductor heterojunction interface," J. Vac. Sci. Technol., vol. 17, pp. 1130-1131, 1980.

65. K. Hess, "Impurity and phonon scattering in layered structures," Appl. Phys. Lett., vol. 35, pp. 484-486, 1979.

66. T. J. Drummond, H. Morkoç, K. Hess, and A. Y. Cho, "Experimental and theoretical mobility of modulation-doped $Al_xGa_{1-x}As/GaAs$ heterostructures grown by molcular beam epitaxy," J. Appl. Phys., vol. 52, pp. 5231-5234, 1981.

67. K. Hess, "Lateral transport in superlattices," 3rd Int. Conf. on Hot Electrons, Montpellier, France, published in Journal de Physique, Oct. 1981.

68. L. C. Witkowski, T. J. Drummond, C. M. Stanchak, and H. Morkoç, "High mobilities in $Al_xGa_{1-x}As$-GaAs heterojunctions," Appl. Phys. Lett., vol. 37, pp. 1033-1035, 1980.

69. T. J. Drummond, H. Morkoç, and A. Y. Cho, "Dependence of electron mobility on spatial separation of electrons and donors in $Al_xGa_{1-x}As/GaAs$ heterostructures," J. Appl. Phys., vol. 52, pp. 1380-1386, 1981.

70. H. L. Störmer, A. Pinczuk, A. C. Gossard, and W. Wiegmann, "Influence of an undoped (AlGa)As spacer on mobility enhancement in GaAs-(AlGa)As superlattices," Appl. Phys. Lett., vol. 38, pp. 691-693, 1981.

71. L. C. Witkowski, T. J. Drummond, S. A. Barnett, H. Morkoç, A. Y. Cho, and J. E. Greene, "High mobility GaAs-$Al_xGa_{1-x}As$ single-period modulation-doped heterojunctions," Electron. Lett., vol. 17, pp. 126-128, 1981.

72. P. Delescluse, M. Laviron, J. Chaplart, D. Delagebeaudeuf, and N. T. Linh, "Transport properties in GaAs-$Al_xGa_{1-x}As$ heterostructures and mesfet application," Electron. Lett., vol. 17, pp. 342-344, 1981.

73. T. J. Drummond, W. Kopp, and H. Morkoç, "Three-period (AlGa)As/GaAs heterostructures with extremely high mobilities," Electron. Lett., vol. 17, pp. 442-444, 1981.

74. T. J. Drummond, W. Kopp, M. Keever, H. Morkoç, and A. Y. Cho, "Electron mobility in single and multiple-period modulation-doped (Al,Ga)As/GaAs heterostructures," J. Appl. Phys., vol. 53, pp. 1023-1027, 1982.

75. H. L. Störmer, A. C. Gossard, W. Wiegmann, and K. Baldwin, "Dependence of electron mobility in modulation-doped GaAs-(AlGa)As heterojunction interfaces on electron density and Al concentration," Appl. Phys. Lett., vol. 39, pp. 912-914, 1981.

76. T. J. Drummond, R. Fischer, H. Morkoç, and P. Miller, "Influence of substrate temperature on the mobility of modulation-doped $Al_xGa_{1-x}As$/GaAs heterostructures grown by molecular beam epitaxy," Appl. Phys. Lett., vol. 40, pp. 430-432, 1982.

77. F. Stern and W. E. Howard, "Properties of semiconductor surface inversion layers in the electric quantum limit," Phys. Rev., vol. 163, pp. 816-835, 1967.

78. P. J. Price, "Two-dimensional electron transport in semiconductor layers, II: Screening," J. Vac. Sci. Technol., vol. 19, p. 599-604, 1981.

79. T. J. Drummond, W. Kopp, R. Fischer, and H. Morkoç, "Influence of AlAs mole fraction on the electron mobility of (Al,Ga)As/GaAs heterostructures," J. Appl. Phys., vol. 53, pp. 1028-1029, 1982.

80. A. Pinczuk, J. Worlock, H. L. Störmer, R. Dingle, W. Wiegmann, and A. C. Gossard, "Intersubband spectroscopy of two-dimensional electrn gases: Coulomb interactions," Solid State Commun., vol. 36, pp. 43-46, 1980.

81. H. L. Störmer, A. C. Gossard, and W. Wiegmann, "Observation of intersubband scattering in a 2-dimensional electron system," Solid State Commun., vol. 41, pp. 707-709, 1982.

82. T. J. Drummond, W. Kopp, H. Morkoç, K. Hess, A. Y. Cho, and B. G. Streetman, "Effect of background doping on the electron mobility of (Al,Ga)As/GaAs heterostructures," J. Appl. Phys., vol. 52, pp. 5689-5690, 1982.

83. H. Morkoç, T. J. Drummond, W. Kopp, and R. Fischer, "Influence of substrate temperature on the morphology of $Al_xGa_{1-x}As$ grown by molecular beam epitaxy," J. Electrochem. Soc., vol. 129, pp. 824-826, 1982.

84. C. Weisbuch, R. Dingle, A. C. Gossard, and W. Wiegmann, "Optical properties and interface disorder of GaAs-$Al_xGa_{1-x}As$ multi-quantum well structures," Int. Symp. on GaAs and Related Compounds, 1980, Inst. Phys. Conf. Ser. 56, London, 1981, pp. 711-720.

85. D. V. Lang and R. A. Logan, "A search for interface states in an LPE GaAs-$Al_xGa_{1-x}As$ heterojunction," Appl. Phys. Lett., vol. 32, pp. 683-684, 1977.

86. R. C. Miller and W. T. Tsang, "Al-Ga disorder in $Al_xGa_{1-x}As$ alloys grown by molecular beam epitaxy," Appl. Phys. Lett., vo. 39, pp. 334-335, 1981.

87. H. L. Störmer, A. C. Gossard, and W. Wiegmann, "Backside-gated modulation-doped GaAs-(AlGa)As heterojunction interface," Appl. Phys. Lett., vol. 39, pp. 493-495, 1981.

88. T. J. Drummond, H. Morkoç, S. L. Su, R. Fischer, and A. Y. Cho, "Enhanced mobility in inverted $Al_xGa_{1-x}As$/GaAs heterojunctions: Binary on top of ternary," Electron. Lett., vol. 17, pp. 870-871, 1981.

89. H. Morkoç, T. J. Drummond, and R. Fischer, "Interfacial properties of (Al,Ga)As/GaAs structures: Effect of substrate temperature during growth by molecular beam epitaxy," J. Appl. Phys., vol. 53, pp. 1030-1033, 1982.

90. H. Morkoç, T. J. Drummond, R. Fischer, and A. Y. Cho, "Moderate mobility enhancement in single period $Al_xGa_{1-x}As$/GaAs heterojunctions with GaAs on top," J. Appl. Phys., vol. 53, pp. 3321-3323, 1982.

91. W. I. Wang, S. Judaprawira, C. E. C. Wood, and L. F. Eastman, "Molecular beam epitaxial GaAs-$Al_xGa_{1-x}As$ heterostructures for metal semiconductor field effect transistor applications," Appl. Phys. Lett., vol. 38, pp. 708-710, 1981.

92. T. J. Drummond, M. Keever, and H. Morkoç, "Comparison of single and multiple-period modulation-doped $Al_xGa_{1-x}As$/GaAs heterostructures for FETs," Jpn. J. Appl. Phys., vol. 21, pp. L65-L67, 1982.

93. M. Heiblum, M. I. Nathan, and C. A. Chang, "Characteristics of AuGeNi ohmic contacts to GaAs," Solid-State Electron., vol. 25, pp. 185-195, 1982.

94. M. N. Yoder, "Ohmic contacts in GaAs," Solid-State Electron., vol. 23, pp. 117-119, 1980.

95. M. Wittmer, R. Pretorius, J. W. Mayer, and M. A. Nicolet, "Investigation of the Au-Ge-Ni system used for alloyed contacts to GaAs," Solid-State Electron., vol. 20, pp. 433-439, 1977.

96. K. Heime, U. König, E. Kohn, and A. Wortman, "Very low resistance Ni-AuGe-Ni contacts to n-GaAs," Solid-State Electron., vol. 17, pp. 835-837, 1974.

97. D. C. Miller, "The alloying of gold and gold alloy ohmic contact metallizations with gallium arsenide," *J. Electrochem. Soc.*, vol. 127, pp. 467-475, 1980.

98. K. K. Shih and J. M. Blum, "Contact resistances of Au-Ge-Ni, Au-Zn and Al to III-V compounds," *Solid-State Electron.*, vol. 15, pp. 1177-1180, 1972.

99. B. L. Sharma, "Ohmic contacts to III-V compound semiconductors," *Semiconductors and Semimetals*. Academic Press, Inc., New York, 1981, vol. 15, pp. 1-38.

100. V. L. Rideout, "A new review of the theory and technology for ohmic contacts to group III-V compound semiconductors," *Solid-State Electron.*, vol. 18, pp. 541-550, 1975.

101. O. Aina, W. Katz, and B. J. Baliga, "Low-temperature sintered AuGe/GaAs ohmic contact," *J. Appl. Phys.*, vol. 53, pp. 777-780, 1982.

102. J. G. Werthen and D. R. Scifres, "Ohmic contacts to n-GaAs using low-temperature anneal," *J. Appl. Phys.*, vol. 52, pp. 1127-1129, 1981.

103. A. M. Andrews and N. Holonyak, Jr., "Properties of n-type Ge-Doped epitaxial GaAs layers grown from Au-rich melts," *Solid-State Electron.*, vol. 15, pp. 601-604, 1972.

104. Cameca Instruments, Inc., Technical Information, 1979.

105. J. D. Oberstar, "Encapsulation and implantation studies of InP," Ph.D. dissertation, University of Illinois at Urbana-Champaign, 1982. Also *Coordinated Science Laboratory Report R-958, UILU-ENG 82-8224*.

106. H. Morkoç, S. G. Bandy, R. Sankaran, G. A. Antypas, and R. L. Bell, "A study of normally-off and normally-on $Al_{0.5}Ga_{0.5}As$ heterojunction gate FETs (HJFET)," *IEEE Trans. on Electron Dev.*, vol. ED-25, pp. 619-627, 1978.

107. K. Hess and C. T. Sah, "Hot carriers in silicon surface inversion layers," *J. Appl. Phys.*, vol. 45, pp. 1254-1257, 1973.

108. B. K. Ridley, "The electron-phonon interaction in quasi-two-dimensional semiconductor quantum-well structures," *Phys. Rev.*, to be published.

109. K. Hess, N. Holonyak, Jr., W. D. Laidig, B. A. Vojak, J. J. Coleman, and P. D. Dapkus, "Hot electrons and phonons in quantum-well $Al_xGa_{1-x}As$-GaAs heterostructures," *Solid State Commun.*, vol. 34, pp. 749-752, 1980.

110. K. Hess, "Phenomenological physics of hot carriers in semiconductors," *Physics of Nonlinear Transport in Semiconductors*, edited by D. K. Ferry, J. R. Barker, and C. Jacoboni. Plenum Press, New York-London, 1979, pp. 1-51.

111. H. Weiss, "Magnetoresistance," *Semiconductors and Semimetals*, edited by R. K. Willardson and A. C. Beer. Academic, New York, 1966, pp. 315-376.

112. K. Seeger, *Semiconductor Physics*. Springer-Verlag, Berlin, 1973.

113. T. C. Hsieh, private communication.

114. P. J. Price, "Hot electrons in a GaAs heterolayer at low temperature," *J. Appl. Phys.*, vol. 53, pp. 6863-6866, 1982.

115. S. Datta and B. J. Hunsinger, "Analysis of surface waves using orthogonal functions," *J. Appl. Phys.*, vol. 49, pp. 475-479, 1978.

116. T. H. Glisson, J. R. Hauser, M. A. Littlejohn, K. Hess, B. G. Streetman, and H. Shichijo, "Monte Carlo simulation of real-space electron transfer in GaAs-AlGaAs heterostructures," *J. Appl. Phys.*, vol. 51, pp. 5445-5449, 1980.

117. S. M. Sze, *Physics of Semiconductor Devices*, 2nd ed. John Wiley and Sons, New York, 1981.

118. T. H. Ning, "Hot-electron emission from silicon into silicon dioxide," *Solid-State Electron.*, vol. 21, pp. 273-282, 1978.

119. K. Hess, A. Neugroschel, C. C. Shiue, and C. T. Sah, "Non-ohmic electron conduction in silicon surface inversion layers at low temperatures," *J. Appl. Phys.*, vol. 46, pp. 1721-1727, 1975.

120. B. Hakki and S. Knight, "Microwave phenomena in bulk GaAs," *IEEE Trans. Electron. Dev.*, vol. ED-13, pp. 94-105, 1966.

121. D. V. Lang and R. A. Logan, "Trapping characteristics and a donor-complex (DX) model for the persistent-photoconductivity trapping center in Te-doped $Al_xGa_{1-x}As$," *Phys. Rev. B*, vol. 19, pp. 1015-1030, 1979.

122. B. Bereznak, "Measurements of persistent photoconductivity in aluminum gallium arsenide/gallium arsenide heterostructures," M.S. thesis, University of Illnois at Urbana-Champaign, 1982.

123. D. V. Lang and R. A. Logan, "Large-lattice-relaxation model for persistent photoconductivity in compound semiconductors," Phys. Rev. Lett., vol. 39, pp. 635-639, 1977.

124. R. J. Nelson, "Long-lifetime photoconductivity effect in n-type GaAlAs," Appl. Phys. Lett., vol. 31, pp. 351-353, 1977.

125. R. H. Bube, Photoconductivity of Solids. John Wiley and Sons, New York, 1960.

126. T. J. Drummond, W. Kopp, R. Fischer, H. Morkoç, R. E. Thorne, and A. Y. Cho, "Photoconductivity effects in extremely high mobility modulation-doped (Al,Ga)As/GaAs heterostructures," J. Appl. Phys., vol. 53, pp. 1238-1240, 1982.

127. A. K. Saxena, "Photoconductivity storage in $Ga_{1-x}Al_xAs$ alloys at low temperatures," Solid-State Electron., vol. 25, pp. 127-131, 1981.

128. J. W. Farmer and D. R. Locker, "Persistent photoconductivity in thin epitaxial GaAs," J. Appl. Phys., vol. 52, pp. 5718-5721, 1981.

129. K. Hess and N. Holonyak, Jr., "Hot electrons in layered semiconductors," Physics Today, vol. 33, no. 10, pp. 90-98, 1980.

130. N. Holonyak, Jr., R. M. Kolbas, W. D. Laidig, M. Altarelli, R. D. Dupuis, and P. D. Dapkus, "Phonon-sideband MO-CVD quantum-well $Al_xGa_{1-x}As$-GaAs heterostructure lasers," Appl. Phys. Lett., vol. 34, pp. 502-505, 1979.

131. N. Holonyak, Jr., R. M. Kolbas, W. D. Laidig, B. A. Vojak, K. Hess, R. D. Dupuis, and P. D. Dapkus, "Phonon-assisted recombination and stimulated emission in quantum-well $Al_xGa_{1-x}As$-GaAs heterostructures," J. Appl. Phys., vol. 51, pp. 1328-1337, 1980.

132. N. Holonyak, Jr., R. M. Kolbas, R. D. Dupuis, and P. D. Dapkus, "Quantum-well heterostructure lasers," IEEE J. Quant. Electron., vol. QE-16, pp. 170-185, 1980.

133. N. Holonyak, Jr., W. D. Laidig, B. A. Vojak, K. Hess, J. J. Coleman, P. D. Dapkus, and J. Bardeen, "Alloy clustering in $Al_xGa_{1-x}As$-GaAs quantum-well heterostructures," Phys. Rev. Lett., vol. 45, pp. 1703-1706, 1980.

VITA

Mark Robert Keever was born on June 19, 1955 in Council Bluffs, Iowa. He attended Iowa State University in Ames, Iowa where he graduated "with distinction" in May, 1977 with a Bachelor of Science degree in Physics and Mathematics. He has been attending the University of Illinois at Urbana-Champaign since September, 1977. He received a Master of Science degree in Physics in January, 1979. While in the Physics Department he served as a teaching assistant and was regularly cited by his students for excellence in undergraduate teaching. In the fall of 1979, he transferred to the Electrical Engineering Department and became a research assistant in the Coordinated Science Laboratory.

Mr. Keever has been elected to Phi Eta Sigma, Sigma Pi Sigma (Physics), Pi Mu Epsilon (Math), and Phi Beta Kappa honor societies. He is a member of the American Physical Society and the Institute of Electrical and Electronics Engineers. He is presently a candidate for the degree of Doctor of Philosophy from the University of Illinois.

4-

DT